Coexistence of Magnetic and Superconducting Order in the High-T$_c$ Materials

Brian Møller Andersen

Ørsted Laboratory
Niels Bohr Institute
University of Copenhagen

Ph.D. thesis

Preface

The studies of the high-temperature superconductors is still not settled 17 years after their discovery. To date more than 120,000 papers dealing with these materials have been published, and our knowledge about their properties is quite remarkable indeed. Nevertheless, the understanding of their phase diagram remains an outstanding challenge in condensed matter theory and there is no consensus on the correct effective model for these materials.

The systems are characterized by strong correlation, large Coulomb repulsions, low dimensionality, and a competition between a plethora of different phases that are separated by small energy differences. The high-T_c materials are antiferromagnetic Mott insulators at half-filling, and the question is what happens when electrons are progressively removed from the CuO_2 planes?

Like a good game, enormous complexities arise in spite of the fact that the rules are simple: anti-align adjacent spins but allow for holes to hop. Then find the state that simultaneously minimizes the kinetic energy of the doped holes *and* the exchange energy. The tricky business arises because these two terms are equally important and *compete*: a localized hole with a spatially confined wavefunction has a high kinetic energy. Therefore, it tends to delocalize by hopping to neighboring sites. In doing so, it scrambles the antiferromagnetic background resulting in high energy exchange bonds. It is fascinating that in spite of these simple rules, the solutions appear to be surprisingly rich and complex. For instance, the notion of self-organized topological spin and charge structures inhomogeneous at the nano length-scale is a robust feature of models that correctly include the rules of the game. Experimentally, the existence of these electronic stripes is firmly established for the lanthanum based high-T_c compounds. In the second half of the thesis, the origin and experimental consequences of the stripe ordering will be discussed.

In each chapter of this thesis, the main part has been (or is about to be) published in a physical journal. The other sections in each chapter are intended to clarify the calculations and explain the motivation for the study. This includes a presentation of experimental results as well as a discussion of

i

previous theoretical work. In a few chapters, this has caused a brief overlap between these background sections and the introductory part of the article. It would have been easier to simply assemble the articles in the appendices, but in the present format I hope that the thesis has become more readable for those who actually embark on that journey.

I am grateful to my advisor Per Hedegård for ideas, and for his encouragement throughout the years. I have benefitted from numerous stimulating discussions with H. Bruus, V. Cheianov, N.B. Christensen, J.C. Davis, K. Flensberg, M. Granath, J. Jensen, B. Lake, K. Lefmann, D. Mcmorrow, J. Paaske, H.M. Rønnow, S. Sachdev, K.M. Shen, S.C. Zhang, and M. Zvonarev. Lastly, I thank Christy Lee, my family and my friends for their encouragement and patience throughout the past few years.

Brian Møller Andersen
Copenhagen, May 2004.

'. . . I like arguments,' said the Rocket.

'I hope not,' said the Frog complacently. 'Arguments are extremely vulgar, for everybody in good society holds exactly the same opinions. Good-bye a second time; I see my daughters in the distance;' and the little Frog swam away.

'You are a very irritating person,' said the Rocket, 'and very ill-bred. I hate people who talk about themselves, as you do, when one wants to talk about oneself, as I do. It is what I call selfishness, and selfishness is a most detestable thing especially to any one of my temperament, for I am well known for my sympathetic nature. In fact, you should take example by me, you could not possibly have a better model. . . '

'There is no good talking to him,' said a Dragon-fly, who was sitting on the top of a large brown bulrush; 'no good at all, for he has gone away.'

'Well, that is his loss, not mine,' answered the Rocket. 'I am not going to stop talking to him merely because he pays no attention. I like hearing myself talk. It is one of my greatest pleasures. I often have long conversations all by myself, and I am so clever that sometimes I don't understand a single word of what I am saying.'

- "The Remarkable Rocket" by Oscar Wilde

Contents

1 Introduction to the high-T$_c$ materials

The understanding of the electronic structure of the high-T$_c$ materials is the problem of doped Mott insulators. What happens when we dilute a quasi two-dimensional antiferromagnetic Mott insulator? Experimentally, it was found in 1986 by Bednorz and Müller that La$_{2-x}$Ba$_x$CuO$_2$ becomes a superconductor with $T_c = 30$K[1]. Because of the poor conductivity in the normal state, this discovery was unexpected and prompted intense activity in the field of ceramic oxides. Materials such has YBa$_2$Cu$_3$O$_{7-\delta}$ and Bi$_2$Sr$_2$CaCu$_2$O$_{8+\delta}$, both of which contain two CuO$_2$ planes per unit cell, were found to have maximum T$_c$'s around 80-90 K. To date the trilayer material HgBa$_2$Ca$_2$Cu$_3$O$_{8+x}$ has the highest T$_c$ of 134 K at atmospheric pressure. The mentioned materials follow the general empirical rule that the critical temperature T$_c$ scales with the number n of CuO$_2$ layers in the unit cell up to $n = 3$. For $n > 4$, T$_c$ drops monotonically, a mystery that was only recently resolved[2]: for $n > 1$ the possibility of inter-layer tunnelling of Cooper pairs initially increase T$_c$, but for $n > 3$ a charge imbalance in the CuO$_2$ stack causes the inner layers to contain less carriers than the outer, effectively pushing the inner layers toward the underdoped regime even though the overall doping of the entire material is at optimal doping. As will be discussed in more detail in later chapters, the underdoped region supports several orders that *compete* with the superconductivity. In inner layers therefore nucleate this competing order which suppress the superconductivity.

Having introduced some of the main characters, I review below some of their basic experimental properties and the models proposed to describe them.

1.1 Crystal structure and the phase diagram

The crystal structure of the mother material, La$_2$CuO$_4$, of cuprate superconductors consists of CuO$_2$ planes and insulating LaO spacer layers. In the CuO$_2$ planes each copper ion is surrounded by four oxygen ions. Two additional apical O ions positioned out of the planes result in each Cu ion being surrounded by a octahedra of oxygens forming a perovskite structure. The octahedron is elongated since the distance to the apical oxygen ions is large compared to the planar Cu-O separation. Therefore, the planar Cu-O bonds dominate. All other cuprate materials also consist of copper-oxygen planes, the electron-doped ones missing the apical oxygen ions.

In the bulk crystal the planar oxygen is in the O^{2-} valence state with all three p orbitals occupied completing the p shell. Lanthanum releases three electrons becoming La^{3+} and to conserve charge neutrality the copper atoms must have charge $4 \times 2 - 2 \times 3$, i.e. be in a Cu^{2+} state with nine electrons in the five d orbitals. Thus, Cu loses the $4s$ and one of the $3d$ electrons creating a *hole in the 3d shell* resulting in a net spin of 1/2 per copper ion. For each Cu^{2+} ion the

surrounding octahedron breaks the rotational invariance of the isolated ions lifting the degeneracy of the $3d$ orbitals. The state with the highest energy turns out to be the $3d_{x^2-y^2}$ state, which is therefore the state in which the hole resides.

The ceramic oxides are usually strongly insulating, and this is also the case for undoped copper oxides. The undoped materials are dominated by strong Coulomb electron-electron correlations confining the electrons of the crystal ions. Therefore, these materials are Mott insulators and not regular band insulators. In fact, from the odd number of electrons per unit cell, simple tight-binding band considerations (ignoring Coulomb interactions) erroneously predict a half-filled band, i.e. a metallic state.

A schematic phase diagram covering all the hole doped cuprate materials is shown in Fig. 1.1. Without any doping the system consists of a square spin 1/2 system. The spins order antiferromagnetically by superexchange involving virtual hopping processes and the finite Néel temperature T_N comes from the coupling between the CuO$_2$ planes.

With doping, the intervening layers mainly act as charge reservoirs. For
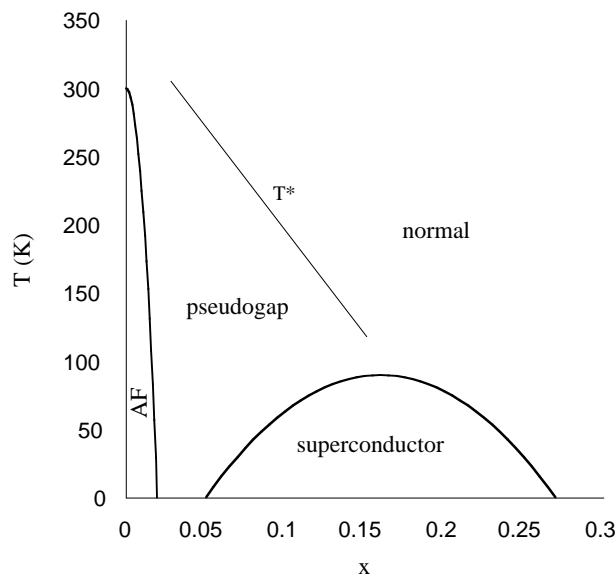
Figure 1.1: Schematic phase diagram (temperature T vs hole doping x) of the cuprates. At half-filling ($x = 0$) the materials are antiferromagnetic insulators. As holes are doped into the CuO$_2$ planes ($x > 0$) the system becomes superconducting at low temperatures and shows "strange" metallic behavior at higher temperature. The temperature T^* indicates a crossover from the "normal" to the pseudogap phase.

instance, upon replacing trivalent La^{3+} by divalent Sr^{2+} fewer electrons are available to the CuO$_2$ layers, corresponding to *hole doping*. The added holes occupy oxygen ions changing these from the O^{2-} to the O$^-$ configuration.

When increasing the doping x from half-filling the materials quickly loose their antiferromagnetic ordering, at least in its simplest commensurate form. At lower temperature the cuprates become superconducting.

The superconducting dome which peaks around $x \approx 0.15$, divides the phase diagram into an underdoped (T_c increasing with doping x), optimally doped (T_c maximum), and an overdoped regime (T_c decreasing).

In many respects the superconducting phase is similar to the conventional BCS superconductors, at least in the optimal and overdoped regimes. Exceptions include the pairing symmetry and the superfluid density. The gap symmetry is known to be $d_{x^2-y^2}$ from a large number of experiments including spectroscopy and phase sensitive techniques such as Josephson tunnelling and SQUID magnetometry. The low superfluid density extracted from muon spin relaxation measurements presumably derives from the low carrier density of the doped Mott insulator[3, 4]. This leads to relatively small phase-stiffness and poor screening which cause large phase fluctuations of the superconducting order parameter and a non-mean field transition. Experimentally, the maximum value of the pairing gap is found to *decrease* with doping, which is opposite to the doping dependence of the superfluid density[5]. This has led to the suggestion that in general the phase coherence energy scale and the pairing energy scale are separated[6]. Therefore, in the underdoped regime, preformed singlet pairs may form at a temperature $T^* > T_c$ giving rise to a gap in the spin and charge spectrum. T_c is the temperature at which the pairs Bose condense into the superconducting state. In fact, this is one of many suggestions for the origin of the pseudogap phase which exists in the underdoped regime above T_c.

Experiments sensitive to the pseudogap find a partial suppression of low-energy spectral weight when decreasing the temperature below $T > T_c$. Historically the pseudogap state was first discovered by nuclear magnetic resonance measurements showing that the onset of a decreasing spin-lattice relaxation rate occurs well above T_c. To date the pseudogap phase is well established by a large number of experimental probes. In particular, angular resolved photoemission has shown from the position of the leading edge that the gap exhibits the same $d_{x^2-y^2}$-wave symmetry as the superconducting pairing gap[7, 8]. The pseudogap temperature scale T^* falls monotonically with increased doping and merges with T_c near the top of the superconducting dome. The true origin of the pseudogap phase remains unknown but there exists many proposals including various exotic types of order. The position of the pseudogap state in the phase diagram shows that it necessarily contains important information of the electronic state of a doped Mott insulator *before* it becomes a superconductor. Therefore, one may hope that identifying the origin of the pseudogap phase can unlock the mystery of the high-T_c materials. It still remains controversial whether the pseudogap is caused by true long-range order or a precursor phenomenon as mentioned above. Recent experimental support for the latter, comes from measurements of the Nernst effect by Ong *et al.*[9] In the underdoped region of the phase diagram they find a large Nernst signal which

persists well above T_c. This is strong evidence that the pseudogap state contains vortices. In later chapters I return to the discussion of the order that characterize the pseudogap phase and how to identify it experimentally.

The normal state is everything but "normal", and has been dubbed more appropriately "the strange metal phase". The conventional BCS theory for superconductivity in metals rests on the Fermi-liquid foundation which seems unable to support the electronic structure in the normal state of the cuprates. A notorious example of the unusual behavior is given by the in-plane resistivity near optimal doping which remains linear in temperature over several decades of temperature T. This has led to the suggestion of a marginal Fermi liquid description of the strange metal phase[10, 11]. In this model the electrons scatter off a bosonic spectrum that remain linear in energy up to T after which it becomes constant. Thus, the only energy scale that enter is the temperature T. This phenomenology has been supported by photoemission data that shows a linear scattering rate as a function of energy[12, 13]. Further discussion of the properties in the pseudogap and strange-metal phases can be found throughout this thesis and in recent reviews[14, 15].

1.2 Electronic models

The microscopic Hamiltonian that correctly describes the physics of the cuprates is given by "the theory of everything"

$$\mathcal{H} = \sum_i \frac{\mathbf{p}_i^2}{2m_e} + \sum_{ij} \frac{e^2}{|\mathbf{r}_i - \mathbf{r}_j|} + \sum_i \frac{\mathbf{P}_i^2}{2M} + \sum_{ij} \frac{Z_i Z_j e^2}{|\mathbf{R}_i - \mathbf{R}_j|} + \sum_{ij} \frac{Z_i e^2}{|\mathbf{R}_i - \mathbf{r}_j|} \quad (1.1)$$

which includes all the Coulomb interactions between all the particles and constitute an immense problem since the number of particles is of order 10^{23}. Unfortunately, we do not know how to solve this model for many particles and resort therefore to constructing effective models that capture the essential physics.

As mentioned above, if we ignore the interactions we would predict a band metal with a half-filled conduction band since the number of electrons in each unit cell is odd. The failure of the single-particle band model to describe the undoped cuprates lies in the on-site electron-electron Coulomb repulsion U which is much larger than the bandwidth. As a consequence, the charge fluctuations are strongly suppressed and the material exhibits a Mott gap as seen for instance in the optical excitation gap of a few eV. In the cuprates, the charge transfer gap Δ between the Cu and the O ions is smaller than the on-site Cu Coulomb interaction U. Thus these materials are correctly characterized as charge-transfer insulators[16]. To describe the low energy physics Emery[17] and Varma[18] proposed a three band Hubbard model that includes the hybridization of the copper $d_{x^2-y^2}$ and oxygen p_x and p_y orbitals and the Coulomb interaction U on doubly occupied Cu sites.

However, by studying a CuO_4 cluster containing two holes, Zhang and Rice[19] showed that a hole located at the Cu site hybridizes strongly with a hole located on a linear combination of the four surrounding O hole states forming a singlet and a triplet state. A large energy difference between the singlet and triplet states allows one to project out the triplets, resulting in a effective low-energy spin singlet subspace in which the hole at the O site has been replaced by a spin singlet state centered at the Cu site. In this way the oxygens have been mapped out of the problem and the added hole is equivalent to removing one Cu spin 1/2 from the 2D square lattice of Cu spins. The resulting one-band model proposed was the $t - J$ Hamiltonian

$$\mathcal{H} = -t \sum_{\langle i,j \rangle \sigma} P \left(\hat{c}_{i\sigma}^\dagger \hat{c}_{j\sigma} + \text{H.c.} \right) P + J \sum_{\langle i,j \rangle} \left(\mathbf{S}_i \cdot \mathbf{S}_j - \frac{\hat{n}_i \hat{n}_j}{4} \right), \qquad (1.2)$$

where $J = 4t^2/U$ is the exchange interaction between neighboring spins. Here, $\mathbf{S}_i$ denotes the spin 1/2 operator, $n_i = \hat{c}_{i\uparrow}^\dagger \hat{c}_{i\uparrow} + \hat{c}_{i\downarrow}^\dagger \hat{c}_{i\downarrow}$ the charge density operator, and P is the projection operator that excludes double occupancy. At half-filling this reduces to the Heisenberg model with antiferromagnetic exchange coupling. Away from half filling the ground state of the $t-J$ model is unknown in two dimensions.

The $t - J$ model is realized as the large-U limit of the well-known single-band Hubbard model given by

$$\mathcal{H} = -t \sum_{\langle i,j \rangle \sigma} \hat{c}_{i\sigma}^\dagger \hat{c}_{j\sigma} + U \sum_i \hat{n}_{i\uparrow} \hat{n}_{i\downarrow}. \qquad (1.3)$$

The *delocalizing* kinetic energy term $-t \sum_{\langle i,j \rangle \sigma} \hat{c}_{i\sigma}^\dagger \hat{c}_{j\sigma}$ allows for hopping between nearest-neighbor sites $\langle i, j \rangle$ whereas the *localizing* term $U \sum_i \hat{n}_{i\uparrow} \hat{n}_{i\downarrow}$ describes the competing on-site Coulomb repulsion with $\hat{n}_{i\sigma} = \hat{c}_{i\sigma}^\dagger \hat{c}_{i\sigma}$. The role of the U interaction is to split the half-filled conduction band into an empty upper Hubbard band and a filled lower Hubbard band. Since the first electron-removal state corresponds to the Zhang-Rice singlet band the cuprates are effectively equivalent to a Mott-Hubbard insulator with the Zhang-Rice band having the role of the lower Hubbard band. The upper Hubbard band is separated from the lower band by the charge transfer gap Δ. In this way the one-band Hubbard model simulates the charge transfer nature of the materials by an effective Hubbard gap.

1.3 A minimal model

In the last section I advocated that the one-band Hubbard model is the minimal model describing the carriers in the high-T_c materials. Unfortunately this deceptively simple model still constitutes a problem of immense complexity

and no exact solutions are known in the general 2D case. Luckily, life becomes easier when dealing with ordered states where a mean-field description often suffices. In principle, since the CuO_2 planes the high-T_c materials are 2D, the Mermin-Wagner-Coleman theorem prohibits true long-range order at any non-zero temperature. The fact that these materials do have a large T_{Neel} at half filling is caused by the inter-layer exchange coupling. Thus, when dealing with ordering in the 2D CuO_2 planes away from $T = 0$ one should remember the quasi-2D-ness of these planes.

In the antiferromagnetic phase the magnetic order parameter is given by

$$M_i = me^{i\mathbf{Q}\cdot\mathbf{R_i}} = \begin{cases} +m & \text{if } \mathbf{R}_i \text{ belongs to sublattice A} \\ -m & \text{if } \mathbf{R}_i \text{ belongs to sublattice B} \end{cases} \qquad (1.4)$$

where the bipartite lattice has been divided into two sublattices, A and B, hosting the spin-↑ and spin-↓ electrons, respectively. As for any magnetic order, M_i breaks the time-reversal invariance $\mathcal{T}\mathbf{S} = -\mathbf{S}$. Furthermore, antiferromagnetism breaks spin-rotation invariance and translational invariance. The spin density in Eqn. (1.4) is only invariant under translations of two lattice constants a. Concomitantly the reciprocal lattice vectors are integral multiples of $2\pi/2a = \pi/a$, and the Brillouin zone is halved.

The spin rotation invariance of the Hubbard model becomes manifest if we rewrite the interaction term $\hat{n}_{i\uparrow}\hat{n}_{i\downarrow}$ as follows

$$\hat{n}_{i\uparrow}\hat{n}_{i\downarrow} = c_{i\uparrow}^\dagger c_{i\uparrow} c_{i\downarrow}^\dagger c_{i\downarrow} = c_{i\uparrow}^\dagger c_{i\uparrow}(1 - c_{i\downarrow}^\dagger c_{i\downarrow}) = \hat{n}_{i\uparrow} - c_{i\uparrow}^\dagger c_{i\downarrow} c_{i\downarrow}^\dagger c_{i\uparrow} = \hat{n}_{i\uparrow} - \hat{S}_i^+ \hat{S}_i^-. \quad (1.5)$$

As usual, the spin $\frac{1}{2}$ lattice operator is given by

$$\hat{\mathbf{S}}_i = \frac{1}{2} \sum_{\alpha\beta} \hat{c}_{i\alpha}^\dagger \boldsymbol{\sigma}_{\alpha\beta} \hat{c}_{i\beta}, \qquad (1.6)$$

where $\boldsymbol{\sigma} = (\sigma_x, \sigma_y, \sigma_z)$ denotes the vector consisting to the Pauli matrices. Similarly we have

$$\hat{n}_{i\uparrow}\hat{n}_{i\downarrow} = \hat{n}_{i\downarrow} - \hat{S}_i^- \hat{S}_i^+. \qquad (1.7)$$

From the square of $\hat{S}_i^z$ we have

$$(\hat{S}_i^z)^2 = \frac{1}{4}(\hat{n}_{i\uparrow} - \hat{n}_{i\downarrow})^2 = \frac{1}{4}(\hat{n}_{i\uparrow} + \hat{n}_{i\downarrow} - 2\hat{n}_{i\uparrow}\hat{n}_{i\downarrow}) \qquad (1.8)$$

since $\hat{n}_{i\sigma}^2 = \hat{n}_{i\sigma}$ and $\hat{n}_{i\uparrow}\hat{n}_{i\downarrow} = \hat{n}_{i\downarrow}\hat{n}_{i\uparrow}$. Combining these three different expressions for $\hat{n}_{i\uparrow}\hat{n}_{i\downarrow}$ we get

$$\hat{n}_{i\uparrow}\hat{n}_{i\downarrow} = \frac{\hat{n}_{i\uparrow} + \hat{n}_{i\downarrow}}{2} - \frac{2}{3}\hat{\mathbf{S}}_i \cdot \hat{\mathbf{S}}_i. \qquad (1.9)$$

Therefore the on-site one band Hubbard model can be expressed as

$$\mathcal{H} = - \sum_{<ij>\sigma} \left[t_{ij} c_{i\sigma}^\dagger c_{j\sigma} + \text{H.c.} \right] - \mu \sum_i \hat{n}_i - \frac{2U}{3} \sum_i \hat{\mathbf{S}}_i \cdot \hat{\mathbf{S}}_i + \frac{UN}{2}, \qquad (1.10)$$

where $N = \sum_i \hat{n}_{i\uparrow} + \hat{n}_{i\downarrow}$. In the following we discard additive constants to the Hamiltonian since we are not interested in the total energy.

As can be seen explicitly from Eqn. (1.10) the Hubbard model is invariant under continuous SU(2) spin rotations. Thus if $|0\rangle$ denotes the ground state, by applying the symmetry operation to $|0\rangle$, $U|0\rangle$, we can transform it into a new ground state. Since the symmetry is continuous the ground state is infinitely degenerate. However, the physical system may pick out a unique state among this infinite manifold and break the symmetry spontaneously by spin ordering along the, say, z-direction. The remaining symmetry is U(1) corresponding to spin rotations about the z-axis. In this case there exist excitations (spin waves) with vanishing excitation energy at the ordering vector. This is an example of Goldstone's theorem. The Goldstone mode is the excitation that tries to push the system to one of the other ground states in the infinite manifold of ground states. Since these states all have the same energy the excitation energy for this transition is zero. Thus, the Goldstone mode tries to sample all ground states and in this sense restore the symmetry. Other examples of Goldstone modes include phonons in solids occurring due to broken translational invariance, ferromagnetic spin waves also from broken rotational invariance in spin space, and acoustic modes in Josephson junction arrays due to broken phase invariance.

In the more realistic case of the extended Hubbard model the longer ranged parts of the Coulomb interaction is also included

$$\mathcal{H} = - \sum_{<ij>,\sigma} \left[t_{ij} c_{i\sigma}^\dagger c_{j\sigma} + \text{H.c} \right] - \mu \sum_i \hat{n}_i - \frac{2U}{3} \sum_i \hat{\mathbf{S}}_i \cdot \hat{\mathbf{S}}_i - \frac{V}{2} \sum_{i,j} \hat{n}_i \hat{n}_j \quad (1.11)$$

where $\hat{n}_i = \hat{n}_{i\uparrow} + \hat{n}_{i\downarrow}$. Since in the last term $i \neq j$, this interaction term is identical under normal ordering

$$\hat{n}_i \hat{n}_j = \sum_{\sigma\sigma'} c_{i\sigma}^\dagger c_{j\sigma'}^\dagger c_{j\sigma'} c_{i\sigma}. \qquad (1.12)$$

This Hamiltonian remains SU(2) invariant under spin rotations since $[\hat{\mathbf{S}}_i, V\hat{n}_i\hat{n}_j] = 0$. This will be important later when we discuss transverse spin fluctuations since, as mentioned above, any state that breaks the continuous symmetry supports massless Goldstone bosons guaranteed by the relevant Ward-Takahashi identity.

At this junction we need make a serious decision as to which road we what to follow (many of which lead straight to hell). The hidden road to paradise is

the one where, with no further assumptions, one finds the d-wave superconductor. For now we shall be content with the fact that the d-wave superconductor exists and discuss the interesting physics of this phase and its possible coexistence with spin density wave order. Thus, we are interested in these ordered phases of Eqn. (1.11). To this end, we *assume* that V is actually a nearest neighbor *attraction* which in the mean-field decoupling leads to a d-wave superconducting state. We will not be deeply concerned with the microscopic origin of the attraction V. At the mean-field level the model (1.11) is a reduced effective model similar in methodology to the effective BCS Hamiltonian proposed for conventional superconductors. This being said, it has been shown by Simon *et al.*[20] that an effective attraction in the spin singlet channel is generated as a result of the mapping of the three-band Hubbard model to the one-band model. Furthermore, Daul *et al.*[21] argued that the appropriate model that incorporates the charge transfer nature of the cuprate Mott insulators is in fact the $t - U - J$ model. It was shown that the antiferromagnetic exchange term strongly enhances the pairing in the $d_{x^2-y^2}$-wave channel. This pairing tendency is exactly what we attempt to capture at the mean-field level of the attractive nearest neighbor interaction term in Eqn. (1.11).

The advantage of our approach is that it is simple and allows us to study various physical observable in the mixed state of d-wave superconductivity and spin density wave order. A similar approach has been taken by Martin *et al.*[22] who studied qualitatively the phase diagram of the effective minimal model. Later, it has been extensively used to obtain the electronic structure near impurities and vortices in d-wave superconductors on the verge of a spin density wave instability[23, 24].

In the following I will discuss some aspects of symmetry broken states in interacting Fermi systems. Therefore, it is convenient to use the tools of path integrals and Hubbard-Stratonovich transformations. The partition function, $Z = \mathrm{Tr}\exp(-\beta H)$ where $\beta = 1/kT$, can be represented using Grassmann coherent states c, c^*

$$Z = \int \mathcal{D}[c^*, c] \exp(-S[c, c^*]), \tag{1.13}$$

with the Euclidean action given by

$$S = \int d\tau \mathcal{L}[c^*, c] = \int d\tau \left(\sum_{i\sigma} c_{i\sigma}^* \partial_\tau c_{i\sigma} + \mathcal{H}[c^*, c] \right), \tag{1.14}$$

where $\mathcal{L}$ is the Lagrangian, and $\tau \in [0, \beta[$ is the Wick rotation of the time, $\tau = it$. The measure is defined as $\mathcal{D}[c^*, c] = \Pi_{i,\tau_i} dc_i^*(\tau_i) dc_i(\tau_i)$, which in discrete Matsubara space, $c_i(\tau) = \frac{1}{\beta} c_{i,n} \exp(-i\omega_n \tau)$, is $\mathcal{D}[c^*, c] = \Pi_{i,n} dc_{i,n}^* dc_{i,n}$ since the transformation is unitary and hence has Jacobian equal to unity.

The standard Gaussian integral identities for real bosonic vector fields

$$\int \mathcal{D}\varphi_i e^{-\frac{1}{2}\varphi_i A_{ij}\varphi_j + \varphi_i J_i} = [\det A]^{-\frac{1}{2}} e^{\frac{1}{2}J_i A_{ij}^{-1} J_j}, \qquad (1.15)$$

becomes for the single-band Hubbard model

$$\int \mathcal{D}\mathbf{M}_i e^{-\frac{1}{2}\frac{3}{4U}\mathbf{M}_i \cdot \mathbf{M}_i + \mathbf{M}_i \cdot \mathbf{S}_i} = C e^{\frac{1}{2}\frac{4U}{3}\mathbf{S}_i \cdot \mathbf{S}_i}, \qquad (1.16)$$

where C is an unimportant constant and the fermions are hidden in the spin operator $\hat{\mathbf{S}}_i = \frac{1}{2}\sum_{\alpha\beta} \hat{c}_{i\alpha}^\dagger \boldsymbol{\sigma}_{\alpha\beta} \hat{c}_{i\beta}$. It should be noted that the normal ordered interaction that enters the path integral (with Grassmann variables replacing the operators) is identical to the $\mathbf{S} \cdot \mathbf{S}$ term except from a constant $-UN/2$. The identity Eqn. (1.16) can be easily verified by completing the square on the left hand side

$$-\frac{1}{2}\frac{3}{4U}\mathbf{M}_i \cdot \mathbf{M}_i + \mathbf{M}_i \cdot \mathbf{S}_i = -\frac{1}{2}\frac{3}{4U}\left(\mathbf{M}_i - \frac{4U}{3}\mathbf{S}_i\right)^2 + \frac{2U}{3}\mathbf{S}_i^2, \qquad (1.17)$$

and shifting the integration variable $\mathbf{M}_i \rightarrow \mathbf{M}_i + \frac{4U}{3}\mathbf{S}_i$.
Likewise for a complex bosonic scalar field we have the identity

$$\int \mathcal{D}\Delta\mathcal{D}\Delta^* e^{-\frac{2}{V}\Delta_{ij\sigma\sigma'}^* \Delta_{ij\sigma\sigma'} + \Delta_{ij\sigma\sigma'}^* c_{j\sigma'} c_{i\sigma} + \Delta_{ij\sigma\sigma'} c_{i\sigma}^* c_{j\sigma'}^*} = C e^{\frac{V}{2}c_{i\sigma}^* c_{j\sigma'}^* c_{j\sigma'} c_{i\sigma}}, \qquad (1.18)$$

where, again, C is some constant. Again we can convince ourselves of this identity by completing the square $-\frac{2}{V}\Delta_{ij\sigma\sigma'}^* \Delta_{ij\sigma\sigma'} + \Delta_{ij\sigma\sigma'}^* c_{j\sigma'} c_{i\sigma} + \Delta_{ij\sigma\sigma'} c_{i\sigma}^* c_{j\sigma'}^* = -\frac{2}{V}(\Delta_{ij\sigma\sigma'}^* - \frac{V}{2}c_{i\sigma}^* c_{j\sigma'}^*)(\Delta_{ij\sigma\sigma'} - \frac{V}{2}c_{j\sigma'} c_{i\sigma}) + \frac{V}{2}c_{i\sigma}^* c_{j\sigma'}^* c_{j\sigma'} c_{i\sigma}$, shifting the integration variables $\Delta_{ij\sigma\sigma'} \rightarrow \Delta_{ij\sigma\sigma'} + \frac{V}{2}c_{j\sigma'} c_{i\sigma}$ and perform the gaussian integral C. Introducing these Hubbard-Stratonovich transformations at each site allows the partition function to be written in terms of the new auxiliary fields $\mathbf{M}_i$ and $\Delta_{ij\sigma\sigma'}$

$$Z = \int \mathcal{D}c\mathcal{D}c^* \mathcal{D}\mathbf{M}\mathcal{D}\Delta\mathcal{D}\Delta^* \exp(-S_{\text{eff}}), \qquad (1.19)$$

where the *effective* action is $S_{\text{eff}}(c^*, c, \mathbf{M}, \Delta) = \int d\tau \left(\sum_{i\sigma} c_{i\sigma}^* \partial_\tau c_{i\sigma} + H_{\text{eff}}(c^*, c)\right)$. In the effective Hamiltonian the Hubbard-Stratonovich fields $\mathbf{M}_i$ and $\Delta_{ij\sigma\sigma'}$ couple bilinearly to the fermions which can now be thought of as free fermions moving in a fluctuating background field. This can be seen explicitly from the form $H_{\text{eff}} = H_0 + H_{\text{int}} + H_{M,\Delta}$, with

$$\mathcal{H}_0 = -\sum_{<ij>\sigma} [t_{ij} c_{i\sigma}^* c_{j\sigma} + \text{H.c}] - \mu \sum_i n_i, \qquad (1.20)$$

and

$$\mathcal{H}_{\text{int}} = -\sum_i \mathbf{M}_i \cdot \mathbf{S}_i - \sum_{i,j\sigma\sigma'} \left[\Delta^*_{ij\sigma\sigma'} c_{i\sigma} c_{j\sigma'} + \Delta_{ij\sigma\sigma'} c^*_{j\sigma'} c^*_{i\sigma} \right], \qquad (1.21)$$

and lastly

$$\mathcal{H}_{M,\Delta} = \frac{3}{8U} \sum_i |\mathbf{M}_i|^2 + \frac{2}{V} \sum_{i,j\sigma\sigma'} \Delta^*_{ij\sigma\sigma'} \Delta_{ij\sigma\sigma'}. \qquad (1.22)$$

In these expressions the negative sign in the nearest neighbor interaction $-\frac{V}{2} \sum_{i,j} \hat{n}_i \hat{n}_j$ has already been incorporated so that $V > 0$.
Restricting the fields $\Delta_{ij\sigma\sigma'}$ to be of the form of singlet pairing

$$\Delta_{ij\sigma\sigma'} = \frac{\Delta_{ij}}{2} (\delta_{\sigma\uparrow}\delta_{\sigma'\downarrow} - \delta_{\sigma\downarrow}\delta_{\sigma'\uparrow}), \qquad (1.23)$$

H_{int} and $\mathcal{H}_{M,\Delta}$ become

$$\mathcal{H}_{\text{int}} = -\sum_i \mathbf{M}_i \cdot \mathbf{S}_i - \sum_{i,j} \left[\frac{\Delta^*_{ij}}{2} \left(c_{i\uparrow} c_{j\downarrow} - c_{i\downarrow} c_{j\uparrow} \right) + \frac{\Delta_{ij}}{2} \left(c^*_{j\downarrow} c^*_{i\uparrow} - c^*_{j\uparrow} c^*_{i\downarrow} \right) \right], \ (1.24)$$

$$\mathcal{H}_{M,\Delta} = \frac{3}{8U} \sum_i |\mathbf{M}_i|^2 + \frac{1}{V} \sum_{i,j} \Delta^*_{ij} \Delta_{ij}. \qquad (1.25)$$

If $\Delta_{ij} = +(-)\Delta$ when $\mathbf{R}_i - \mathbf{R}_j$ is the unit vector along the $x(y)$-axis and zero otherwise, the last term in Eqn. (1.24) is nothing but the BCS pairing term with $\text{d}_{x^2-y^2}$-wave pairing symmetry. This kind to off-site pairing (as opposed to s-wave on-site pairing) is natural in systems with strong on-site Coulomb repulsion U.
From the effective Lagrangian density

$$\begin{aligned}
\mathcal{L} &= c^*_{i\sigma}(\partial_\tau - \mu)c_{i\sigma} - [t_{ij} c^*_{i\sigma} c_{j\sigma} + \text{H.c}] - \mathbf{M}_i \cdot \mathbf{S}_i + \frac{3}{8U}|\mathbf{M}_i|^2 \\[2mm]
&\quad - \left[\frac{\Delta^*_{ij}}{2} \left(c_{i\uparrow} c_{j\downarrow} - c_{i\downarrow} c_{j\uparrow} \right) + \frac{\Delta_{ij}}{2} \left(c^*_{j\downarrow} c^*_{i\uparrow} - c^*_{j\uparrow} c^*_{i\downarrow} \right) \right] + \frac{1}{V}|\Delta_{ij}|^2, \ (1.26)
\end{aligned}$$

we see directly that the equations of motion (the saddle point approximation) for the Hubbard-Stratonovich fields Δ_{ij} and $\mathbf{M}_i$ are given by

$$0 = \frac{\delta S_{\text{eff}}}{\delta \Delta^*_{ij}} \quad \Rightarrow \quad \Delta_{ij} = \frac{V}{2} \langle c_{i\uparrow} c_{j\downarrow} - c_{i\downarrow} c_{j\uparrow} \rangle, \qquad (1.27)$$

$$0 = \frac{\delta S_{\text{eff}}}{\delta \mathbf{M}_i} \quad \Rightarrow \quad \mathbf{M}_i = \frac{4U}{3} \langle \mathbf{S}_i \rangle. \qquad (1.28)$$

Historically the use of two mean-field conditions is not common even though there certainly are precedents. For example, P.W. Anderson used both a mean-field condition for the electron density and the BCS pairing field to study the role of plasmons in restoring the gauge invariance of the BCS ground state and discovered the Anderson-Higgs mechanism[25].

The equation (1.28) is identical to what we would immediately expect from the conditions obtained within the conventional Hartree-Fock decoupling. For example, if we consider only the magnetism, the on-site Hubbard Hamiltonian given in Eqn. (1.10) can be decoupled within Hartree-Fock by writing $\mathbf{S}_i = \mathbf{S}_i - \langle \mathbf{S}_i \rangle + \langle \mathbf{S}_i \rangle$

$$\mathbf{S}_i^2 = (\mathbf{S}_i - \langle \mathbf{S}_i \rangle + \langle \mathbf{S}_i \rangle)^2 = (\mathbf{S}_i - \langle \mathbf{S}_i \rangle)^2 + \langle \mathbf{S}_i \rangle^2 + 2\langle \mathbf{S}_i \rangle \cdot (\mathbf{S}_i - \langle \mathbf{S}_i \rangle), \quad (1.29)$$

and discarding the fluctuation term, $(\mathbf{S}_i - \langle \mathbf{S}_i \rangle)^2$. The resulting Hartree-Fock Hamiltonian H_{HF} is bilinear in fermi fields and given by

$$\mathcal{H}_{HF} = - \sum_{<ij>\sigma} \left[t_{ij} c_{i\sigma}^\dagger c_{j\sigma} + \text{H.c} \right] - \mu \sum_i n_i - \frac{4U}{3} \sum_i \langle \mathbf{S}_i \rangle \cdot \mathbf{S}_i + \frac{2U}{3} \sum_i \langle \mathbf{S}_i \rangle^2. \quad (1.30)$$

As seen by inspection this is equivalent to the theory of Eqn. (1.26) when $\langle \mathbf{S}_i \rangle = \frac{3}{4U} \mathbf{M}_i$ which is identical to the condition given by Eqn. (1.28).

As is well-known, there is no quantitative justification for the saddle point approximation of the one band Hubbard model since there is no small expansion parameter. On the other hand, for large spin this semi-classical treatment becomes more accurate similarly to the usual spin-wave theory of ordered magnets.

From Eqn. (1.27) it is clear that Δ_{ij} is symmetric upon interchanging the sites, $\Delta_{ji} = \Delta_{ij}$ so that the original field $\Delta_{ij\sigma\sigma'}$ is antisymmetric upon interchange of the two Cooper pair electrons. We may use this property to slightly simplify H_{int} to yield

$$\mathcal{H}_{\text{int}} = - \sum_i \mathbf{M}_i \cdot \mathbf{S}_i + \sum_{<ij>} \left[\Delta_{ij}^* c_{j\downarrow} c_{i\uparrow} + \Delta_{ij} c_{i\uparrow}^* c_{j\downarrow}^* \right]. \quad (1.31)$$

In addition to the hopping term, this expression constitutes *the minimal model* to study the electronic structure when the order include both antiferromagnetism and d-wave superconductivity. We will use it quite extensively in the following chapters of this thesis.

Since the effective action S_{eff} is quadratic in the fermion Grassmann fields c^*, c they can be integrated out by use of the identity

$$\int \mathcal{D}[c^*, c] \exp(-c^* A c) = \det A \quad (1.32)$$

Equivalently, by shifting the variable $c \to c - A^{-1}J$, where J is an arbitrary vector, this becomes

$$\int \mathcal{D}[c^*, c] \exp(-c^* A c + J^* c + c^* J) = \det A \ \exp(\int J^* A^{-1} J). \qquad (1.33)$$

In Eqn. (1.33), A denotes the matrix that contains the couplings of the Fermi fields c^*, c to the auxiliary bose fields in addition to the quadratic hopping terms. The result of this procedure is an effective action for the bose fields $\mathbf{M}_i$ and Δ_{ij}.

Let us introduce the generalized Nambu spinor $\psi_i(\tau)$ by

$$\psi_i(\tau) = (c_{i\uparrow}(\tau), c_{i\downarrow}(\tau), c_{i\uparrow}^*(\tau), c_{i\downarrow}^*(\tau)). \qquad (1.34)$$

In the following we choose the phase of the superconducting gap function such that Δ_{ij} becomes real. In terms of this 4-spinor the effective action

$$
\begin{aligned}
S_{\text{eff}} \ = \ & \int d\tau \sum_{ij\sigma} (c_{i\sigma}^*(\partial_\tau - \mu)c_{i\sigma} - [t_{ij}c_{i\sigma}^* c_{j\sigma} + \text{H.c}] - \mu c_{i\sigma}^* c_{i\sigma} - \mathbf{M}_i \cdot \mathbf{S}_i \\
& + \ \left[\Delta_{ij}c_{j\downarrow}c_{i\uparrow} + \Delta_{ij}c_{i\uparrow}^* c_{j\downarrow}^*\right] + \frac{3}{8U}|\mathbf{M}_i|^2 + \frac{1}{V}\Delta_{ij}^2 \Big)
\end{aligned}
\qquad (1.35)
$$

becomes

$$S_{\text{eff}} = \int d\tau \frac{1}{2} \sum_{ij} \psi_i^*(1_{4\times4}\partial_\tau - H_0(t_{ij}, \mu, \mathbf{M}_i, \Delta_{ij}))\psi_j + \sum_i \frac{3}{8U}|\mathbf{M}_i|^2 + \sum_{ij} \frac{1}{V}\Delta_{ij}^2, \qquad (1.36)$$

where $1_{4\times4}$ is the 4×4 identity matrix. The matrix, $H_0(t_{ij}, \mu, \mathbf{M}_i, \Delta_{ij})$, is given by

$$
\mathcal{H}_0 = \begin{pmatrix}
(\frac{M_i^z}{2})\delta_{i,j} + K_{ij} & \left(\frac{M_i^x - iM_i^y}{2}\right)\delta_{ij} & 0 & -\Delta_{ij} \\
\left(\frac{M_i^x + iM_i^y}{2}\right)\delta_{ij} & (-\frac{M_i^z}{2})\delta_{i,j} + K_{ij} & \Delta_{ij} & 0 \\
0 & \Delta_{ij} & (-\frac{M_i^z}{2})\delta_{i,j} - K_{ij} & -\left(\frac{M_i^x - iM_i^y}{2}\right)\delta_{ij} \\
-\Delta_{ij} & 0 & -\left(\frac{M_i^x + iM_i^y}{2}\right)\delta_{ij} & (+\frac{M_i^z}{2})\delta_{i,j} - K_{ij}
\end{pmatrix},
\qquad (1.37)
$$

or in more condense tensor product notation

$$\mathcal{H}_0 = -K_{ij}1_{2\times2} \otimes \tau^z - \delta_{i,j}(\mathbf{M}_i \cdot \frac{\boldsymbol{\sigma}}{2}) \otimes \tau^z - \Delta_{ij}\sigma^y \otimes \tau^y, \qquad (1.38)$$

where τ^α denote the Pauli matrices in Nambu space with $1_{2\times2}$ being the 2×2

identity matrix and K_{ij} is defined by

$$K_{ij} = \mu\delta_{i,j} + \sum_j t_{ij}. \tag{1.39}$$

Above, Δ_{ij} couples only to nearest neighbors whereas the sum in the hopping term, $\sum_j t_{ij}$, in the last expression extends over the sites in some range of site i parameterized by t, t', t'' etc. Note, that ∂_τ enters with the same sign in all entries, i.e. $1_{4\times4}\partial_\tau$, since the lower hole-particle part of the matrix gains both a minus sign from the anti-commuting Grassmann fields *and* from a partial integration.

After integrating out the fermions ψ_i by use of Eqn. (1.33) the effective action for the Bose fields can be written in terms of the Fredholm determinant as

$$S_{\text{eff}} = \int d\tau \sum_i \frac{3}{8U}|\mathbf{M}_i|^2 + \sum_{<ij>} \frac{1}{V}\Delta_{ij}^2 - \frac{1}{2}\ln \text{Det}\left[1_{4\times4}\partial_\tau - H_0(t_{ij}, \mu, \mathbf{M}_i, \Delta_{ij})\right]. \tag{1.40}$$

We can use the identity (which is easily proven for finite matrices in a representation where A is diagonal)

$$\ln \text{Det}A = \text{Tr}\ln A, \tag{1.41}$$

to obtain

$$S_{\text{eff}} = \int d\tau \left(\sum_i \frac{3}{8U}|\mathbf{M}_i|^2 + \sum_{<ij>} \frac{1}{V}\Delta_{ij}^2 \right) - \frac{1}{2}\text{Tr}\ln\left[1_{4\times4}\partial_\tau - H_0(t_{ij}, \mu, \mathbf{M}_i, \Delta_{ij})\right]. \tag{1.42}$$

From this expression one can again determine the stable fields within the saddle point approximation to obtain the conditions given in Eqn. (1.27)-(1.28). The bosonic action Eqn. (1.42) will be used later on to study the collective modes given by the fluctuations around various stabilized mean-field states.

1.4   Discussion

A few more words are in order regarding the effective Lagrangian density obtained in Eqn. (1.26)

$$\begin{aligned} \mathcal{L} &= c_{i\sigma}^*(\partial_\tau - \mu)c_{i\sigma} - [t_{ij}c_{i\sigma}^*c_{j\sigma} + \text{H.c}] - \mathbf{M}_i \cdot \mathbf{S}_i + \frac{3}{8U}|\mathbf{M}_i|^2 \\ &\quad - \left[\Delta_{ij}^*c_{i\uparrow}c_{j\downarrow} + \Delta_{ij}c_{j\downarrow}^*c_{i\uparrow}^*\right] + \frac{1}{V}|\Delta_{ij}|^2, \end{aligned} \tag{1.43}$$

and the corresponding self-consistency equations

$$0 = \frac{\delta S_{\text{eff}}}{\delta \Delta_{ij}^*} \quad \Rightarrow \quad \Delta_{ij} = \frac{V}{2} \langle c_{i\uparrow} c_{j\downarrow} - c_{i\downarrow} c_{j\uparrow} \rangle, \tag{1.44}$$

$$0 = \frac{\delta S_{\text{eff}}}{\delta \mathbf{M}_i} \quad \Rightarrow \quad \mathbf{M}_i = \frac{4U}{3} \langle \mathbf{S}_i \rangle. \tag{1.45}$$

On an N site lattice we will study the Hamiltonian

$$\mathcal{H}_{\text{HF}} = -\sum_{<ij>\sigma} \left[t_{ij} c_{i\sigma}^\dagger c_{j\sigma} + \text{H.c} \right] - \mu \sum_{i\sigma} n_{i\sigma} + \sum_{ij} \left[\Delta_{ij}^* c_{i\uparrow} c_{j\downarrow} + \Delta_{ij} c_{j\downarrow}^* c_{i\uparrow}^* \right]$$

$$- \sum_i \mathbf{M}_i \cdot \mathbf{S}_i. \tag{1.46}$$

This real-space version of $\mathcal{H}_{\text{HF}}$ will be used extensively in the following chapters to study various magnetic inhomogeneities (impurities, vortices and stripes) in a d-wave superconductor. Of course this kind of mean-field decoupling cannot be used in the critical regions close to phase transitions, but can be used inside the ordered phases.

From the phase diagram of the cuprate materials it is natural to consider models with incipient coexistence of antiferromagnetism and d-wave superconductivity. In fact, ever since the discovery of the high-T_c's it was proposed that superconducting correlations already exist in the antiferromagnetic Mott insulator. Thus, there have been several studies of an antiferromagnet with competing d-wave Cooper pairing. Close to half-filling, any mean-field model containing both orders fail to superconduct due to the large insulating antiferromagnetic gap. As will be discussed in detail in later chapters, away from half-filling this is no longer the case. Finally, one may also wonder about the presence of weak antiferromagnetism "on top of" a well-established BCS d-wave superconductor. This will gap the nodal quasi-particles of the d-wave superconductor and open a full gap in the density of states. As mentioned, we return to these issues below.

2 Andreev bound states in d-wave superconductors

*Some of the material in this chapter has been published by the author and P. Hedegård in Physical Review B **66**, 104515 (2002)[26].*

Andreev reflection is a remarkable phenomenon taking place at the boundary between a normal and a superconducting region[27]. It has played a crucial role in determining the nature of the superconducting pairing symmetry of the high-T_c compounds. Unlike the conventional s-wave BCS superconductors, the d-wave pairing state of the high-T_c cuprates has an internal phase of the pair potential. This phase has important contributions to the electric properties of tunnelling junctions. This includes the existence of unusual zero-bias conductance peaks (ZBCP) and fractional flux quanta[28]. Since these effects arise from the internal sign change of the pairing symmetry they give information not included in conventional spectroscopic probes which are sensitive only to the amplitude squared of the gap.

The study of Andreev scattering serves as a first (introductory) application of the minimal model derived in the last chapter. We will study the simplest possible geometry of antiferromagnetic and d-wave superconducting order: an interface. Initially, however, I review briefly the Andreev physics and the origin of the ZBCP in the case to $d_{x^2-y^2}$-wave pairing symmetry.

2.1 Conventional Andreev reflection

The discussion of Andreev physics in conventional s-wave BCS superconductors begins from the local Bogoliubov-de Gennes equations

$$\left(\begin{array}{cc} \mathcal{K} & \Delta \\ \Delta^* & -\mathcal{K} \end{array} \right) \left(\begin{array}{c} u(\mathbf{r}) \\ v(\mathbf{r}) \end{array} \right) = E \left(\begin{array}{c} u(\mathbf{r}) \\ v(\mathbf{r}) \end{array} \right), \tag{2.1}$$

where $\mathcal{K} = -\frac{\hbar^2 \nabla^2}{2m} - \mu$ and $u(\mathbf{r})$ and $v(\mathbf{r})$ denote the electron and hole components of the wavefunction, respectively.

In the normal state $\Delta = 0$ there exists electrons and holes, described by the vectors

$$\psi_N^e(\mathbf{r}) = \left(\begin{array}{c} 1 \\ 0 \end{array} \right) \exp(\pm i\mathbf{k}_+ \cdot \mathbf{r}) \qquad \psi_N^h(\mathbf{r}) = \left(\begin{array}{c} 0 \\ 1 \end{array} \right) \exp(\pm i\mathbf{k}_- \cdot \mathbf{r}), \tag{2.2}$$

with $k_\pm = k_F\sqrt{1 \pm E/\mu} \approx k_F \pm E/\hbar v_F$ where $k_F(v_F)$ denote the Fermi wavevector (velocity). Here, we assumed that the Fermi energy is much larger

than the quasi-particle energy E.

In the bulk superconductor we can solve Eqn. (2.1) with the ansatz $\psi_S(\mathbf{r}) = (u, v)^T \exp(i\mathbf{q} \cdot \mathbf{r})$, the secular equation restricting the amplitude of the momentum vectors $q_\pm = k_F\sqrt{1 \pm (\sqrt{E^2 - \Delta^2}/\mu)} \approx k_F \pm \frac{\xi}{\hbar v_F}$ where $\xi = \sqrt{E^2 - \Delta^2}$ and we assume for simplicity that the Fermi vectors are identical in the normal and superconducting regions. We then have two types of wavefunctions, electron-like $\psi_S^e(\mathbf{r})$ and hole-like $\psi_S^h(\mathbf{r})$, depending on the corresponding solution in the normal limit $\Delta \to 0$,

$$\psi_S^e(\mathbf{r}) = \begin{pmatrix} u \\ v \end{pmatrix} \exp(\pm i\mathbf{q}_+ \cdot \mathbf{r}) \qquad \psi_S^h(\mathbf{r}) = \begin{pmatrix} v \\ u \end{pmatrix} \exp(\pm i\mathbf{q}_- \cdot \mathbf{r}), \qquad (2.3)$$

where it follows from the Bogoliubov-de Gennes equations (and $|u|^2 + |v|^2 = 1$) that

$$u = u(E) = \sqrt{\frac{1 + \sqrt{1 - \Delta^2/E^2}}{2}}, \qquad v = v(E) = \sqrt{\frac{1 - \sqrt{1 - \Delta^2/E^2}}{2}}. \quad (2.4)$$

These wavefunctions correspond to the propagating solutions $|E| > \Delta$. However, there also exists exponentially decaying solutions important at the surfaces. By defining $\xi = i\sqrt{\Delta^2 - E^2}$ when $|E| < \Delta$ the above expressions also describe these decaying sub-gap solutions.

Now, imagine the following 1D situation of a normal metal - superconductor N/S interface positioned at $x = 0$,

$$\Delta(x) = \begin{cases} 0, & x \leq 0 \\ \Delta e^{i\chi}, & x > 0 \end{cases} \qquad (2.5)$$

and an electron incident on the superconductor from the normal metal

$$\Psi_N = \begin{pmatrix} 1 \\ 0 \end{pmatrix} \exp(ik_+x) + r_{eh} \begin{pmatrix} 0 \\ 1 \end{pmatrix} \exp(ik_-x) + r_{ee} \begin{pmatrix} 1 \\ 0 \end{pmatrix} \exp(-ik_+x). \quad (2.6)$$

As seen from Eqn. (2.6), we have included the possibility that the electron is reflected as an electron *as well as a hole*. On the superconductor side we have transmitted electron-like and hole-like Bogolons

$$\Psi_S = t_{ee} \begin{pmatrix} u \\ ve^{-i\chi} \end{pmatrix} \exp(iq_+x) + t_{eh} \begin{pmatrix} v \\ ue^{-i\chi} \end{pmatrix} \exp(-iq_-x) \qquad (2.7)$$

By matching the wavefunctions and their derivatives at $x = 0$ it is straightforward to obtain the expressions for the reflection r_{ee}, r_{eh} and transmission t_{ee}, t_{eh} amplitudes. In the so-called Andreev approximation, i.e. to lowest

non-vanishing order in $\frac{\max(\Delta, E)}{\mu}$, the reflection amplitudes can be written as

$$r_{eh} = e^{-i\chi}\frac{E - \sqrt{E^2 - \Delta^2}}{\Delta}, \qquad r_{ee} = \frac{E - \sqrt{E^2 - \Delta^2}}{4\mu}. \qquad (2.8)$$

Thus, the Andreev reflection amplitude acquires the phase $-\chi$ from Δ. χ changes sign when considering hole-electron reflection. Therefore, in the Andreev approximation we may write for the Andreev reflection amplitudes

$$r_{eh(he)} = e^{\mp i\chi} \times \begin{cases} e^{-i\arccos\frac{E}{\Delta}}, & E \leq \Delta \\ e^{-\operatorname{arccosh}\frac{E}{\Delta}}, & E > \Delta \end{cases} \qquad (2.9)$$

For sub-gap particles we see that there is total Andreev reflection $|r_{eh(he)}|^2 = 1$. Charge conservation is fulfilled by insertion of a Cooper pair into the superconducting condensate. The Andreev reflected particle is said to be retro-reflected since it changes sign on *all* the components of its momentum.

2.2 Andreev surface bound states and the origin of the zero-energy state in d-wave superconductors

The possibility of bound states at the surface of materials that exhibit a gap in the bulk electron spectrum is well known. In particular, at superconducting surfaces quasi-particles with energies inside the superconducting gap may be trapped in bound states formed by total reflection against the vacuum surface and total Andreev retro-reflection against the superconductor. Saint-James and de Gennes[29] first studied the quasi-particle surface states for the insulator - normal metal - s-wave superconductor (INS) quantum well similar to the one shown to the left in Fig. 2.1. From the quasi-classical Bohr-Sommerfeld quantization condition the bound state energy is determined by equating the total phase accumulated during one cycle to an integer times 2π. If $\gamma(E) = \arccos(E/|\Delta|)$, then for the trajectory shown in Fig. 2.1 we have

$$\beta(E) - \gamma(E) - \overline{\gamma}(E) - \chi + \overline{\chi} = 2n\pi, \qquad (2.10)$$

where $-\gamma(E) - \chi$ ($-\overline{\gamma}(E) + \overline{\chi}$) is the contribution from the Andreev reflections with propagation in the θ ($\overline{\theta}$) direction. The phase χ and $\overline{\chi}$ changes sign when considering the time reversed path. The phase contribution from propagation in the normal region is $\beta(E) = 2L(k_+ - k_-) + \beta_0$, the first term coming from the ballistic motion and the latter from the normal reflection at the I/N interface. For the s-wave case, where $\chi = \overline{\chi}$, Eqn. (2.10) reduces to $-2\gamma(E) + \beta(E) = 2n\pi$, which results in the spectral equation

$$E = \pm\Delta\cos\left(\frac{\beta(E)}{2}\right). \qquad (2.11)$$

The energy of the surface bound states lie inside the bulk gap, but $E = 0$ is clearly not a solution. When the ballistic phase $2L(k_+ - k_-) \approx 4LE/\hbar v_F \cos\theta$ dominates over β_0, Eqn. (2.11) takes the form $E = \pm\Delta \cos\left(\frac{E}{\Delta} \frac{2L}{\xi_0 \cos\theta}\right)$, which is the dispersion relation found by Saint-James and de Gennes in 1963[29]. Integrating over the angle θ results in the surface density of states displayed in the top right graph (a) of Fig. 2.1.

Historically, the existence of surface bound states in superconductors with unusual pairing symmetry was first studied by Buchholtz and Zweicknagl[30] in the context of unconventional pairing in the heavy-fermion superconductors. In the high-T_c literature Hu[31] predicted the existence of zero-energy states on the surface of d-wave superconductors. The d-wave symmetry of the pairing potential of the cuprates results in an orientational dependent boundary condition at surfaces. This is shown by the rotated cloverleaf $\Delta(\theta) = \Delta_0 \cos(2(\theta-\alpha))$ in Fig. 2.1. As seen, the Andreev reflections against the superconductor can
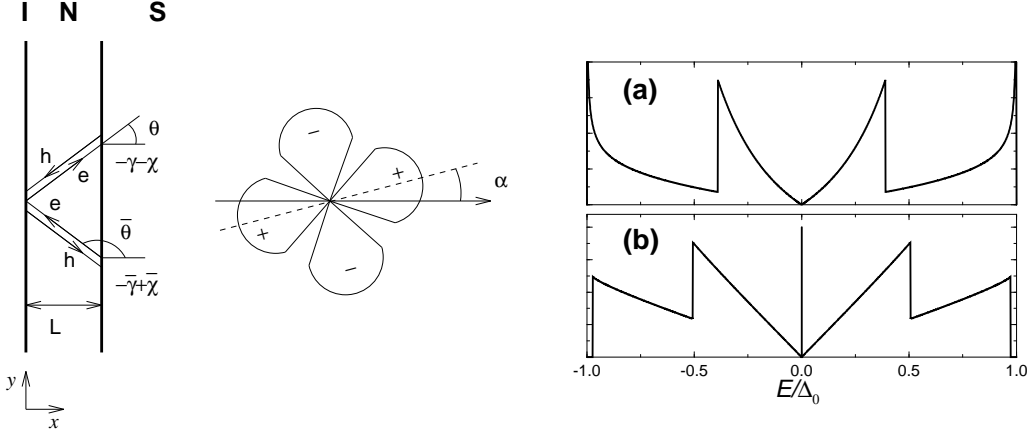

Figure 2.1: Left: I/N/S well and the quasi-classical path giving the bound states at a specular surface to a 2D superconductor with gap symmetry $\Delta(\theta) = \Delta_0 \cos(2(\theta - \alpha))$ for d-wave and $\Delta(\theta) = \Delta_0$ for s-wave superconductors. Here, θ is the propagation angle and α denotes the orientation of the crystal axes of the superconductor compared to the N/S boundary. Right: Density of surface states at an s-wave (a) and d-wave (b) superconductor surface with a normal metal over-layer of thickness $L = 1.5\xi_0$. Adapted from Ref. [32].

probe different lobes of the d-wave clover and thereby acquire *an extra π phase shift, $\chi = \overline{\chi} - \pi$*. The Bohr-Sommerfeld condition now becomes[1]

$$\beta(E) - \gamma(E) - \overline{\gamma}(E) + \pi = 2n\pi, \qquad (2.12)$$

---

[1]Note that in the case of d-wave pairing symmetry the Bogoliubov-de Gennes equations become non-local. Therefore, it is non-trivial that the phases entering the Bohr-Sommerfeld equation (2.12) are identical to the expressions derived for the s-wave case. This, however, can be shown to be true by separating out the fast $1/k_F$ oscillations of u and v and solving the d-wave Bogoliubov-de Gennes equations for the slowly varying envelope functions to lowest order in $1/k_F\xi_0$[33].

which *always have a zero-energy solution* since $\gamma(0) = \overline{\gamma}(0) = \pi/2$ and $\beta(0) = 0$. This is the mid-gap state discovered by Hu[31]. For arbitrary α, the mid-gap state exists within the angle window $\frac{\pi}{2} - \alpha < |\theta| < \frac{\pi}{2} + \alpha$. Hence, for $\alpha = \pm\frac{\pi}{4}$ ($\alpha = 0, \frac{\pi}{2}$) the mid-gap states exists for all (none) quasi-particle trajectories, $-\frac{\pi}{2} < \theta < \frac{\pi}{2}$. When $\alpha = \frac{\pi}{4}$, Eqn. (2.12) becomes

$$E = \pm|\Delta| \sin\left(\frac{E}{|\Delta|} \frac{2L}{\xi_0 \cos\theta}\right), \qquad (2.13)$$

with the corresponding surface density of states shown in the lower right-hand graph (b) of Fig. 2.1.

The zero-energy state is extremely robust since it originates from the topological property of the d-wave pairing gap. Therefore, it exists at any defect that cause quasi-particle scattering between lobes of different sign of the d-wave gap. Furthermore, the mid-gap state is degenerate with respect to both spin and the direction of the quasi-particle momentum parallel to the surface $\pm k_y$. However, as has been discussed extensively in the literature, the mid-gap state positioned exactly at the Fermi level is actually energetically unstable. By lifting the degeneracy and inducing a gap at the Fermi level, the system lowers the energy with only the lower level occupied. Several mechanisms for splitting the mid-gap state has been proposed: 1) the pairing symmetry acquires a subdominant component near the surface region $d \to d \pm is$, 2) self-induced Doppler shifts, and 3) surface spin-density wave formation. Note that when the $\pm k_y$ degeneracy is split, at low temperature when only the, say, $+k_y$ state is occupied, a net current flows along the surface. This spontaneous current manifests the broken time reversal symmetry[34].

Experimentally, the ZBCP was observed already in 1990 in the $I-V$ characteristic of electron tunnelling into thin YBCO films by Geerk *et al*[35]. However, its origin in the d-wave pairing was not realized until the seminal studies by Hu[31] and Kashiwaya[36].

The internal d-wave sign change also has important consequences for the properties of Josephson junctions involving combinations of d-wave, s-wave or misoriented d-wave superconducting electrodes. If the junction electrodes have different sign of the order parameter, this is equivalent to adding an extra π phase shift to the phase difference across the junction. In fact, a whole industry has evolved around the study of these π-junctions. For further details about the properties of mid-gap states and π-junctions the reader is referred to the recent extensive reviews by Löfwander *et al.*[32] and Kashiwaya *et al.*[37] and reference therein.

2.3   Andreev bound states at the interface of antiferromagnets and d-wave superconductors

In this section we set up a simple transfer matrix formalism to study the existence of bound states at interfaces and in junctions between antiferromagnets and d-wave superconductors. The well-studied zero energy mode at the {110} interface between an insulator and a $d_{x^2-y^2}$ wave superconductor is spin split when the insulator is an antiferromagnet. This has as a consequence that any competing interface induced superconducting order parameter that breaks the time reversal symmetry needs to exceed a critical value before a charge current is induced along the interface.

The discovery of the symmetry of the superconducting order parameter has been one of the most successful studies of the High-T_c materials. Angular resolved photoemission spectroscopy has revealed the nodes in the gap function and tunnelling experiments have proven the sign change between adjacent lobes of the $d_{x^2-y^2}$ wave gap[38, 39, 40]. It was first shown by Hu[31] that this sign change can lead to zero energy Andreev bound states (ZEBS) at the surface of an insulator and a d-wave superconductor. These Andreev bound states were later identified with the zero bias conductance peaks observed in tunnelling experiments. The experiments by Covington *et al.*[41] indicated, however, that the surface states were spontaneously split by a minigap. Several ideas were proposed for this effect[32]; one of which included the induction of a time reversal symmetry breaking *is* component of the order parameter near the interface[42]. The resulting gap $d + is$ lowers the condensation energy by lifting the directional degeneracy of the ZEBS[34]. Later Honerkamp *et al.*[43] used a tight-binding model with onsite repulsion and spin dependent nearest neighbor interaction to self-consistently study the competition between additional induced orders near the surface of an insulator and a $d_{x^2-y^2}$ wave superconductor.

Motivation for studying close domains of antiferromagnetism and superconductivity arises from the existence of striped domains in the cuprate materials. This was further emphasized by recent elastic neutron scattering experiments showing that static antiferromagnetic order is induced in a superstructure around the vortices in the mixed state of $La_{2-x}Sr_xCuO_4$[44] and $La_2CuO_{4+\delta}$[45]. These experiments are consistent with a static environment of alternating antiferromagnetic and d-wave superconducting stripes around the vortex cores. Thus the electronic states in such an environment is an important question.

Inspired by these experiments we set up a simple transfer matrix method to identify bound states on interfaces and junctions between antiferromagnets and d-wave superconductors. In particular we discuss a single interface separating antiferromagnetic and d-wave superconducting half-planes (AF/dSC), and point out a few differences from the conventional non-magnetic insulator-d-wave superconductor interface (I/dSC). Note that the antiferromagnetism

forces us to study a lattice model which is contrary to the usual discussion of Andreev interference in terms of semi-classical continuum models[33].

A simple lattice model that includes both d-wave superconductivity and antiferromagnetism is given by the following Hamiltonian

$$
H = -t \sum_{\langle n,m \rangle \sigma} c_{n\sigma}^\dagger c_{m\sigma} + \text{H.c.} - \mu \sum_{n\sigma} c_{n\sigma}^\dagger c_{n\sigma} \tag{2.14}
$$

$$
+ \sum_{\langle n,m \rangle} \Delta_{n,m} c_{n\uparrow}^\dagger c_{m\downarrow}^\dagger + \text{H.c.} \tag{2.15}
$$

$$
+ \sum_n M_n \left(c_{n\uparrow}^\dagger c_{n\uparrow} - c_{n\downarrow}^\dagger c_{n\downarrow} \right) \tag{2.16}
$$

where $\langle n,m \rangle$ denotes nearest neighbors. M_n and $\Delta_{n,m}$ are the spatially dependent magnetic and superconducting order parameters. This Hamiltonian is quadratic and can be diagonalized by a Bogoliubov-de Gennes (BdG) transformation

$$
\gamma_\sigma^\dagger = \sum_n u_\sigma(n) c_{n\sigma}^\dagger + \sigma v_\sigma(n) c_{n-\sigma}. \tag{2.17}
$$

with σ equal to +1 (-1) for spin up (down). We use the notational convention that the spin indices on u_σ and v_σ follow that on the Bogoliubov operators $\gamma_\sigma^\dagger$. In the case of a $d_{x^2-y^2}$-wave superconductor there are two qualitatively different orientations of the interface; the {100} and {110} directions corresponding to a vertical and diagonal stripe respectively. Both cases are studied below with the x-axis (y-axis) chosen perpendicular (parallel) to the interface which is placed at $x = 0$. The lattice constant is set to unity. Assuming translational invariance along the y-direction the AF/dSC interface reduces to a one dimensional problem. For the {100} interface the resulting Bogoliubov-de Gennes equations have the form

$$
\epsilon_\sigma u_{q\sigma}(x) = -t\left(u_{q\sigma}(x+1) + u_{q\sigma}(x-1) + 2\cos(q) u_{q\sigma}(x) \right) - \mu u_{q\sigma}(x)
$$

$$
+ \sigma M_x u_{q+Q\sigma}(x) + \left(\Delta_{x+1,x}^d \right) v_{q\sigma}(x+1) + \left(\Delta_{x-1,x}^d \right) v_{q\sigma}(x-1)
$$

$$
+ 2\cos(q) \left(-\Delta_x^d \right) v_{q\sigma}(x) \tag{2.18}
$$

$$
\epsilon_\sigma v_{q\sigma}(x) = t\left(v_{q\sigma}(x+1) + v_{q\sigma}(x-1) + 2\cos(q) v_{q\sigma}(x) \right) + \mu v_{q\sigma}(x)
$$

$$
+ \sigma M_x v_{q+Q\sigma}(x) + \left(\Delta_{x+1,x}^{*d} \right) u_{q\sigma}(x+1) + \left(\Delta_{x-1,x}^{*d} \right) u_{q\sigma}(x-1)
$$

$$
+ 2\cos(q) \left(-\Delta_x^{*d} \right) u_{q\sigma}(x) \tag{2.19}
$$

after Fourier transforming along the y direction. The corresponding equations for the Fourier components $u_{q+Q\sigma}$ and $v_{q+Q\sigma}$ are obtained by simply performing the substitution $q \rightarrow q + Q$. These BdG equations are diagonal in the spin index with the only difference between spin up and down being the sign of the magnetic term.

A simple way to study bound states at the interface is in terms of the transfer matrix method[46]. Thus we introduce a (q, ϵ)-dependent matrix $T(x+1, x)$ defined by

$$\Psi(x+1) = T(x+1, x)\,\Psi(x). \qquad (2.20)$$

which transfers the spinor Ψ from site x to site $x+1$. For a model with nearest neighbor coupling Ψ takes the explicit form $\Psi(x) = (\psi(x), \psi(x-1))$ where

$$\psi(x) = (u_{q\sigma}(x), v_{q\sigma}(x), u_{q+Q\sigma}(x), v_{q+Q\sigma}(x)). \qquad (2.21)$$

The associated 8×8 transfer matrix has the general form

$$T(x+1, x) = \begin{pmatrix} A & B \\ 1 & 0 \end{pmatrix} \qquad (2.22)$$

where A (B) denotes the 4×4 coefficient-matrix connecting $\psi(x+1)$ and $\psi(x)$ $(\psi(x-1))$ determined from the BdG equations (2.18-2.19). In the simplest case of a sharp interface we have the following spatial dependence of M_x and Δ_x

$$M_x \;=\; M(-1)^x \qquad \text{for} \quad x \leq 0 \qquad (2.23)$$

$$\Delta_x \;=\; \Delta_d \qquad\qquad \text{for} \quad x > 0 \qquad (2.24)$$

Thus there are effectively three different transfer matrices; one in the bulk magnetic region T_M, one in the bulk superconducting region T_{SC} and one associated with transfer through the interface T_I. By diagonalizing T_M and T_{SC} there exists decaying, growing or propagating eigenstates depending on whether the eigenvalues are less, larger or equal to one, respectively. Here, decaying and growing are referred to propagation along the x-axis for increasing x. If PET_M denotes the matrix obtained after propagating the eigenvectors of the bulk magnetic transfer matrix through the interface we introduce a matrix α given by

$$PET_M = ET_{SC}.\alpha \qquad (2.25)$$

where ET_{SC} is the matrix containing the eigenvectors of the bulk superconducting region as column vectors. The dot indicates matrix multiplication. Now, let S_g^m and S_g^{sc} denote the subspace of growing eigenstates of PET_M and ET_{SC} respectively, and consider the following linear combination of the
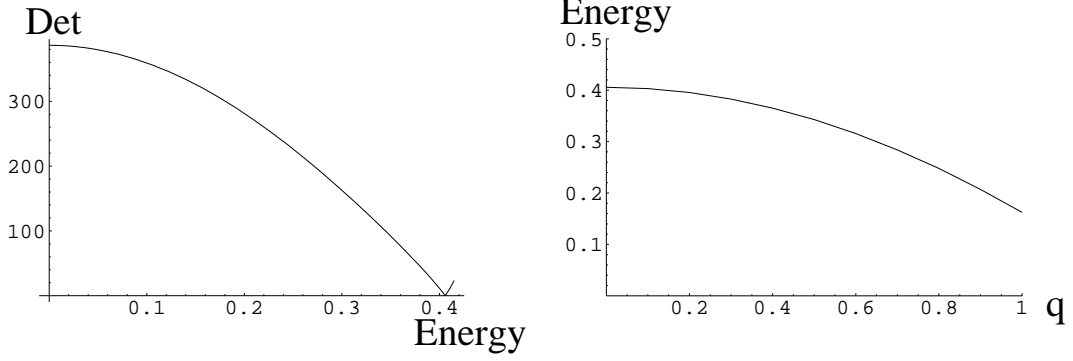
Figure 2.2: {100} interface between an antiferromagnet and a d-wave super-conductor: a) Determinant of α_r as a function of energy ϵ for $q = 0.1$. There is a de Gennes/Saint-James bound state close to the superconducting gap edge which is located at $\epsilon = 0.42t$ for $q = 0.1$. As seen in b), their dispersion has the expected downward cosine form until it merges with the continuum.

growing states of PET_M

$$\sum_{i \in S_g^m} \beta_i |PET_M i> \quad = \quad \sum_{i \in S_g^m} \sum_{j \in S_g^{sc}} \beta_i \alpha_{ji} |ET_{SC} j> \qquad (2.26)$$

$$= \quad \sum_{j \in S_g^{sc}} \left(\sum_{i \in S_g^m} \alpha_{ji} \beta_i \right) |ET_{SC} j>$$

From equation (2.26) it is evident that to have a bound state at the interface the vector β must belong to the null space of the reduced matrix α_r, which is the $S_g^{sc} \times S_g^m$ upper left part of the original matrix α since the matrices PET_M and ET_{SC} are organized to have the eigenstates with the largest eigenvalues as column vectors to the left. In the case that the two subspaces S_g^{sc} and S_g^m have the same dimension a bound state at the interface is characterized by the vanishing of the determinant of α_r

$$\text{Bound states:} \qquad \det(\alpha_r) = 0. \qquad (2.27)$$

Plots of the wavefunctions with values of (q, ϵ) that satisfy Eqn. (2.2) verifies that these states indeed are bound to the interface (not shown). The following explicit values of the input parameters are chosen: $t = 1$, $\Delta_d = 0.14$, $M = 2.0$ and $\mu = -0.99$ (for simplicity we ignore next-nearest neighbor coupling). Fig. 2.2a shows the determinant plotted as a function of energy for the {100} interface. There are bound states close to the superconducting gap edge that disperses downward in a cosine form (Fig. 2.2b). These are the well-known

de Gennes/Saint-James states[2] existing on the surface of an insulator and a superconductor[29]. These sub-gap states are bound to the interface and disappear when $M \to 0$.

The induction of additional gap symmetries, extended s-wave or p-wave, near the {100} interface of a d-wave superconductor and an antiferromagnet has been studied self-consistently by Kuboki[47]. These local gap perturbations will slightly modify the graphs in Figure 1. There is no spin splitting of the dGSJ mode in this geometry.

We turn now to the more interesting configuration of a {110} interface. Allowing for a possible interface induced sub-gap order with extended s-wave symmetry the Bogoliubov-de Gennes equations have the form

$$
\begin{aligned}
\epsilon_\sigma u_{q\sigma}(x) = {} & -2t\cos(p)\left(u_{q\sigma}(x+1) + u_{q\sigma}(x-1)\right) - \mu u_{q\sigma}(x) + \sigma M_x u_{q\sigma}(x) \\[2mm]
& - 2i\sin(q)\left(\Delta^d_{x+1,x} v_{q\sigma}(x+1) - \Delta^d_x v_{q\sigma}(x-1)\right) \\[2mm]
& + 2i\cos(q)\left(\Delta^s_{x+1,x} v_{q\sigma}(x+1) + \Delta^s_x v_{q\sigma}(x-1)\right) \quad\quad (2.28)
\end{aligned}
$$

$$
\begin{aligned}
\epsilon_\sigma v_{q\sigma}(x) = {} & 2t\cos(p)\left(v_{q\sigma}(x+1) + v_{q\sigma}(x-1)\right) + \mu v_{q\sigma}(x) + \sigma M_x v_{q\sigma}(x) \\[2mm]
& - 2i\sin(q)\left(\Delta^{*d}_{x+1,x} u_{q\sigma}(x+1) - \Delta^{*d}_x u_{q\sigma}(x-1)\right) \\[2mm]
& - 2i\cos(q)\left(\Delta^{*s}_{x+1,x} u_{q\sigma}(x+1) + \Delta^{*s}_x u_{q\sigma}(x-1)\right) \quad\quad (2.29)
\end{aligned}
$$

These equations are diagonal in the Fourier component q obtained after Fourier transforming parallel to the {110} interface since there is no staggering of the moments along a diagonal line in a square antiferromagnetic lattice. In Fig. 2.3 we plot again the determinant of the reduced matrix α_r as a function of energy ϵ when $\Delta^s = 0$. As seen the spin degeneracy of the ZEBS (blue curve) is lifted at a {110} AF/dSC interface. As opposed to the usual dGSJ states in Fig. 2.2, this splitting is also caused by the fact that a {110} interface belongs to only one sublattice whereas the {100} interface studied above contains the same amount of spin up and down sites.

The splitting of the ZEBS by Δ^s-mixing in the usual situation of a I/dSC interface has been extensively studied in the literature[42, 34, 43]. It is also well-known that a magnetic field further splits the ZEBS[41]. The above spin splitting at AF/dSC interfaces is similar to this magnetic field effect in the sense that the magnetic interface effectively acts as a local magnetic field. A similar effect caused by a correlation induced magnetization near the interface

---

[2]The dGSJ states are usually thought of as existing in a narrow normal region (within the superconducting coherence length ξ) from the surface. However, it is known that these states survive in the limit $\xi \to 0$. See also Ref. [32] for a pedagogical discussion of dGSJ states.
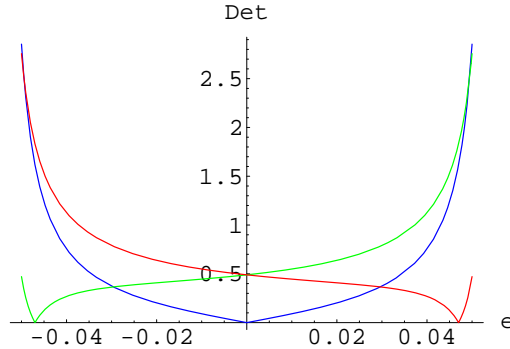
Figure 2.3: Determinant of α_r versus the energy ϵ for the {110} AF/dSC interface. Again this is plotted inside the superconducting gap and with $q = 0.1$. The blue curve is the usual case of an I/dSC interface which clearly contains a ZEBS (the insulator state is obtained by performing the substitution $M_n \rightarrow -M_n$ for the hole part of the BdG equations only). The red and green curves show the spin splitting of the ZEBS for this particular value of q.

in the case of a I/dSC surface was discussed by Honerkamp et al.[43] This "Zeeman" effect is also directly related to the split zero energy Andreev mode observed in the center of vortex cores of underdoped cuprates where local antiferromagnetism has been shown to exist[49, 50, 51, 52, 53, 54].

To the best of our knowledge there has been no self-consistent calculation investigating any {110} AF/dSC interface induced subdominant order parameters. However, we know from the study of I/dSC surfaces[42, 48] that the strong pair breaking effects of a {110} geometry, as opposed to a {100} surface, tends to stabilize the subdominant s-wave component. Thus, even though there is no Fermi surface instability begging for removal of the ZEBS from the Fermi level in the case of a AF/dSC {110} interface, one should still consider the effect of an additional local superconducting order parameter *is* competing with the splitting caused by the magnetism. The consequences of this competition for the ZEBS are discussed in Fig. 2.4.

The induction of a surface current is a well-known consequence of the time reversal symmetry broken state of I/dSC interfaces[42, 34]. However, for the AF/dSC interface with a locally induced $d \pm is$ order parameter there is a critical value of Δ_c^s before a current runs along the interface[3]. In Fig. 2.4a we show the situation when the induced Δ^s has exceeded this critical value. Fig. 2.4b is a schematic representation of the splitting of the original ZEBS with the first sketch corresponding to the parameters from Fig. 2.3 and the last sketch to those from Fig 2.4a. We stress that only a self-consistent model calculation can determine the magnitude of the directional splitting caused by *is* compared to the spin splitting caused by the antiferromagnetism, and hence

---

[3]Here we assume the large effect is the spin splitting since M gives rise to the Hubbard gap in the bulk antiferromagnet, and Δ^s is an extra perturbation. In the opposite case it would take a critical magnetization M_c to prevent the interface current induced by Δ^s.
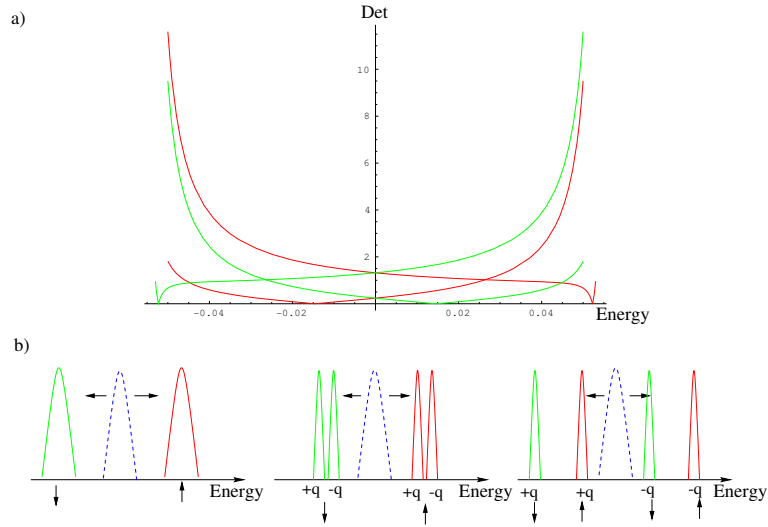
Figure 2.4: a) Same as in Fig. 2.3, but with an induced extended s-wave gap function near the interface, i.e. $d \to d + is$. For clarity we do not show the original ZEBS (blue curve from Fig. 2.3). b) Schematic representation of the splitting of the original zero energy Andreev bound state (blue dashed curve): 1) The antiferromagnetic interface breaks the spin degeneracy, as shown in Fig. 2.3. 2) Induction of a possible sub-dominant s-wave gap parameter Δ^s further splits the spin up/down states by breaking the directional degeneracy. 3) Only when Δ^s exceeds a critical value is an interface current induced. In this last figure, which corresponds to the situation from a), Δ^s is equal to Δ^d on the interface and decreases linearly to zero within 20 sites of the interface.

the relevancy of the interface current.

In conclusion we have set up a simple method so determine the existence of bound states at the interfaces of d-wave superconductors and antiferromagnets. In particular we studied the energetics of the notorious zero energy mode bound to {110} I/dSC interfaces first discovered by Hu[31]. This state is always spin split when the insulator is an antiferromagnet and is analogous to the split states found around the magnetic vortex cores of YBCO and BSCCO crystals. In the case of an array of junctions corresponding to a periodic domain of vertical or diagonal stripes these states will hybridize and eventually form a band. A current along the interface exists only when the effect of a competing, interface induced *is* component exceeds the spin splitting.

3 Impurities in a superconductor

*Some of the material in this chapter has been published by the author and P. Hedegård in Physical Review B **67**, 8127 (2003)[55].*

During the last decade the technique of scanning tunnelling microscopy (STM) has been tremendously improved. Examples of state of the art STM measurements include the recent studies of quantum corrals and quantum mirages built atom by atom on metallic surfaces and studied with atomic resolution in space and better than one meV resolution in energy[56].

The study of inhomogeneities and disorder in general and single impurities in particular in high-T_c materials is a subject of great controversy and is still largely unsettled. Even the physics governing a single nonmagnetic impurity in the superconducting phase is unresolved. The main reason for the interest in impurities is that they act as probes of the underlying electronic structure. For instance, a d-wave superconductor displays clear characteristics in the vicinity of e.g. a nonmagnetic impurity. Indeed, as shown below, this was one of the cornerstones in proving that the superconducting state has d-wave pairing symmetry.

The controversy is mainly caused by a bias toward the type of order that 'pops up' when an impurity locally destroys the superconductivity. This is also related to the question of how to deal theoretically with the impurities in the first place, e.g. is a conventional scattering potential sufficient or are there strong correlations between the impurity states and the surrounding electrons that need be taken into account?

After a brief survey of the current experimental status, the following sections deal with this question. We will see that by performing scanning tunnelling experiments in the proximity of several impurities, it is possible to resolve this issue.

3.1 Experimental STM measurements around single impurities

According to Fermi's golden rule, the current I at position i and STM bias voltage V is (see e.g. Tersoff and Hamann[57])

$$I(i) = \frac{2\pi e}{\hbar} \sum_{i,\nu} |M_{t,\nu}(i)|^2 f(\varepsilon_t)(1 - f(\varepsilon_\nu))\delta(\varepsilon_t - \varepsilon_\nu + eV) \qquad (3.1)$$

where e is the electron charge, t and ν denote the tip and surface states respectively, f is the Fermi function, and $M_{t,\nu}(i)$ is the tunnelling matrix element

from the tip state t to the surface state ν at site i. Thus, the tunnelling current is simply related to the square of M and the probability of an occupied tip state and an empty surface state. As usual, the delta function guarantees energy conservation. Treating the tip as a point source[57], $|M_{t,\nu}(i)|^2 \propto |\Psi_\nu(i)|^2$, where $\Psi_\nu(i)$ denotes the eigenfunctions of the surface. Now, using the relation $\int d\omega \delta(\varepsilon_t + eV - \omega)\delta(\omega - \varepsilon_\nu) = \delta(\varepsilon_t - \varepsilon_\nu + eV)$ we can write (at low temperature)

$$I(i) \propto \int_0^{eV} \sum_\nu d\varepsilon |\Psi_\nu(i)|^2 \delta(\varepsilon - \varepsilon_\nu) = \int_0^{eV} d\varepsilon N(i, \varepsilon). \qquad (3.2)$$

Here, we assumed a constant density of states for the tip (and pulled it out of the integral) and defined the local density of states (LDOS) $N(i, \varepsilon)$

$$N(i, \varepsilon) = \sum_\nu |\Psi_\nu(i)|^2 \delta(\varepsilon - \varepsilon_\nu). \qquad (3.3)$$

Thus, the differential tunnelling conductance $dI/dV(i, \varepsilon)$ measured at site i is directly proportional to the LDOS

$$\frac{dI}{dV}(i, \varepsilon) \propto N(i, \varepsilon) \qquad (3.4)$$

It is this equation that allows us to compare the LDOS calculated within scattering theory to the STM measurements. In a spectroscopic STM measurement the tip-surface distance is fixed and the energy dependence of the LDOS is measured by sweeping the bias voltage. This type of measurement can be used to reveal resonance states near impurity sites.

Below, I discuss briefly some important STM experiments performed near single impurities in the superconducting phase of BSCCO. From the history of superconductivity we know the importance of tunnelling experiments. Indeed Giaever[58] found the first direct evidence of the BCS pairing gap $\Delta(T)$ in the superconducting density of states by measuring the minimum energy required to insert an electron into a superconductor by a tunnelling process.

3.1.1 Nonmagnetic impurities in the unitary limit

The first atomic scale cryostatic STM measurements around nonmagnetic (presumably Au) impurities on the surface of overdoped $Bi_2Sr_2CaCu_2O_8$ single crystals were performed by Yazdani *et al.*[59] and by Hudson *et al.*[60] In the superconducting state, it was found that nonmagnetic impurities create localized low-energy states as evidenced by strong tunnelling peaks near zero bias, i.e. in the middle of the superconducting gap. The existence of impurity (virtual) bound states around nonmagnetic defects is in strong contrast to the conventional s-wave superconductors in which similar bound states are only created around magnetic impurities. This, of course, is closely related to Anderson's theorem concerning the superconductor's indifference to nonmagnetic

impurities. On the other hand, since one of the assumptions of Anderson's theorem is that the momentum dependence of the gap function is weak, it breaks down in anisotropic superconductors.

For conventional superconductors such as Nb or Pb, the presence of small concentrations of time-reversal symmetry breaking magnetic impurities locally destroy the superconductivity. Similar to the effect of a magnetic field the local magnetic moments act as pair breakers by spin-flip scattering. This strongly distinct behavior between magnetic and nonmagnetic impurities in s-wave BCS superconductors has also been verified by atomic scale STM experiments[61]. More recent and higher spatially resolved tunnelling spectroscopy around well-identified nonmagnetic impurities was performed by Pan *et al.*[62] By swapping zinc atoms for copper in optimally doped BSCCO, localizing the zinc impurities, and performing STM scans resulted in the data displayed in Fig. 3.1. In
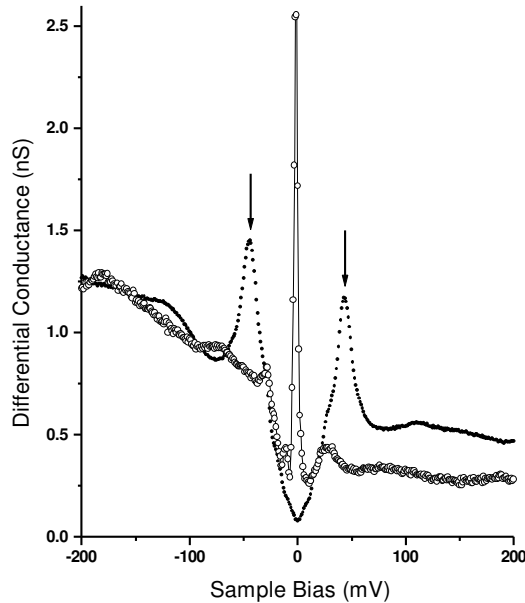

Figure 3.1: Differential tunnelling conductance versus sample bias taken at two different locations on the Zn-BSCCO crystal. Solid (open) bullets correspond to STM tip away from (right on top of) the Zn impurity. Clearly, the impurity induces a low-energy state and strongly suppress the coherence peaks indicated by the arrows. Adapted from Ref. [62]

the bulk superconductor the d-wave gap and the accociated coherence peaks are clearly seen. But at the zinc site there is a strong scattering resonance at low energy, $\Omega \approx -2.0$meV, (as measured from the Fermi level) and the coherence peaks are strongly suppressed, indicating a local destruction of the superconductivity. Thus the main conclusions are identical to those by Yazdani *et al.*[59]

The characteristic spatial feature of the localized state was found by Pan *et al.*

to be cross shaped, rotated 45 degrees compared to the Cu-O bonds, which is a very strong indication of a d-wave condensate. Colloquially, the quasi-particles can be said to escape from the scattering site along the nodal direction where the superconducting gap vanishes. In fact, as will be shown below, the characteristics of the measured state are expected within a potential scattering scenario of nonmagnetic impurities in d-wave superconductors.

A technical detail which may be of importance in understanding the measured LDOS is related to a interlayer filtering of the STM signal. The spatial cross shape of the resonance state as seen by Pan *et al.*[62] seems to be superimposed on another cross aligned along the Cu-O bond directions. When the BSCCO crystals are cleaved, the top surface is the BiO layer, the next a SrO_2 layer, and only the third layer is the CuO_2 plane. The two topmost nonconducting layers may "filter" the STM signal and modify both the energetics and the spatial structure of that expected around an impurity in a clean superconductor. The filtering effect arises from quantum interference between several distinct paths from the impurity to the STM tip. This effect was first pointed out by Zhu *et al.*[63] and Martin *et al.*[64] The tunnelling may happen either directly between the tip and the $3d_{x^2-y^2}$ wave functions in the CuO_2 planes or indirectly through excited states from overlapping intermediate orbitals in the SrO_2 and BiO layers. It can be argued that the typical distance of 10 Å in a STM experiment between the probing tip and the CuO_2 planes strongly reduces the direct tunnelling signal[64]. On the other hand, indirect tunnelling may happen through the strongly overlapping $6p_z$ Bi orbital and the $2p_z$ and 3s orbitals of the apical oxygen. The latter overlaps with the 4s Cu orbitals which extend out of the CuO_2 planes (as opposed to $3d_{x^2-y^2}$). Since the 4s Cu orbital is orthogonal to the on-site $3d_{x^2-y^2}$ it follows that when keeping the STM tip right above a surface Bi atom it does not probe the Cu ion two layers directly beneath it. However, since, in the CuO_2 plane, the Cu 4s orbital does couple to the four *neighboring* Cu $3d_{x^2-y^2}$ orbitals the resulting tunnelling amplitude at site i_x, i_y is proportional to the norm square of $\Psi_{i_x+1,i_y} + \Psi_{i_x-1,i_y} - \Psi_{i_x,i_y+1} - \Psi_{i_x,i_y-1}$, where Ψ_{i_x,i_y} is the impurity state wave function at site i_x, i_y. Thus, in conclusion, the tunnelling amplitude right above an impurity does not probe its $3d_{x^2-y^2}$ orbitals but rather a linear combination of its four nearest Cu neighbors. This path of interlayer tunnelling through overlapping orbitals is similar to the early proposed interlayer tunnelling mechanism as the origin of the d-wave superconductivity[65].

3.1.2   Magnetic impurities in the unitary limit

In contrast to the strong modifications caused by Zn, magnetic Ni atoms inserted into a d-wave superconductor has very little effect on the local environment. This was initially taken as evidence for a magnetic mechanism of high-T_c superconductivity[66].

The first atomically resolved STM measurements around Ni atoms substituting Cu in the CuO_2 planes of optimally doped BSCCO were obtained by Hudson *et*

al.[67] By the obtained real-space LDOS maps it was found that the particle-like (positive sample bias) and hole-like (negative sample bias) parts of the impurity state are rotated 45 degrees with respect to each other. This means that the particle-like LDOS peaks where the hole-like LDOS is low and vice versa.

The energy dependence of the LDOS is shown in Fig. 3.2 at four loca-
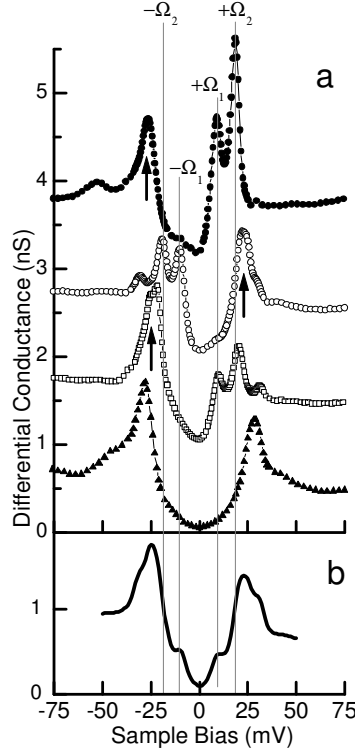

Figure 3.2: a) Differential tunnelling conductance versus sample bias at the Ni position (top), the two nearest neighbors (middle scans), and 30 Å away from the impurity. The two resonance peaks at $eV = \pm\Omega_1$ and $eV = \pm\Omega_2$ are clearly identified. b) LDOS averaged around the impurity site. Adapted from Ref. [67]

tions near the Ni site: above the Ni atom (top image), above the nearest Cu neighbor, above the second nearest Cu neighbor, and at a distance 30 Å away from the impurity site. Clearly, the two particle-like impurity resonances at $\Omega \approx 9.2, 18.6$meV at the Ni site become hole-like at the nearest neighbor and again particle-like at the second nearest neighbor, a pattern that is in agreement with the overall real-space scattering structure mentioned above. The coherence peaks are not modified when approaching the impurity site, indicating that the superconductivity is left intact by a magnetic impurity moment.

3.1.3   Impurities in the weak limit

As clarified below, the measured LDOS around single impurities can be thought of as arising from *strong* potential scattering sites. Recently, there has also been considerable discussion of experiments probing the LDOS around *weak* impurities in the superconducting state of BSCCO. The technique is dubbed Fourier transform scanning tunnelling spectroscopy.

From such scattering sites (whose precise identity remain unknown) elastic scattering of quasi-particles mixes eigenstates with different wave vectors but on the same contour of constant energy and leads to characteristic interference patterns around the impurities. In this way the impurities cause rippling patterns of the electron waves similar to how pebbles cause ripples in a pond[68]. By Fourier transforming measured real-space LDOS maps containing a large number of impurity sites it is possible to map out the dispersion of the eigenstates of the homogeneous system. Indeed, this technique has been utilized to map out the Fermi surface for several semiconductor materials[69, 70].

For a d-wave superconductor with the normal state Fermi surface shown by the dashed lines in Fig. 3.3, the contours of constant energy below the maximum gap value evolve from a single point at zero energy to the characteristic banana-shaped closed contours. Since the tips (where $|dE(\mathbf{k})/d\mathbf{k}|^{-1}$ is
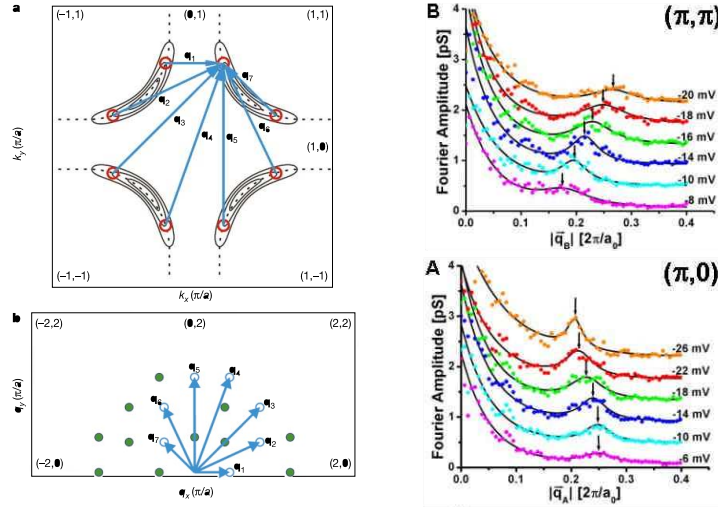

Figure 3.3: Left: a) Evolution of the banana-shaped contours of constant energy with increasing energy, and b) the expected dominating wavevectors of quasi-particle interference. Right: Dispersion of the interference peaks along the A) $(\pi, 0)$ and B) (π, π) direction. Note that the peak disperse to A) lower and B) larger wavevectors, respectively. This agrees well with the expected behavior form the Fermi surface shown to the right. Adapted from Ref. [71, 72]

largest) contribute the most to the quasi-particle density of states, we expect the Fourier transformed spatial LDOS maps to be dominated by peaks at the wave vectors $\mathbf{q}_{1...7}$ shown in the lower left part of Fig. 3.3. This is because

a quasi-particle near one tip has a large probability of being scattered to another tip in an elastic scattering event, the scattering vector being given by $\mathbf{k}_{final} - \mathbf{k}_{initail} = \mathbf{q}_{1...7}$[73].

For the BSCCO systems this type of experiment was first performed by Hoffman *et al.*[71] and later by McElroy *et al.*[72]. Some results are shown on the right hand side of Fig. 3.3, which displays the Fourier amplitude at various energies as a function of wave vector along the $(\pi, 0)$ (A) and (π, π) (B) direction. The dispersive peaks can be identified with the $\mathbf{q}_1$ (A) and $\mathbf{q}_7$ (B) scattering vectors, respectively. As shown by McElroy *et al.*[72] dispersions corresponding to the other $\mathbf{q}_1$-vectors can also be identified even though some are suppressed in intensity due to destructive effects caused by coherence factors[74]. The doping dependence (not shown) also agrees with that expected from a shrinking Fermi surface and agrees quantitatively with ARPES measurements (which probes only the occupied states) on the same materials.

These experiments are important because they seem to indicate that the superconducting state is very well described by a homogeneous d-wave superconductor with the expected Bogoliubov excitations. If other order parameters were lurking near by (in energy) one might expect them to be revealed when the superconducting phase is perturbed around the impurities. Indeed, as discussed later in this thesis there is strong experimental evidence for spin density wave (stripe) formation near vortex cores. Recent elastic neutron scattering measurements indicate that similar pinned stripe order emerges around non-magnetic impurities. The spin order is oriented along the crystalline directions of CuO_2 planes. In the STM experiments such local order should display a nondispersive peak when displayed similar to the right of Fig. 3.3. In fact, a closer look at the lower right graph of Fig. 3.3 does show some evidence for a nondispersive peak around $|\mathbf{q}_A|/2\pi \approx 0.25$ which matches the periodicity of eight lattice constants seen in the neutron scattering data. More experimental evidence for pinned stripe order proximate to the impurity centers have come from Howald *et al.*[75] and has been discussed in detail by Bindloss *et al.*[76]. At present this issue remains unresolved, but certainly the quasi-particle scattering interference dominates the low-energy Fourier images for BSCCO around optimal doping. It would be very interesting to perform similar STM experiments on LSCO crystals which are available at all doping levels and known to exhibit stripe order in the underdoped regime.

The discussion above was for energies below the maximum gap, $\omega < \Delta_0$. At $\omega \sim \Delta_0$ the STM patterns changes significantly to reveal two non-mixing distinct regimes. It has been speculated that these represent two electronic states of matter constituting the "true" nature of the quantum liquid governing the physics of the high-T_c materials[72]. In fact, recent STM measurements by Vershinin *et al.*[77] and McElroy *et al.*[78] strongly support the notion that in the underdoped regime, the electronic structure is dominated by inhomogeneous pseudogap islands which in turn are characterized by charge checkerboard order with a periodicity close to $4a$.

3.2 One impurity in a s-wave superconductor

The study of low-energy impurity-induced states in superconductors was initiated by the work of Yu[79] and Shiba[80] on magnetic impurities in s-wave superconductors. In this case, it is well known that increasing the impurity concentration increases the number of bound states, deceases the gap, and leads first to gapless superconductivity and finally to the destruction of superconductivity (Abrikosov-Gorkov theory[81]).

In the following, we ignore the quantum mechanical nature of the impurity spin. This classical limit of the spin is obtained by, $J \to \infty$ and $S \to 0$, whereas $JS \to V_s$. The probability of spin-flip scattering is proportional to J, not the spin S. Therefore, in this limit, the impurity potential is spin dependent but does not flip the spin of the quasi-particles. Below, when dealing with magnetic impurities, I always choose the spin quantization axis of the superconducting electrons to be parallel to the impurity spin. This renders the impurity problem formally equivalent to that of a perturbation caused by a local magnetic field.

To introduce method and notation let us consider in more detail the case of a single magnetic impurity in a s-wave superconductor. The BCS Hamiltonian is given by

$$\mathcal{H}_0 = \sum_{\mathbf{k},\sigma} \xi(\mathbf{k}) \hat{c}^\dagger_{\mathbf{k}\sigma} \hat{c}_{\mathbf{k}\sigma} + \sum_{\mathbf{k}} \left(\Delta(\mathbf{k}) \hat{c}^\dagger_{\mathbf{k}\uparrow} \hat{c}^\dagger_{-\mathbf{k}\downarrow} + \text{H.c.} \right), \qquad (3.5)$$

where $\xi(\mathbf{k}) = \varepsilon(\mathbf{k}) - \mu$ and for s-wave pairing, $\Delta(\mathbf{k}) = \Delta$. In terms of the Nambu spinor $\hat{\psi}^\dagger_{\mathbf{k}} = (\hat{c}^\dagger_{\mathbf{k}\uparrow}, \hat{c}_{-\mathbf{k}\downarrow})$, the corresponding Nambu Greens function $\mathcal{G}^{(0)}(\mathbf{k}, \omega_n) = -\int d\tau d\mathbf{r} \langle T_\tau \hat{\psi}(0,0) \hat{\psi}^\dagger(\mathbf{r}, \tau) \rangle \exp(i(\mathbf{k} \cdot \mathbf{r} - \omega_n \tau))$ is given by

$$\mathcal{G}^{(0)}(\mathbf{k}, \omega_n) = \frac{i\omega_n \tau_0 + \xi(\mathbf{k})\tau_3 + \Delta \tau_1}{(i\omega_n)^2 - \xi(\mathbf{k})^2 - \Delta^2}, \qquad (3.6)$$

where $\boldsymbol{\tau} = (\tau_0, \tau_1, \tau_2, \tau_3)$ is a vector containing the 2×2 identity matrix (τ_0) and the three Pauli matrices (τ_1, τ_2, τ_3). The perturbation caused by a magnetic impurity moment oriented along the z-axis and positioned at the origin is modelled by

$$\mathcal{H}_{imp} = V_m \left(\hat{c}^\dagger_{0\uparrow} \hat{c}_{0\uparrow} - \hat{c}^\dagger_{0\downarrow} \hat{c}_{0\downarrow} \right) = V_m \sum_{\mathbf{k},\mathbf{k}'} \left(\hat{c}^\dagger_{\mathbf{k}\uparrow} \hat{c}_{\mathbf{k}'\uparrow} - \hat{c}^\dagger_{\mathbf{k}\downarrow} \hat{c}_{\mathbf{k}'\downarrow} \right), \qquad (3.7)$$

V_m determining the strength of this magnetic delta-function potential. Since the impurity spin S is coupled to the surrounding electron spin density through the exchange coupling J, $V_m = JS$. In Nambu space the Hamiltonian becomes

$$\mathcal{H}_{imp} = V_m \hat{\psi}^\dagger_0 \tau_0 \hat{\psi}_0 = V_m \sum_{\mathbf{k},\mathbf{k}'} \hat{\psi}^\dagger_{\mathbf{k}} \tau_0 \hat{\psi}_{\mathbf{k}'}. \qquad (3.8)$$

The full Greens function for this system is, of course, determined by the total Hamiltonian, $\mathcal{H} = \mathcal{H}_0 + \mathcal{H}_{imp}$. Thus, if we for the moment let a, b, c denote arbitrary quantum numbers, the equations of motion for the two Greens functions $\mathcal{G}^{(0)}(a, b) = -\langle T_\tau \hat{\psi}(a)\hat{\psi}^\dagger(b)\rangle_0$ and $\mathcal{G}(a, b) = -\langle T_\tau \hat{\psi}(a)\hat{\psi}^\dagger(b)\rangle$ are given by

$$[-\partial_{\tau_a} - H_0(a)]\,\mathcal{G}^{(0)}(a, b) \;=\; \delta_{a,b} \tag{3.9}$$

$$[-\partial_{\tau_a} - H(a)]\,\mathcal{G}(a, b) \;=\; \delta_{a,b} \tag{3.10}$$

from which we see that

$$[-\partial_{\tau_a} - H(a)]\,\mathcal{G}(a, b) \;=\; [-\partial_{\tau_a} - H(a) + H_{imp}(a)]\,\mathcal{G}^{(0)}(a, b) \tag{3.11}$$

$$=\; [-\partial_{\tau_a} - H(a)]\,\mathcal{G}^{(0)}(a, b) + H_{imp}(a)\mathcal{G}^{(0)}(a, b)$$

$$=\; [-\partial_{\tau_a} - H(a)]\,\mathcal{G}^{(0)}(a, b) + \sum_c \delta_{a,c} H_{imp}(c)\mathcal{G}^{(0)}(c, b).$$

Acting in the left by the matrix $[-\partial_{\tau_a} - H(a)]^{-1}$ we get the Dyson integral equation for the full Greens function $\mathcal{G}(a, b)$

$$\mathcal{G}(a, b) = \mathcal{G}^{(0)}(a, b) + \sum_c \mathcal{G}(a, c)H_{imp}(c)\mathcal{G}^{(0)}(c, b). \tag{3.12}$$

Now, if we let the indices above denote both Nambu space (which are not written explicitly, i.e. $\mathcal{G}$ and $\mathcal{H}_{imp}$ are 2×2 matrices like in Eqn. (3.6) and (3.24)) and sites on a real space lattice, we obtain in the case of a single impurity at the origin

$$\mathcal{G}(i, j) = \mathcal{G}^{(0)}(i - j) + \mathcal{G}(i, 0)H_{imp}(0)\mathcal{G}^{(0)}(0 - j). \tag{3.13}$$

Then since

$$\mathcal{G}(i, 0) = \mathcal{G}^{(0)}(i) + \mathcal{G}(i, 0)H_{imp}(0)\mathcal{G}^{(0)}(0), \tag{3.14}$$

we have

$$\mathcal{G}(i, 0) = \mathcal{G}^{(0)}(i)\left[1 - H_{imp}(0)\mathcal{G}^{(0)}(0)\right]^{-1} \tag{3.15}$$

and therefore the *exact* solution to Eqn. (3.13) is

$$\mathcal{G}(i, j) = \mathcal{G}^{(0)}(i - j) + \mathcal{G}^{(0)}(i)\left[1 - H_{imp}(0)\mathcal{G}^{(0)}(0)\right]^{-1} H_{imp}(0)\mathcal{G}^{(0)}(-j), \tag{3.16}$$

which contains only the unperturbed Greens function $\mathcal{G}^{(0)}$ on the right hand side. Note that only $\mathcal{G}^{(0)}$ is translational invariant. In terms of the T-matrix T

$$T(0) = \left[1 - H_{imp}(0)\mathcal{G}^{(0)}(0)\right]^{-1} H_{imp}(0). \tag{3.17}$$

the expression for the full Greens function is given by

$$\mathcal{G}(i,j) = \mathcal{G}^{(0)}(i-j) + \mathcal{G}^{(0)}(i)T(0)\mathcal{G}^{(0)}(-j). \tag{3.18}$$

From Eqn. (3.18) it is clear that the particle can propagate from site j to site i either directly or scatter off the impurity site at the origin. It is also clear that the study of single impurities becomes the study of the properties of the corresponding T-matrix. In order to get a better feel for the unusual properties of impurities in d-wave superconductors it is instructive to first study briefly the case of conventional s-wave pairing.

From the solution of the impurity problem given by Eqn. (3.17) and (3.18) the remaining exercise is to determine $\mathcal{G}^{(0)}(0)$. From the expression (3.6) (after continuing to the real axis) we get

$$\sum_{\mathbf{k}} \frac{\omega \pm \xi(\mathbf{k})}{\omega^2 - \xi(\mathbf{k}) - \Delta^2} \;\;=\;\; N(0) \int_{-A}^{B} d\xi \frac{\omega \pm \xi}{\omega^2 - \xi - \Delta^2} =$$

$$-N(0)\frac{\omega \arctan\left(\frac{\xi}{\sqrt{\Delta^2-\omega^2}}\right)}{\sqrt{\Delta^2-\omega^2}}\Bigg|_{-A}^{B} \;\;\mp\;\; \frac{N(0)}{2}\log\left(\Delta^2+\xi^2-\omega^2\right)\Bigg|_{-A}^{B} =$$

$$-\frac{\pi N(0)\omega}{\sqrt{\Delta^2-\omega^2}} \;\;\mp\;\; \frac{N(0)}{2}\log\left(\frac{B^2+\Delta^2-\omega^2}{A^2+\Delta^2-\omega^2}\right)$$

$$=\;\; -\frac{\pi N(0)\omega}{\sqrt{\Delta^2-\omega^2}}, \tag{3.19}$$

assuming that the band limits $|A|, |B| \gg \Delta, \omega$ and $\omega < \Delta$. Here, $N(0)$ denotes the normal density of states at the Fermi energy. Similarly we get for the off-diagonal matrix element

$$\sum_{\mathbf{k}} \frac{\Delta}{\omega^2 - \xi(\mathbf{k}) - \Delta^2} = -\frac{\pi N(0)\Delta}{\sqrt{\Delta^2-\omega^2}}. \tag{3.20}$$

Since the bound states are determined by zeros in the denominator of the T-matrix we have the following condition for bound states with energy ω_B

$$\det\left[1 - H_{imp}(0)\mathcal{G}^{(0)}(0,\omega_B)\right] = 0. \tag{3.21}$$

For the magnetic impurity in a s-wave superconductor this leads to

$$0 \;\;=\;\; (1 - V_m\mathcal{G}_{11}^{(0)}(0))(1 - V_m\mathcal{G}_{22}^{(0)}(0)) - V_m^2\mathcal{G}_{12}^{(0)}(0)\mathcal{G}_{21}^{(0)}(0) \Leftrightarrow$$

$$0 = \left(1 + \frac{V_m \pi N(0) \omega_B}{\sqrt{\Delta^2 - \omega_B^2}}\right)^2 - \left(\frac{V_m \pi N(0) \Delta}{\sqrt{\Delta^2 - \omega_B^2}}\right)^2 \Leftrightarrow$$

$$\omega_B = \pm \Delta \frac{1 - (V_m \pi N(0))^2}{1 + (V_m \pi N(0))^2}. \tag{3.22}$$

Since $\omega_B < \Delta$ bound state solutions exist inside the superconducting gap. Furthermore, since the s-wave gap fully suppresses states with energy less that the gap Δ these impurity states are *bona fide* bound states. In Fig. 3.4 we plot the two bound state energies as a function of the scattering strength V_m. As seen there is a level crossing at a critical interaction strength V_m^c. As
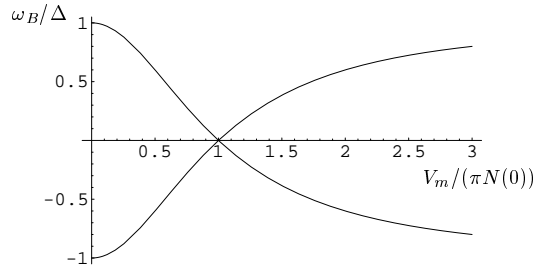

Figure 3.4: Energy of the impurity states versus magnetic scattering strength V_m.

discussed first by Sakurai[82] and later by Salkola *et al.*[83] this corresponds to a first order quantum phase transition where the spin quantum number of the superconducting ground state changes from zero for $V_m < V_m^c$ to 1/2 for $V_m > V_m^c$. The total spin then becomes $S \pm 1/2$ depending on the sign of the interaction V_m (i.e. the sign of the exchange interaction).

For a nonmagnetic impurity V_s it is easy to verify from the condition

$$0 = (1 - V_s \mathcal{G}_{11}^{(0)}(0))(1 + V_s \mathcal{G}_{22}^{(0)}(0)) + V_s^2 \mathcal{G}_{12}^{(0)}(0) \mathcal{G}_{21}^{(0)}(0), \tag{3.23}$$

that no impurity bound states are generated.

Historically, the bound state of a single classical magnetic impurity in a s-wave BCS superconductor given by Eqn. (3.22) was first discussed by Shiba[80] and Yu[79] in 1968. More extensive studies of the thermodynamic effects of incoherent spin-flip scattering off magnetic impurities in the superconducting phase performed by Abrikosov and Gorkov (AG) in 1961[81] were done in the first Born approximation. Shiba bridged the two approaches by showing that in this approximation the result (3.22) reduces to the AG results, and the impurity bound state is indistinguishably close to the gap edge. Further studies of classical impurities in superconductors can be found in the extensive review by Flatté and Byers[84].

3.3 One impurity in a $d_{x^2-y^2}$-wave superconductor

In this section we will see how most of the experimental features discussed during the brief experimental survey in the beginning of this chapter can be understood from quasi-particle scattering off a single impurity in a d-wave BCS superconductor.

We study the electronic structure around a single nonmagnetic (scalar) impurity in a d-wave superconductor

$$\mathcal{H}_{imp} = V_s \hat{\psi}_0^\dagger \tau_3 \hat{\psi}_0. \tag{3.24}$$

An example is zinc which is in the Zn^{2+} state and thus has spin $S = 0$. Let us introduce the conventional notation, $E_{\mathbf{k}}^2 = \xi_{\mathbf{k}}^2 + \Delta_{\mathbf{k}}^2$. Initially the problem appears simpler with d-wave pairing symmetry since $\sum_{\mathbf{k}} \Delta_{\mathbf{k}} = 0$, and therefore the off-diagonal elements in $\mathcal{G}^{(0)}(0)$ obtained from the Fourier transform of

$$\mathcal{G}^{(0)}(\mathbf{k}, \omega_n) = \frac{i\omega_n \tau_0 + \xi(\mathbf{k})\tau_3 + \Delta(\mathbf{k})\tau_1}{(i\omega_n)^2 - \xi(\mathbf{k})^2 - \Delta(\mathbf{k})^2}, \tag{3.25}$$

vanishes. Hence the T-matrix becomes diagonal

$$T(\omega) = \begin{pmatrix} \frac{V_s}{1 - \sum_{\mathbf{k}} \frac{V_s \omega}{\omega^2 - E_{\mathbf{k}}^2}} & 0 \\ 0 & \frac{-V_s}{1 + \sum_{\mathbf{k}} \frac{V_s \omega}{\omega^2 - E_{\mathbf{k}}^2}} \end{pmatrix}. \tag{3.26}$$

Clearly the poles are found at

$$\pm \frac{1}{V_s} = \sum_{\mathbf{k}} \frac{\omega}{\omega^2 - E_{\mathbf{k}}^2}. \tag{3.27}$$

On the other hand, the momentum dependence of the pairing gap makes the Fourier transform of the Greens function $\mathcal{G}^{(0)}(\mathbf{k}, \omega)$ more complicated than in the s-wave case

$$
\begin{aligned}
\sum_{\mathbf{k}} \frac{\omega}{\omega^2 - E_{\mathbf{k}}^2} &= N(0) \int_{-A}^{B} d\xi \int_0^{2\pi} d\varphi \frac{\omega}{\omega^2 - \xi^2 - \Delta_0^2 \cos^2 2\varphi} \\
&= -N(0)\omega \int_0^{2\pi} d\varphi \frac{1}{\sqrt{-\omega^2 + \Delta_0^2 \cos^2 2\varphi}} \arctan\left(\frac{\xi}{\Delta_0^2 \cos^2 2\varphi - \omega^2}\right) \Bigg|_{-A}^{B} \\
&= -4\pi N(0) \int_0^{\frac{\pi}{2}} d\varphi \frac{1}{\sqrt{\frac{\Delta_0^2 \cos^2 2\varphi}{\omega^2} - 1}}
\end{aligned}
$$

$$= -4\pi N(0) \frac{\omega}{\sqrt{\Delta_0^2 - \omega^2}} \int_0^{\frac{\pi}{2}} \frac{d\varphi}{\sqrt{1 - \left(\sqrt{\frac{\Delta_0^2}{\Delta_0^2 - \omega^2}}\right)^2 \sin^2 2\varphi}}$$

$$= -4\pi N(0) \frac{\omega}{\Delta_0} \frac{1}{\sqrt{1 - \frac{\omega^2}{\Delta_0^2}}} K\left(\frac{1}{\sqrt{1 - \frac{\omega^2}{\Delta_0^2}}}\right) \tag{3.28}$$

Here, we have again assumed that the band limits $|A|, |B|$ are large compared to the maximum gap Δ_0. $K(x)$ is the complete elliptic integral of the first kind. We can use the properties of K to get (Gradshteyn and Ryzhik, 8.128.3, p. 913 and 8.112.1, p. 908)

$$\frac{\omega}{\Delta_0} \frac{1}{\sqrt{1 - \frac{\omega^2}{\Delta_0^2}}} K\left(\frac{1}{\sqrt{1 - \frac{\omega^2}{\Delta_0^2}}}\right) =$$

$$\frac{\omega}{\Delta_0} \frac{1}{\sqrt{1 - \frac{\omega^2}{\Delta_0^2}}} \left(\sqrt{1 - \frac{\omega^2}{\Delta_0^2}} \left[K(\sqrt{1 - \frac{\omega^2}{\Delta_0^2}}) + iK'(\sqrt{1 - \frac{\omega^2}{\Delta_0^2}})\right]\right) =$$

$$\frac{\omega}{\Delta_0} \left(K(\sqrt{1 - \frac{\omega^2}{\Delta_0^2}}) + iK(\frac{\omega}{\Delta_0})\right), \tag{3.29}$$

where K' is defined through $K'(k') = K(k)$ with $k' = \sqrt{1 - k^2}$. Thus the impurity resonance condition becomes

$$\pm\frac{1}{V_s} = -4\pi N(0) \frac{\omega}{\Delta_0} \left(K(\sqrt{1 - \frac{\omega^2}{\Delta_0^2}}) + iK'(\sqrt{1 - \frac{\omega^2}{\Delta_0^2}})\right), \tag{3.30}$$

which in the limit $\omega/\Delta_0 \ll 1$ reduces to

$$\pm\frac{1}{V_s} = 4\pi N(0) \frac{\omega}{\Delta_0} \left(\ln\frac{4\Delta_0}{\omega} + i\frac{\pi}{2}\right). \tag{3.31}$$

We cannot solve this equation for ω_B in closed form, but to logarithmic accuracy the result is

$$\omega_B + i\Gamma = \Delta_0 \frac{\pi c}{2\ln(\frac{8}{\pi c})} \left(1 + i\frac{\pi}{2} \frac{1}{\ln(\frac{8}{\pi c})}\right) \tag{3.32}$$

in terms of $c = 1/\pi N(0)V_s = \cot\delta$ where δ is the scattering phase shift. The above result is valid in the limit where c becomes small, i.e. $\cot\delta \to 0$ or

equivalently $\delta \to \frac{\pi}{2}$ which is the unitary limit corresponding to a strong impurity with large scattering potential V_s. The result (3.32) was first obtained by Balatsky *et al.*[85] in 1995. The impurity state is only virtually bound (i.e. a resonant state) due to the low-energy quasi-particle states near the gap nodes. Thus, since the DOS decreases only linearly inside the d-wave gap, at the resonance energy there exists always an overlap with the continuum causing a decay rate evidenced by the imaginary part of Eqn. (3.32). In the limit where $V_s \to \infty$ the state sharpens, i.e. the energy $\omega_B \to 0$ and $\Gamma \to 0$ and becomes marginally bound. This is because the only position where the DOS of the clean system vanishes is exactly at $\omega = 0$. In the opposite limit, the state will eventually become ill defined when the width becomes comparable to the resonance energy $\omega_B \sim \Gamma$. This evolution of the resonance can be seen from Fig. 3.5. The impurity-induced quasi-particle states are hole-like (particle-
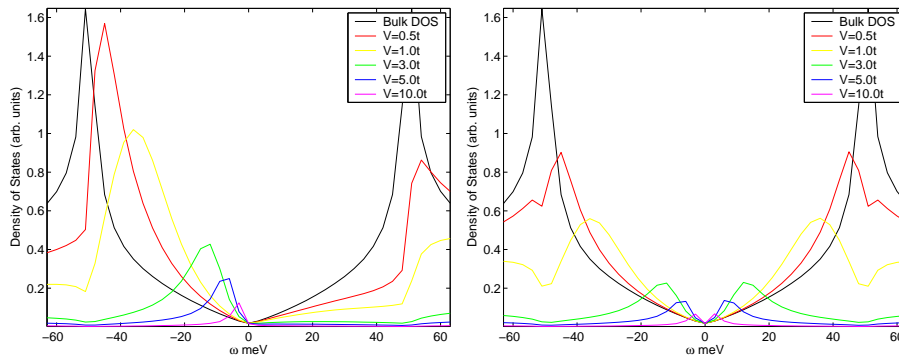

Figure 3.5: DOS at (0,0) for a single nonmagnetic (left) and magnetic (right) impurity positioned at (0,0) in a d-wave superconductor. Upon the sign change $V \to -V$ the nonmagnetic DOS peaks become hole-like, i.e. shift to negative bias, whereas the magnetic peaks are invariant.

like) for repulsive (attractive) potential. Therefore, the particle residing at a strongly scattering impurity site is predominantly of hole ($V_s > 0$) or electron ($V_s < 0$) character, leading to local pair-breaking effects. This is also seen in self-consistent calculations which show a local suppression of the gap near the impurity. It can be shown, however, that this modified gap amplitude has only minor changes on the energetics and spatial structure of the resonance state[86].

Having established these impurity states, the spatial structure of their wave-function will reflect in the spatial modulation of the local density of states around the impurity site. Since the local density of states (LDOS) can be obtained directly from the imaginary part of the full Greens function

$$N(i, \omega) = -\text{Im} \frac{\mathcal{G}_{11}(i, \omega_n \to \omega + i\Gamma)}{\pi}, \qquad (3.33)$$

where (still for a single impurity at the origin) from Eqn. (3.18)

$$\mathcal{G}(i,\omega_n) = \mathcal{G}(i,i,\omega_n) = \mathcal{G}^{(0)}(0,\omega_n) + \mathcal{G}^{(0)}(i,\omega_n)T(\omega_n)\mathcal{G}^{(0)}(-i,\omega_n). \quad (3.34)$$

Thus, to calculate the modified DOS we need the full form of the Fourier transform

$$\mathcal{G}^{(0)}(i,\omega_n) = \sum_{\mathbf{k}} \frac{i\omega_n\tau_0 + \xi(\mathbf{k})\tau_3 + \Delta(\mathbf{k})\tau_1}{(i\omega_n)^2 - \xi(\mathbf{k})^2 - \Delta(\mathbf{k})^2} \exp(i\mathbf{k}\cdot\mathbf{r}_i), \quad (3.35)$$

which for d-wave pairing symmetry is not easily integrated (along the nodal and anti-nodal directions approximate results were obtained by Joynt[86]). It is clear, however, that the momentum dependence of the $d_{x^2-y^2}$-wave gap function leads to exponential (power law) decay along the antinodal (nodal) direction. In the following we resort to numerics to perform the sum in Eqn. (3.35) by cutting the 2D Brillouin zone into many (typically 800×800) tiny squares. This was also the method used to obtain the graphs displayed in Fig. 3.5.

For the T-matrix given by Eqn. (3.26) the contribution to the LDOS from the impurity $\delta N(i,\omega_n) = -\frac{1}{\pi}\text{Im}\mathcal{G}^{(0)}(i,\omega_n)T(\omega_n)\mathcal{G}^{(0)}(-i,\omega_n)$ is given by

$$\delta N(i,\omega_n) = -\frac{1}{\pi}\text{Im}\left(V_s\frac{\mathcal{G}^{(0)}_{11}(i,\omega_n)\mathcal{G}^{(0)}_{11}(-i,\omega_n)}{1 - V_s\mathcal{G}^{(0)}_{11}(0,\omega_n)} - V_s\frac{\mathcal{G}^{(0)}_{12}(i,\omega_n)\mathcal{G}^{(0)}_{21}(-i,\omega_n)}{1 + V_s\mathcal{G}^{(0)}_{22}(0,\omega_n)}\right)$$
$$(3.36)$$

From the vanishing of the denominators in this expression we see that two resonance frequencies appear. Also, since $\mathcal{G}^{(0)}_{22}(0,\omega_n) = -\mathcal{G}^{(0)}_{11}(0,-\omega_n)$ as is evident from Eqn. (3.25), for the particle-hole symmetric case these resonance states appear symmetrically around zero energy. The existence of these two states is due to particle-hole mixing in the superconducting state. In other ordered non-superconducting phases only one state will typically be generated, an example is given in the next chapter dealing with the possible orbital antiferromagnetic ordering in the underdoped region of the cuprate materials, the d-density wave state.

Exactly at the impurity site $i = 0$ only a single peak should be seen in the DOS at $1 - V_s\mathcal{G}^{(0)}_{11}(0,\omega) = 0$ as solved analytically above. This is because the other resonance does not have weight at $i = 0$ since the off-diagonal (anomalous) Greens function vanishes at this site, $\mathcal{G}^{(0)}_{12}(0,\omega_n) = 0$, which can again be seen from the d-wave gap property $\sum_{\mathbf{k}}\Delta_{\mathbf{k}} = 0$. In general, i.e. at other sites near the impurity, this will not be the case. Fig. 3.6 shows the overall DOS around a single nonmagnetic impurity in a d-wave superconductor at the resonance energy $\Omega = -2.0\text{meV}$ (left) and at $\Omega = +2.0\text{meV}$ (right). Clearly, the real-space LDOS distribution has maximum at the nearest neighbor sites. This is not in agreement with the experiments which reveal a strong peak exactly at the impurity site and a second highest intensity on the next-nearest
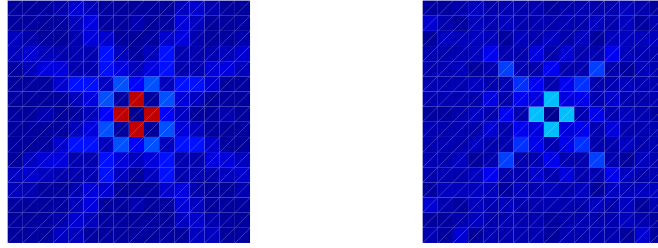
Figure 3.6: Real-space map of the LDOS around a nonmagnetic impurity at the resonance energy $\Omega = -2.0$meV (left) and at $\Omega = +2.0$meV (right). No filter function is included here.

neighbor. In Fig. 3.7 we plot the LDOS again but "through" the Bi-O filter function. Since the filter samples the four nearest neighbors it is clear why
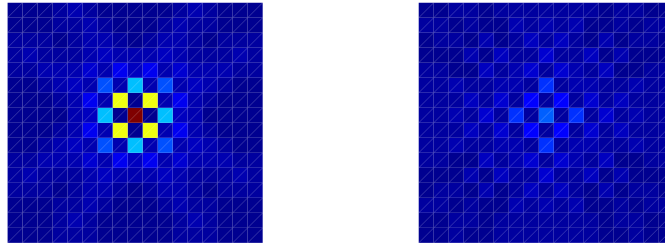

Figure 3.7: Same as Fig. 3.6 but seen through the surface filter function.

the intensity distribution looks like in Fig. 3.7. This is in agreement with the experiments. An important difference between the figures 3.7 and 3.6 is the value of the potential V_s needed to generate a resonance state at -2.0 meV. In Fig. 3.6 the potential needed was strongly repulsive whereas in Fig. 3.7 the zinc impurity acts as a strongly attractive site. The latter agrees better with that expected from bandstructure considerations: the 10 electrons of Zn^{2+} fill all the 3d orbitals and therefore the relevant $3d_{x^2-y^2}$ orbital is well below the Fermi level. This inert shell will strongly repel holes, i.e. attract electrons.

At this point we recognize many of the important experimental features around zinc impurities in the superconducting phase of BSCCO observed by Yazdani *et al.*[59] and Pan *et al.*[62]: the presence of a resonance at the impurity site giving rise to a large peak in the differential tunnelling conductance and the spatial structure of this impurity state (when including contributions from the indirect tunnelling). But what about the magnetic nickel impurities and the case of weak scattering sites?

For strong magnetic scatterers in a d-wave superconductor, and still allow-

ing for some normal potential scattering V_s, the T-matrix reads

$$T(\omega_n) = \begin{pmatrix} \frac{V_m+V_s}{1-\sum_{\mathbf{k}}\frac{(V_m+V_s)\omega_n}{\omega_n^2-E_{\mathbf{k}}^2}} & 0 \\ 0 & \frac{V_m-V_s}{1+\sum_{\mathbf{k}}\frac{(V_m-V_s)\omega_n}{\omega_n^2-E_{\mathbf{k}}^2}} \end{pmatrix}. \qquad (3.37)$$

In this case, the resonance peak spin splits and a calculation similar to the one for a purely nonmagnetic scatterer (see also Eqn. (3.32)) yields the resonance energies

$$\omega_B = -\Delta_0 \frac{1}{2N(0)(V_s \pm V_m)\ln|8N(0)(V_s \pm V_m)|} \qquad (3.38)$$

In particular, four resonance states, two at both positive and negative bias, should be observed in a tunnelling experiment. Indeed this is what was reported by Hudson *et al.*[67] The spatial structure can also be understood within the potential scattering model, but only when including the interlayer filtering[64].

Finally in this discussion of single impurity physics, let us briefly turn to the case of weak nonmagnetic impurities, i.e. the situation where V_s is no longer the dominating energy scale. The expected results caused by elastic quasi-particle scattering and the corresponding interference seen in the Fourier transformed real-space LDOS images have already been discussed in the presentation of the experimental results by Hoffman *et al.*[71] and McElroy *et al.*[72] In Fig.
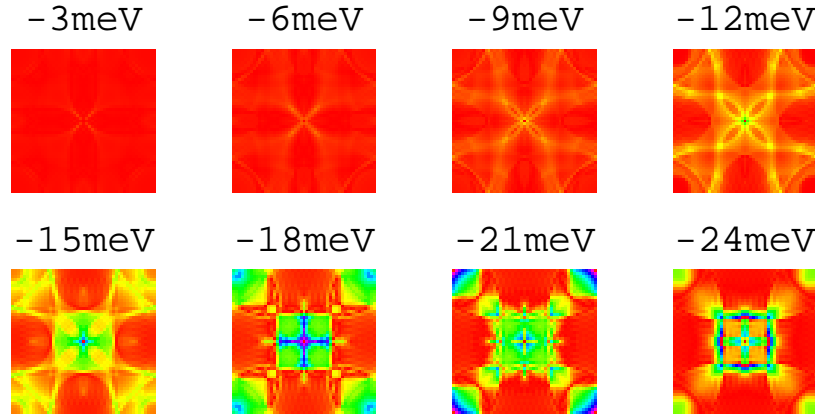

Figure 3.8: Fourier amplitude of the LDOS maps at constant energy. The amplitudes are shown as a function of momenta k_x and k_y in the first Brillouin zone.

3.8 I show the power spectrum of the Fourier images at constant energy for a nonmagnetic impurity with $V_s = 100$ meV. For clarity the $q = 0$ Fourier component at the center has been subtracted. For such a weak scattering site the

resonance is strongly overdamped and no sharp resonance state can be clearly identified in the DOS as was the case studied above. On the other hand, we clearly see a set of dispersing features in the images displayed in Fig. 3.8 (which would, of course, be completely featureless in the clean case since then, at the chosen energy, the LDOS has the same value at each site). Focusing on
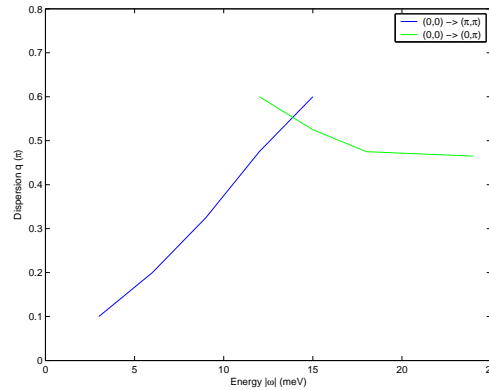

Figure 3.9: Dispersion of the momentum vector associated with scattering processes $\mathbf{q}_1$ (green) and $\mathbf{q}_7$ (blue) as defined in the top left image of Fig. 3.3.

the antinodal $(0, \pi)$ and the nodal (π, π) direction, we have plotted the dispersing peaks as a function of energy in Fig. 3.9. Clearly for these directions the calculated result agrees with that expected from the quasi-particle scattering scenario and the STM measurements as seen from Fig. 3.3. The discussion of what happens at higher energy and lower doping belongs to the discussion of what is the origin of the pseudogap state. We will not elaborate further on this largely unsettled issue here, but return to it in the following chapter.

In conclusion one may access that the salient STM findings around a single impurity can be understood in terms of a conventional d-wave superconductor perturbed by potential scattering with the possible importance of both direct and indirect tunnelling. Nevertheless, in the following section I briefly discuss the motivation and results of an alternative scenario. This will also motivate our study of the LDOS around two nonmagnetic impurities.

3.4   Discussion

An important fact that was discovered early on in the study of the cuprates, and which was not mentioned above, is the strong experimental evidence for localized $S = 1/2$ magnetic moments induced near nonmagnetic impurities such as zinc and lithium in the d-wave superconducting phase. This has become particularly evident from NMR measurements[87, 88, 89, 90, 91]. A possible explanation is related to 1) the pair-breaking (gap suppressing) property of nonmagnetic impurities in a d-wave superconductor, and 2) the fact that the superconducting phase may be proximate to a coexisting phase of super-

conducting and spin density wave order. In this picture, by suppressing the pairing condensate near the impurity the subdominant magnetic order is allowed to appear. In fact, it has been shown recently by Chen and Ting[92] that the minimal model introduced in chapter one, which at a self-consistent level includes the competition between antiferromagnetism and d-wave superconductivity, induces a moment near a nonmagnetic impurity with $S_z = 0, 1/2$, or 1 depending on the strength of the impurity potential compared to the onsite Coulomb repulsion.

There are, however, other more strongly correlated scenarios in which moments also develop near nonmagnetic impurities[93, 94, 95]. For instance within the RVB picture, the nonmagnetic impurity effectively breaks a singlet bond creating a single unpaired spinon. Thus, a nonmagnetic impurity *induces a magnetic moment* and the resonance peak is a Kondo resonance. However, it is an unusual Kondo resonance since the density of states of the surrounding d-wave superconductor vanishes linearly at low energies whereas, in the usual Kondo effect the density of states is assumed constant at low energies[96, 97]. In the bond-ordered singlet state by Sachdev *et al*[98] the spinon is naturally confined to the holon (i.e. the nonmagnetic impurity) since propagation of the spinon frustrates the bond order and costs energy. It turns out that in the Kondo scenario the real-space distribution agrees with the experiments *without the filter effect*. Thus, it appears that nonmagnetic impurities in the superconducting phase of the cuprates act either as strong attractive potential scatterers or as inductors of Kondo moments. In the following section I propose to study the two-impurity problem in order of resolve this important issue.

3.5 Two impurities in a $d_{x^2-y^2}$-wave superconductor

We perform a numerical study of the quantum interference between impurities in d-wave superconductors within a potential scattering formalism that easily applies to multiple impurities. The evolution of the low-energy local density of states for both magnetic and nonmagnetic point scatterers is studied as a function of the spatial configuration of the impurities. Further we discuss the influence of a subdominant bulk superconducting order parameters on the interference pattern from multiple impurities.

The past few years have proved the importance of experimental techniques which can directly test the wealth of information associated with modifications of the local density of states (LDOS) around impurities, grain boundaries and vortices in strongly correlated electron systems. In particular scanning tunneling microscopy (STM) measurements have provided detailed LDOS images around single nonmagnetic[59, 62] (Zn) and magnetic[67] (Ni) impurities on the surface of the high temperature superconductor $Bi_2Sr_2CaCuO_{4+\delta}$ (BSCCO).

For conventional superconductors Yu and Shiba[80] showed that as a result of the interaction between a magnetic impurity and the spin density of the conduction electrons, a bound state located around the magnetic impurity is formed inside the gap in the strong-scattering (unitary) limit. For anisotropic

superconductors a number of authors generalized the Yu-Shiba approach to study the LDOS around single impurities[85]. It was found, for instance, that for a single nonmagnetic impurity there is only a virtual bound (or resonant) state due to the existence of the low-energy nodal quasi-particles. The one-impurity problem was recently reviewed by several authors[99, 100].

Recently Hoffman *et al.*[71] measured the energy dependence of the Fourier transformed LDOS images on the surface of optimally doped BSCCO below T_c. The dispersive features were explained from the point of elastic quasi-particle interference resulting from a single *weak*, nonmagnetic impurity[73]. This gives credence that a scattering potential picture can yield valuable predictions in the superconducting state of these materials. Evidence for quantum interference between *strong* scatterers has been observed in the CuO chains of $YBa_2Cu_3O_{6+x}$ by Derro *et al.*[101] Future experimental ability to control the position of the impurities on the surface of a superconductor and perform detailed STM measurements around multiple impurity configurations motivates further theoretical studies of the resulting quantum interference.

Previous calculations have studied the formation of bonding and antibonding states around two magnetic impurities in s-wave superconductors[102, 103]. For d-wave superconductors it was found that the interference effects between two nonmagnetic unitary scatterers depends crucially on the distance and orientation of the impurities[99, 100, 104]. The orientational dependence arises from the anisotropic gap function, and provides an alternative method to identify the symmetry of the superconducting gap. Several authors[85, 105] have previously suggested similar ideas in the case of one impurity.

In this section we study multiple impurity effects by exactly inverting the Gorkov-Dyson equation. In particular, we discuss the effect of quantum interference between: 1) nonmagnetic impurities in the strong scattering limit, 2) nonmagnetic impurities in the case of induced subdominant superconducting order parameters, and 3) magnetic and nonmagnetic impurities. All the calculations are performed within a quasi-particle scattering framework with classical impurities[80, 105]. The main purpose is to use quantum interference to obtain results that pose further tests on this approach and to illustrate the strong sensitivity of the LDOS on the positions of the impurities.

The Greens function $\hat{G}^{(0)}(\mathbf{k}, \omega)$ for the unperturbed d-wave superconductor is given in Nambu space by

$$\hat{G}^{(0)}(\mathbf{k}, \omega) = [i\omega_n \hat{\tau}_0 - \xi(\mathbf{k})\hat{\tau}_3 - \Delta(\mathbf{k})\hat{\tau}_1]^{-1}, \qquad (3.39)$$

where $\hat{\tau}_\nu$ denotes the Pauli matrices in Nambu space, $\hat{\tau}_0$ being the 2×2 identity matrix. For a system with $d_{x^2-y^2}$-wave pairing $\Delta(\mathbf{k}) = \frac{\Delta_0}{2}(\cos(k_x) - \cos(k_y))$. Below, $\Delta_0 = 25\text{meV}$ and the lattice constant a_0 is set to unity. In this section we use a normal state quasi-particle energy $\xi(\mathbf{k})$ relevant for BSCCO around optimal doping (14%)

$$\xi(\mathbf{k}) = -2t(\cos(k_x) + \cos(k_y)) - 4t'\cos(k_x)\cos(k_y) - \mu \qquad (3.40)$$

with $t = 300\text{meV}$, $t' = -0.4t$ and $\mu = -1.18t$. Here t (t') refers to the nearest (next-nearest) neighbor hopping integral and μ is the chemical potential.

We model the presence of scalar and magnetic impurities in the system by the following δ-function interactions

$$\hat{H}^{int} = \sum_i \left[\left(V_i^S + V_i^M \right) \hat{c}_{i\uparrow}^\dagger \hat{c}_{i\uparrow} + \left(V_i^S - V_i^M \right) \hat{c}_{i\downarrow}^\dagger \hat{c}_{i\downarrow} \right]. \tag{3.41}$$

Here i denotes the set of lattice sites containing magnetic and/or scalar impurities and V_i^M (V_i^S) is the strength of the corresponding effective potential. We consider only the z-component of the magnetic impurity interaction and ignore spin-flip scattering.

For a single nonmagnetic impurity at the origin it is well-known that the scattering modifies the Greens function by

$$\delta G_{11}(\mathbf{r}, i\omega_n) = \frac{\left[G_{11}^{(0)}(\mathbf{r}, i\omega_n) \right]^2}{\frac{1}{V^S} - G_{11}^{(0)}(0, i\omega_n)} - \frac{\left[G_{12}^{(0)}(\mathbf{r}, i\omega_n) \right]^2}{\frac{1}{V^S} - G_{11}^{(0)}(0, -i\omega_n)}. \tag{3.42}$$

Here $\mathbf{r}$ is the distance to the origin and $G_{\alpha\beta}$ refers to the $\alpha\beta$th entry of the 2×2 Nambu subspace.

Naturally one can derive equivalent expressions for the LDOS modulations around several impurities. Thus for N impurities all of strength V_s positioned at $R_1, ... R_N$ the full Greens function is given by the generalization of Eqn. (3.18)

$$\mathcal{G}(i, j, \omega_n) = \mathcal{G}^{(0)}(i - j, \omega_n) + \sum_{k,l}^{N} \mathcal{G}^{(0)}(i - R_k, \omega_n) T(R_k, R_l, \omega_n) \mathcal{G}^{(0)}(R_l - j, \omega_n), \tag{3.43}$$

with the T-matrix obtained from the Bethe-Salpeter equation

$$T(R_k, R_l, \omega_n) = V_s \tau^3 \delta(R_k - R_l) + V_s \tau^3 \sum_m^N \mathcal{G}^{(0)}(R_k - R_m, \omega_n) T(R_m, R_l, \omega_n). \tag{3.44}$$

In the case of two impurities at sites R_1 and R_2 we can solve Eqn. (3.43)-(3.44) to get

$$\mathcal{G}(i, j, \omega_n) = \mathcal{G}^{(0)}(i - j, \omega_n) + \mathcal{G}^{(0)}(i - R_1, \omega_n) T(\omega_n) \mathcal{G}^{(0)}(R_1 - j, \omega_n) +$$

$$\left[\mathcal{G}^{(0)}(i - R_1, \omega_n) T(\omega_n) \mathcal{G}^{(0)}(R_1 - R_2, \omega_n) V_s \tau^3 + \mathcal{G}^{(0)}(i - R_2, \omega_n) V_s \tau^3 \right] \times$$

$$\left[1 - \mathcal{G}^{(0)}(R_2 - R_1, \omega_n) T(\omega_n) \mathcal{G}^{(0)}(R_2 - R_1, \omega_n) V_s \tau^3 - \mathcal{G}^{(0)}(0, \omega_n) V_s \tau^3 \right]^{-1} \times$$

$$\left[\mathcal{G}^{(0)}(R_2 - j, \omega_n) + \mathcal{G}^{(0)}(R_2 - R_1, \omega_n) T(\omega_n) \mathcal{G}^{(0)}(R_1 - j, \omega_n) \right], \tag{3.45}$$

where $T(\omega_n) = V_s\tau^3(1 - \mathcal{G}^{(0)}(0,\omega_n)V_s\tau^3)^{-1}$. It can be easily verified that this expression reduces the single impurity Greens function when either of the impurities vanishes. Thus, though trivial, it is tedious to calculate the LDOS around several impurities. Therefore, for a numerical study of the evolution of the LDOS for multiple impurities positioned at arbitrary lattice sites, we find that it is easier to invert directly the real-space Gorkov-Dyson equation. The full Greens function $\hat{G}(\mathbf{r},\omega)$ is then obtained by solving the equation

$$\underline{\underline{\hat{G}}}(\omega) = \underline{\underline{\hat{G}}}^{(0)}(\omega)\left(\underline{\underline{\hat{I}}} - \underline{\underline{\hat{H}}}^{int}\underline{\underline{\hat{G}}}^{(0)}(\omega)\right)^{-1}, \tag{3.46}$$

where the double lines indicate that the elements of this equation are matrices written in real- and Nambu space. The size of these matrices depends on the number of impurities and the dimension of the Nambu space. We have previously utilized this method to study the electronic structure around vortices that operate as pinning centers of surrounding stripes[106]. We perform the 2D Fourier transform of the clean Greens function $\hat{G}^{(0)}(\mathbf{k},\omega)$ numerically by dividing the first Brillouin zone into a 1400×1400 lattice and introducing a quasi-particle energy broadening of $\delta = 0.5$meV with δ defined from $i\omega_n \rightarrow \omega + i\delta$.

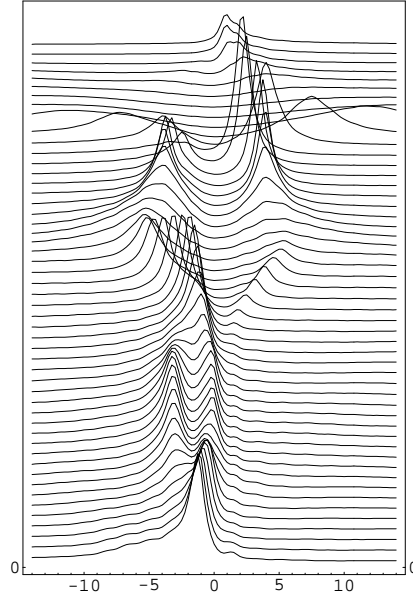The differential tunnelling conductance is proportional to the LDOS $\rho(\mathbf{r},\omega)$

Figure 3.10: DOS at $(0,0)$ as a function of distance $\mathbf{r}$ between two nonmagnetic impurities ($V^S = 700$meV) at $\mathbf{r}_1 = (0,0)$ and $\mathbf{r}_2 = (\mathbf{r},0)$. $\mathbf{r} = 0$ ($\mathbf{r} = 10$) corresponds to the top (bottom) scan. The distance is measured in units of the lattice constant and the horizontal energy axis in units of meV.

which in turn is determined from

$$\rho(\mathbf{r}, \omega) = -\frac{1}{\pi} \text{Im} \left[G_{11}(\mathbf{r}, \omega) + G_{22}(\mathbf{r}, -\omega) \right]. \qquad (3.47)$$

In the following we model the nonmagnetic unitary scatterers with a potential $V^S = 700\text{meV}$ which gives rise to resonance energies around $\pm 1.5\text{meV}$ in agreement with experiment[62]. (This is seen from the holelike resonance evident in the bottom LDOS scan in Fig. 3.15a. For a single impurity only one of the two resonances evident from Eqn. (3.42) has weight on the impurity site since the anomalous part of the Greens function, $G_{12}(r, \omega)$, vanishes at $r = 0$ due to the symmetry of the d-wave gap.) For interference between two nonmagnetic unitary impurities Morr *et al.*[99] found strong variations in the LDOS as the distance between the impurities R is varied along one of the crystal axes. This is reproduced in Fig. 3.10. The single-impurity spectrum
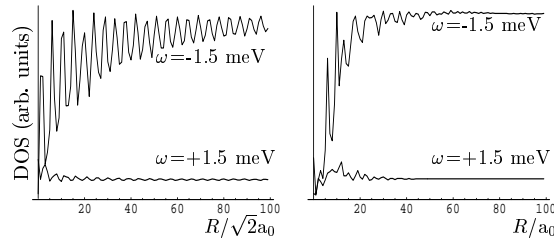

Figure 3.11: DOS at (0,0) and at the single-impurity resonance energy $\pm 1.5\text{meV}$ as a function of distance between the two nonmagnetic impurities separated along the (a) nodal direction and (b) anti-nodal direction. The y-axis scale is identical for the two figures.

was obtained when R exceeds approximately $10a_0$. However, as expected for a $d_{x^2-y^2}$-wave superconductor, this length scale is much larger along the nodal directions. This is seen from Fig. 3.11. Here the density of states is measured above one of the impurities fixed at the origin while the other is moved away along the nodal (a) or anti-nodal (b) direction. The single impurity LDOS is obtained for R well above $100a_0$. Thus only for impurity concentrations below 0.1% does the LDOS correspond to the expected result from a single strong nonmagnetic impurity. For weaker scatterers the decay length will be considerably reduced.

For quantum interference between multiple fixed nonmagnetic unitary scatterers Fig. 3.12 shows the LDOS as the STM tip is scanned along a crystal axis on which the impurities are positioned.

In general the resonances are split by the proximity of other impurities and the number of resonances is directly proportional to the number of interfering impurities. However, locally the density of states may be strongly influenced by destructive interference. For instance, for the two impurities (Fig. 3.12a,c)
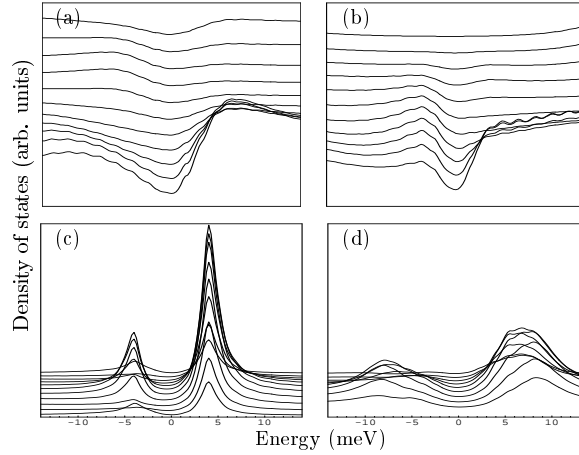
Figure 3.12: Low bias STM scans along the horizontal axis in steps of $a_0/5$ from $(0,0)$ (top line) to $(2,0)$ (bottom line). The scans are off-set for clarity. In (a) and (c) there are two nonmagnetic impurities fixed at: (a) $(0,0)$ and $(1,0)$; (c) $(0,0)$ and $(2,0)$. In (b) and (d) there are three nonmagnetic impurities at: (b) $(-1,0)$, $(0,0)$, $(1,0)$; (d) $(-2,0)$, $(0,0)$, $(2,0)$.

sharp resonances exist only when $R = 2a_0$ as is evident from Fig. 3.12c. When a third impurity is added at $(-2,0)$ these resonances appear to broaden and shift to higher energies, Fig. 3.12d. Contrary to this, Fig. 3.12a,b show that the addition of a third impurity has only a minor effect when $R = a_0$.

The case of three nonmagnetic impurities is studied further in Fig. 3.13 which shows the evolution of the LDOS at $(0,0)$ as a function of the distance to a third impurity along the nodal (b,d) and anti-nodal (a,c) direction. The case without the third impurity corresponds to the topmost LDOS in Fig. 3.12a and 3.12c.

As in the case of two nonmagnetic impurities[99, 100] there are very strong variations in the final LDOS; the number of apparent resonances, their width and resonance energy depends crucially on the positions of the three impurities. The small modulations added by the third impurity seen in Fig. 3.13a,b agree with the destructive interference evident from the corresponding cases seen in Fig. 3.12a,b. Contrary to this, large modulations are again seen when increasing the distance between the two fixed impurities by a single lattice constant, Fig. 3.13c,d.

Recently Zhu *et al.*[100] suggested a careful study of the two-impurity problem to extract information of the bulk Greens function of the clean system. In the following we show how the quantum interference between unitary scatterers is strongly affected by the induction of a small subdominant superconducting order parameter. Thus one may utilize the quantum interference between several impurities as an alternative method to detect a small subdominant order parameter.

For instance, tuning through a quantum phase transition from a $d_{x^2-y^2}$ to a
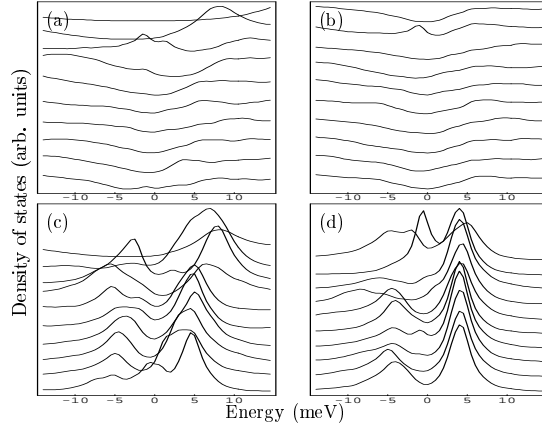
Figure 3.13: LDOS at $(0,0)$ as a function of distance to a third impurity along the antinodal (a,c) or nodal (b,d) direction. The two fixed impurities are positioned at: In (a) and (b): $(-1,0)$ and $(0,0)$; in (c) and (d): $(-2,0)$ and $(0,0)$. In (a),(c) the third impurity is positioned at (top to bottom) $(1,0),(2,0),...,(10,0)$. In (b),(d) the third impurity is positioned at (top to bottom) $(1,1),(2,2),...,(10,10)$.

$d_{x^2-y^2}+id_{xy}$ superconductor at a critical doping level[107], magnetic impurity concentration[108] or magnetic field strength[109], a small d_{xy} order could *qualitatively* alter the interference pattern. For $\Delta_{xy}(\mathbf{k}) = \Delta_{xy}^0 \sin(k_x)\sin(k_y)$ with Δ_{xy}^0=5.0meV, we compare in Fig. 3.14 the LDOS at physically realizable impurity positions to the case with Δ_{xy}^0=0. Also we show the difference between $d+id$ and $d+is$ pairing symmetry for these impurity configurations. For most spatial configurations the secondary pairing (id or is) leads to a sharpening of the resonances but at particular positions there is a qualitative difference as shown in Fig. 3.14. For instance, the induction of d+id pairing (Fig. 3.14b) can result in three apparent resonances contrary to the ground state with pure $d_{x^2-y^2}$-wave pairing (Fig. 3.14a). Similarly, by comparing the LDOS at (1,1) (dashed lines) in Fig. 3.14d-f, it is evident that the interfering scatterers can provide a clear distinction between d+id and d+is pairing. Information of the induction of *local* order around the impurities can also be inferred from STM measurements of specific impurity configurations[108].

We turn now briefly to the study of the classical magnetic impurities in $d_{x^2-y^2}$-wave superconductors. The interference of two magnetic scatterers in a s-wave superconductor was studied recently by Flatte *et al.*[102] For comparison to the nonmagnetic case we use a magnetic potential strength $|V^M| = 700$meV which does, however, not model all magnetic impurities (e.g. Ni) on the surface of BSCCO[67, 110]. Future experiments will reveal whether the scattering potential formalism utilized here is appropriate or whether more correlated effects are required[93, 94].

Fig. 3.15 shows the quantum interference between two unitary scatterers: (a,d)
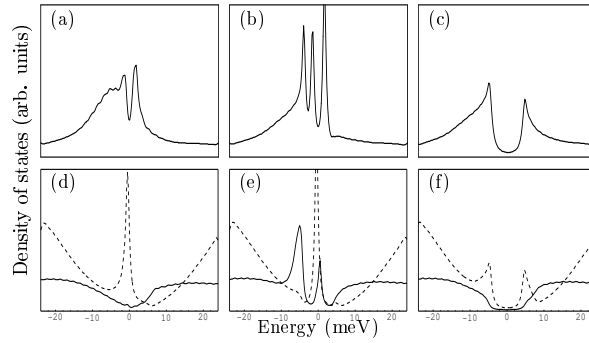
Figure 3.14: Top row: DOS at $(0,0)$ for two nonmagnetic impurities at (0,0) and (2,4). Bottom row: DOS at $(0,0)$ (solid line) and $(1,1)$ (dashed line) for three nonmagnetic impurities at (-1,1), (1,-1) and (-1,-1). Pairing symmetry: (a) and (d) $d_{x^2-y^2}$, (b) and (e) $d_{x^2-y^2}+id_{xy}$, (c) and (f) $d_{x^2-y^2}+is$.

one magnetic and one nonmagnetic, (b,e) two parallel magnetic, and (c,f) two antiparallel magnetic. In all figures one impurity is fixed below the STM tip at the origin $(0,0)$ while the other is displaced along the: (a-c) horizontal crystal axis or (d-f) along the nodal direction. In Fig. 3.15a,d it is the nonmagnetic impurity that is fixed at the origin. Again the number of resonances, their position, amplitude and width depends in detail on the distance and nature of the two scatterers. Further, the spatial evolution of the LDOS is quite similar for case (a),(b), and (d),(e). These are, however, very different from the interference between two antiparallel magnetic impurities (c,f) which is dominated by strong destructive interference at small separations along the antinodal direction and a surprisingly fast recovery to the single impurity case along both the nodal and antinodal directions.

  The results presented above remain qualitative since fits to a specific experiment in addition to details from the tunnelling matrix elements could also include modified hopping integrals around the impurities, gap suppression and possibly *both* magnetic and nonmagnetic scattering potentials[110]. We have checked that a gap suppression on the bonds around the impurity site does not produce any qualitative changes[73]. However, on a phenomenological level the gap suppression could allow for a competing magnetic order parameter to develop around the impurity. Thus, the gap suppression might be important for explaining the formation of magnetic moments around nonmagnetic impurities as seen by NMR experiments. These issues are currently controversial but the vast amount of information inferred from the quantum interference between multiple impurities may help settle this, and more importantly settle the validity of the scattering potential scenario versus more correlated models.
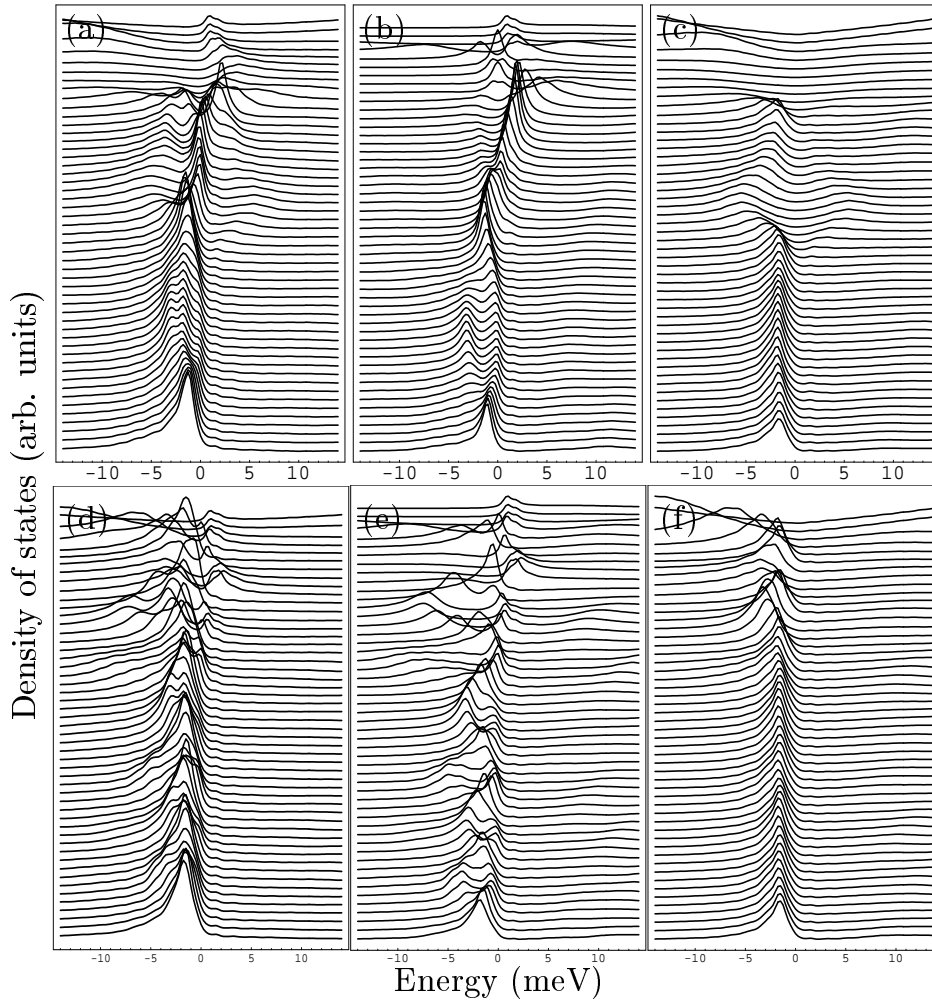
Figure 3.15: DOS at $(0,0)$ for: (a,d) one magnetic and one nonmagnetic impurity, (b,e) two magnetic $(V_1^M = V_2^M)$, (c,f) two magnetic $(V_1^M = -V_2^M)$. The topmost graph in each figure is the DOS when the two scatterers are both positioned at the origin whereas in the lowermost at $(0,0)$ and $(10,0)$. Antinodal separation: (a-c), and nodal separation: (d-f).

4   Impurities in the d-density wave phase

*Most of the material in this chapter has been published by the author in Physical Review B **68**, 094518 (2003)[111] and Brazilian Journal of Physics **33**, 775 (2003)[112].*

The underdoped regime of the high-T_c materials appears to be dominated by competing instabilities and associated exotic order. The various kinds of order are often close in energy making it a difficult task to determine the true ground state. The robust pseudogap in the low energy spectral weight has been observed e.g. by tunnelling, NMR, and photoemission experiments[14]. Some of the clearest data comes from tunnelling (see e.g. Fig. 4.2) and ARPES measurements which for temperatures above T_c find clear evidence for gap-like structure in the density of states and the leading edge of the energy distribution curves, respectively. Some of the earliest evidence for a pseudogap came from NMR studies which found that both the Knight shift and the spin-lattice relaxation rate $1/T_1T$ began to decrease well above T_c. It is very probable that the reduction of weight in the single-particle spectrum is caused by the stabilization of one or several ordered states. The important question remains, however, what is the dominating order parameter? The d-density wave (DDW) state is a qualified guess to answer this question! In the following section I review briefly why the guess is 'qualified'. The second section suggests new scanning tunnelling experiments near isolated impurities to further test the validity of the DDW ansatz.

4.1   D-Density wave order

The d-density wave (DDW) order is characterized by an order parameter y which breaks time-reversal, translational and rotational symmetries

$$y = i \sum_{\mathbf{k}\sigma} f_{\mathbf{k}} \langle \hat{c}_{\mathbf{k}\sigma}^{\dagger} \hat{c}_{\mathbf{k}+\mathbf{Q}\sigma} \rangle \tag{4.1}$$

with $f_{\mathbf{k}} = \cos(k_x) - \cos(k_y)$. The order is a particle-hole condensate with internal angular momentum 2. At the level of a phenomenological Ginzburg-Landau functional with both DDW and DSC order parameters the generic features of the high-T_c phase diagram can be reproduced as shown by Chakravarty *et al.*[113] Starting from the overdoped regime T_c increases as the doping is decreased, saturates around optimal doping and decreases upon further reduction of the doping. The latter is caused by the stabilization of the competing (in this case DDW) order which onsets at optimal doping.

The DDW mean-field Hamiltonian is given by

$$\mathcal{H} = \sum_{\mathbf{k}\sigma} (\varepsilon_{\mathbf{k}} - \mu)\hat{c}^{\dagger}_{\mathbf{k}\sigma}\hat{c}_{\mathbf{k}\sigma} + \sum_{\mathbf{k}\sigma} D_{\mathbf{k}}\hat{c}^{\dagger}_{\mathbf{k}\sigma}\hat{c}_{\mathbf{k}+\mathbf{Q}\sigma}, \qquad (4.2)$$

with

$$D_{\mathbf{k}} = \frac{y}{2}\left(\cos(k_x) - \cos(k_y)\right) \qquad (4.3)$$

resulting in the bands $E_{\mathbf{k}} = \pm\sqrt{\varepsilon_{\mathbf{k}}^2 + D_{\mathbf{k}}^2} - \mu$. The complex i in Eqn. (4.1) is necessary for the Hamiltonian to be Hermitian: $\left(\sum_{\mathbf{k}\sigma} D_{\mathbf{k}}\hat{c}^{\dagger}_{\mathbf{k}\sigma}\hat{c}_{\mathbf{k}+\mathbf{Q}\sigma}\right)^{\dagger} = -\sum_{\mathbf{k}\sigma} D_{\mathbf{k}}\hat{c}^{\dagger}_{\mathbf{k}+\mathbf{Q}\sigma}\hat{c}_{\mathbf{k}\sigma} = -\sum_{\mathbf{k}\sigma} D_{\mathbf{k}+\mathbf{Q}}\hat{c}^{\dagger}_{\mathbf{k}\sigma}\hat{c}_{\mathbf{k}+\mathbf{Q}\sigma} = \sum_{\mathbf{k}\sigma} D_{\mathbf{k}}\hat{c}^{\dagger}_{\mathbf{k}\sigma}\hat{c}_{\mathbf{k}+\mathbf{Q}\sigma}$. As usual, we denote by $\mathbf{Q}$ the antiferromagnetic ordering vector (π, π). In the underdoped regime we add to this Hamiltonian a term representing the BCS d-wave ordering: $\sum_{\mathbf{k}} \Delta_{\mathbf{k}}\hat{c}^{\dagger}_{\mathbf{k}\uparrow}\hat{c}^{\dagger}_{-\mathbf{k}\downarrow} + \text{H.c.}$, which competes with the DDW order. Thus, the main idea is that in the underdoped regime, the pure DDW order describes the normal state (the pseudogap state) while the phase with pure DSC or possibly coexisting DDW and DSC order describes the superconducting state.

If we rewrite the DDW order parameter y

$$y = i\sum_{\mathbf{k}\sigma} f_{\mathbf{k}}\langle\hat{c}^{\dagger}_{\mathbf{k}\sigma}\hat{c}_{\mathbf{k}+\mathbf{Q}\sigma}\rangle. \qquad (4.4)$$

in real-space, we can identify the order to be that of circulating currents alternating on neighboring plaquettes

$$
\begin{aligned}
y &= i\sum_{\mathbf{k}ij\sigma} \frac{D}{2}\left(\cos(k_x) - \cos(k_y)\right)\langle\hat{c}^{\dagger}_{i\sigma}\hat{c}_{j\sigma}\exp(-i(\mathbf{k}+\mathbf{Q})\cdot\mathbf{r}_i)\exp(i\mathbf{k}\cdot\mathbf{r}_j)\rangle \\[2mm]
&= \frac{iD}{4}\sum_{i\sigma}\langle(-1)^{\mathbf{r_i}}\left(\hat{c}^{\dagger}_{i\sigma}\hat{c}_{i+e_x\sigma} + \hat{c}^{\dagger}_{i\sigma}\hat{c}_{i-e_x\sigma} - \hat{c}^{\dagger}_{i\sigma}\hat{c}_{i+e_y\sigma} - \hat{c}^{\dagger}_{i\sigma}\hat{c}_{i-e_y\sigma}\right)\rangle \\[2mm]
&= \frac{iD}{4}\sum_{i\sigma}\langle(-1)^{\mathbf{r_i}}\left(\hat{c}^{\dagger}_{i\sigma}\hat{c}_{i+e_x\sigma} - \hat{c}^{\dagger}_{i+e_x\sigma}\hat{c}_{i\sigma} - \hat{c}^{\dagger}_{i\sigma}\hat{c}_{i+e_y\sigma} + \hat{c}^{\dagger}_{i+e_y\sigma}\hat{c}_{i\sigma}\right)\rangle \\[2mm]
&= \frac{iD}{4}\sum_{i\sigma}(-1)^{\mathbf{r_i}}\langle\hat{j}_{i\rightarrow i+e_x} - \hat{j}_{i\rightarrow i+e_y}\rangle. \qquad (4.5)
\end{aligned}
$$

Here the current operator is defined as

$$\hat{j}_{i\rightarrow i+e_x} = \left(\hat{c}^{\dagger}_{i\sigma}\hat{c}_{i+e_x\sigma} - \hat{c}^{\dagger}_{i+e_x\sigma}\hat{c}_{i\sigma}\right). \qquad (4.6)$$

Thus the DDW order is equivalent to the orbital antiferromagnet studied first by Halperin and Rice in 1968[114]. More recently the order was awakened in the staggered flux state of the $t - J$ model by Marston and Affleck[115]. Fur-
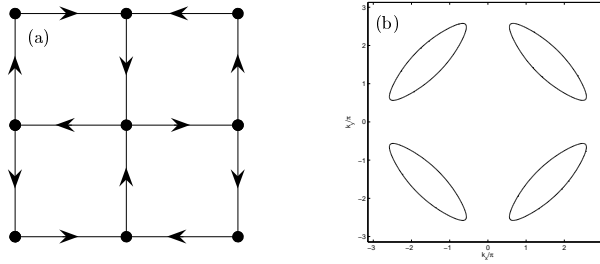
Figure 4.1: (a) The circulating plaquette currents constituting the order in the d-density wave state. (b) Fermi surface pockets: $t' = -0.3t$, $D = 0.06t$ and $\mu = -t$ corresponding to 14 % hole doping.

thermore, the fluctuating staggered flux state (i.e. a state that does not order) exists in the gauge theory formulations of the resonating valence bond theories for the cuprates[116, 117]. However, in the DDW state this order is static and an intrinsic part of the microscopic electronic structure. If $D_{\mathbf{k}}$ had s-wave symmetry the resulting order would be that of a charge density wave, hence the name d-wave density wave or simple d-density wave order. The DDW order is shown in Fig. 4.1a and is clearly seen to break the symmetries mentioned above. The bandstructure of the pure DDW state, $E_{\mathbf{k}} = \pm\sqrt{\varepsilon_{\mathbf{k}}^2 + D_{\mathbf{k}}^2} - \mu$, contains, at half filling, only quasi-particles at the nodal points $\mathbf{k} = (\pm\pi/2, \pm\pi/2)$. At finite hole doping the Fermi surface is disconnected as shown in Fig. 4.1b with hole pockets around the nodal points leading to a metallic normal state. When d-wave superconductivity competes with the DDW order the bands are of the form

$$E_{\mathbf{k}} = \pm\sqrt{(\sqrt{\varepsilon_{\mathbf{k}}^2 + D_{\mathbf{k}}^2} - \mu)^2 + \Delta_{\mathbf{k}}^2}. \tag{4.7}$$

This bandstructure can explain quite naturally many of the spectroscopic probes of the pseudogap. An example is the tunnelling experiments by Renner *et al.*[50] shown in Fig. 4.2 where the electronic gap is seen to evolve continuously from the superconducting gap below T_c to the pseudogap above T_c. Furthermore, in agreement with ARPES experiments the DDW theory has (per construction) the angular $d_{x^2-y^2}$-wave dependence of both the pseudogap and the superconducting gap. Digressing a bit on the ARPES data one may worry about the lacking evidence for hole pockets. Instead, ARPES measurements on underdoped BSCCO find a Fermi arc in the first magnetic Brillouin zone (inner arc of the elliptic-shaped hole pockets shown in Fig. 4.1b) but no arc in the second zone needed to complete the pocket. However, as shown recently by Chakravarty *et al.*[118] proper treatment of the DDW coherence factors masks the second arc leading to an apparent single Fermi arc in the measurements.

Several other experimental probes including measurements of the specific heat, high-field transport and c-axis optical conductivity have been recently argued to reveal DDW order. For a thorough discussion of these quantities I refer to
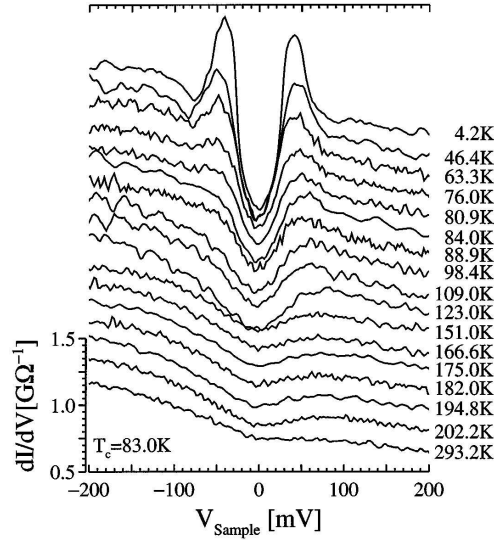
Figure 4.2: dI/dV measured as a function of sample bias V in an underdoped BSCCO sample. Clearly, the gap continues to exist above $T_c = 83$K. Adapted from Ref. [50].

the literature [113, 119, 120].

What does the spin susceptibility measured by neutron scattering have to say about the DDW order? Since the constant circulating currents of the DDW order should produce a magnetic moment one would expect new Bragg peaks at $\mathbf{Q} = (\pi, \pi)$ in the neutron measurements when entering the DDW state. The alternating plaquettes of orbital current would be equivalent to an Ising order and therefore one expects a gap in the spin excitation spectrum. There have been several experiments trying to identify the DDW order by neutron scattering but the results remain inconclusive except from the fact that any DDW moment must be very weak. The broken discrete Z_2 Ising symmetry and the concomitant normal state spin gap is very different from the long-range ordered stripe phase. In the latter case the broken continuous spin rotation symmetry implies low-energy Goldstone modes and no spin excitation gap. Recent measurements on $YBa_2Cu_3O_{6.5}$ show no signs of a normal state spin gap[121].

4.2   One impurity in the DDW state

It has been proposed[122, 123, 124] that the LDOS around a single impurity should be able to reveal whether the nature of the background electronic phase exhibits DDW or d-wave superconducting order. This proposal is based on the potential scattering model discussed at length in the previous chapter.

From Eqn. (4.2), we can write the DDW mean-field Hamiltonian $\mathcal{H}$ in the

form

$$\mathcal{H} = \sum_{\mathbf{k}\sigma} \xi(\mathbf{k}) c^{\dagger}_{\mathbf{k}\sigma} c_{\mathbf{k}\sigma} + i \sum_{\mathbf{k}\sigma} D(\mathbf{k}) c^{\dagger}_{\mathbf{k}\sigma} c_{\mathbf{k}+\mathbf{Q}\sigma} \tag{4.8}$$

where $\mathbf{Q} = (\pi, \pi)$ and $D(\mathbf{k}) = \frac{D_0}{2}\left(\cos(k_x) - \cos(k_y)\right)$ (D_0 real). The corresponding unperturbed Greens function reads

$$\hat{G}^0(\mathbf{k}, i\omega_n) = \frac{\begin{pmatrix} i\omega_n - \xi(\mathbf{k}+\mathbf{Q}) & -iD(\mathbf{k}) \\ iD(\mathbf{k}) & i\omega_n - \xi(\mathbf{k}) \end{pmatrix}}{(i\omega_n - \xi(\mathbf{k}))(i\omega_n - \xi(\mathbf{k}+\mathbf{Q})) - D(\mathbf{k})^2}. \tag{4.9}$$

Performing the Fourier transform, $\hat{G}^0(\mathbf{r}_i, \mathbf{r}_j, i\omega_n) = \sum_{\mathbf{k}\mathbf{k}'} \hat{G}^0(\mathbf{k}, \mathbf{k}', i\omega_n) e^{i\mathbf{k}\cdot\mathbf{r}_i - i\mathbf{k}'\cdot\mathbf{r}_j}$, we get

$$\hat{G}^0(\mathbf{r}_i, \mathbf{r}_j, i\omega_n) = \sum_{\mathbf{k}} [G^0_{11}(\mathbf{k}, i\omega_n) + G^0_{12}(\mathbf{k}, i\omega_n) e^{-i\mathbf{Q}\cdot\mathbf{r}_j} +$$

$$G^0_{21}(\mathbf{k}, i\omega_n) e^{i\mathbf{Q}\cdot\mathbf{r}_i} + G^0_{22}(\mathbf{k}, i\omega_n) e^{i\mathbf{Q}\cdot(\mathbf{r}_i - \mathbf{r}_j)}] e^{i\mathbf{k}\cdot(\mathbf{r}_i - \mathbf{r}_j)}, \tag{4.10}$$

where the sum extends over the reduced Brillouin zone. For delta-function impurity potentials we can use $\hat{G}^0(\mathbf{r}_i, \mathbf{r}_j, i\omega_n)$ to solve exactly the Dyson equation for the full Greens function $\hat{G}(\mathbf{r}_i, \mathbf{r}_j, i\omega_n)$ and obtain the resulting LDOS. In the case of a nonmagnetic impurity the T-matrix $T(\omega_n)$ becomes

$$T(\omega_n) = \frac{V_s}{1 - V_s G^{(0)}(0, \omega)}. \tag{4.11}$$

Therefore, the impurity contribution to the full Greens function $\delta\hat{G}(i, \omega_n) = \hat{G}^{(0)}(\mathbf{r}_i, i\omega_n) T(\omega_n) \hat{G}^{(0)}(-\mathbf{r}_i, i\omega_n)$ can generate only one resonance as opposed to the d-wave superconducting phase where we have seen that for a nonmagnetic impurity

$$\delta\hat{G}(i, \omega_n) = V_s \frac{\hat{G}^{(0)}_{11}(i, \omega_n)\hat{G}^{(0)}_{11}(-i, \omega_n)}{1 - V_s\hat{G}^{(0)}_{11}(0, \omega_n)} - V_s \frac{\hat{G}^{(0)}_{12}(i, \omega_n)\hat{G}^{(0)}_{21}(-i, \omega_n)}{1 + V_s\hat{G}^{(0)}_{22}(0, \omega_n)}. \tag{4.12}$$

In Fig. 4.3 I show the calculated LDOS at the impurity site for a series of different impurity strengths in the presence of DDW order. The d-wave property of the clean DDW phase has the same effect on the impurity resonance as for d-wave superconductivity: the resonance moves toward the Fermi level and sharpens as the impurity potential increases. Whereas in the dSC phase at the nearest neighbor sites both resonances have weight this is obviously not the case for DDW order. Thus, in principle, this property can be utilized to distinguish the DDW from the dSC order. However, we know that the real-space distribution of the LDOS around a single impurity within the potential scattering formalism is only correct when incorporating the interlayer filtering which
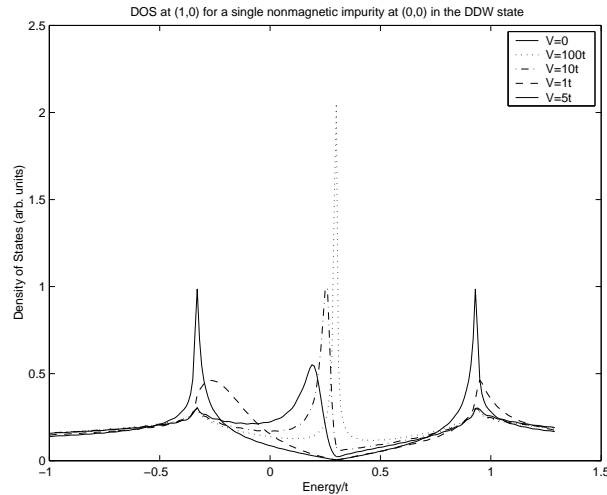
Figure 4.3: Density of states in the d-density wave phase at the site of a nonmagnetic impurity of strength V.

acts to wash out this effect. In the next section we show that this problem can again be solved by scanning the STM tip in the vicinity to two impurities. The more degrees of freedom in the two impurity problem allow configurations (and STM scan lines) where the amplitude of the resonances again permits one to clearly distinguish the DDW order form the superconducting order.

4.3   Multiple impurities in the d-density wave ordered phase

In this section, the quantum interference between two nonmagnetic impurities is studied numerically in both the d-wave superconducting (DSC) and the d-density wave (DDW) state. In all calculations we include the tunnelling through excited states from the CuO_2 planes to the BiO layer probed by the STM tip. Compared to the single impurity case, a systematic study of the modulations of the two-impurity local density of states can distinguish between the DSC or DDW states. This is important if the origin of the pseudogap phase is caused by preformed pairs or DDW order. Furthermore, in the DSC state the study of the LDOS around two nonmagnetic impurities provide further tests for the potential scattering model versus more strongly correlated models.

The study of magnetic and nonmagnetic impurities in the CuO_2 planes of the High-T_c superconductors is far from settled. Experimentally, the local density of states (LDOS) measured by scanning tunnelling microscopy (STM) in $Bi_2Sr_2CaCu_2O_{8+\delta}$ (BSCCO) around a nonmagnetic impurity such as Zn displays a sharp peak close to the Fermi level on the impurity site and a second maximum on the next-nearest neighbor sites[59, 62]. Theoretically, the question remains whether a traditional potential scattering formalism[80, 85] or

more strongly correlated models[107] are needed to describe the impurity effects. Though still a subject of controversy, it was recently shown that at least for *weak* impurities a potential scattering scenario qualitatively agrees with the measured results for optimally doped BSCCO[71, 73, 125, 126, 127]. Furthermore, it was shown by Martin *et al.*[64] that both the energetics and the spatial dependence of the resonance state around a strong potential scatterer (e.g. Zn) can be accounted for by including the tunnelling (the filter) through excited states from the CuO_2 planes to the top BiO layer probed by the STM tip[31]. There is also evidence from NMR measurements that magnetic moments are induced around nonmagnetic impurities[87, 88, 89, 90, 91]. In this paper we assume, however, that the large potential scattering off the impurity site *itself* is dominating the final LDOS.

Recently the experimental ability to manipulate the positions of surface impurities has increased the interest in quantum interference phenomena between multiple impurities. This includes the physics of quantum mirages[56] and various multiple impurity effects in superconductors[99, 100, 55, 128]. For example, it was shown in Ref. [55] that impurity interference can be utilized as a sensitive probe for the gap symmetry of exotic superconductors. Motivated by the experimental progress we compare the expected LDOS around one and two strong nonmagnetic impurities in either the d-wave superconducting (DSC) or the d-density wave (DDW) state. Though still controversial we include the filter effect in all the calculations presented below. As has become clear only recently[99, 100, 55], we stress that the probed impurities need be well separated (10-50 lattice constants) from other possible defects.

The DDW state was recently proposed as a model for the pseudo-gap state of the cuprates[113]. Any difference in the impurity modified LDOS between the DSC and DDW states may reveal the hidden DDW order and distinguish between the scenario of preformed pairs versus static staggered orbital currents as the origin for the pseudo-gap state[122, 123, 124]. Recently, there has been several other proposals to probe the DDW order in the cuprates[119, 129].

4.3.1   Model

In this section we briefly discuss the models for the DSC and DDW states and how to calculate the LDOS around several impurities. The BCS Greens function $\hat{G}^0(\mathbf{k}, i\omega_n)$ for the unperturbed d-wave superconductor is given by

$$\hat{G}^0(\mathbf{k}, i\omega_n) = [i\omega_n\hat{\tau}_0 - \xi(\mathbf{k})\hat{\tau}_3 - \Delta(\mathbf{k})\hat{\tau}_1]^{-1}, \qquad (4.13)$$

where $\hat{\tau}_\nu$ denotes the Pauli matrices in Nambu space, $\hat{\tau}_0$ being the 2×2 identity matrix, $\xi(\mathbf{k})$ the quasi-particle dispersion, and ω_n is a Matsubara frequency. For a system with $d_{x^2-y^2}$-wave pairing symmetry, $\Delta(\mathbf{k}) = \frac{\Delta_0}{2}(\cos(k_x) - \cos(k_y))$.

In the DDW state the mean-field Hamiltonian is given by[113]

$$H = \sum_{\mathbf{k}\sigma} \xi(\mathbf{k}) c_{\mathbf{k}\sigma}^{\dagger} c_{\mathbf{k}\sigma} + i \sum_{\mathbf{k}\sigma} D(\mathbf{k}) c_{\mathbf{k}\sigma}^{\dagger} c_{\mathbf{k}+\mathbf{Q}\sigma} \tag{4.14}$$

where $c_{\mathbf{k}\sigma}^{\dagger}$ creates an electron with momentum $\mathbf{k}$ and spin σ, $\mathbf{Q} = (\pi, \pi)$ and $D(\mathbf{k}) = \frac{D_0}{2} (\cos(k_x) - \cos(k_y))$. Below, $\Delta_0 = D_0 = 50$meV and the lattice constant is set to unity. The large value of the gap corresponds roughly to the experimentally measured maximum gap in the underdoped regime of BSCCO. The Greens function for the clean DDW state is given by

$$\hat{G}^0(\mathbf{k}, i\omega_n) = \frac{\begin{pmatrix} i\omega_n - \xi(\mathbf{k}+\mathbf{Q}) & -iD(\mathbf{k}) \\ iD(\mathbf{k}) & i\omega_n - \xi(\mathbf{k}) \end{pmatrix}}{(i\omega_n - \xi(\mathbf{k}))(i\omega_n - \xi(\mathbf{k}+\mathbf{Q})) - D(\mathbf{k})^2}. \tag{4.15}$$

Performing the Fourier transform, $\hat{G}^0(\mathbf{r}_i, \mathbf{r}_j, i\omega_n) = \sum_{\mathbf{k}\mathbf{k}'} \hat{G}^0(\mathbf{k}, \mathbf{k}', i\omega_n) e^{i\mathbf{k}\cdot\mathbf{r}_i - i\mathbf{k}'\cdot\mathbf{r}_j}$, of the Greens function with reference to the entries of Eqn. (4.15) gives

$$\hat{G}^0(\mathbf{r}_i, \mathbf{r}_j, i\omega_n) = \sum_{\mathbf{k}} [G_{11}^0(\mathbf{k}, i\omega_n) + G_{12}^0(\mathbf{k}, i\omega_n) e^{-i\mathbf{Q}\cdot\mathbf{r}_j} +$$

$$G_{21}^0(\mathbf{k}, i\omega_n) e^{i\mathbf{Q}\cdot\mathbf{r}_i} + G_{22}^0(\mathbf{k}, i\omega_n) e^{i\mathbf{Q}\cdot(\mathbf{r}_i - \mathbf{r}_j)}] e^{i\mathbf{k}\cdot(\mathbf{r}_i - \mathbf{r}_j)}, \tag{4.16}$$

with the sum extending over the reduced Brillouin zone. The presence of scalar impurities is modelled by the following delta-function potentials

$$\hat{H}^{int} = \sum_{\{i\}\sigma} U_i \hat{n}_{i\sigma}, \tag{4.17}$$

where $\hat{n}_{i\sigma}$ is the density operator on site i. Here $\{i\}$ denotes the set of lattice sites hosting the impurities and U_i is the strength of the corresponding effective potential. In this article all the presented results arise from impurities modelled by a potential, $U = -15t$, corresponding to -4.5eV. In the DSC state this U generates resonances at a few meV for a single nonmagnetic impurity[59, 62, 64]. The large scale of this potential renders the effects on the LDOS from corrections to other energy scales around the impurity site less important. For instance, we have checked that gap suppression near the impurity or slightly larger spatial extension of the impurity does not qualitatively affect the results reported below. In general these effects tend to push the resonances slightly further towards zero bias. We have also performed calculations (not shown here) with other values of U and comment on the results below.

The full Greens function $\hat{G}(\mathbf{r}, \omega)$ in the presence of the impurities can be ob-

tained by solving the real-space Gorkov-Dyson equation

$$\hat{G}(\omega) = \hat{G}^0(\omega) \left(\hat{I} - \hat{H}^{int} \hat{G}^0(\omega) \right)^{-1}. \tag{4.18}$$

The size of the matrices in this equation depends on the number of impurities and the dimension of the Nambu space. We have previously utilized this method to study the electronic structure around impurities[55] and vortices that operate as pinning centers of surrounding stripes[106, 181]. This method is identical to the traditional T-matrix formalism. However, for a numerical study of several impurities at arbitrary positions we find it easier to solve Eqn. (4.18) directly.

The 2D Fourier transform of the clean Greens function $\hat{G}^0(\mathbf{k}, \omega)$ is performed numerically by dividing the first Brillouin zone into a 800×800 lattice and introducing a quasi-particle energy broadening of $\delta = 1$meV with δ defined from the analytic continuation $i\omega_n \to \omega + i\delta$. The differential tunnelling conductance is proportional to the LDOS which is determined from the imaginary part of the full Greens function.

So far nothing has been said about the form the band-structure. It is still controversial which quasi-particle energy applies to the DSC and DDW states[124, 130, 131]. The expression for $\xi(\mathbf{k})$ is important since it will influence the final LDOS around the impurities. We illustrate this in the following by studying two generic band structures: the nested situation, and a t-t' band believed to be relevant for BSCCO around 10% hole doping. With the notation $\xi(\mathbf{k}) = \epsilon(\mathbf{k}) - \mu$, and

$$\epsilon(\mathbf{k}) = -2t \left(\cos(k_x) + \cos(k_y) \right) - 4t' \cos(k_x) \cos(k_y), \tag{4.19}$$

t (t') refers to the nearest (next-nearest) neighbor hopping integral and μ is the chemical potential. The nested situation corresponds to $t' = \mu = 0.0$ while the parameters for the 10% hole doped band are: $t = 300$meV, $t' = -0.3t$ and $\mu = -0.9t$. These parameters correspond to the ones previously studied for a single impurity by Morr[124]. As discussed in Ref. [124] there are physical reasons to expect the nested band to be relevant for the DDW state and the t-t' band for the DSC phase. However, recent photoemission measurements on LSCO by Zhou *et al.*[131] observed a Fermi surface consisting of straight lines connecting the antinodal regions which may indicate that the nested band is more relevant for impurity studies in LSCO. Thus we find it important for study both cases below.

In the results presented we include the LDOS filter[64]. This effect modifies the LDOS, $\rho(\mathbf{r}, \omega) = \sum_n |\psi_n(\mathbf{r})|^2 \delta(\omega - \epsilon_n)$, by including the four nearest Cu neighbors in the underlying CuO$_2$ layer, $\psi_n(\mathbf{r}) \longrightarrow \psi_n(\mathbf{r} + \mathbf{e}_x) + \psi_n(\mathbf{r} - \mathbf{e}_x) - \psi_n(\mathbf{r} + \mathbf{e}_y) - \psi_n(\mathbf{r} - \mathbf{e}_y)$. Here $\mathbf{e}_i$ denote the unit vectors in the CuO$_2$ plane. It is important to keep in mind that the filtering effect is still controversial. However, determining experimentally the interference effects around two impurities

in the DSC state may help resolve the relevance of the filter.

4.3.2 Results for a single impurity

Before studying the two impurity interference effects it is worthwhile to briefly review the single impurity LDOS in the DSC and DDW states and discuss the influence of the filter. Without the tunnelling filter we find full agreement with previously published results[73, 99, 122, 123, 124]. We will see that a single impurity is not a good probe for distinguishing between these two states.

In the DDW phase one can utilize Eqn. (4.16) and (4.18) to calculate the full Greens function $\hat{G}(\mathbf{r}_i, \mathbf{r}_j, i\omega_n) = \hat{G}^0(\mathbf{r}_i - \mathbf{r}_j, i\omega_n) + \hat{G}^0(\mathbf{r}_i, i\omega_n)T(i\omega_n)\hat{G}^0(-\mathbf{r}_j, i\omega_n)$ with the T-matrix given by, $T(i\omega_n) = U[1 - UG^0(0, i\omega_n)]^{-1}$. The single resonance condition, $1 = U\mathrm{Re}[G^0(0, \omega)]$, has been previously studied for the DDW state without the filtering effect[122, 123, 124]. It is well known that the resulting LDOS strongly depends on the band structure. In Fig. 4.4a we plot the DOS in the clean DDW state for the nested and the t-t' band without the filter. Even though the above resonance condition is satisfied at certain energies for the t-t' band, we expect the large value of the DOS at all frequencies to over-damp the impurity peaks. This is contrary to the nested situation where a sharp impurity resonance is allowed to appear in the gap. This is clearly verified in Fig. 4.4b(c) which depicts the LDOS for the nested(t-t') set of band parameters including the filter. The peaks in Fig. 4.4c are not impurity resonances (note scale), which are overdamped, but simply the shifted DDW gap edges. The impurity can only slightly modify the amplitude of these gap edges. We note that it is t' which causes the impurity resonances to be strongly overdamped. When $t' = 0$, $\mu \neq 0$ the density of states always vanishes at minus the chemical potential[123] allowing a well-defined resonance peak to appear.

As is evident from Fig. 4.4b the most important influence of the filter is to shift the LDOS maximum from the nearest neighbors to the impurity site and induce a second maximum on the next-nearest neighbor sites. This weight redistribution is identical to the situation in the superconducting phase[64].

In the DSC state, the clean DOS is plotted in Fig. 4.5a for both the nested and the t-t' band. By comparison to Fig. 4.4a we see the well known result that the nested DOS is identical for the clean DDW and DSC phase. Indeed this motivated the original studies of single impurity resonances in the DSC versus DDW states[122, 123, 124]. The single impurity resonance condition in the DSC phase, $1 = U\mathrm{Re}[G^0(0, \pm\omega)]$, generates peaks at positive *and* negative energies around a single nonmagnetic impurity. However, the majority of the quasi-particle weight may reside on only one of these resonances[55]. It is evident from *both* Fig. 4.5b and Fig. 4.5c that indeed only one resonance has weight. This is contrary to the situation without the filter[124]. Thus, by comparing Fig. 4.4b to Fig. 4.5b (or 4.5c) the result is two almost identical figures. Therefore, since no qualitative difference is guaranteed to exist the single nonmagnetic impurity cannot easily distinguish the DSC and DDW
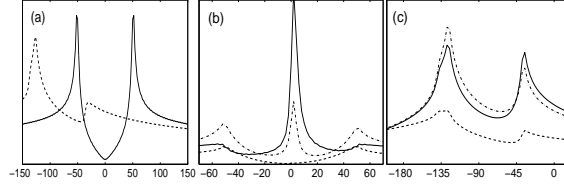
Figure 4.4: DOS (arb. units) as a function of energy (meV) in the DDW state: (a) for the clean system with nested (solid) or t-t' (dashed) band. (b) DOS at $(0,0)$ (solid), $(1,0)$ (dashed), and $(1,1)$ (dash-dotted) for a nested band with the impurity at $(0,0)$. (c) same as (b) but for a t-t' band.
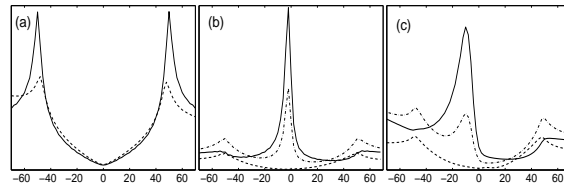

Figure 4.5: Same as Fig. 4.4 but for the DSC state.

phases. However, as shown below, the interference between several impurities can be utilized to *tune the amplitude* of the potential resonances and thus clearly distinguish the phases.

The impurity LDOS plotted in Fig. 4.4 and Fig. 4.5 was for a potential $U = -15t$. Though of less experimental relevance, we briefly mention another difference between the DSC and DDW states. This relates to the fate of the resonance in the unitary limit, $U \to \infty$: for the DDW phase the resonance energy approaches minus the chemical potential, $\omega = -\mu$, whereas it approaches the Fermi level in the DSC phase (except for a small residual energy shift caused by a possible particle-hole asymmetry[86]). The different resonance energy (as $U \to \infty$) arises from the way the chemical potential enters the bands of the clean DDW ($E_\pm(\mathbf{k}) = |\sqrt{\epsilon(\mathbf{k})^2 + D(\mathbf{k})^2} \pm \mu|$) and DSC ($E_\pm(\mathbf{k}) = \sqrt{(|\epsilon(\mathbf{k})| \pm \mu)^2 + \Delta(\mathbf{k})^2}$) states[122, 123].

4.3.3 Results for two impurities, nested band

In general when several impurities are in close proximity the resonances split, and one expects to see additional peaks in the density of states. The evolution of the LDOS as a function of distance and angular orientation between two nonmagnetic impurities in the DSC state has been already studied by several authors[55, 99, 100]. In the following we elaborate on this work by a numerical study of the LDOS including the filtering effect and study for the first time the quantum interference between two strong nonmagnetic impurities in the DDW

state. In the superconducting phase Fig. 4.6a shows the resulting LDOS for the nested band when one impurity is fixed at the origin $(0,0)$ while the other is moved out along a crystal axis to $(10,0)$. In Fig. 4.6b the impurities are fixed at $(-1,0)$ and $(+1,0)$ while the STM tip is moved from $(0,0)$ to $(8,0)$. As seen from both figures there are strong variations in the LDOS in agreement with previous studies without the extra tunnelling effect[55, 99]. The number
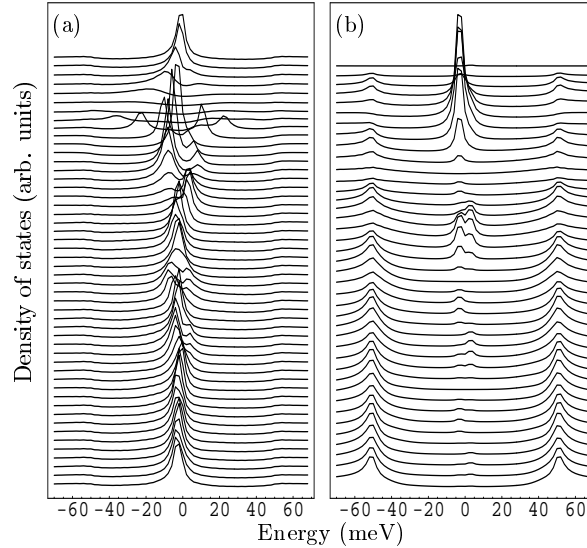

Figure 4.6: (a) DOS at $(0,0)$ as a function of the distance between two nonmagnetic impurities in the d-wave superconducting state (here: $t' = \mu = 0.0$). One impurity is fixed at $(0,0)$ while the other moves from $(0,0)$ (top) to $(10,0)$ (bottom). (b) the impurities are fixed at $(\pm 1,0)$ while the STM tip is moved from $(0,0)$ (top) to $(8,0)$ (bottom). The difference between each scan is 0.2 lattice constants and the graphs are off-set for clarity.

of apparent resonances, their energetic position and width strongly depend on the impurity configuration and the position of the STM tip. In particular, for certain impurity separations the resonances completely disappear. In Fig. 4.7 we show the LDOS for the same impurity and STM positions as in Fig. 4.6 but for the DDW state. Clearly, strong quantum interference between the two nonmagnetic impurities also exists in this state. However, by comparison with Fig. 4.6 it is evident that the additional resonance states in the DSC allows one to distinguish this from the DDW phase. We have performed identical calculations to the ones presented in Fig. 4.6-4.7 for other (but still large) values of the scattering potential U, and always find qualitatively the same interference pattern.

As mentioned above, the resonances split when two impurities are in close proximity. It is therefore nontrivial that only a single, nondispersive peak is seen in e.g. Fig. 4.7b. This is closely connected to the particular STM scan and one may worry about the robustness of this result. However, we always
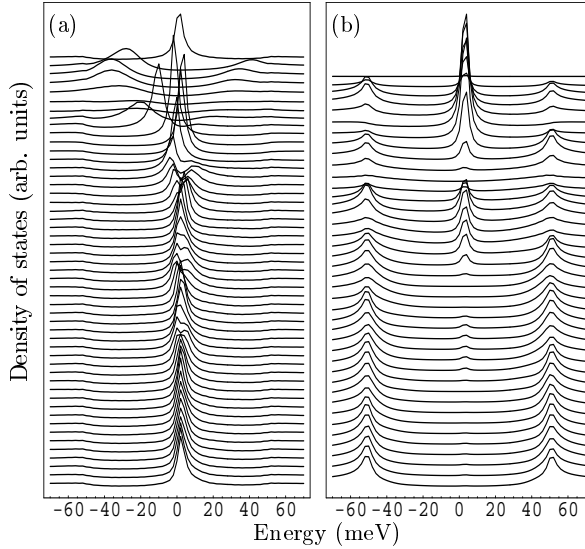
Figure 4.7: Same as Fig. 4.6 but for the d-density wave state.

find that whenever the impurity positions are invariant under mirror reflection through the STM scan line, only a single nondispersive peak remains[4] in the DDW state. Importantly, for these same configurations we find the alternating double peak structure (similar to Fig. 4.6b,4.8b) to be a robust feature in the superconducting phase. Furthermore, as expected for a d-wave gap[55], we find (not shown) that the quantum interference patterns are longer ranged along the nodal directions than along the Cu-O bonds.

As expected from the discussion of the single impurity in the DDW state, we end this section by noting that when $t' = 0.0$, $\mu \neq 0.0$ the interference pattern is identical to that shown in Fig. 4.7 except for a shifted (by $-\mu$) energy range.

4.3.4 Results for two impurities, t-t' band

We now turn to the quasi-particle dispersion given by Eqn. (4.19) with $t' = -0.3t$, $\mu = -0.9t$. In this case we know from Fig. 4.4a and Fig. 4.5a that the clean DOS is clearly different in the DDW and DSC states. This section serves as an illustration of the importance of the quasi-particle dispersion in the final LDOS. Fig. 4.8 shows the LDOS in the superconducting phase from the same STM and impurity positions as Fig. 4.6. It is clear that again the strong interference between the impurity wavefunctions survive the filtering effect and pose new constraints on the potential scattering scenario versus more strongly correlated models[107]. We note that despite the very different band structure used to calculate the LDOS in Fig. 4.6 and Fig. 4.8, the overall

---

[4]This is also valid when the impurity positions coincide with the STM scan line as in Fig. 4.6b-4.9b.

evolution of the resonances is quite similar except that the apparent resonances are shifted to higher energies for the t-t' band. As mentioned above, it has been previously suggested that the nested (t-t') band is appropriate for the DDW (DSC) state, respectively[124]. In that case we need compare Fig. 4.7 and Fig. 4.8. As opposed to the single impurity LDOS, the configuration in Fig. 4.7b and Fig. 4.8b again allows one to distinguish the DDW and DSC states by the number of resonance peaks. This is contrary to Fig. 4.7a and Fig. 4.8a which are remarkably similar.

In the DDW phase we know from the single impurity case that the current
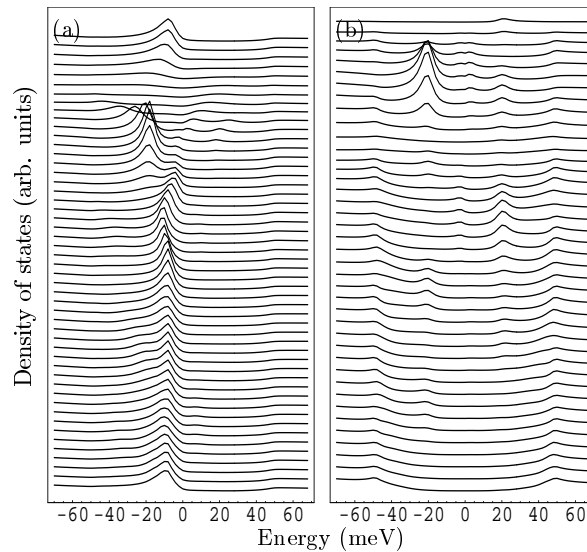

Figure 4.8: Same as Fig. 4.6 but for $t' = -0.3t$ and $\mu = -0.9t$.

choice of band parameters leads to strongly overdamped impurity resonances (Fig. 4.4c). However, for completeness we show the calculated STM scans in Fig. 4.9. As expected the quantum interference is weak and causes only minor changes in the DDW gap edges. Furthermore, the LDOS shown in Fig. 4.9 changes only slightly upon varying the strength of the impurity potential U or the impurity positions.

4.3.5   Conclusion

In summary we have shown that a systematic STM study around two non-magnetic impurities can clearly distinguish the DSC and DDW phases. In particular, we suggest to perform STM scans with the positions of the impurities being invariant under a mirror reflection through the scan line. Even for the nested band, where the clean and the single impurity LDOS are not a good probe for the underlying state, this situation provides a robust test for DSC versus DDW order.
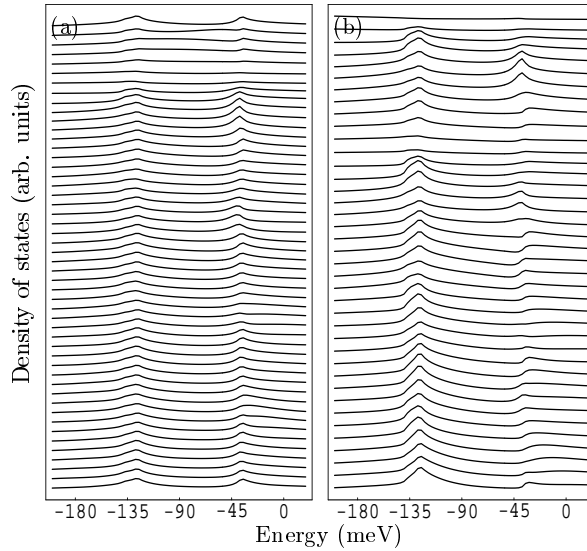
Figure 4.9: Same as Fig. 4.8 but for the d-density wave state. Note the energy range. The peaks evident in these scans are the shifted DDW gap edges (not impurity resonances).

The impurities are modelled as potential scatterers and the results pose further tests on this approach. An important question remains whether phase fluctuations present about T_c in the pseudo-gap state are strong enough to wash out the interference patterns. This will be discussed in a future publication[132]. It would also be interesting to study similar multiple impurity interference effects within other pseudo-gap models and within other proposed scenarios for the resonances around nonmagnetic impurities in d-wave superconductors. In particular, within models explaining the single impurity LDOS as a Kondo resonance arising from a confined spinon[107, 98], one may expect more novel changes as the distance between two nonmagnetic impurities is decreased. This is because the cost of frustrated dimers decrease in this limit making it unfavorable to break another dimer, and hence no spin is expected near the nonmagnetic impurities.

4.4 Discussion

In the previous sections I discussed the final expected LDOS from impurities of resonant character. In the future, it should be investigated what is the resulting LDOS in a coexisting phase of DSC and DDW order. Furthermore, one should study the DOS and quantum interference within models that contain Cooper pairs but no long-range ordered off-diagonal superconducting order. The latter should be compared with the pure DDW order whereas the former need be compared to the pure DSC phase. This is because within the DDW

scenario we expect, in the underdoped regime, the pure DDW order to exist above T_c and the mixed DDW-DSC phase below T_c.

In the previous chapter we also discussed how quasi-particle scattering off weak impurities in the d-wave superconducting leads to interference patterns in agreement with the Fourier transformed field of view LDOS maps obtained in STM experiments. It is interesting to understand the changes in these quantum interference patterns in a phase with pure DDW order, or with coexisting DSC and DDW order. Experimentally, an equivalent change in the patterns is expected when increasing the temperature through T_c.

The interference patterns in the presence of DDW order around a static non-magnetic scatterer were calculated recently by Bena *et al*[133, 134]. In the mixed phase, at energies below the superconducting gap, the LDOS is identical to the pure DSC state, while at larger energies there are significant differences to the pure DSC patterns. The differences lie in the detailed dispersion of the high-weight features. In the pure DDW state similar differences can be identified, and we refer to Ref. [133, 134] for more details.

Thus we may conclude this chapter by stressing the large amount of information contained in tunnelling spectra around both strong and weak potential scatterers. Though the final LDOS maps are sensitive to the bandstructure, future STM experiments should be able to determine whether the DDW order is relevant to describe the underdoped regime of the cuprate superconductors.

5 Introduction to the stripe phase

In this chapter I review some essential aspects of the emerging discipline of stripology. the chapter serves as a background study of the remaining chapters in this thesis.

The essence of stripology is the self-organization of electrons into inhomogeneous nano-scale structures providing a new state of matter. I will discuss some of the important experimental evidence for the existence of this phenomenon in the cuprates. However, the important results of stripe evidence originating from photoemission and STM experiments are not discussed in this chapter, but can be found in beginning of the following chapters.

The last section contains a brief review of the theories of stripes. This chapter is by no means a complete review but merely a summary of some important results (according to the author's biased opinion). There currently exists rather comprehensive review articles on the properties of stripes[135, 136].

5.1 Experimental evidence for stripes

What are the experiments that point to the relevance of stripes ? In fact, there are many. Particularly for the lanthanum based compounds and particularly at low doping levels. Experimental probes include NMR, NQR, μSR, transmission electron microscopy (TEM), tunnelling and photoemission spectroscopy, X-ray- and neutron scattering and transport measurements. Below I discuss mainly the latter two probes.

5.1.1 Neutron diffraction

Neutrons are natural-born spin detectives. In 1995 Tranquada *et al.*[137] performed elastic neutron scattering measurements on $La_{1.6-x}Nd_{0.4}Sr_xCuO_4$ and found magnetic Bragg peaks as shown in Fig. 5.1. The peaks are positioned in an incommensurate quartet around the antiferromagnetic ordering vector (π, π), i.e. at $(\pi(1 \pm \delta), \pi)$ and $(\pi, \pi(1 \pm \delta))$. Since the neutrons have no charge they cannot scatter directly from modulations in the electron density, but can detect the modulation of the atomic positions induced by the electron charge density modulation. Importantly, such charge Bragg peaks were also found by Tranquada *et al.*[137] at the Fourier points $(0, 2\pi(1 \pm \delta)$ and $(2\pi(1 \pm \delta), 0)$ suggesting that the charges form domain walls with half the spin periodicity. These measurements were the first solid evidence for spin- and charge ordering into stripe domains in the cuprate materials. A cartoon picture of the stripe ordered system is shown in Fig. 5.2. The holes prefer to segregate into periodically spaced rivers of charge, which are separated by antiferromagnetic ordered copper spins. Thus, the ordered stripe phase refers to a state with unidirectional density wave order, i.e. discrete translational symmetry breaking in one direction.
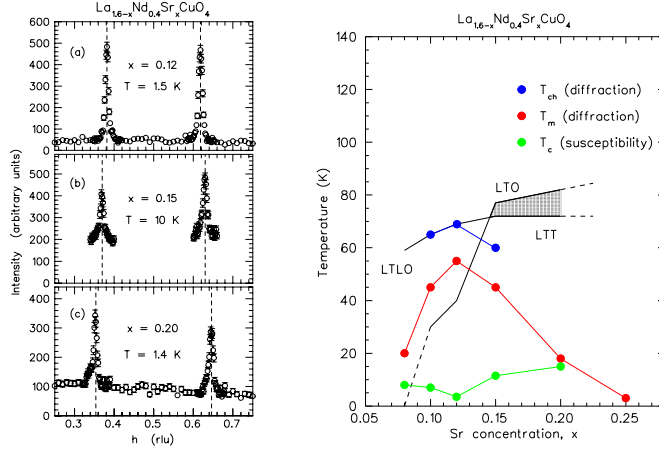
Figure 5.1: Left: elastic superlattice peaks found in $La_{1.6-x}Nd_{0.4}Sr_xCuO_4$ with $x = 0.12, 0.15, 0.20$. Right: experimental phase diagram obtained by Ichikawa *et al.*[138]. The temperature below which spin and charge ordering is detected is denoted by T_m and T_{ch}, respectively. T_c is shown by the green line and the structural transition from the low-temperature orthorhombic (LTO) to the low-temperature tetragonal (LTT) by the black line. Note that at low temperature static charge and spin stripes coexist with superconductivity.
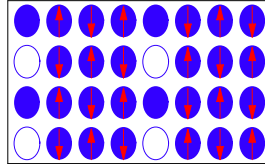

Figure 5.2: Idealized electronic spin and charge ordering in the CuO_2 plane in the stripe phase.

The spin order gains an additional π phase when crossing a charge stripe which causes the spin periodicity to be twice the charge periodicity, $2\pi/\delta_{spin} = 2(2\pi/\delta_{charge})$. Because of these hole-induced solitons in the antiferromagnetic background this has been dubbed topological doping. Other forms of stripes including stripe liquids, nematics and stripe glasses have also been discussed in the literature. In the experiments, four incommensurate peaks arise because the stripes form domains with equal probability of being oriented along the x- or the y-axis[5]. Alternatively the quartet may arise from a bilayer effect, i.e. the tendency of the stripes on neighboring planes to be oriented perpendicularly to each other. Certainly, this is relevant in the LTT phase of Nd doped LSCO where the tilt pattern of the CuO_6 octahedra causes lines of displaced

---

[5]In the ideal case of all stripes ordered along the, say, x-axis, we would except two neutron diffraction peaks at $\mathbf{Q} \pm \pi\delta\hat{e}_y$, where $\hat{e}_y$ is the unit vector along the y-direction and $2\pi/\delta$ is the stripe spin periodicity.

oxygen atoms rotated 90° between the adjacent layers.

In Fig. 5.2 the size of the unit cell dictates a density of one hole per two Cu sites in the charge stripe, and the stripes are characterized as quarter-filled.

Around (and above) optimal doping elastic Bragg peaks are *not* seen in pure $La_{2-x}Sr_xCuO_4$. The role of the neodymium doping is to cause a buckling of the oxygen octahedra surrounding the Cu ion inducing a structural transition from orthorhombic to tetragonal which effectively locks the stripes.

From inelastic neutron scattering on $La_{2-x}Sr_xCuO_4$ it was measured as early as in 1991 by Cheong *et al.*[139] that the magnetic excitation spectrum is dominated at low energies by four incommensurate peaks at $(\pi(1 \pm \delta), \pi)$ and $(\pi, \pi(1 \pm \delta))$, i.e. *at exactly the same positions as the stripe Bragg peaks*. The original explanation of the incommensurability was given in terms of Fermi surface geometry: as the hole-doping increases the Fermi surface hole volume this shifts the magnetic peaks from commensurate to incommensurability[140]. However, in light of the $La_{1.6-x}Nd_{0.4}Sr_xCuO_4$ measurements, it is natural to associate these peaks with the spin *fluctuations* from an incommensurate stripe state.

As can be seen from Fig. 5.3 the incommensurability δ varies with the doping. For Nd free $La_{2-x}Sr_xCuO_4$ a linear dependence of δ as a function of doping x was found for $x < 1/8$ indicating that the hole density in each stripe remains quarter-filled[141]. By increasing the amount of holes in the CuO_2 planes, the
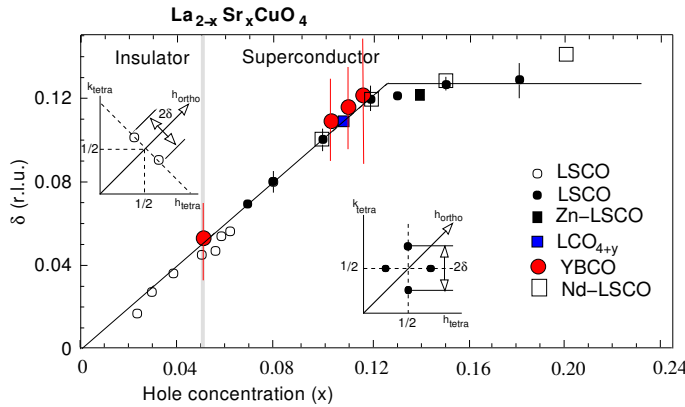

Figure 5.3: Incommensurability δ as a function of doping x obtained for different high-T_c materials. Adapted from Ref. [136].

number of quarter-filled stripes increase and hence their average separation $1/\delta$ is reduced. In this regime the stripes act as an incompressible quantum fluid. For $x > 1/8$ the incommensurability δ saturates at $\delta = 1/4$ (In units where the antiferromagnetic (π, π) point is denoted instead $(1/2, 1/2)$, δ saturates at $1/8$ as used in Fig. 5.3).

At present, elastic neutron scattering involving both the magnetic and nuclear structure function $S(\mathbf{k}, \omega)$, and to some extent X-ray scattering, has detected

the stripe ordered phase in a number of cuprates: $La_{1.6-x}Nd_{0.4}Sr_xCuO_4$ for $0.05 < x < 0.2$, $La_{2-x}Sr_xCuO_4$ for $0.02 < x < 0.13$, $La_{2-x}Ba_xCuO_4$, and in under- and optimally doped $La_2CuO_{4+\delta}$[135, 136].

In the $YBa_2Cu_2O_{6+y}$ materials, incommensurate spin fluctuations are found throughout the doping range where the material is superconducting. The incommensurate peaks are found only above a spin gap whose magnitude is of the order of the superconducting pairing gap. The fact that superconductivity seems important for these fluctuations may indicate that they are a collective mode in a homogeneous d-wave superconductor as will be shown later. However, there is also evidence that stripes are lurking in the YBCO materials. For instance, Mook *et al.*[142] performed neutron scattering studies of a partially (1:2) detwinned $YBa_2Cu_3O_{6+y}$ sample and found incommensurate peaks with a 1:2 intensity ratio between the pairs corresponding to horizontal and vertical stripes, respectively. This supports the notion that in YBCO the stripe ordering prefers to align perpendicular to the Cu-O chains. Furthermore, static charge stripe order persisting up to 300K has been recently observed in underdoped $YBa_2Cu_3O_{6.35}$[143].

In the non-superconducting nickel-oxides, e.g. $La_{2-x}Sr_xNiO_{4+\delta}$, which is a structural analogue of $La_{2-x}Sr_xCuO_4$, it is very well established that diagonal stripe spin and charge ordering appear in the nickel-oxygen planes[144]. This is similar to the very underdoped regime of $La_{2-x}Sr_xCuO_4$ ($0.02 < x < 0.05$) where Wakimoto *et al.*[145] and Matsuda *et al.*[146] have used neutrons to detect insulating (half-filled, i.e. one hole per Cu site within the stripe) diagonal stripes.

Finally it is interesting to note that when cooling down from a high temperature, the charge Bragg peaks always appear before the spin superlattice peaks. This has been advocated by Kivelson *et al.*[135] to be strong evidence for charge-driven stripe formation.

5.1.2   Transport

Whereas the neutron scattering data show strong evidence for spin stripes, they remain elusive for charge stripes. Though evidence has been reported in LSCO and YBCO, only in the pinned phase of Nd doped LSCO could charge Bragg peaks be unambiguously verified. It is therefore important to perform other experiments that *directly* probe the charges and test their transport properties.

At low doping Ando *et al.*[147, 148, 149] found that the in-plane resistivity ρ_{ab} and the Hall coefficient R_H of $La_{2-x}Sr_xCuO_4$ show metallic behavior ($\frac{d\rho_{ab}}{dT} > 0$, $\frac{dR_H}{dT} = 0$) at temperatures down to 100K-150K. The result of measurements of the temperature dependence of the inplane resistivity is shown in Fig. 5.4 for doping levels covering the whole underdoped regime. Note that for the low-doped crystals even the Neel ordering at T_N does not affect the metallic dependence. Similar metallic behavior has been reported in $YBa_2Cu_3O_y$. Furthermore, by normalizing the resistivity ρ_{ab} by the nominal hole concentration
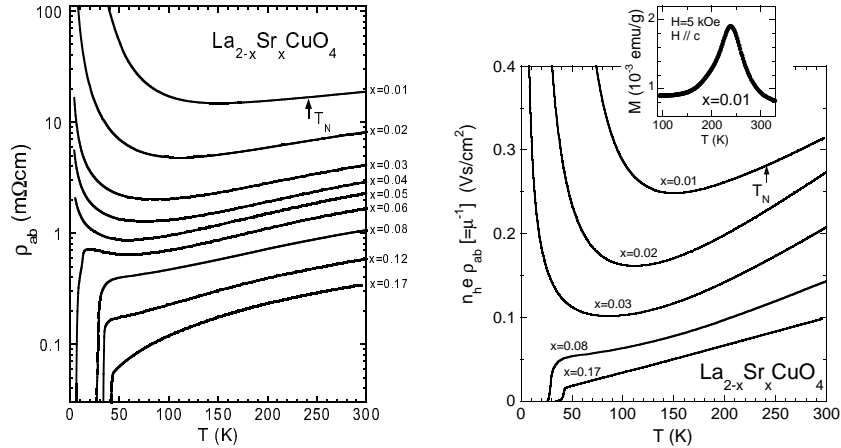
Figure 5.4: Left: inplane resistivity (logarithmic scale) ρ_{ab} as a function of temperature T. With decreasing doping the magnitude of the resistivity increases, but the metallic behavior remains down to low temperatures. For $x = 0.01$ this is true even below the Neel ordering temperature $T_N = 240$ (inset on the right figure). Right: temperature dependence of the inverse mobility. Adapted from Ref. [147].

n_h one may determine the conductivity per charge, i.e. the mobility of the doped holes. As can be seen on the right hand side of Fig. 5.4, above 150K the temperature dependence (the slope) and the absolute magnitude of the doped hole mobility $(n_h \rho_{ab} e)^{-1}$ differ only slightly in the doping range from $x = 0.01$ to $x = 0.17$. This hints that whatever dominate the physics at low doping may dominate throughout the underdoped regime of the cuprate phase diagram.

How, then, is it possible for doped holes in an antiferromagnetic background to display metallic behavior with relatively high mobility? Certainly, it is well-known that an isolated hole in a 2D LRO antiferromagnetic state is localized due to the energy cost of frustrating the spin bonds upon hopping (Trugman loops restore the anti-parallel spin arrangement but are important only when $J \ll t$). The transport experiments suggest that the holes manage to circumvent this energy penalty. The stripe phase offer an explanation since the self-organization of holes into charge stripe domain walls can facilitate the charge mobility. The holes gain kinetic energy by propagating along the stripes. In a later chapter I show the emergence of states inside the Mott-Hubbard gap induced by the stripe domain walls. This generates states near the Fermi level along short patches in the Brillouin zone. By correctly taking these states into account it was shown by Ando *et al.*[150] how the temperature and doping dependence of the resistivity and Hall coefficient can be understood.

The stripes prefer to align along one of the unit axes in the orthorhombic unit cell due to a slight crystalline anisotropy. Because, in the twinned crystals there are equal domains of x- and y-axis oriented stripes, the stripe domains are fully

disordered and one does not expect to detect any transport anisotropies at the macroscopic level. However, in carefully detwinned crystals one would expect to measure a transport anisotropy corresponding to whether the current runs parallel or perpendicular to the main stripe ordering vector. In fact, transport anisotropies have already been used to verify the existence of conducting charge stripes in the higher Landau levels of 2D electron gases[151, 152].

Fig. 5.5 shows the inplane resistivity ρ_a (along the a-axis) and ρ_b (along the b-axis) of heavily underdoped LSCO and superconducting YBCO[153]. Clearly,
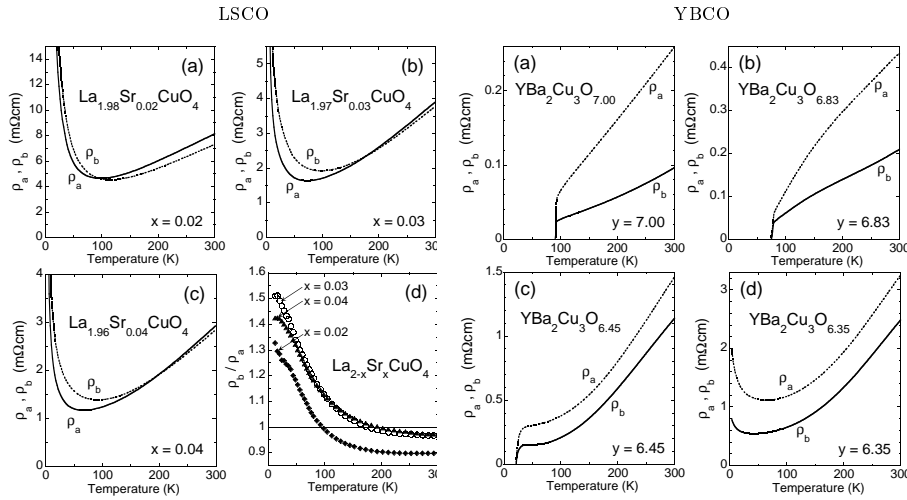

Figure 5.5: Resistivity as a function of temperature revealing a resistivity anisotropy for lightly doped LSCO (left) and $YBa_2Cu_3O_y$ with $y = 6.35 - 7.00$ (right). Adapted from Ref. [153].

at almost all temperatures the resistivity differs in the two in-plane directions, $\rho_a/\rho_b \neq 1$. This cannot be accounted for by crystalline anisotropy alone. For example, from the YBCO data at moderate temperatures on the right hand side of Fig. 5.5, we see that the resistivity anisotropy ρ_a/ρ_b grows with doping y (below $y \sim 6.60$), whereas it is well-known that the crystal anisotropy decrease with y due to a gradual destruction of the CuO chains. Again this indicates the presence of self-organized electronic stripes. The localization behavior at low temperatures is caused by disorder, a relevant perturbation in low-dimensional systems.

Finally we note that recent neutron scattering results[146] revealed that at low temperatures the static spin stripes prefer to align along the a-axis of the orthorhombic lattice of LSCO with $x \leq 0.05$. Since below 100K $\rho_a < \rho_b$, this points to the fact that stripes seem to be intrinsically conducting at finite temperatures.

5.2 Stripe models

From a theoretical point of view the interesting question remains what is the origin of these stripes? Though it is clear that they originate from a competition between the magnetic and kinetic energies, the details remain unclear. In the following I discuss the formation of stripes in the Hubbard model and their possible relation to the superconductivity.

5.2.1 Hartree-Fock equations of the Hubbard model

The stripe phase was first found theoretically in 1989 by studies of the 2D two-band Hubbard model at the mean-field level[154]. However, almost immediately after, several authors reported incommensurate spin and charge ordering in the single-band version[155]. These studies relate to the soliton physics of magnetic systems, i.e. the fact that upon addition of excess carriers the spatially modulated spin states are more energetically advantageous than uniform phases. Allowing for such solutions therefore drastically changes the phase diagram of the mean-field Hubbard model.

It is instructive to consider what we initially may expect about the spin ordering from a Stoner argument: magnetically ordered states turning stable when $1 - U\chi_0(\mathbf{k}) = 0$, where $\chi_0(\mathbf{q})$ is the paramagnetic Lindhard function at $\omega = 0$[156]. Fig. 5.6 shows the calculated structure of $\chi_0(\mathbf{k})$ in the case of half-filling (a) and $n_h = 0.20$ hole doped (b). These results are obtained by numerical summation of the momentum sums entering $\chi_0(\mathbf{k})$. As expected at half-filling the perfect nesting leads to a strong antiferromagnetic instability at $\mathbf{Q} = (\pi, \pi)$. However, with hole doping the peaks are centered at the incommensurate positions $(\pi, \pi(1 \pm \delta))$ and $(\pi(1 \pm \delta), \pi)$. Therefore, with increasing U we expect SDW modulations along the axes of the CuO$_2$ planes with periodicity $N = 2\pi/\pi\delta = 2/\delta$. From the diagonal nesting vector of the pure antiferromagnetic state, one may have expected a diagonal SDW modulation. However, for a given modulation vector $\mathbf{Q}$, the gap opens at points in the Brillouin zone where the single-particle dispersion $\varepsilon_{\mathbf{k}}$ satisfies, $\varepsilon_{\mathbf{k}} = \varepsilon_{\mathbf{k}+\mathbf{Q}}$. The magnetic state is stabilized compared to the paramagnetic phase by the opening of a gap on parts of the Fermi surface. For the simplest case where $\varepsilon_{\mathbf{k}} = -2t(\cos(k_x) + \cos(k_y))$, Fig. 5.7 shows that indeed the wave vectors corresponding to the vertical/horizontal peak positions in Fig. 5.6 should be energetically favored[156]. However these features change considerably for other shapes of the Fermi surface and other values of the Coulomb repulsion U and the hole doping n_h. The best way to understand the stripe formation at the mean-field level is to simply perform the calculation.

Hence, consider the Hubbard model

$$\mathcal{H} = -t \sum_{\langle i,j \rangle \sigma} \hat{c}_{i\sigma}^\dagger \hat{c}_{j\sigma} + U \sum_i \hat{n}_{i\uparrow} \hat{n}_{i\downarrow} \tag{5.1}$$
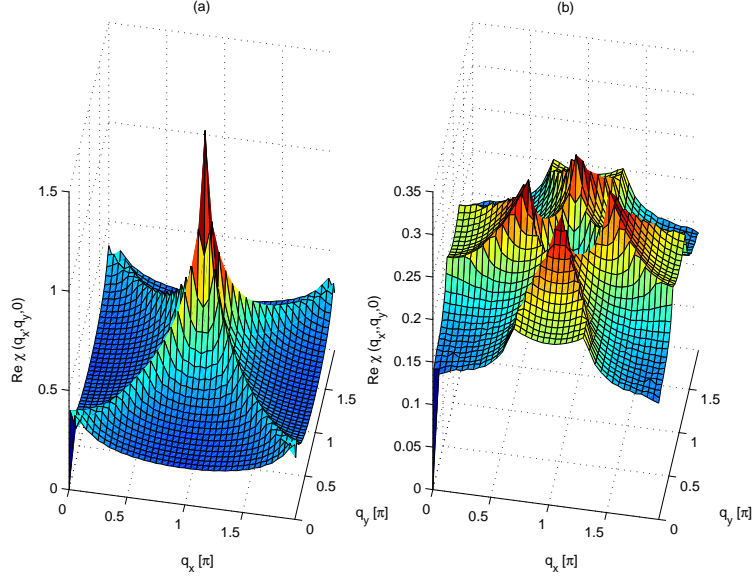
Figure 5.6: Real part of $\chi_0(\mathbf{k})$ over the Brillouin zone for (a) the half-filled band ($\mu = 0$) and (b) the hole doped case corresponding to $n_h = 0.20$ ($\mu = -t$).

$$\rightarrow \quad -t \sum_{\langle i,j \rangle \sigma} \hat{c}_{i\sigma}^\dagger \hat{c}_{j\sigma} + U \sum_i [\langle \hat{n}_{i\downarrow} \rangle \hat{n}_{i\uparrow} + \langle \hat{n}_{i\uparrow} \rangle \hat{n}_{i\downarrow}] - U \sum_i \langle \hat{n}_{i\uparrow} \rangle \langle \hat{n}_{i\downarrow} \rangle,$$

which we may solve self-consistently. Specifically, we divide the plane into a large number of supercells of size $N_x \times N_y$ (the total number of sites in the supercell equals N) and write $\hat{c}_{i\sigma}^\dagger = \sum_{\mathbf{k}n} u_{\mathbf{k}n\sigma}^*(i)\gamma_{\mathbf{k}n\sigma}^\dagger \exp(i\mathbf{k} \cdot \mathbf{R}_i)$ where $\mathbf{R}_i$ points to the supercell where site i resides and $\mathbf{k}$ belongs to the reduced Brillouin zone, $2\pi/N_x \times 2\pi/N_y$. In other words, the spatial dependence of $u_{\mathbf{k}n\sigma}(\mathbf{r}_i) = u_{\mathbf{k}n\sigma}(\mathbf{R}_i + i) = u_{\mathbf{k}n\sigma}(i)\exp(i\mathbf{k} \cdot \mathbf{R}_i)$ has the Bloch form in the supercell vectors and need only be determined on the N sites inside a supercell for each $\mathbf{k}$. Demanding that the γ's diagonalize the Hamiltonian is equivalent to solving for each $\mathbf{k}$ and σ the $N \times N$ linear eigenvalue problem

$$\sum_j \mathcal{H}(i, j, \mathbf{k}, \sigma)u_{\mathbf{k}n\sigma}(j) = E_{\mathbf{k}n\sigma}u_{\mathbf{k}n\sigma}(i). \tag{5.2}$$

One should remember that the eigenvalues $E_{\mathbf{k}n\sigma}$ and eigenvectors $u_{\mathbf{k}n\sigma}(i)$ depend inherently on all the densities $\langle n_{i\sigma} \rangle$. The self-consistency is enforced by first guessing the form of $\langle \hat{n}_{i\sigma} \rangle$, diagonalize the Hamiltonian, and then calculate the new densities $\langle \hat{n}_{i\sigma} \rangle$. These are then inserted into $\mathcal{H}$ and the procedure is repeated until convergence. This procedure is equivalent to finding the density configuration with the smallest energy. The loop runs with the constraint that

$$\frac{1}{N} \sum_{i\sigma} \langle \hat{n}_{i\sigma} \rangle = 1 - n_h, \tag{5.3}$$
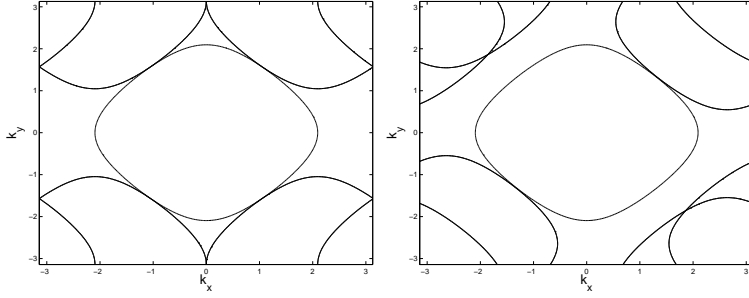
Figure 5.7: The central ring is the Fermi surface for $\mu = -t$. The rest of the lines show the contour-plot $\varepsilon_{\mathbf{k}+\mathbf{Q}} = \mu$ for $\mathbf{Q} = (\pi, \pi(1 \pm \delta))$ (left) and $\mathbf{Q} = (\pi(1 \pm \delta), \pi(1 \pm \delta))$ (right). As seen, the $\mathbf{Q} = (\pi, \pi(1 \pm \delta))$ modulation vector allows for larger parts of the original Fermi surface to be gapped out.

where n_h is the hole doping, i.e. $n_h = 0$ corresponds to half-filling and N is the total number of sites in the supercell. The condition (5.3) is fulfilled by adjusting automatically the chemical potential μ in each run using the fact that $\langle \hat{n}_{i\sigma} \rangle = \langle \hat{c}_{i\sigma}^\dagger \hat{c}_{i\sigma} \rangle = \sum_{\mathbf{k}n} |u_{\mathbf{k}n\sigma}(i)|^2 f(E_{\mathbf{k}n\sigma} - \mu)$, where $u_{n\sigma}$ and $E_{n\sigma}$ denote the eigenvectors and eigenvalues of $\mathcal{H}$, respectively.

The antiferromagnetic case yields a nice testing ground for the computer routines since in this case we know the answer and can easily perform analytical calculations. Thus, at half-filling, the up-down periodicity allows us to write

$$\langle \hat{n}_{i\sigma} \rangle = \frac{1}{2} \left(1 + \sigma m(-1) \right) \tag{5.4}$$

$$\langle \hat{n}_{i\uparrow} \rangle + \langle \hat{n}_{i\downarrow} \rangle = 1. \tag{5.5}$$

The parameter m ranges from 0 to 1, with $m = 1$ being the fully polarized state corresponding to the large U limit. Using the relations (5.4)-(5.5), we can rewrite the Hamiltonian (5.1) in terms of m, perform the Fourier transform and obtain the bands. When $t' = 0.0$ the result is

$$E_{\mathbf{k}}^\pm = \frac{U}{2} - \mu \pm \sqrt{\varepsilon_{\mathbf{k}}^2 + \left(\frac{Um}{2} \right)^2}, \tag{5.6}$$

with $\varepsilon_{\mathbf{k}} = -2t(\cos(k_x) + \cos(k_y))$. In this case the total energy per site is given by

$$\mathcal{E} = -U \left(\frac{1}{2} + \frac{m}{2} \right) \left(\frac{1}{2} - \frac{m}{2} \right) + 2 {\sum_{\mathbf{k}}}' E_{\mathbf{k}}^-, \tag{5.7}$$

with the momentum sum restricted to the reduced Brillouin zone. In this case the free energy minimum is equivalent to the gap equation

$$\sum_{\mathbf{k}}' \frac{1}{\sqrt{\varepsilon_{\mathbf{k}}^2 + \left(\frac{Um}{2}\right)^2}} = \frac{1}{U}, \tag{5.8}$$

which determines m for a given U. We have solve this relation $m(u)$ and found that the same magnetization m results from the iteration procedure. However, when the system gains incommensurate spin and charge structure away from half-filling we rely fully on the numerical solutions.

In Fig. 5.8 I show some results for the spin and charge density when $n_h = 0.125$. For vertical stripes to be stable we find that the Coulomb interaction needs to exceed some critical value depending on the doping level. Clearly, away
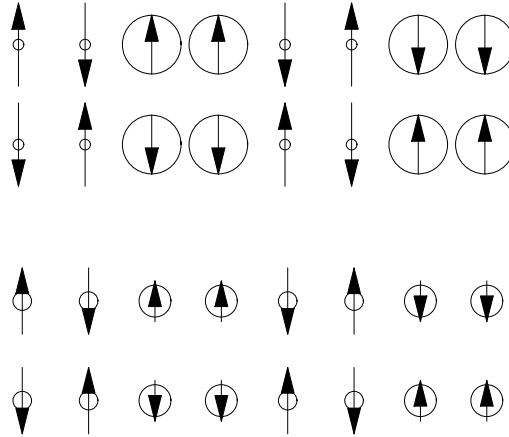

Figure 5.8: Examples of the self-consistently generated bond-centered spin and charge stripe modulations within a 2×8 unit supercell of the one-band 2D Hubbard model. The length of arrow and the radius of the circle is proportional to the spin and the hole density, respectively. Parameters used to generate these results: $n_h = 0.125$, $t' = 0$, and $U = 6.0t$ (top) and $U = 4.0t$ (bottom).

from half-filling the commensurate antiferromagnetic state becomes unstable. The modulation of the spin is non-sinusoidal and supports the anti-phase shift across the charge stripes. The magnetization grows with U but vanishes when the hole doping n_h becomes too large. It is also possible to stabilize site-centered stripes, but I find that they as a general rule have higher energy than the bond-centered configurations. The energy difference is, however, extremely small, which indicates that the real systems may fluctuate between the two. Similar conclusions have been made by other groups[22, 157]. For example, in Fig. 5.8 I find that for the $U = 4, t' = 0, n_h = 0.125$ case that the energy per site in for the bond-ordered solution is $E = -0.88399t$ whereas for the site-centered solution it is $E = -0.88279t$. Similarly, when $U = 6, t' = 0, n_h = 0.125$ for the bond-centered configuration we have $E = -0.68940t$ whereas

the energy of the site-centered solution is $E = -0.67740t$. The same conclusion results from many calculations performed at other doping levels n_h and Coulomb interaction U.

The filling of the stripes is determined by the filling of the mid-gap band generated by the anti-phase stripes (see e.g. the chapter on the stripe effects on ARPES and DOS). In the present approach we find that when $n_h = 2/\delta$ the stripes are always insulating when $t' = 0$. However, for finite $t' < 0$ it is well-known that the mid-gap band becomes partially filled and hence the system becomes metallic[22, 157]. For $t' > 0$ we find that it is generally not possible to stabilize the stripe state. Fig. 5.9 shows the stripe filling (when the overall system doping is 6%) as a function of t' for $U = 4.0t$ and $V = 0$ reproduced from Ref. [22]. When including a next-nearest neighbor attraction V to induce
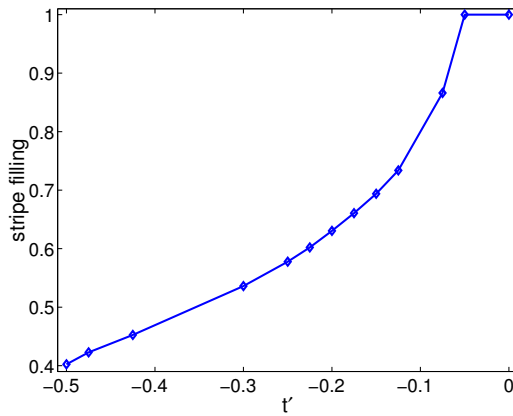

Figure 5.9: The stripe filling versus next-nearest neighbor hopping integral t' ($U = 4.0t, V = 0$). From Ref. [22].

the d-wave superconductivity at the mean-field level, a moderate value of the attraction $V \sim t$ induces the instability for the metallic state whereas a larger V is required to overcome the gap in the insulating state. In this way the mid-gap states are crucial to the occurrence of superconductivity. We return to the question of coexisting d-wave superconductivity and spin and charge stripes within mean-field minimal model in later chapters.

The stability of vertical (VIC) versus diagonal (DIC) incommensurate stripe phase has been studied in detail by Ichioka *et al.*[157, 158]. There is was found that the total energy is lower for the DIC phase than that of the VIC for higher U and smaller doping n_h. For example in Fig. 5.10 where $U = 3.0t$ and $t' = -0.1t$ the transition occurs at $n_{hc} = 0.1$. For larger (smaller) U this critical doping level n_{hc} increases (decreases). Furthermore, it was found that when raising t', n_{hc} is decreased. The DIC state was found to be always insulating. That is, even though for a parameter range of U, t', and n_h the DIC bands cross the Fermi level, the VIC phase has lower energy in this region. This agrees with the experiments: the diagonal stripe phase observed in
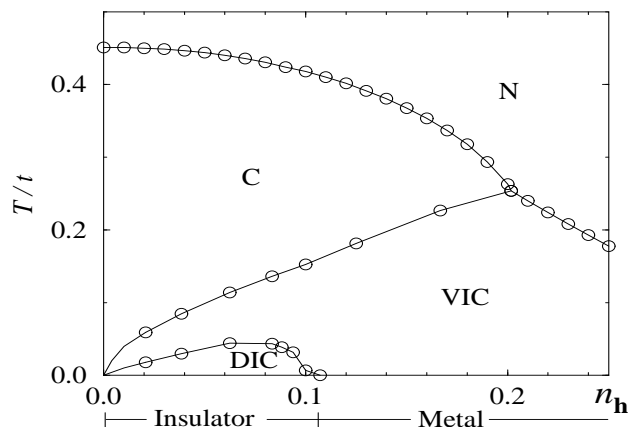
Figure 5.10: Phase diagram (temperature T vs hole-concentration n_h) obtained within the Hartree-Fock treatment of the single-band Hubbard model for $U = 3t$ and $t' = -0.1t$. In the figure, N denotes normal state, C commensurate antiferromagnetism, VIC (DIC) vertical (diagonal) incommensurate stripe order. Since the DIC phase is insulating and the VIC phase metallic this model explains the metal-to-insulator transition at $n_h = 0.1$ ($\delta = 0.05$). Adapted from Ref. [157].

heavily underdoped $La_{2-x}Sr_xCuO_4$ and in $La_{2-x}Sr_xNiO_{4+\delta}$ is insulating. The case of electron doping $n_h < 0$ has also been studied within the Hartree-Fock version of the Hubbard model. Here, the commensurate antiferromagnetic state competes with the VIC state, the latter having the lowest energy for large $|n_h|$ and Coulomb repulsion U. The diagonal stripe state is never stable for $n_h < 0$. The stable VIC stripes found by Ichioka *et al.*[157] are antiphase. However, since the neutron scattering experiments on the electron doped materials show commensurate antiferromagnetism, it would be interesting to search for in-phase stripes as well.

Below I review some of the other approaches to the stripe phase. Of course, in a strongly interacting electron system where quantum fluctuations are important, the Hartree-Fock solutions are not quantitatively correct. However, even in that case they can provide a guide for other strong-coupling studies. In fact, we will see that the above Hartree-Fock solutions capture much of the physics of the stripe phase quite accurately.

5.2.2 Frustrated phase separation and numerical studies

In the large-U limit the Hubbard model maps into the $t - J$ model

$$\mathcal{H} = -t \sum_{\langle i,j \rangle \sigma} \hat{P} \left(\hat{c}_{i\sigma}^\dagger \hat{c}_{j\sigma} + \text{H.c.} \right) \hat{P} + J \sum_{\langle i,j \rangle} \left(\mathbf{S}_i \cdot \mathbf{S}_j - \frac{\hat{n}_i \hat{n}_j}{4} \right), \qquad (5.9)$$

where $J = 4t^2/U$ is the exchange interaction between neighboring spins, $\hat{n}_i = \hat{c}_{i\uparrow}^\dagger \hat{c}_{i\uparrow} + \hat{c}_{i\downarrow}^\dagger \hat{c}_{i\downarrow}$ is the charge density operator, and $\hat{P}$ is the projection operator onto states with single site occupancy only. At half-filling Eqn. 5.9 reduces to the Heisenberg model with antiferromagnetic spin ordering. Away from half filling the ground state of the $t - J$ model is unknown in two dimensions.

Now, assume that $J/t \gg 1$, then it costs a lot of energy to break a singlet spin bond when adding a hole. Thus, in order to minimize the number of broken spin bonds the holes cluster together and the system *phase separates*, globally, into hole-rich and hole-poor regions with electron density per site of zero and one, respectively. However, the holes are charged and this state is expensive in charging energy. Therefore, when including the long-range Coulomb interaction (neglected already at the level of the Hubbard model) the phase separation becomes frustrated, and the system seeks a compromise which for certain combinations of the coupling constants leads to the stripe phase. This is the idea behind the frustrated phase separation scenario by Emery *et al.*[159, 160]. In the limit of very large exchange coupling, $J/t \gg 1$, this picture is correct, but for the physically relevant regime, $J < t$, where the kinetic energy plays an increasingly important role, there is only weak evidence for phase separation in the 2D $t - J$ model.

Because of the lack of controlled analytical methods to deal with strong correlation in the two-dimensional $t - J$ or Hubbard model, most of our knowledge comes from numerical approaches. Unfortunately, advanced numerical calculations are limited to relatively small systems due to the rapid growth of the number of states with the system size. This poses some obvious limitations on these studies. First, small changes in the model such as longer range hopping t' or the choice of boundary conditions can have large effects on the obtained results. Second, only in a few cases has it been possible to determine the long distance physics from a finite size scaling analysis over a large range of different system sizes. In the latter case, it was again found that small changes in the Hamiltonian can lead to very different long distance physics due to the large number of competing states that are close in energy in the strong correlation limit. Nevertheless, numerical studies are certainly very valuable and can give important insight into the properties of a given model. Therefore, let us review what $t - J$-numerics tell us about phase separation and stripe formation.

Fig. 5.11 shows the current consensus on global phase separation of the doped holes in the $t - J$ model in quasi-1D ladder systems and 2D clusters. Besides being interesting in their own right (exists for instance in $Sr_{2n-2}Cu_{2n}O_{4n-2}$), the ladders are important toy models for stripes. Furthermore, a weakly coupled 2D ladder system may constitute a very realistic model for the electronic structure in the CuO_2 planes. From Fig. 5.11a we see that the ladders are fully separated into a filled ($\langle n_e \rangle = 1$) and an empty ($\langle n_e \rangle = 0$) phase for large J/t. At low hole doping the phase boundary moves to lower J/t with increased number of legs, i.e. wider ladders. From density matrix renormalization group (DMRG) calculations known to be very accurate for ladder systems, Rommer
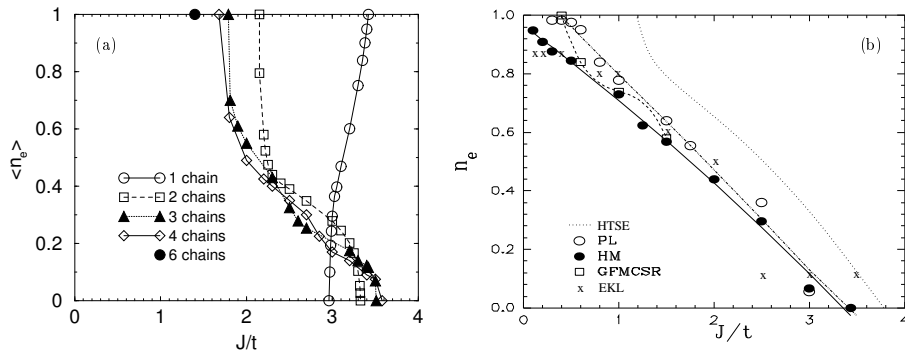
Figure 5.11: Phase separation in the n_e vs J/t plane of the $t - J$ model. (a) for the ladder systems, $\langle n_e \rangle$ is the average electron density, and phase separation is realized to the right of the curves. Adapted from Ref. [161]. (b) phase separation line as obtained by different authors for 2D $t - J$ clusters. Adapted from Shin *et al.*[162].

et al.[161] compared the phase separation boundary at very low doping as a function of ladder width and estimated that the 2D $t - J$ model would phase separate (also at very low doping) at $J/t \geq 1$.

As seen from Fig. 5.11b there is considerable dispute whether the 2D $t - J$ model phase separates at low doping at the physical value $J/t = 0.3 - 0.4$. Early studies by Emery, Kivelson and Lin[160] (EKL) found that phase separation happens at all interaction strengths. Hellberg and Manousakis (HM) reached a similar conclusion from Greens function Monte Carlo methods[163]. All other numerical studies of 2D $t - J$ clusters, some of which have also been shown in Fig. 5.11b, agree on the phase boundary at low electron density. When approaching half-filling, however, most find that the phase separation boundary remain above a critical value J_c/t larger than the physically relevant ratio $J/t = 0.35$. For instance, Putikka *et al.*[164] used a high-temperature series expansion (HTSE) to conclude that phase separation does not occur for any doping level when $J/t < 1.2$. From power Lanczos (PL) techniques Shin *et al.*[162] found the lower bound $J/t = 0.3 - 0.5$. White and Scalapino[165] performed extensive DMRG calculations on 2D $t - J$ clusters and found no phase separation when $J/t = 0.35$. In fact, they found stripes.

A typical result of the calculated spin and charge density is shown in Fig. 5.12. Question: where do the stripes originate from, if the frustrated phase separation is not in play? Answer: it is already contained in the competition between the exchange energy and the kinetic energy in Eqn. (5.9). Indeed, this agrees with the stripe Hartree-Fock solutions of the Hubbard model (i.e. no need for long-range Coulomb interactions) presented above. The DMRG calculations show that even at $J/t = 0.35$ two holes added to a $t - J$ cluster bind into a pair. Upon further doping these pairs can lower their energy further by forming a domain wall. The π phase shift in the antiferromagnetic
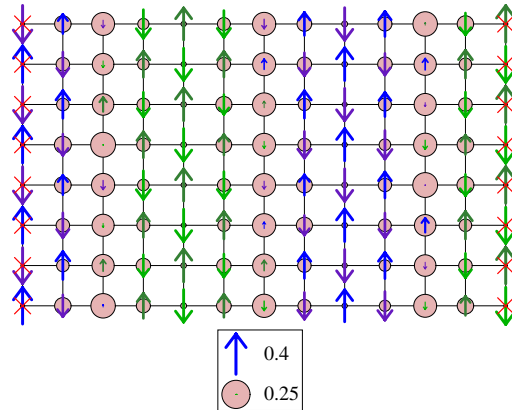
Figure 5.12: Spin and charge density modulations in the ground state of the $t - J$ model as found from DMRG calculations on a 13×8 cylinder with 12 holes[165]. The length of the arrows is proportional to $\langle S_z \rangle$ and the diameter of the circles to the hole density $1 - \langle n_e \rangle$ according the the scale displayed below the main figure.

background across the wall reduces both the frustration of the exchange bonds produced by the hopping of the holes and the transverse kinetic energy of the holes. It is the lowering to transverse kinetic energy that drives the domain wall formation. Had the antiferromagnetic background not gained an extra π phase shift across the stripe, a costly ferromagnetic bond would be generated upon hopping to a nearest neighbor site perpendicular to the stripe. For the same reason the holes cannot propagate into the antiferromagnetic regions, they are confined to the domain walls and their immediate vicinity.

To obtain a better understanding of the importance of the π phase shift let us consider the two site-centered stripe domain walls shown in Fig. 5.13[166]. When $t = 0$ the empty (i.e. electron empty) stripes with in-phase and anti-phase boundaries are degenerate. To determine the importance of the trans-
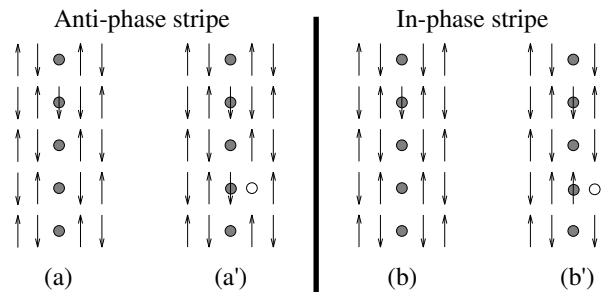

Figure 5.13: Spin arrangement for the anti-phase and in-phase stripes. Adapted from Ref. [166].

verse hopping let us ignore kinetic motion along the stripes. Then the $t - J$

Hamiltonian is given by $\mathcal{H} = \sum_i \mathcal{H}_i$, where

$$\mathcal{H}_i = -t \sum_{i\sigma} \left[\left(c^\dagger_{1,i,\sigma} c_{0,i,\sigma} + c^\dagger_{-1,i,\sigma} c_{0,i,\sigma} \right) + \text{H.c.} \right] + J \sum_{\langle jj'\rangle\langle ii'\rangle} \mathbf{S}_{j,i} \cdot \mathbf{S}_{j',i'}. \quad (5.10)$$

Here, i index the 3×1 unit cells along the stripe and j is either -1,0 or 1 ($j = 0$ is the stripe position). Thus, for instance, $c^\dagger_{-1,i,\sigma}$ creates an electron to the left of the domain wall. Consider first an empty wall and let the energy of the states $|\uparrow\downarrow 0\rangle$ and $|\uparrow\uparrow 0\rangle$ be denoted by E^a and E^i, respectively. The energy difference $\varepsilon = E^i - E^a$ between the good bond and the bad bond is proportional to the exchange J ($\varepsilon = J$ for a Ising model). With this notation the Hamiltonian becomes

$$\mathcal{H}^{(a,i)} = \begin{pmatrix} 0 & -t & -t \\ -t & E^{(a,i)} & 0 \\ -t & 0 & E^{(a,i)} \end{pmatrix} \quad (5.11)$$

which gives the ground state energy $E_g^{(a,i)} = \frac{1}{2}(E^{(a,i)} - \sqrt{(E^{(a,i)})^2 + 8t^2})$. Thus if we assume that $E^{(a,i)} \ll t$, the difference in kinetic energy gain due to transverse hopping is given by

$$E_g^a - E_g^i \approx -\frac{\varepsilon}{2} - \frac{1}{4\sqrt{8}t} \left((E^a)^2 - (E^i)^2 \right). \quad (5.12)$$

Therefore the transverse zero-point kinetic fluctuations "pick out" the anti-phase stripe which we already expected from Fig. 5.13. Note, however, that when electrons are pumped into the stripe there will be a competing term favoring the in-phase boundary due to the antiferromagnetic exchange interaction. This can be seen in the second row in fig. 5.13. This competition leads to a transition between anti-phase and in-phase stripes as a function of stripe filling which has been studied in more detail by Zacher[166] and Liu and Fradkin[167].

Depending on the boundary conditions the DMRG calculations find both bond- and site-centered anti-phase stripes. These are found to be extremely close in energy. Stripes oriented along the Cu-O bonds have lower energy than the diagonal stripes. Thus, the main conclusions are very similar to those obtained from the Hartree-Fock treatments. The stripe energy as a function of the filling revealed that quarter filling has the lowest energy for $J/t = 0.35$. This is contrary to the mean-field studies where the nearest neighbor hopping t' is necessary in order to generate metallic stripes.

5.2.3 Stripe liquids

The theoretical discussion above was related to static ordered stripe arrays (stripe crystals) which break both the translational- , four-fold rotational-, and the spin rotation symmetry. The experiments show, however, that large parts of the phase diagram is dominated by short-range fluctuating, disordered, and meandering stripe configurations. This has lead to numerous phenomenological "string theories" attempting to incorporate the notion of a stripe fluid by describing the low-energy degrees of freedom of the stripes[135].

For instance, Zaanen *et al.*[168] mapped the transverse kink excitations of the stripes to a quantum spin-1 chain described by an anisotropic Heisenberg model with easy-axis terms. The phase diagram for this spin-1 chain and the effects of stripe pinning by dopants were studied by Morais Smith *et al.*[169, 170, 171] Starting from the stripe crystal, one can imagine transverse stripe fluctuations becoming more important as we increase the temperature and the transverse zero-point quantum fluctuations, and eventually melt the crystal. Kivelson *et al.*[172] classified the stripe liquids with terminology borrowed from the field of liquid crystals: 1) the stripe smectic[6] phase breaks the translational symmetry along one spatial direction and remains a liquid along the other. In this state the root mean square magnitude of the transverse stripe fluctuations is below the inter-stripe spacing. 2) On the other hand, when they become larger than the inter-stripe spacing, we enter the so-called nematic[7] phase which breaks the four-fold rotation symmetry of the underlying lattice but remain translational invariant. In this phase the stripes meander and dislocations restore the translational invariance. Still, the nematic phase maintain a degree of orientational order by being preferentially aligned along one direction. This is similar the the conventional nematic liquid crystal phase, which consists of rod shaped particles with long-range orientational order but no long-range translational order. Snap-shots of these different phases are shown in Fig. 5.14.

5.3 What do stripes have to do with superconductivity?

It is still controversial whether the stripe formation is important for the occurrence of superconductivity or simply another competing order in the underdoped regime of the phase diagram. The latter seems to be the conclusion from extensive numerical studies of projected wavefunctions by Sorella *et al.*[173]. Here the d-wave superconducting state is found to be the ground state of the 2D $t - J$ model at low doping and moderate J/t with no need for stripes. Unfortunately, the possible bias in the chosen wavefunction questions the generality of this result.

Experimentally, the pinned stripes suppress the superconductivity as seen by a

---

[6]From the Greek word $\sigma\mu\epsilon\gamma\mu\alpha$, which means soap and was use to make the original smectic liquid crystals.

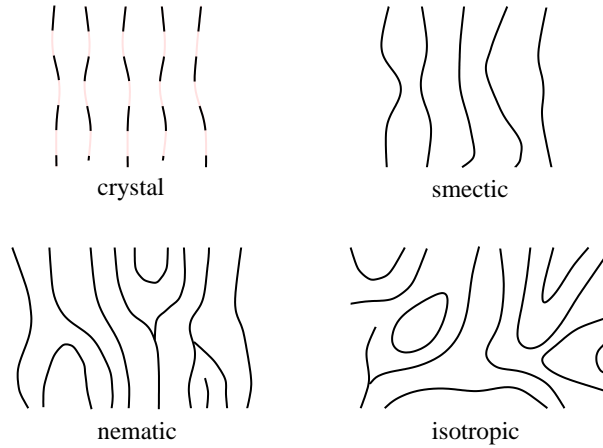[7]Comes from the Greek $\nu\epsilon\mu\omega\sigma$, meaning thread.

Figure 5.14: Schematic illustration of snap-shots of the local stripe order in the electronic quantum liquid-crystal phases. The broken lines indicate charge density modulations along the stripes whereas the solid lines show liquid stripes. From Ref. [172].

lowering of T_c in the neodymium doped samples. This is presumably also the explanation of the "1/8 anomaly", i.e. a strong suppression of T_c around $x \sim 1/8$, known from many experiments on $La_{2-x}Ba_xCuO_4$ and $La_{1.6-x}Nd_{0.4}Sr_xCuO_4$[174]. On the other hand, the $\delta \sim x \sim T_c$ relation (the so-called Yamada relation[141]) has been taken as evidence for the importance of fluctuating stripes in generating the superconductivity: as the inter-stripe distance decreases, the Josephson coupling between the stripes increase and so does T_c. Optimal doping on the other hand, is characterized by a transition into a regime where the stripes begin to disintegrate which is the reason that T_c drops in the overdoped regime. Besides, the question of whether self-organized electronic structures can generate a superconducting state is interesting and seems sufficiently radical that it may actually be the long-sought high-T_c "mechanism".

In addition to the experimental evidence for stripes, there is also purely theoretical motivation for attempting to build a 2D high-T_c superconductor from 1D arrays. An example is given by the exact solutions (using Bethe ansatz) to the 1D Hubbard chain by Fye *et al.*[175] and Chakravarty *et al.*[176]. Consider a 1D Hubbard ring with N sites and $N + Q$ electrons and let $E(Q, S)$ denote the lowest lying eigenvalue with charge Q and total spin S. The pair-binding energy $E_P(Q)$ is defined as

$$E_P(Q) = 2E(Q+1) - (E(Q+2) + E(Q)), \qquad (5.13)$$

where $E(Q)$ has been minimized with respect to S. Thus, a positive pair-binding energy corresponds to an effective electron attraction: given two N site rings and $2(N + Q + 1)$ electrons, it is more favorable to place $N + Q + 2$ electrons on one ring and $N + Q$ on the other than to place $N + Q + 1$ electrons

on each ring. The results of adding two electron to a neutral ring $(Q = 0)$ is displayed in Fig. 5.15a as a function of the length of the ring. As seen, pair-binding occurs within this purely repulsive model when $N = 4n$, n being a positive integer[8]. In the thermodynamic limit $N \to \infty$ the pair-binding vanishes $E_P \to 0$. The main lesson obtained from Fig. 5.15a is that the pairing is maximal at *intermediate* values of the length N.

When the ground state is a spin singlet, the spin gap defined as $\Delta_S(Q) =$
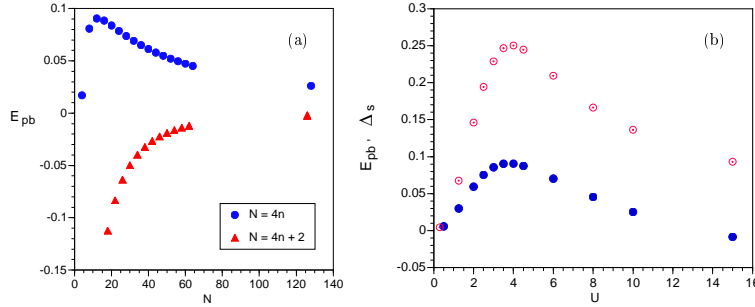

Figure 5.15: a) Pair-binding energy E_P of $N = 4n$ and $N = 4n + 2$ Hubbard chains with $U/t = 4$, n is a positive integer. b) The spin gap Δ_S (open symbols) and E_P (solid symbols) as a function of U/t for a $N = 12$ site Hubbard ring. From Ref. [176].

$E(Q, 1) - E(Q, 0)$ yields the energy gap to the lowest $S = 1$ excitation. In Fig. 5.15b, $\Delta_S(0)$ and $E_P(0)$ are plotted as a function of the Coulomb repulsion U/t. As seen, they both peak at the same intermediate value of the interaction strength U/t. In fact, as shown in Ref. [176], for large N, $E_P \approx \Delta_S$, indicating that the pair-binding energy is intimately related to the spin gap formation. For the chains E_P and Δ_S both vanish in the thermodynamic limit $N \to \infty$. However, for the two-leg $S = 1/2$ $t - J$ ladder DMRG calculations show that the spin gap and E_P remain finite in the $N \to \infty$ limit for a wide range of doping levels due to strong rung spin-singlet formation. In particular, for $J/t = 0.35$ they show that two holes added to the ladder form a *d-wave pair* in order to minimize their kinetic energy and the disturbance of the antiferromagnetic background[177]. The pairing is d-wave in the sense that the rung-rung (x-direction) and the rung-leg (y-direction) pairing correlations have the same amplitude but opposite sign. This is different from the regime $J \gg t$, where the two holes are nearest neighbors in order to reduce the number of broken exchange bonds. As discussed above, several pairs prefer to order in stripes. However, the energy per hole in the stripe is *only slightly lower than in a pair*, and this energy difference can be tuned by increasing the pair mobility by e.g. a next-nearest hopping term t'. As t' increases the stripes coexist with

---

[8]As shown in Ref. [176], the occurrence of pair-binding for the $N = 4n$ chain as opposed to the $N = 4n + 2$ ring is caused by the fact that the ground state for $Q = \pm 2$ is a spin singlet for $N = 4n$, while for $N = 4n + 2$ it is a spin triplet.

the d-wave superconducting phase until they eventually evaporate from the ground state giving way to a homogeneous d-wave superconducting state[178]. In this sense the *static stripes compete* with the d-wave superconductivity in agreement with the suppression of T_c seen in the pinned stripe phase of $La_{1.6-x}Nd_{0.4}Sr_xCuO_4$.

This conclusion, however is for static stripes in small clusters. It is still an interesting question whether it is possible to build a high-T_c superconductor from a 1D stripe array. From the discussion above it follows that one might expect to generate a 2D superconducting state from an array of coupled two-leg Hubbard ladders. This is a system at the intermediate length scale in the transverse direction which exhibits a spin gap. Spatially this configuration is exactly the bond-centered stripe state[9].

There is a problem, however, with building a superconducting state from the stripe phase consisting of an array of one-dimensional weakly coupled metals (Luttinger liquids). For such a system the low-temperature phase is known to be an insulating charge density wave state. This is indicated in Fig. 5.14a where charge density modulations occur in both the vertical and horizontal direction. For the isolated stripe with a gap Δ_S in the spin excitation spectrum, the low-temperature T low-energy degrees of freedom are the charge density wave and the superconducting fluctuations whose susceptibilities diverge as $\chi_{cdw} \sim \Delta_s T^{-2+K_c}$ and $\chi_{sc} \sim \Delta_s T^{-2+1/K_c}$ when $T \rightarrow 0$. Here, the charge Luttinger parameter K_c is a critical exponent which for repulsive interactions satisfy $0 < K_c < 1$. When $K_c > 1/2$ both susceptibilities diverge as $T \rightarrow 0$, with χ_{cdw} being the most divergent. When a coupling between the stripes is included, this causes a 2D insulating charge density wave state. Therefore, despite the motivation mentioned above for the starting point of a 1D array of charge rivers each with a built-in tendency for superconductivity (of course there cannot be true LRO at finite T in a 1D system due to the strong quantum fluctuations. The point is that the *local* correlations and enhanced susceptibilities in the 1D system may imply the occurrence of true LRO in the 2D system), the charge density wave ordered state wins out. Hence, the problem becomes that of finding a way to tip the balance in favor of the 2D superconducting state. There are at least two proposals for resolving this problem: transverse stripe *fluctuations* or arrays of static stripes of *alternating type*, ...*ABAB*..., differing in e.g. the electron density.

Regarding the first proposal, Kivelson *et al.*[172] and Emery *et al.*[179] showed that the transverse zero-point fluctuations of the stripes in the smectic phase cause the effective charge density wave coupling between adjacent stripes to vanish. At the same time, because the Josephson tunnelling amplitude of pairs of electrons between the stripes depends exponentially on the distance between

---

[9]For wider undoped ladders the spin gap Δ_S decreases exponentially with the width and for odd-leg ladders the spin gap is completely absent in the thermodynamic limit. However, it is not crucial to identify the stripes with two-leg ladders. For instance, even the odd-leg ladders develop a spin gap as a function of doping. In this case the $d_{x^2-y^2}$-wave pairing correlations are *concurrent with* the onset of the spin gap Δ_S

neighboring stripes, it can be greatly enhanced when the stripes are allowed to fluctuate. Thus, below a finite temperature T_c the smectic stripe phase is globally superconducting (for $K_c > 1/2$). It is largely an open question whether the superconductivity survives (or becomes stronger) into the nematic phase where the quantum stripe fluctuations become even more pronounced.

Another way to circumvent the χ_{cdw}-most-divergent problem, is to consider an array to stripes of alternating types, $...ABAB....$ similar to the bond-centered stripes discussed above. In this case the tendency for an overall 2D charge density wave state can be strongly suppressed due to the mismatch of the ordering vectors between stripes of type A and B. Indeed, by assuming that the hopping is strongly modulated perpendicular to the stripes, Arrigoni *et al.*[180] showed that when both type A and B are in the spin gapped Luther-Emery phase and the charge Luttinger parameters satisfy $K_{cA}^{-1} + K_{cB}^{-1} - K_{cA} < 2$ and $K_{cA}^{-1} + K_{cB}^{-1} - K_{cB} < 2$, then the superconducting susceptibility becomes the most divergent as $T \rightarrow 0$. Therefore, the superconducting transition preempts the charge density wave transition. This constitutes another example where static stripes coexist with superconductivity.

5.4 The next chapters

Given this strong circumstantial evidence for stripe phases in the high-T_c cuprates, the following chapters will deal in more detail with model calculations that show the existence of stripes and how to detect them in STM, ARPES and neutron scattering experiments.

6 Stripes in the mixed state

*Most of the material in this chapter has been published by the author and P. Hedegård in Physical Review B **67**, 134528 (2003)[106], and in Journal of Low Temperature Physics **131(3)**, 281-285 (2003)[181].*

6.1 Pinning of stripes in the mixed state

There exists substantial evidence that when suppressing the condensate of the superconducting phase by an applied magnetic field the magnetic order (possibly fluctuating) reappears inside the vortex cores. This is contrary to conventional BCS superconductors in which the suppression of the order parameter inside the vortex cores is equivalent to locally raising the temperature, i.e. entering the normal metallic Fermi liquid state. In the cuprates, suppression of the superconducting order parameter is equivalent to *decreasing the doping*. The enhanced antiferromagnetic order inside the vortex cores results in insulating core regions as opposed to the metallic Caroli-de-Gennes cores of conventional superconductors. This was first predicted within the SO(5) theory where the vortex state is a non-trivial topological texture of the five component superspin vector[51, 182, 183].

Experimentally, the first evidence for an antiferromagnetic vortex state was reported in the mixed state of YBCO by Vaknin *et al.*[184] Further elastic neutron scattering measurements by Katano *et al.*[185] on LSCO crystals also found enhanced antiferromagnetism when applying a large magnetic field. More detailed recent measurements by Lake *et al.*[44] are discussed below. Other probes such as μSR and NMR measurements on underdoped YBCO under high magnetic fields show enhanced antiferromagnetic order in the vicinity of the vortex cores[53, 186, 187]. In the NMR experiments the Larmor frequency of the probed nucleus is a measure of their location relative to the vortex core, allowing for site-sensitive NMR. The inverse spin-lattice relaxation time $1/T_1$ is a measure of the spin fluctuations, and for ^{17}O the rate $1/T_1$ is seen to increase rapidly as the core region is approached and the decrease inside the cortex cores. This indicates vortex-induced magnetic fluctuations occurring outside the core and strongly suppressed density of states inside the core region[188].

In the following I discuss in more detail two specific experiments that both give evidence of more complex magnetic structures emerging near the cuprate vortices.

6.1.1   Tunnelling spectroscopy near a single vortex

Hoffman *et al.*[189] performed scanning tunnelling spectroscopy near the vortex cores in the mixed state of slightly overdoped BSCCO. Specifically they measured the real-space maps of the local density of states (LDOS) at a range of energies both with and without an applied magnetic field. Additional spectral weight induced by the applied field near the vortices can then be seen in the difference function

$$S_{E_1}^{E_2}(x, y, B) = \sum_{E_1}^{E_2} \left(\text{LDOS}(E, x, y, B) - \text{LDOS}(E, x, y, B = 0) \right) dE. \quad (6.1)$$

Experimental plots of $S_1^{12}(x, y, 5T)$ show that checkerboard patterns emerge in the vicinity of the vortices. Fig. 6.1a shows the power spectrum of the Fourier transform of $S_1^{12}(x, y, 5T)$ and 6.1b is the schematic version of 6.1a. Similar
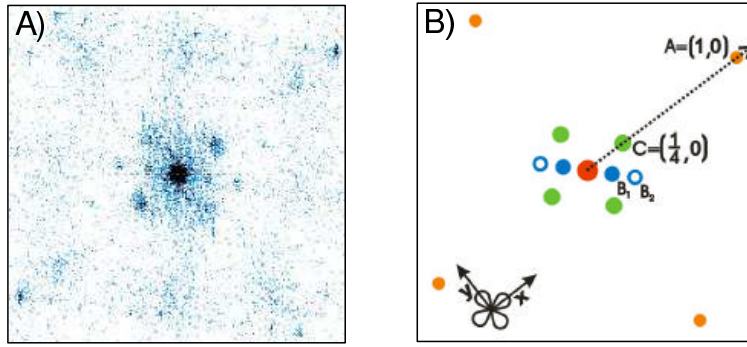

Figure 6.1: Two dimensional power spectrum of $S_1^{12}(x, y, 5T)$ plotted as intensity versus k_x and k_y: (A) Raw data, and (B) a schematic representation of (A). The distance is measured in units of $2\pi/a$ where a is the lattice constant. The atomic peaks (label A) are positioned at the k-space positions $(0, \pm 1)$ and $(\pm 1, 0)$, B labels the surface supermodulation peaks, whereas the magnetic field induced peaks C occur at $(0, \pm 1/4)$ and $(\pm 1/4, 0)$.

maps are obtained from measurements performed with other magnetic field strengths. The important new result is the vortex-induced peaks seen near $(\pm 1/4, 0)$ and $(0, \pm 1/4)$ in units of $2\pi/a$ (a denotes the lattice spacing). This means that the checkerboard pattern in Fig. 6.1a has spatial periodicity $4a$ and is oriented along the Cu-O bonds as indicated in Fig. 6.1b. The spatial extent for the LDOS modulations was found to be around 30 Å, which certainly exceeds the core radius estimated to be around 8-10 Å. This means that at 5T about 25 % of the surface is covered by the checkerboard electronic structure. Finally, from the intensity distribution of the checkerboard peaks in Fig. 6.1b it is clear that one direction corresponding to $(\pm\frac{1}{4}, 0)$ is preferred. This is evidence for one-dimensionality in the origin of the checkerboard patterns. More recently similar LDOS patterns have been observed in the absence of an

applied magnetic field[75, 77, 78, 190], the origin of which is currently highly controversial as discussed in the previous chapter on quantum interference effects near weak impurities. It is becoming evident that the STM measurements on underdoped samples support evidence for charge order in addition to the purely low-energy dispersing quantum interference patterns as expected from a Fermi surface argument. Several authors have attempted to explain these zero-field STM measurements[107, 192, 191, 193, 194]. Particularly, Podolsky *et al.*[191] succeeded in modelling the detailed LDOS modulations by including a weak dimerization of the hopping integral and the pairing amplitude. Similar results can be obtained within the stripe model as will be shown in the following chapter.

6.1.2 Elastic neutron scattering in a magnetic field

Here, I review recent neutron measurements performed in the mixed state of $La_{2-x}Sr_xCuO_4$.

Near optimal doping the magnetic excitation spectrum is dominated by four incommensurate peaks centered at $(\frac{1}{2}, \frac{1}{2} \pm \delta)$ and $(\frac{1}{2} \pm \delta, \frac{1}{2})$ with $\delta \sim \frac{1}{8}$ (in units of $2\pi/a$). This corresponds to a fluctuating magnetic density wave with periodicity $8a$ oriented along the Cu-O bonds. In the superconducting phase these fluctuations disappear at low energies ($\omega \leq 7\text{meV}$) due to the opening of a spin gap[195].

The first evidence for field-induced magnetic order as seen by inelastic neutron scattering on $La_{2-x}Sr_xCuO_4$ ($x = 0.163$) was reported by Lake *et al.*[196] They found that upon applying a 7.5T field the intensity of the magnetic fluctuations *reappear* at the same incommensurate positions, i.e. at $(\frac{1}{2}, \frac{1}{2} \pm \delta)$ and $(\frac{1}{2} \pm \delta, \frac{1}{2})$ with $\delta \sim \frac{1}{8}$. The sharpness of the peaks reveals a coherence over distances of over 60 Å.

It is well known that in the underdoped region of $La_{2-x}Sr_xCuO_4$ superconductivity coexists with static magnetic order. How the static order develops with an applied magnetic field was recent investigated by neutron diffraction[44]. Fig. 6.2a shows the strongly increased intensity at the incommensurate wave vector in the superconducting state when applying a magnetic field of 14.5T. The resolution-limited peaks correspond to an in-plane correlation length of over 400 Å. This is greater than both the coherence length and the inter-vortex distance. Therefore, throughout the bulk of these underdoped materials, d-wave superconductivity and incommensurate antiferromagnetism coexists. The temperature dependence of the field-induced signal is shown in Fig. 6.2b. Clearly the incommensurate peaks are strongly enhanced at low temperatures. Note that a zero-field response also exists and increases as the temperature is lowered.

Similar field-induced elastic neutron scattering results have been obtained on La_2CuO_{4+y} by Khaykovich *et al.*[45]
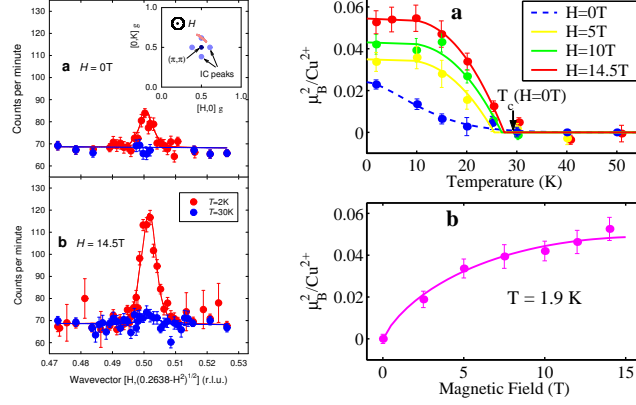
Figure 6.2: Left: a) Magnetic elastic neutron intensity for underdoped $La_{2-x}Sr_xCuO_4$ (x=0.10) as a function of scattering vector through an incommensurate peak in zero magnetic field. b) Same as a) but in a magnetic field of 14.5 T. Right: The square of the ordered spin moment as a function of magnetic field and temperature. At T=1.9K the lower figure shows the magnetic field dependence of the moment. Adapted from Ref. [44].

6.1.3   Discussion

How may we understand these experiments? One explanation is that the antiferromagnetic vortex cores act as pinning sites for charge- (as seen by STM) and spin- (as seen by neutron scattering) density waves. In the previous chapter I discussed how neodymium doped into $La_{2-x}Sr_xCuO_4$ leads to a bulk LTT phase which 'traps' the stripes. Here, similarly, the vortices and impurities can locally pin the stripes.

By assuming that the superconducting phase of $La_{2-x}Sr_xCuO_4$ is proximate to a bulk quantum phase transition to a state with coexisting superconductivity and spin density wave order, Demler *et al.*[197, 198] and Kivelson *et al.*[199] formulated a generalized Landau theory for the mixed state. This is well in line with the emerging notion that cuprate systems are dominated (especially in the underdoped regime) by competing order parameters. In this model, in addition to the usual Ginzburg-Landau action S_{GL} for the superconductor, there is a bosonic contribution arising from the tendency of the system to form magnetic order $\mathbf{M}_i(\tau)$

$$
\begin{aligned}
S_M \quad = \quad & \int d\tau \sum_i \{ \frac{1}{2}|\partial_\tau \mathbf{M}_i(\tau)|^2 + c^2 |\nabla \mathbf{M}_i(\tau)|^2 \qquad (6.2) \\
+ \quad & (r + v|\Psi_i|^2)|\mathbf{M}_i(\tau)|^2 + \frac{u}{2}(|\mathbf{M}_i(\tau)|^2)^2 \},
\end{aligned}
$$

where c, r, v, u are coupling constants that depend on doping and temperature. As seen, the important quadratic term includes the coupling to the superconducting order parameter Ψ. The magnetic field couples to the superconducting order through the term $|(\nabla - i\mathbf{A})\Psi|^2$ in S_{GL}. The resulting $r - H$ phase diagram is shown in Fig. 6.3: when $H = 0$ there is a quantum phase transition at r_c between the coexistence phase ($\langle \mathbf{M} \rangle \neq 0, \langle \Psi \rangle \neq 0$) to the purely superconducting state ($\langle \mathbf{M} \rangle = 0, \langle \Psi \rangle \neq 0$). Since the coexistence state is separated from
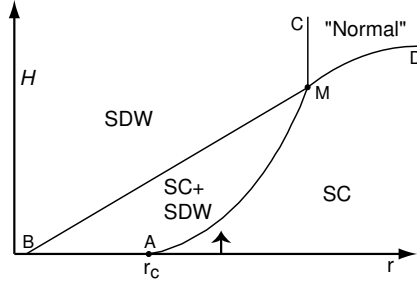

Figure 6.3: $r - H$ phase diagram obtained from the saddle-point equations of the total action $S_{GL} + S_M$ in the low temperature and large N limit, where $\mathbf{M} \to M_1, M_2, ..., M_N$ (From Demler *et al.*[197]).

the superconducting state by the line defined by $H = (r - r_c)/\ln[1/(r - r_c)]$, it follows that for a system in the superconducting phase, say along the vertical arrow in Fig. 6.3, a *modest* magnetic field H (modest compared to the large H_{c2}) drives the system into the coexistence state. Since smaller amount of doping corresponds to a reduced coupling r, this model agrees with the experimental finding of static spin order in the superconducting phase of underdoped $La_{2-x}Sr_xCuO_4$. In this way the application of a magnetic field is similar to adding neodymium as discussed previously: both move the system into the stripe ordered phase.

The intensity $I(H)$ dependence of the neutron diffraction signal on the applied magnetic field is predicted to be, $I(H) = I(0) + C_2(H/H_{c2})\ln(H_{c2}/H)$ (with C_2 being some constant) which from the full line in Fig. 6.2a is seen to fit (by tuning C_2 only) the experimental data quite well. Within this model, the peculiar logarithmic dependence arises from the spatial dependence of the superconducting order parameter Ψ_i outside the vortex cores caused by the superflow, $|\Psi_i| = 1 - 1/(2r_i^2)$, so that $\langle |\Psi_i^2| \rangle = 1 - (H/H_{c2})\ln(H_{c2}/H)$.

It remains unclear: 1) why the spin ordering prefers a periodicity of eight lattice constants a, and 2) whether the pinned-stripe picture agrees with the STM measurements by Hoffman *et al*[189]? In the following section I discuss the latter question by *assuming* a $8a$ spin ordering and calculate the corresponding LDOS surrounding the magnetic vortex.

6.2   Pinned stripes around vortex cores

In this section we discuss recent elastic neutron scattering and scanning tunnelling experiments on High-T_c cuprates exposed to an applied magnetic field. Antiferromagnetic vortex cores operating as pinning centers for surrounding stripes is qualitatively consistent with the neutron data provided the stripes have the antiphase modulation. Within a Green's function formalism we study the low energy electronic structure around the vortices and find that besides the dispersive quantum interference there exists a non-dispersive checkerboard interference pattern consistent with recent scanning tunnelling measurements. Thus both experiments can be explained from the physics of a single CuO_2 plane.

The competing orders in the High-T_c cuprates remain a strong candidate for explaining some of the unusual features of these doped Mott insulators[135, 136, 154, 160]. The competition between superconducting order and antiferromagnetic order has recently attracted a large amount of both experimental and theoretical attention. In particular, experiments in the mixed state have revealed an interesting coexistence of these order parameters.

Elastic neutron scattering results on $La_{2-x}Sr_xCuO_2$ (x=0.10) have shown that the intensity of the incommensurate peaks in the superconducting phase is considerably increased when a large magnetic field is applied perpendicular to the CuO_2 planes[44]. This enhanced intensity corresponds to a spin density periodicity of eight lattice constants $8a_0$ extending far outside the vortex cores. Nuclear magnetic resonance experiments have shown evidence for antiferromagnetism in and around the vortex cores of near-optimally doped $Tl_2Ba_2CuO_{6+\delta}$[188]. Furthermore, muon spin rotation measurements from the mixed state of $YBa_2Cu_3O_{6.50}$ find static antiferromagnetism in the cores[53]. Consistent with these findings scanning tunnelling microscopy (STM) measurements performed on the surface of $YBa_2Cu_3O_{7-\delta}$ and $Bi_2Sr_2CaCu_2O_{8+x}$[50, 62]have revealed very low DOS inside the vortex cores[51, 200, 201]. Thus, there is increasing evidence for antiferromagnetic correlations in the vortex cores of the under- and optimally-doped regime of the hole doped cuprates. More recent STM measurements of slightly overdoped $Bi_2Sr_2CaCu_2O_{8+x}$ have shown a checkerboard halo of the local density of states (LDOS) around the vortex cores[189]. This LDOS modulation observed at low energy $|\omega| < 12$ meV was found to have half the period of the spin density wave (SDW) observed by neutron scattering (i.e. four lattice constants $4a_0$), and to be oriented along the crystal axes of the Cu-O plane.

The neutron experiments have been analyzed within phenomenological models that assume close proximity to a quantum phase transition between ordinary superconductivity and a phase with antiferromagnetism or a phase where superconductivity coexists with SDW and charge density wave (CDW) order[183, 197, 198, 194]. In these models the suppression of the superconducting order inside the vortex cores allows the competing magnetic order to arise.

Demler *et al.*[197] found that around the vortices the circulating supercurrents can similarly weaken the superconductivity and induce a SDW.

The field-induced checkerboard LDOS pattern in the mixed state has been recently considered within the framework of several models[94, 193, 194, 202, 203, 204]. In this paper we add to the discussion by calculating the LDOS in regions where a d-wave superconductor has been perturbed by induced magnetism. First, however, we note that a checkerboard *spin* modulation is inconsistent with the elastic neutron scattering experiments by Lake *et al.*[44] on La$_{2-x}$Sr$_x$CuO$_2$ (x=0.10). For example, assuming that the checkerboard CDW is intrinsic to the Cu-O planes where it gives rise to a static SDW checkerboard pattern (Fig. 6.4a), the expected neutron diffraction pattern is shown in Fig. 6.4b. As is evident there is a 45 degree rotation of the four main
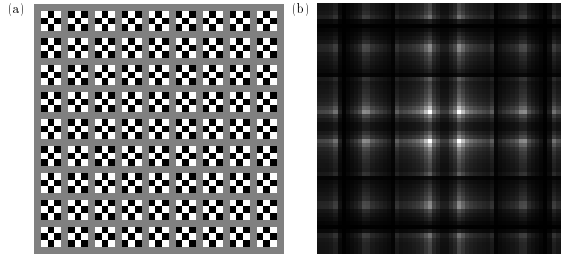

Figure 6.4: a) Real space picture of the spin structure in a checkerboard spin geometry. Black (white) represent spin up (down) while gray reveals the superconducting background. In order to simulate the induced incommensurability each island of antiferromagnetic spins is out of phase with its nearest neighbor. b) Fourier spectrum of the spin checkerboard structure shown in a).

incommensurate peaks and a plaid pattern of the higher harmonics. The rotated incommensurability (with the correct absence of an increased signal at (π, π)) shows that this spin structure does not apply to LSCO for doping levels close to $x = 0.10$. It is interesting to note that a rotation of the incommensurable peaks at low dopings ($x < 0.055$, close the insulator-superconductor phase transition) has been observed in LSCO[145]. However, there is no simple way to create an antiphase spin geometry without frustrating the spins at low dopings where droplets of charge in an antiferromagnetic background is the expected situation[205]. However, this might be possible in the highly overdoped regime where the droplets have been inverted to separate magnetic islands. In that case a 45 degree rotation of the incommensurable peaks would be consistent with a checkerboard spin pattern. In this light it would be very interesting to perform an experiment similar to Lake *et al.*[44] on highly overdoped LSCO. In the case of a connected antiferromagnetic background one would also expect a large weight at (π, π).

The physical picture we have in mind is presented in Fig. 6.5a. In this real space picture an antiferromagnetic core (center) has pinned a number of surrounding stripes. This pinning effect of SDW by magnetic vortex cores is a
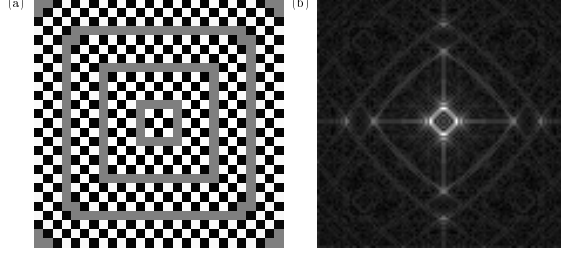
Figure 6.5: a) The idealized version of a real space spin configuration consistent with our physical picture. b) Fourier spectrum of the spin density order from a). Almost all the induced weight is located in the four incommensurable peaks.

well-known effect from numerical studies[202].

Both experimentally[137] and theoretically[135, 154, 197, 207] we expect an antiphase modulation of the induced antiferromagnetic ring domains. Indeed as seen in Fig. 6.5b the related diffraction pattern is qualitatively consistent with measurements by Lake *et al.*[44] of enhanced intensity at the incommensurate points.

Without an applied magnetic field, only disorder can produce a similar pinning effect of the fluctuating stripes[190]. In addition to the creation of more pinning centers when applying a magnetic field, the single site impurities are expected to pin much weaker than the large "impurities" created by the flux lines. This is qualitatively consistent with the measurements by Lake *et al.*[44] of the temperature dependence of the increased magnetic signal for different magnetic field strengths.

This leads to the question of the electronic structure around extended magnetic perturbations in d-wave superconductors. The many experiments indicating coexistence of d-wave superconductivity and antiferromagnetism mentioned above motivate studies of simple models that enable one to calculate the LDOS in such regions.

The model Hamiltonian defined on a 2D lattice is given by

$$\mathcal{H}^0 = -\sum_{\langle n,m \rangle \sigma} t_{nm} \hat{c}_{n\sigma}^\dagger \hat{c}_{m\sigma} - \mu \sum_{n\sigma} \hat{c}_{n\sigma}^\dagger \hat{c}_{n\sigma} \qquad (6.3)$$

$$+ \sum_{\langle n,m \rangle} \left(\Delta_{n,m} \hat{c}_{n\uparrow}^\dagger \hat{c}_{m\downarrow}^\dagger + H.c. \right)$$

$$\mathcal{H}^{int} = \sum_n M_n \left(\hat{c}_{n\uparrow}^\dagger \hat{c}_{n\uparrow} - \hat{c}_{n\downarrow}^\dagger \hat{c}_{n\downarrow} \right) \qquad (6.4)$$

where $\hat{c}_{n\sigma}^\dagger$ creates an electron with spin σ at site n and μ is the chemical potential. The staggering is included in $M_n = (-1)^{\mathbf{n}} M$. The strength of the antiferromagnetic and superconducting coupling is given by M and Δ,

respectively.

As discussed previously, the model in Eqn. (6.3)-(6.4) can be viewed as the mean-field Hamiltonian of a $t - U - V$ Hubbard model, where the nearest neighbor attraction V gives rise to the d-wave superconductivity. In contrast the on-site Coulomb repulsion U only causes the antiferromagnetism. In this section we do not diagonalize $\hat{H}$ in the Bogoliubov-de Gennes scheme since such lattice calculations require unrealistically large magnetic field values. Instead, we solve the Dyson equation exactly by inverting a large matrix. This approach has previously been utilized extensively to study various short-ranged impurity effects in superconductors[105], but can also be used for extended perturbations embedded in a $\hat{G}_0$ medium. Here $\hat{G}_0$ is the Green's function of the parent medium, in this case a d-wave BCS superconductor. This Green's function is given by

$$\hat{G}_0^{-1}(\mathbf{p}, \omega) = (\omega + i\delta)\tau_0 - \xi_{\mathbf{p}}\tau_3 - \Delta_{\mathbf{p}}\tau_1 \tag{6.5}$$

where τ_ν denote the Pauli matrices in Nambu space and the gap function $\Delta_{\mathbf{p}} = \frac{\Delta_0}{2}(\cos(p_x) - \cos(p_y))$. The lattice constant a_0 is set to unity and $\xi_{\mathbf{p}} = \epsilon_{\mathbf{p}} - \mu$ with

$$\epsilon_{\mathbf{p}} = -2t(\cos(p_x) + \cos(p_y)) - 4t'(\cos(p_x)\cos(p_y)). \tag{6.6}$$

Here $t(t')$ refers to the nearest (next-nearest) neighbor hopping integral and μ is the chemical potential. We perform the 2D Fourier transform of $G_0(\mathbf{p}, \omega)$ numerically by utilizing a real space lattice of 1000×1000 sites and a quasi-particle energy broadening of $\delta = 1.0$meV.

To simulate the situation around optimal doping of the hole doped cuprates the following parameters are chosen: $t = 300$meV, $t' = -120$meV, $\Delta_0 = 25$meV, $\mu = -354$meV. When the real space domain affected by $\mathcal{H}^{int}$ involves a finite number of lattice sites $N \times N$ we can solve the Dyson equation exactly to find the full Greens function. Writing the Dyson equation in terms of real-space (and Nambu) matrices it becomes

$$\underline{\underline{G}}(\omega) = \underline{\underline{G}}^0(\omega)\left(\underline{\underline{1}} - \underline{\underline{\mathcal{H}}}^{int}\underline{\underline{G}}^0(\omega)\right)^{-1}. \tag{6.7}$$

The size of the matrix $\left(\underline{\underline{1}} - \underline{\underline{\mathcal{H}}}^{int}\underline{\underline{G}}^0(\omega)\right)$ is given by $(d \times N^2) \times (d \times N^2)$ where d is an integer equal to the number of components in the Nambu particle-hole spinor and N denotes the total number of lattice sites affected by the magnetic perturbation. Therefore a real-space lattice with 25×25 sites affected by perturbations results in a (1250×1250) matrix to be inverted.

Knowing the full Greens function we obtain the LDOS

$$\rho(\mathbf{r}, \omega) = -\frac{1}{\pi}\text{Im}\left[G_{11}(\mathbf{r}, \omega) + G_{22}(\mathbf{r}, -\omega)\right], \tag{6.8}$$

which is proportional to the differential conductance measured in the STM experiments.

We have checked that the above approach reproduces the expected LDOS for unitary non-magnetic impurities in d-wave superconductors[85]. Also in this one-impurity case we reproduce the constant-energy LDOS maps recently calculated by Wang *et al.*[73][10]

Motivated by the qualitative agreement of the spin structure in figure 6.5a with the neutron data, we assume that this represents the induced magnetism around the vortices and calculate the LDOS in this striped environment. To this end we simply restrict the sum in Eqn. (6.4) to include the sites within these magnetic regions. The system is depicted in figure 6.5a where the grey background reveals the underlying superconducting state. Again the black (white) squares correspond to the sites affected by the staggered magnetic perturbation.

Figures 6.6 and 6.7 show real-space maps of the LDOS summed over a small energy window from -12 meV to +12 meV in intervals of 1meV for different strengths of the antiferromagnetic perturbation M. The vortex center is located in the center of the images. Fig. 6.6 (6.7) is calculated with (without) the antiphase modulation of the adjacent stripes. Thus, the spin configuration of figure 6.5a corresponds to the images in figure 6.6. The clear difference between the LDOS images of figures 6.6 and 6.7 reveals that the STM technique can be used to determine this phase relation. It is clearly seen from both figures 6.6 and 6.7 that the low energy LDOS structure eventually becomes ring-shaped as the magnitude of M increases. In this limit the pinned stripes operate as steep potential walls. Figures 6.6a and 6.6b seem to display the closest resemblance to the experimental data[189] which indicates that the induced magnetism is very weak. In figure 6.8 we show the Fourier transform of several constant energy LDOS images for $M = 100$ meV with the antiphase spin modulation included. In these figures the Fourier component $\mathbf{q} = \mathbf{0}$ is located at the center. The detailed energy dependence of these images is caused by quasi-particle interference effects as first pointed out by Wang *et al.*[73] in the case of a single impurity. The dispersive features of the images presented in figure 5 are dependent on the microscopic parameters and the associated Fermi surface. However, it is also evident that the ringshaped stripes surrounding the vortex cores give rise to non-dispersive intensity around $\mathbf{q} = \frac{2\pi}{a_0}(\pm 1/4, 0)$ and $\mathbf{q} = \frac{2\pi}{a_0}(0, \pm 1/4)$. This in turn leads to the checkerboard pattern in the low energy sums of the LDOS displayed in figures 6.6 and 6.7 whereas the dispersive features fade away in these summed LDOS images[190]. We have confirmed this fact by identifying similar non-dispersive features in the LDOS around configurations with different periodicity. For instance a structure with $2a_0$ charge periodicity leads to non-dispersive intensity around $\mathbf{q} = \frac{2\pi}{a_0}(\pm 1/2, 0)$ and $\mathbf{q} = \frac{2\pi}{a_0}(0, \pm 1/2)$. In the above calculation we have not yet included the

---

[10]Naturally the full agreement is only obtained when using the same quasi-particle energy $\xi_{\mathbf{p}}$ as Wang and Lee[73].
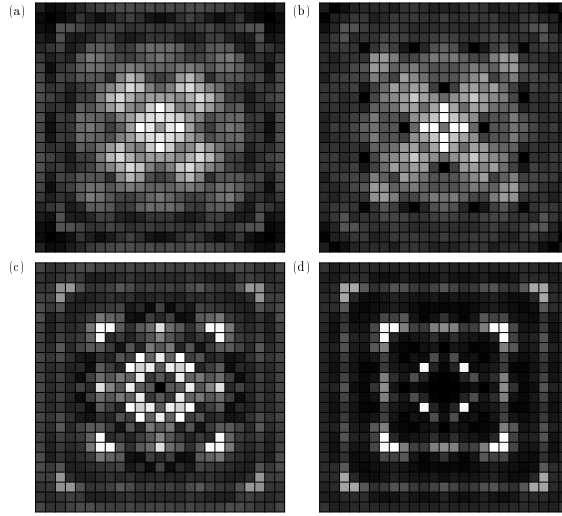
Figure 6.6: Real-space LDOS summed from -12 meV to +12 meV for: a) M = 35 meV, b) M = 100 meV, c) M = 200 meV, d) M = 300 meV.

Doppler shift from the circulating supercurrents or the gap suppression close to the vortex core. As pointed out by Polkovnikov *et al.*[94] the former effect is not expected to produce significant changes of the four-period modulations. As for the latter we have checked that a gap suppression only leads to minor quantitative changes in the dispersive part of the LDOS. Finally, Podolsky *et al.*[191] discussed scenarios of weak translational symmetry breaking and found that in order to explain quantitatively the *zero-field* STM results by Howald *et al.*[190] one needs to include dimerization, the modulation of the electron hopping. This dimerization will also produce quantitative changes, but not alter the qualitative conclusion that pinned stripes produce checkerboard LDOS.

In summary we have discussed the phenomenology of a simple physical picture of pinned stripes around vortex cores which are forced to be antiferromagnetic by an applied magnetic field. The induction of magnetic striped race-tracks around the core is consistent with the neutron diffraction spectra observed on LSCO with a doping level near x=0.10. As expected this is only true if the stripes are out of phase with their neighbors in the usual sense. In materials where a checkerboard spin pattern is relevant (possibly Bi2212 or overdoped LSCO), we show that a 45 degree rotation of the main incommensurable peaks is to be expected. Finally we studied the electronic structure around the vortices and identified a non-dispersive feature in the LDOS arising from the induced static antiferromagnetism. This feature gives rise to the checkerboard LDOS observed experimentally by Hoffman *et al.*[189] Thus both the STM measurements and the enhanced intensity of the incommensurable peaks observed by neutron diffraction can be ascribed to the phenomena of a single CuO_2 plane.
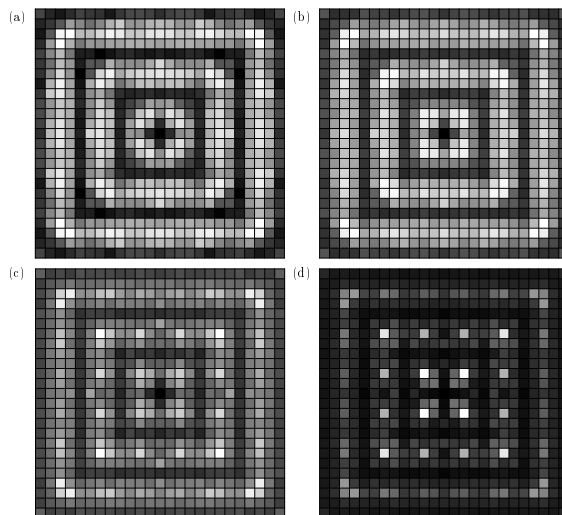
Figure 6.7: Real-space LDOS summed from -12 meV to +12 meV for: a) M = 35 meV, b) M = 100 meV, c) M = 200 meV, d) M = 300 meV.
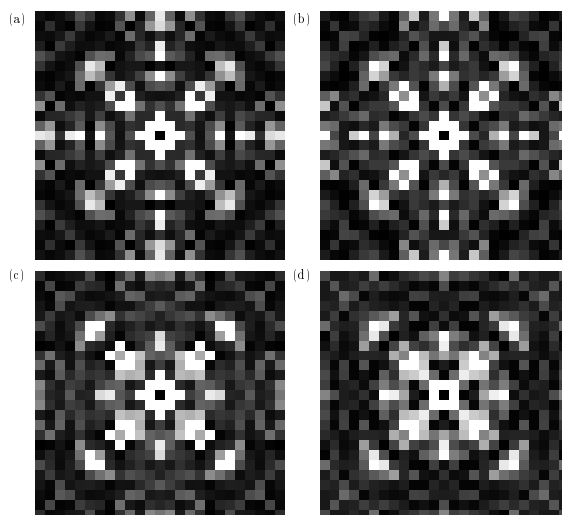

Figure 6.8: Fourier images of the constant energy LDOS maps for M = 100 meV and a) $\omega = 3$ meV, b) $\omega = 6$ meV, c) $\omega = 9$ meV, d) $\omega = 12$ meV.

7 Stripes and photoemission experiments

*Some of the material in this chapter has been published by the author and P. Hedegård in Solid State Communication **121/6-7**, 395 (2002), and Physica C **57**, 8127 (1998).*

7.1 The photoemission technique and a summary of important ARPES results

7.1.1 The technique of photoemission

In 1887 F. Hertz discovered that a spark between two electrodes occur more readily when the cathode is illuminated with ultraviolet light. Subsequently, Thomson and Lenard identified the the phenomenon as the emission of electrons. This effect is called the photoelectric effect. The independence of the energy distribution of the photoemitted electrons on the intensity of the incident light was explained by Einstein. The new picture was one where the light consists of discrete wave packets (photons) that individually impact the electrons and impart them with their full energy. This initiated the early parts of the quantum revolution.

Today, the technique of angular resolved photoemission spectroscopy (ARPES) is a powerful probe of the electronic structure in solid state materials. It has been improved considerably during the last decade and is currently capable of providing high momentum and energy resolved spectra. By its very nature the ARPES technique is surface sensitive.

In an typical ARPES experiment on a 2D material monochromatic light illuminates a sample and two quantities are measured: the emission angles of the photoelectron (θ, φ) and the its kinetic energy K. An electron is only emitted if the incident photon energy is greater then the so-called work function of the particular sample. If ϕ denotes this work function and $h\nu$ the incident photon energy we have

$$K \;=\; h\nu - \phi - E_b, \tag{7.1}$$

$$k_x \;=\; \sqrt{2mK/\hbar^2}\,\sin\theta\cos\varphi, \tag{7.2}$$

$$k_y \;=\; \sqrt{2mK/\hbar^2}\,\sin\theta\sin\varphi, \tag{7.3}$$

$$k_z \;=\; \sqrt{2mK/\hbar^2}\,\cos\theta, \tag{7.4}$$

where $\mathbf{k}$ denotes the momentum of the photoelectron. From these relations one can work backwards to determine the binding energy E_b and crystal momentum $\mathbf{q}$ of the electrons in the solid. For instance, momentum conservation parallel to the surface implies that in the extended zone scheme, $\mathbf{q}_\parallel = \mathbf{k}_\parallel$, since the momentum of the incoming photons are negligible at the typical photon energies used ($\propto 10 - 30$ eV). In general k_z is not simply related to the z component of the electron momentum in the solid due to momentum non-conservation perpendicular to the surface. The work function creates a potential perpendicular to the surface resulting in a surface force. For layered compounds, however, there is only negligible dispersion of the electrons in this direction, and the energy dependence on $\mathbf{q}$ can be mapped out.

With fixed incident photon energy and detector angles θ and φ, scanning the kinetic energy results in a so-called energy distribution curve (EDC) in which the photocurrent intensity is obtained as a function of binding energy. Tracing the intensity maximum as a function of angle allows one to map out the dispersion of the electrons in the solid. It is also possible to fix the energy and obtain the intensity as a function of angle (momentum) which results in a so-called momentum distribution curve (MDC).

But what really happens when the electron is emitted from the surface? In fact there exists no exact tractable theory of the photoemission process and the justifications for the approximations below really lies in the fact that the resulting equations manage to describe the measured data quite well. Usually one considers the emission process as a three step model (developed by Spicer in the early 1960s):

1. the optical excitation of the bulk electron.

2. the transport of the electron to the surface.

3. the transmission form the solid into the vacuum.

The resulting photoemission intensity I is then the product of the corresponding three probabilities. Usually the second step is assumed proportional to an effective mean free path which depends on the probability of an electron making it to the surface without any scattering events. If the electron scatters inelastically it may excite more electrons, generating what is known as secondary electrons. The final escape into the vacuum is simply taken to be either 0 or 1 depending upon whether or not the electron has enough energy to overcome the work function. Hence the first step, the optical excitation of the crystal electron contains all the interesting information about the electronic structure of the solid. For this excitation we employ Fermi's golden rule

$$I \propto \frac{2\pi}{\hbar} \sum_{i,f} |\langle \Psi_f^N | \mathcal{H}_{int} | \Psi_i^N \rangle|^2 \delta(E_f^N - E_i^N - h\nu), \qquad (7.5)$$

where Ψ_i^N, and Ψ_f^N denote the initial and final states of the N-particle system with energies $E_i^N = E_i^{N-1} + E_b$ and $E_f^N = E_f^{N-1} + K$, respectively. The final

state Ψ_f^N includes the photoelectron. The electron-photon interaction is given by, $\mathcal{H}_{int} = \frac{e}{2mc}(\mathbf{A} \cdot \mathbf{p} + \mathbf{p} \cdot \mathbf{A})$, $\mathbf{p}$ being the momentum operator and $\mathbf{A}$ is the electromagnetic vector potential. Within the sudden approximation it is assumed that the relaxation effects of the excited $N - 1$-particle system does not have time to occur before the electron leaves the solid. In other words the photoelectron does not interact with the remaining $N-1$-particle system. This approximation is only justified at high photon energies and is not obviously valid at the range of $10 - 30$eV typically used in the experiments mentioned below. However, within this approximation the final photoemission intensity can be written as

$$I(\mathbf{k}, \omega) \propto \sum_{i,f} |M_{i,f}(\mathbf{k})|^2 A(\mathbf{k}, \omega) f(\omega), \qquad (7.6)$$

where $M_{i,f}(\mathbf{k})$ is a momentum dependent matrix element which depends also on the polarization and frequency of the incident light. The energy of the electron compared to the Fermi level is denoted by ω. In Eqn. (7.6), $f(\omega) = (1 + \exp(\omega/kT))^{-1}$ denotes the Fermi distribution function and $A(\mathbf{k}, \omega)$ is the single particle spectral function indicating that the output intensity at $(\mathbf{k}, \omega)$ is proportional to the probability of an electron occupying a state in the solid with momentum $\mathbf{k}$ and energy ω. Since $A(\mathbf{k}, \omega) = -\frac{1}{\pi}\text{Im}\mathcal{G}(\mathbf{k}, \omega) = -\frac{1}{\pi}\text{Im}\left[\omega - \xi(\mathbf{k}) - \Sigma(\mathbf{k}, \omega)\right]^{-1}$, it is clear that the ARPES spectra provide information on the holy grail a.k.a. the self-energy $\Sigma(\mathbf{k}, \omega)$. In the sudden approximation the matrix element is usually assumed constant or slowly varying, i.e. $M_{i,f}(\mathbf{k}) = M$. This assumption can then be checked by measuring spectra in several Brillouin zones and by varying the incident photon polarization and frequency.

In this way an angular resolved photoemission experiment probes the occupied part of the single particle spectral function. Thus, for a Fermi liquid we expect the EDC's to trace out the broadened quasi-particle delta function at the band energies. Of course, in a strongly correlated material, one may worry that interactions between the excited electron and the photohole and the remaining $N - 1$-particle system cause modifications to the above expressions. For a further discussion of these issues the reader is referred to more extensive works such as Lynch and Olson and references therein[208].

In the following subsections I discuss some of the salient features of ARPES experiments on BSCCO and LSCO. Since there exists an enormous amount of photoemission data on these materials (particularly BSCCO) I restrict the discussion to features that are relevant for the following sections in this chapter.

The BSCCO materials have been extensively studied by ARPES owing to the nice and stable cleavage surfaces in ultrahigh vacuum[210, 211, 212, 213, 214]. But the doping range available is restricted to around optimal doping (there is recent progress in making very underdoped BSCCO samples, see K. Tanaka *et al.*[209]). On the other hand, the LSCO ARPES data has covered the full

doping range with reproducible data of the evolution of the Fermi surface, the pseudogap, and the band dispersion[215, 216, 217, 218]. Furthermore, the LSCO systems have a simple crystal structure with single CuO_2 planes and hence no complications from superstructure and bi-layer effects.

7.1.2 BSCCO

The BSCCO high-T_c material comes in a family of three different crystals with single- (Bi-2201) double- (Bi-2212) and triple-layer (Bi-2223) CuO_2 planes. The electronic structure of the double-layer compounds Bi-2212 is among the most extensively studied subjects in condensed matter physics. By ARPES the Fermi surface topology, the bi-layer splitting (for Bi-2212), the superconducting gap, and the pseudogap have been investigated in great detail. For recent reviews I refer to Damascelli *et al.*[219], and Campuzano *et al.*[220], and Norman and Pepin[221].

Let us restrict the discussion to the data obtained in the superconducting state. There the salient results are: 1) the opening of a d-wave pairing gap, and 2) the appearance of a sharp coherent peak near the $(\pi, 0)$ point around optimal doping. The latter feature is seen in Fig. 7.1: as the temperature is lowered the broad normal state spectrum develops into a peak-dip-hump structure. This
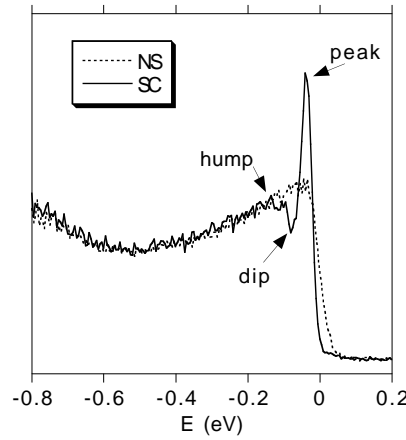

Figure 7.1: ARPES spectra at $(\pi, 0)$ for optimally doped BSCCO in the normal state (NS) and superconducting state (SC). From Norman *et al.*[238]

reveals a strong increase in the lifetime of the quasi-particles below T_c. The superconducting peak around $(\pi, 0)$ fades away when decreasing the doping[230]. The peak-dip-hump structure was first observed in tunnelling experiments[222], and was initially interpreted in terms of bilayer splitting with the hump (peak) caused by the bonding (anti-bonding) band.

Below, we show within the SO(5) model that the peak-dip-hump feature arises due to the coupling between the electrons and the magnetic pseudo-Goldstone mode existing in the superconducting state (see also Appendix .2). The energy

of this π-mode and the fact that it is commensurate in BSCCO, i.e. centered at (π, π), agrees well with the ARPES measurements. For instance, the quasi-particles connected by a (π, π) translation are centered around the antinodal points $(0, \pm\pi)$ and $(\pm\pi, 0)$, which is precisely the location where the dip feature is strongest.

7.1.3 LSCO

The low-temperature photoemission studies of $La_{2-x}Sr_xCuO_4$ was initiated by Ino *et al.*[215, 216, 217] who reported very different electronic structure from that in BSCCO: 1) the Fermi surface undergoes a change from hole-like and centered at (π, π) at optimal- and underdoping to electron-like and centered at $(0, 0)$ in the overdoped regime. 2) along the nodal direction $(0, 0) \rightarrow (\pi, \pi)$ the spectrum near $(\pi/2, \pi/2)$ is very broad compared to a sharp peak in BSCCO. 3) at the antinodal point $(\pi, 0)$ as the doping is increased, a broad high-energy feature in the EDC's slowly evolve into a peak near the Fermi level. The latter is notorious for its very flat dispersion when moving away from $(\pi, 0)$. This flat feature never crosses the Fermi level for $x < 0.2$ and moves to higher binding energies with decreasing doping concentration. There is no experimental evidence for a peak-dip-hump EDC lineshape as seen in BSCCO.

It was proposed by Ino *et al.*[215, 216, 217] that the stripe picture may explain the ARPES data. For instance, along the antinodal direction the high-energy feature should result from the antiferromagnetic ordered regions (exhibiting a Mott gap) and the emerging low-energy peak results from the mid-gap states arising from the charged stripes. Below, I show in more detail what is the importance of the mid-gap induced states in the spectral weight of stripe ordered systems.

In order to obtain a better understanding of the influence of stripe ordering tendency on the electronic structure, Zhou *et al.*[223, 224] studied the neodymium doped compound $La_{2-x-y}Nd_ySr_xCuO_4$ where static stripes are known to thrive. Fig. 7.2a shows the spectral weight obtained by integrating the spectral function $A(\mathbf{k}, \omega)$ over an energy window $\Delta\omega$ below the Fermi level, $I(\mathbf{k}) = \int_{\Delta\omega} d\omega A(\mathbf{k}, \omega)$. In Fig. 7.2, $\Delta\omega = 30$meV. Clearly, at this doping level, the spectral weight is dominated by intensity at the antinodal regions as expected from the low-energy flat band located near these points. Note from Fig. 7.2b the *strong similarity* between the $La_{2-x-y}Nd_ySr_xCuO_4$ and the $La_{2-x}Sr_xCuO_4$ spectra. This is strong evidence for *a common origin of the electronic structure* which, in turn, is known to be stripe ordered in $La_{2-x-y}Nd_ySr_xCuO_4$.

When the integration window is increased, the spectral weight moves toward the first Brillouin zone center Γ, i.e. the momentum distribution function, $n(\mathbf{k}) = \int_{-\infty}^{\infty} d\omega A(\mathbf{k}, \omega)$, consists of straight line segments bounded inside $|k_x| < \pi/4$ and $|k_y| < \pi/4$. This suggests two Fermi surfaces defined by $|k_x| = \pi/4$ and $|k_y| = \pi/4$ which agrees with 1D stripe domains oriented along
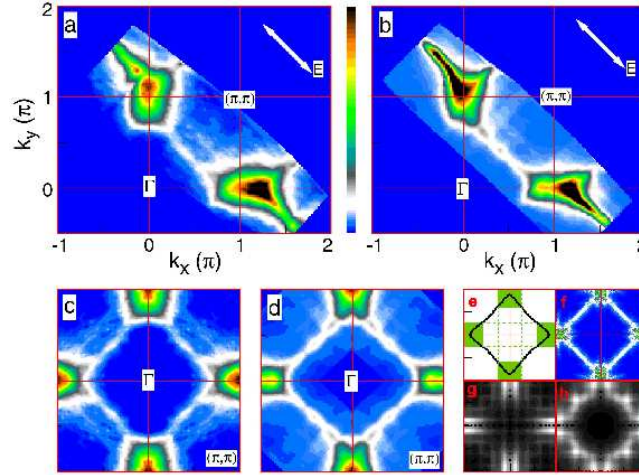
Figure 7.2: Spectral weight obtained by integrating the ARPES spectra over 30meV below the Fermi level for: a) $La_{2-x-y}Nd_ySr_xCuO_4$ ($y = 0.6, x = 0.15$) and b) $La_{2-x}Sr_xCuO_4$ ($x = 0.15$)[224]. c-d) show the corresponding symmetrized weight within the first Brillouin zone. e-f) shows the results of Ref. [225].

the y- and x-axis, respectively. The particular value of $\pi/4$ corresponds to quarter filling of the charge stripe domains since from neutron scattering we know that the charge periodicity is close to $4a$. Furthermore, within the stripe picture, it follows that no quasi-particle peak corresponding to a Fermi surface crossing should emerge at the nodal point $(\pi/2, \pi/2)$.

As seen from Fig. 7.2, however, the antinodal regions are connected by a ghosty white segment which is evidence for nodal weight not expected within a perfectly aligned array of stripes. Due to matrix element effects this nodal weight appears much stronger in the second Brillouin zone[226]. Below, it will be shown that stripe disorder naturally induce weak nodal weight. Finally note from Fig. 7.2c-d that the overall spectral weight is remarkably similar to what one would expect from a simple hole-doped tight-binding band, even though this originates from a completely different homogeneous model.

7.2 SO(5) theory and the peak-dip-hump feature

In this section we consider the effects of a strong electronic coupling to a collective mode within the SO(5) theory for high-T_c superconductors. When applied to the superconducting state the resulting spectral function is shown to have a peak-dip-hump structure due to renormalization effects. The magnitude of the renormalization depends on the strength of the SO(5) coupling parameter. Our model is phenomenological and allows only a qualitative description but the approach shows how the mode coupling arises in the SO(5) theory due to fluctuations allowed by the higher symmetry group.

During the last decade of intense study of the high-T_c superconductors (HTSC) many of the spectacular experimental discoveries have come from high resolution inelastic neutron scattering (INS) and angular resolved photoemission spectroscopy (ARPES). In principle these techniques measure the spin susceptibility and the spectral function, respectively, and can therefore reveal many-body effects in the electronic self-energy. In particular, the sharp neutron scattering resonance (the π-mode) observed in the superconducting state of the bi-layer cuprates YBCO [227] and Bi2212 [228] at the (π, π) point of the Brillouin zone (BZ) has ignited a large amount of both theoretical and experimental activity. On the ARPES side, important contributions include the discovery of the superconducting gap structure, existence and d-wave structure of the pseudogap state and determination of the Fermi Surface (FS)[229]. However, within the last few years the improved momentum and energy resolution of the photoemission data have created a fascinating bridge to other experimental techniques and put severe constraints on microscopic models[13, 230]. A good example of this development is the (ARPES) discovery of the so-called peak-dip-hump structure of the energy distribution curve (EDC) for $T < T_c$ and its possible relation to the dispersion kink in the superconducting state[231, 232, 233]. This feature was initially observed in underdoped Bi2212 near the M=$(\pi, 0)$ point of the BZ but has recently also been seen in the superconducting state of YBCO[234]; exactly the materials where the π-mode is known to exist at $T < T_c$.

As pointed out by Shen and Schrieffer the origin of the peak-dip-hump feature has a natural explanation in terms of a strong coupling of the photohole to a collective mode with a higher energy[235]. The energy scale of the feature and its doping, temperature and momentum dependence led several groups to the conclusion that the relevant mode was in fact the π-mode already seen by INS[236, 237, 238, 239].

One approach to the problem is to use a phenomenological model based on the spin susceptibility $\chi(\mathbf{q}, \omega)$ extracted from the INS data. The electronic self-energy and the resulting spectral function $A(\mathbf{q}, \omega)$ can then be shown to fit nicely with the energy distribution curves measured by ARPES[240].

In this section we also perform a phenomenological calculation, but importantly for a strongly correlated system, our starting point is completely different since we assume an approximate SO(5) symmetry in the underdoped regime. We do not enter the discussion of the fundamental applicability of the SO(5) model and restrain our discussion to the superconducting state where well-defined quasi-particles are known to exist along the ostensible Fermi surface[12]. However, it is interesting that the SO(5) prediction of antiferromagnetic vortex cores recently have been observed in neutron scattering experiments by Lake *et. al.*[196, 241]. In the light of these developments we find it interesting to investigate the ARPES data within the SO(5) model. Note, however, that since ARPES is a surface sensitive probe one should be very careful in comparing calculated spectral functions with the experimental data. An example of a further precaution is the recent observation by Pan *et. al.*[242]

that cleaved surfaces of BSCCO 2212 can be inhomogeneous in the sense that several terraces of atomic planes are revealed upon cleavage.

However, below we assume that ideal ARPES experiments can be performed and address the peak-dip-hump issue in a qualitative calculation starting from a fully SO(5) symmetric Hamiltonian. In the superconducting state, we show how the spontaneous breaking of the higher symmetry naturally leads to a coupling with a mode which in the SO(5) model is a spin triplet particle-particle mode centered at $\mathbf{Q} = (\pi, \pi)$[243]. In a typical strong coupling approach we continue by deriving a set of SO(5) generalized Eliashberg equations. A simple solution of these equations allows us to determine the resulting spectral function which exhibits a clear peak-dip-hump structure.

7.2.1   Model

Originally the SO(5) model was proposed as a superspin non-linear sigma model with emphasis on the phase diagram and the collective (bosonic) modes of the system[182]. For more details about the foundation of the SO(5) model I refer to Appendix .2. The extension to the fermionic sector of the SO(5) model has been clarified by work of Rabello *et al.*[244], Henley[245], and Eder *et al.*[246]. Besides providing the foundation for studying the Fermi sector it was shown that the well known electronic spectrum of the antiferromagnetic (AF) and the *d*-wave superconducting (dSC) phases can be incorporated into a SO(5) scheme.

As utilized earlier[51, 244] a SO(5) symmetric microscopic Hamiltonian can be written as

$$\mathcal{H} \;=\; \mathcal{H}_0 + \mathcal{H}_{\text{int}} = \frac{1}{2} \sum_{\mathbf{p}} \epsilon_{\mathbf{p}} \Psi_{\mathbf{p}}^{\dagger} \Psi_{\mathbf{p}} \tag{7.7}$$

$$- \; V \sum_{\mathbf{p}, \mathbf{p}', a} (w_{\mathbf{p}} \Psi_{\mathbf{p}}^{\dagger} \Gamma^a \Psi_{\mathbf{p}+\mathbf{Q}})(w_{\mathbf{p}'} \Psi_{\mathbf{p}'}^{\dagger} \Gamma^a \Psi_{\mathbf{p}'-\mathbf{Q}}),$$

with $\epsilon_{\mathbf{p}} = -t(\cos p_x + \cos p_y)$ and $w_{\mathbf{p}} = |\cos p_x - \cos p_y|$ (lattice constant equal to unity). The four component spinor $\Psi_{\mathbf{p}}$ is given by

$$\Psi_{\mathbf{p}} = \{c_{\mathbf{p}\uparrow}, c_{\mathbf{p}\downarrow}, \phi_{\mathbf{p}} c_{-\mathbf{p}+\mathbf{Q}\uparrow}^{\dagger}, \phi_{\mathbf{p}} c_{-\mathbf{p}+\mathbf{Q}\downarrow}^{\dagger}\}. \tag{7.8}$$

and V is our new single "grand unified" coupling parameter. The interaction term $\mathcal{H}_{\text{int}}$ is a scalar product of two SO(5) vectors and hence manifestly SO(5) invariant. The five 4×4 Dirac Γ^a-matrices are given in terms of tensor products of the standard 2×2 Pauli matrices: $\Gamma^1 = \sigma_2 \otimes \sigma_2$, $\Gamma^2 = \mathbf{I} \otimes \sigma_1$, $\Gamma^3 = \sigma_3 \otimes \sigma_2$, $\Gamma^4 = \mathbf{I} \otimes \sigma_3$, and $\Gamma^5 = \sigma_1 \otimes \sigma_2$ (see Ref. [244] and Appendix .2 for details).

These definitions constitute a spinor representation of a closed SO(5) Lie alge-

bra when $\phi_{\mathbf{p}} = \text{sign}(\cos p_x - \cos p_y)$[245]. In this representation the symmetry generators become $L_{ab} = \frac{1}{8}\sum_{\mathbf{p}} \Psi_{\mathbf{p}}^{\dagger}\Gamma^{ab}\Psi_{\mathbf{p}}$ with $\Gamma^{ab} = -i\left[\Gamma^a, \Gamma^b\right]$, while the components of the SO(5) order parameter n^a (the superspin) can be written as $n^a = \frac{1}{4}\sum w_{\mathbf{p}}\Psi_{\mathbf{p}}^{\dagger}\Gamma^a\Psi_{\mathbf{p}+\mathbf{Q}}$. Though written in a very compact form, n^a is nothing but a five vector composed of the real and imaginary part of the superconducting order parameter (a=1,5) and the antiferromagnetic order parameter (a=2,3,4). In the superconducting state where the superspin is confined to the 1-5 hyperplane it is easy to show that the mean field form of $\mathcal{H}_{\text{int}}$ reduces to a $d_{x^2-y^2}$-wave BCS superconductor which is known to provide a good description of the dSC state of the high-T_c cuprates[11].

Since we want to explain a phenomenon in the dSC state, we start from a mean field level and introduce the fields $\Delta_{\mathbf{p}}^a = -16V w_{\mathbf{p}}\sum_{\mathbf{p}'} w_{\mathbf{p}'}\langle n_{\mathbf{p}'}^a\rangle$ allowing us to write the Hamiltonian $\mathcal{H}$ as[247]

$$\mathcal{H}_0' = \sum_{\mathbf{p},\mathbf{p}'} \Psi_{\mathbf{p}}^{\dagger} \left(\frac{1}{2}\epsilon_{\mathbf{p}}\delta_{\mathbf{p},\mathbf{p}'} + \sum_a \Delta_{\mathbf{p}}^a\Gamma^a\delta_{\mathbf{p},\mathbf{p}'+\mathbf{Q}}\right)\Psi_{\mathbf{p}'}, \qquad (7.9)$$

In agreement with Ref. [244] this leads to the Green's function[12]

$$G_0(\mathbf{p},\mathbf{p}';ip_n) = \frac{(ip_n + \epsilon_{\mathbf{p}})\delta_{\mathbf{p},\mathbf{p}'} + \sum_a \Delta_{\mathbf{p}}^a\Gamma^a\delta_{\mathbf{p},\mathbf{p}'+\mathbf{Q}}}{(ip_n)^2 - \epsilon_{\mathbf{p}}^2 - (\Delta_{\mathbf{p}}^a)^2}, \qquad (7.10)$$

where p_n is a fermion Matsubara frequency. In the superconducting state the gap function $\Delta_{\mathbf{p}}^{\text{SC}} \equiv \Delta_0\phi_{\mathbf{p}}w_{\mathbf{p}} = \Delta_0(\cos p_x - \cos p_y)$ is determined self-consistently by the gap equation $1 = 16V\sum_{\mathbf{p}} \frac{w_{\mathbf{p}}^2}{2E_{\mathbf{p}}}$ with $E_{\mathbf{p}}^2 = \epsilon_{\mathbf{p}}^2 + (\Delta_{\mathbf{p}}^{\text{SC}})^2$.

Now, lacking a Migdal theorem to guarantee convergence we continue by simply assuming that the coupling parameter V is sufficiently small that a perturbation approach converge. Below, the numerical solution will prove that indeed the qualitative form of the spectra is stable with respect to variations of the coupling parameter V. Thus, following a usual strong coupling approach we make an Ansatz for the general form of the self-energy[247]

$$\Sigma(\mathbf{p},\mathbf{p}';ip_n) = (1 - Z(\mathbf{p},ip_n))\,ip_n\delta_{\mathbf{p},\mathbf{p}'} + \sum_a \Delta_{\mathbf{p}}^a\Gamma^a\delta_{\mathbf{p},\mathbf{p}'+\mathbf{Q}}. \qquad (7.11)$$

Inverting the Dyson equation $G^{-1} = G_0^{-1} - \Sigma$ gives

$$G(\mathbf{p},\mathbf{p}';ip_n) = \frac{(Zip_n + \epsilon_{\mathbf{p}})\delta_{\mathbf{p},\mathbf{p}'} + \sum_a \Delta_{\mathbf{p}}^a\Gamma^a\delta_{\mathbf{p},\mathbf{p}'+\mathbf{Q}}}{(Zip_n)^2 - \epsilon_{\mathbf{p}}^2 - (\Delta_{\mathbf{p}}^a)^2}. \qquad (7.12)$$

---

[11]In the antiferromagnetic state it is shown in [244] how the introduction of an anisotropy term between the magnetic and superconducting sectors removes the d-wave gap nodes in the single-particle excitation spectrum.

[12]The delta functions are kept explicit in this equation to refer to different blocks of the matrix.

We now consider the superconducting state where the SO(5) symmetry allows antiferromagnetic oscillations "out of the valley of the Mexican hat" potential, i.e.

$$\Delta^{\text{sc}} \rightarrow \Delta^{\text{sc}} + \delta\Delta^{\text{af}}. \tag{7.13}$$

This introduces an effective interaction between the quasi-particles in the superconducting state of the form

$$\mathcal{H}'_{int} = V \sum_{\mathbf{pq}} \left(\delta\Delta^{\text{af}}_{\mathbf{q}} \right) \Psi^{\dagger}_{\mathbf{p-q}} \Gamma^{\text{sc}} \Psi_{\mathbf{p+Q}}. \tag{7.14}$$

A conventional second order expansion gives the matrix equation

$$\Sigma(\mathbf{p}, ip_n) = -\frac{V^2}{\beta} \sum_{\mathbf{q}, i\omega_n} \Gamma^{\text{sc}} G_0(\mathbf{p-q}, ip_n - i\omega_n) \Gamma^{\text{sc}} N^{\text{af}}(\mathbf{q}, i\omega_n), \tag{7.15}$$

where we introduced the mode propagator $N^{\text{af}}(\mathbf{q}, \tau) \equiv -\langle T_\tau \{ \delta\Delta^{\text{af}}(\tau)\delta\Delta^{\text{af}}(0)\} \rangle$ and ω_n is a boson Matsubara frequency. Inserting the explicit expression for the Green's function from equation (7.12) into equation (7.15) and comparing to the Ansatz for the self-energy we obtain the following SO(5) generalized equation for the renormalization function $Z(\mathbf{p}, ip_n)$

$$(1 - Z(\mathbf{p}, ip_n))\, ip_n =$$

$$-\frac{V^2}{\beta} \sum_{\mathbf{q}, i\omega_n} \frac{[Z(\mathbf{p-q}, ip_n - i\omega_n)(ip_n - i\omega_n)]\, N^{\text{af}}(\mathbf{q}, i\omega_n)}{(Z(ip_n - i\omega_n))^2 - \epsilon^2_{\mathbf{p-q}} - (\Delta^{\text{sc}}_{\mathbf{p-q}})^2}. \tag{7.16}$$

This expression is a central result of this paper and shows how the antiferromagnetic mode coupling arises naturally within the SO(5) model.

In the following we apply equation (7.16) to show how the dip feature of the ARPES data can arise due to coupling to the π-mode seen in neutron scattering experiments. The analog of the "conventional" superconducting gap $\Delta \rightarrow Z\Delta$ depends in general on both the momentum and frequency. However, in the following we assume that the gap is frequency independent and, for simplicity, we consider only scattering of quasi-particles connected by the antiferromagnetic ordering vector $\mathbf{Q} = (\pi, \pi)$ which is the center of mass momentum for the SO(5) π-mode. These are exactly the hot-spot regions centered around $M = (\pi, 0)$ and symmetry related points of the BZ. Furthermore, these are the points where the d-wave gap attains its maximum value. Thus, in a phenomenological calculation a simple but sufficient form for the mode $N^{\text{af}}(\mathbf{q}, i\omega_n)$ is

$$N^{\text{af}}(\mathbf{q}, i\omega_n) = \delta(\mathbf{q} - \mathbf{Q}) \left(\frac{1}{i\omega_n - \omega_0} - \frac{1}{i\omega_n + \omega_0} \right) \tag{7.17}$$

where ω_0 is the characteristic energy of the resonance mode and damping effects are assumed minimal in agreement with the very sharp resonance seen experi-

mentally. Within the SO(5) model the chemical potential *explicitly* breaks the SO(5) symmetry and renders the fluctuations perpendicular to the (equatorial) superconducting plane massive, hence $\omega_0 \neq 0$[243].

7.2.2 Results

A first order solution to equation (7.16) is obtained by setting $Z = 1$ on the right hand side and then perform the Matsubara sum to obtain the simple result

$$Z(ip_n) = 1 - \frac{V^2}{2}\left(\frac{1}{(ip_n)^2 - (\omega_0 + E_M)^2}\right) \tag{7.18}$$

in the zero temperature limit. In equation (7.18), $E_M^2 = \xi_M^2 + \Delta_M^{\mathrm{SC}\,2}$ and $\xi_M = \epsilon_M - \mu$ with $M = (\pi, 0)$.

In Fig. 7.3 we plot the real end imaginary part of the renormalization $Z(\omega)$ as a function of energy ω in the case where $\Delta_M = 35$meV, $\omega_0 = 41$meV, $V = 30$meV, $\xi_M = -34$meV and $ip_n \to \omega + i\Gamma$ with $\Gamma = 8$meV as an intrinsic lifetime broadening. The value $\xi_M = -34$meV turns out to be appropriate
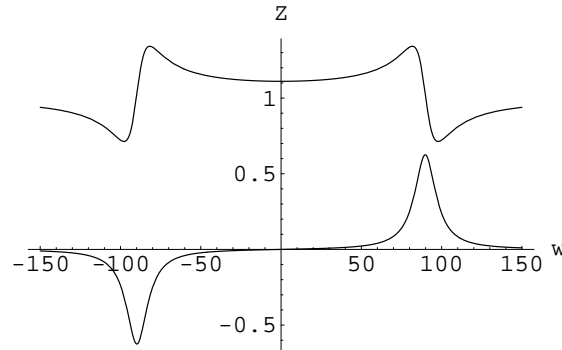

Figure 7.3: Real part of the renormalization $Z(\omega)$ (upper graph) and imaginary part of $Z(\omega)$ (lower graph) as a function of binding energy ω (arbitrary units).

for the flat band at the $M = (\pi, 0)$ point[248]. The qualitative form of the renormalization function $Z(\omega)$ does not change upon iteration of equation (7.16).

In the quasi-2D cuprates the ARPES intensity $I(\mathbf{p}, \omega)$ is believed to be well approximated by $I(\mathbf{p}, \omega) = I(\mathbf{p})f(\omega)A(\mathbf{p}, \omega)$ convolved with the instrumental resolution[249]. In this expression, $I(\mathbf{p})$ is the dipole transition matrix element between initial and final states, $f(\omega)$ is the Fermi function, and $A(\mathbf{p}, \omega)$ is the spectral function. Therefore, assuming constant matrix elements the ARPES spectra essentially map out the spectral function. Though we follow these assumptions below, they are far from obvious and we refer to the literature for

further discussion[249, 250, 251].

As shown in Fig. 7.4 the resulting spectral function

$$A(\mathbf{p}, \omega) = -\frac{1}{\pi} \text{Im} G_{11}(\mathbf{p}, \omega) \tag{7.19}$$

exhibits a dip feature. This can be brought to a form qualitatively similar to the experimental findings (when convolved with a background and a Fermi cut-off function); a quasi-particle peak followed by a dip and a hump. Thus within this model the dip feature is caused by quasi-particles coupled with the π-mode. The distribution of spectral weight and the energetic separation between the peak and the hump is determined by the strength of the SO(5) coupling parameter V. Unfortunately the model presented here is too simple to lead to any quantitative comparisons or predictions. Even a fully self-consistent solution to equation (7.16) would not lead to quantitative results due to the phenomenological nature of the underlying model (7.7) and the uncertainty in the interpretation of the ARPES data.
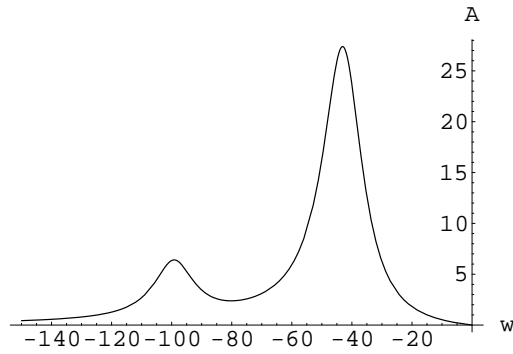

Figure 7.4: Spectral function $A(\mathbf{p}, \omega)$ as a function of energy ω (arbitrary units) in the superconducting state near the $M = (\pi, 0)$ point of the BZ. The mode coupling bound at higher energy suppresses the spectral weight and results in a dip. As seen, the overall feature resembles the peak/dip/hump structure.

7.2.3   Summary and Discussion

We have performed a strong coupling calculation starting from a microscopic SO(5) symmetric Hamiltonian. The symmetry is broken on the mean field level and explicitly by a chemical potential. After deriving a simple expression for the renormalization function $Z(\mathbf{p}, \omega)$ we apply this to show that the resulting spectral function clearly exhibits a dip feature in the superconducting state in qualitative agreement with experiments.

In the historical sense a crucial observation of the conventional strong coupling superconductors such as lead, was the nice fit of the effective tunnelling density

of states (DOS) by Schrieffer *et al.*[252] to the measurements by Rowell *et al.*[253]. In that case, the anomalous features of the DOS is determined by the energy scales (emission threshold) of the phonons. It is intriguing that in the high-T_c superconductors a new characteristic energy scale could be revealed by the peak/dip/hump feature in the energy distribution curves from ARPES. However, if the collective π-mode turns out to be the relevant mode to explain these features it is clear from the above discussion that the origin is completely different. Furthermore, as opposed to the conventional strong coupling case, we have shown that the renormalization function $Z(\omega)$, and not a frequency dependent gap function $\Delta(\omega)$, may be the cause of the feature.

7.3 Photoemission and DOS in a striped system

I now return to the discussion of the electronic structure resulting from stripe ordered domains. In particular, it will be shown that the salient features of the APRES measurements on LSCO and Nd-LSCO can be understood within this picture. Furthermore, some recent results from STM measurements will be shown to find a natural explanation within the stripe phase. Essentially all the peculiar features can be described in terms of doping into new mid-gap states caused by the anti-phase stripe spin configuration[158, 225, 254].

7.3.1 Model

The starting point for discussing the electronic structure in the presence of both antiferromagnetic ordering tendency and d-wave superconductivity is given by the familiar minimal model Hamiltonian introduced in chapter 1 defined on a 2D lattice

$$
\mathcal{H} = -\sum_{\langle i,j \rangle \sigma} t_{ij} \hat{c}_{i\sigma}^\dagger \hat{c}_{j\sigma} + \text{H.c.} - \mu \sum_{i\sigma} \hat{c}_{i\sigma}^\dagger \hat{c}_{i\sigma} \tag{7.20}
$$

$$
+ \ U \sum_i [\langle \hat{n}_{i\downarrow} \rangle \hat{n}_{i\uparrow} + \langle \hat{n}_{i\uparrow} \rangle \hat{n}_{i\downarrow}] + \sum_{\langle i,j \rangle} \left(\Delta_{ij} \hat{c}_{i\uparrow}^\dagger \hat{c}_{j\downarrow}^\dagger + \text{H.c.} \right).
$$

As usual, $\hat{c}_{n\sigma}^\dagger$ creates an electron with spin σ at site n (at $\mathbf{r}_n$) and μ is the chemical potential. The strength of the antiferromagnetic and superconducting coupling is given by U and V, respectively. We include nearest t and a number of next nearest neighbors, i.e. $t_{\langle nm \rangle} = -t$, $t_{\langle\langle nm \rangle\rangle} = -t'$, and $t_{\langle\langle\langle nm \rangle\rangle\rangle} = -t''$. The Hamiltonian (7.20) can be diagonalized by introducing the $\hat{\gamma}$ operators through the Bogoliubov-de Gennes transformation

$$
\hat{c}_{i\sigma}^\dagger = \frac{1}{\sqrt{N}} \sum_{n\mathbf{k}} \left(\hat{\gamma}_{n\mathbf{k}\sigma}^\dagger u_{n\mathbf{k}\sigma}^*(\mathbf{r}_i) + \sigma \hat{\gamma}_{n\mathbf{k}\overline{\sigma}} v_{n\mathbf{k}\overline{\sigma}}(\mathbf{r}_i) \right), \tag{7.21}
$$

and demanding that

$$\mathcal{H} = \sum_{n\mathbf{k}\sigma} E_{n\mathbf{k}\sigma} \hat{\gamma}^\dagger_{n\mathbf{k}\sigma} \hat{\gamma}_{n\mathbf{k}\sigma}. \tag{7.22}$$

Note that the transformation involves both momentum and real-space indices. This is because we Fourier transform with a basis, the basis constituting a supercell of $N_x \times N_y$ sites. The Bloch vectors $\mathbf{k}$ belong to the corresponding reduced Brillouin zone. Therefore, for the coherence factors we have $u^*_{n\mathbf{k}\sigma}(\mathbf{r}_i) = u^*_{n\mathbf{k}\sigma}(\mathbf{R}_i + i) = u^*_{n\mathbf{k}\sigma}(i) \exp(-i\mathbf{k} \cdot \mathbf{R}_i)$.

Specifically, one can obtain the Bogoliubov-de Gennes equations by comparing, on the one hand, the commutator

$$\left[\mathcal{H}, \hat{c}^\dagger_{i\sigma} \right] = \sum_{n\mathbf{k}} \left(E_{n\mathbf{k}\sigma} u^*_{n\mathbf{k}\sigma}(\mathbf{r}_i) \hat{\gamma}^\dagger_{n\mathbf{k}\sigma} - \sigma E_{n\mathbf{k}\overline{\sigma}} v_{n\mathbf{k}\overline{\sigma}}(\mathbf{r}_i) \hat{\gamma}_{n\mathbf{k}\overline{\sigma}} \right) \tag{7.23}$$

to the one obtained by explicitly "commuting through" in Eqn. (7.20)

$$\left[\mathcal{H}, \hat{c}^\dagger_{i\sigma} \right] = - \sum_{\langle i,j \rangle} t_{ij} \hat{c}^\dagger_{j\sigma} + \left(U\langle \hat{n}_{i\overline{\sigma}} \rangle - \mu \right) \hat{c}^\dagger_{i\sigma} + \sigma \sum_{\langle i,j \rangle} \Delta_{ij} \hat{c}_{j\overline{\sigma}}. \tag{7.24}$$

This leads to a set of equations for the coefficients, $u_{n\mathbf{k}\sigma}(i)$ and $v_{n\mathbf{k}\sigma}(i)$ which we may solve by standard diagonalization procedures.

The required hole doping n_h and the self-consistency of the fields $\langle \hat{n}_{i\sigma} \rangle$ and Δ_{ij} are ensured by adjusting the chemical potential μ and running the iteration until all the following relations become stable

$$\frac{1}{N} \sum_{i\sigma} \langle \hat{n}_{i\sigma} \rangle = 1 - n_h, \tag{7.25}$$

$$\langle \hat{n}_{i\sigma} \rangle = \langle \hat{c}^\dagger_{i\sigma} \hat{c}_{i\sigma} \rangle = \sum_{n\mathbf{k}} \left[|u_{n\mathbf{k}\sigma}(i)|^2 f(E_{n\mathbf{k}\sigma}) + |v_{n\mathbf{k}\overline{\sigma}}(i)|^2 f(-E_{n\mathbf{k}\overline{\sigma}}) \right] \tag{7.26}$$

$$\begin{aligned} \Delta_{ij} &= V \langle \hat{c}_{i\uparrow} \hat{c}_{j\downarrow} - \hat{c}_{i\downarrow} \hat{c}_{j\uparrow} \rangle \tag{7.27}\\[6pt] &= V \sum_{n\mathbf{k}\sigma} \left[v^*_{n\mathbf{k}\sigma}(i) u_{n\mathbf{k}\sigma}(j) f(E_{n\mathbf{k}\sigma}) - u_{n\mathbf{k}\sigma}(i) v^*_{n\mathbf{k}\sigma}(j) f(-E_{n\mathbf{k}\sigma}) \right]. \end{aligned}$$

It is common to define the d-wave order parameter on-site by

$$\Delta_i = \left(\Delta_{i+e_x} + \Delta_{i-e_x} - \Delta_{i+e_y} - \Delta_{i-e_y} \right)/4. \tag{7.28}$$

The final eigenstates ($u_{n\mathbf{k}\sigma}(i)$ and $v_{n\mathbf{k}\sigma}(i)$) and the associated eigenvalues $E_{n\mathbf{k}\sigma}$ allow us to calculate e.g. the single-particle spectral function and the local density of states (LDOS).

For the single-particle Greens function, $\mathcal{G}_\sigma(\mathbf{r}_i, \mathbf{r}_j, \tau) = -\langle T_\tau \hat{c}_\sigma(\mathbf{r}_i, \tau) \hat{c}^\dagger_\sigma(\mathbf{r}_j, 0) \rangle$,

it is easy to obtain for $\mathcal{G}_\sigma(\mathbf{r}_i, \mathbf{r}_j, ip_n) = \int_0^\beta d\tau \mathcal{G}_\sigma(\mathbf{r}_i, \mathbf{r}_j, \tau) \exp(ip_n\tau)$,

$$
\mathcal{G}_\sigma(\mathbf{r}_i, \mathbf{r}_j, ip_n) = \sum_{n\mathbf{k}} \frac{u_{n\mathbf{k}\sigma}(i)u_{n\mathbf{k}\sigma}^*(j)}{ip_n - E_{n\mathbf{k}\sigma}} e^{i\mathbf{k}\cdot(\mathbf{R}_i - \mathbf{R}_j)} \tag{7.29}
$$

$$
+ \sum_{n\mathbf{k}} \frac{v_{n\mathbf{k}\bar\sigma}^*(i)v_{n\mathbf{k}\bar\sigma}(j)}{ip_n + E_{n\mathbf{k}\bar\sigma}} e^{-i\mathbf{k}\cdot(\mathbf{R}_i - \mathbf{R}_j)},
$$

where p_n is a Fermi Matsubara frequency and $\mathbf{R}_i$ denotes the supercell in which site i resides.

Typical self-consistent solutions in different parameter regimes and the associated bandstructure, density of states and spectral function are discussed in the following sections.

7.3.2 Density of states and gap structure in the stripe phase

We may use expression (7.29) to study the local density of states on site i, $N_\sigma(i, \omega)$, given by

$$
N_\sigma(i, \omega) = -\frac{1}{\pi}\text{Im} \sum_{n\mathbf{k}} \left[\frac{|u_{n\mathbf{k}\sigma}(i)|^2}{\omega - E_{n\mathbf{k}\sigma} + i\Gamma} + \frac{|v_{n\mathbf{k}\bar\sigma}(i)|^2}{\omega + E_{n\mathbf{k}\bar\sigma} + i\Gamma} \right]. \tag{7.30}
$$

In the following I show the self-consistent results of the spin- and charge density and the superconducting pairing potential in various regimes of doping and U/V and show the effect of t'.

First of all, in the half-filled $n_h = 0.0$ antiferromagnetic case we obtain for $V = 0$, $U = 4.0t$ the staggered spin order and the bands shown to the left in Fig. 7.5. The bands shown here are for spin up, but these are degenerate with the spin down bands. This is also true for the incommensurate spin structures shown below. The chemical potential is situated in the middle of the gap and the state is an insulator. We study the 8×2 unit cell which results in 16 bands in the reduced zone. The bands are plotted as a function of k_y in the range $-\pi/2 < k_y < \pi/2$ and with $k_x = 0.0$, i.e. straight through the center of the reduced Brillouin zone. The bands have been shifted so that the chemical potential corresponds to zero on the vertical axis. The LDOS is seen to the right in Fig. 7.5. All the LDOS plots presented in this section are the sum of the spin-up and spin-down LDOS, i.e. $N(i, \omega) = \sum_\sigma N_\sigma(i, \omega)$.

Let us turn now to the stripe phase away from half-filling. For $n_h = 0.250$, $t' = 0$ and $U = 5.0t$ we obtain a stable stripe configuration with a spin periodicity of eight lattice constants. In Fig. 7.6 I show this self-consistent solution and the associated the bands and density of states. This state is also an insulator since the Fermi level is positioned in the gap as seen from the graphs of the band dispersion and the DOS. The DOS shown to the right in Fig. 7.6 is the spatial average of the LDOS on the stripe and off the stripe. These
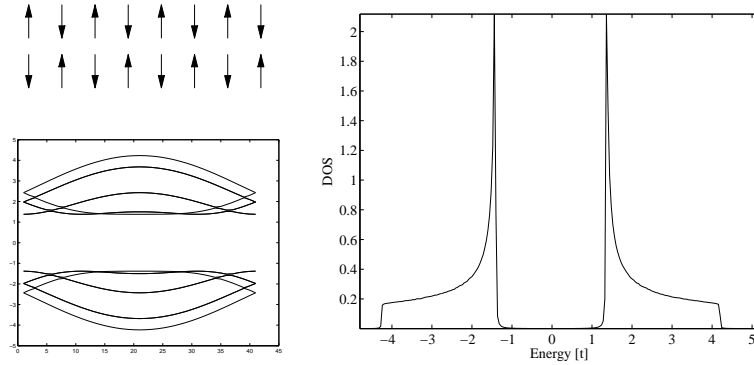
Figure 7.5: At half-filling $n_h = 0$ for $U = 4.0t$, $t' = 0$ we obtain the expected staggered spin configuration (upper left) and the band-dispersion shown in the lower left image. The DOS is displayed to the right.

individual LDOS are shown in Fig. 7.7. The fact that the Hartree-Fock solution is an insulating vertical stripe state for $t' = 0$ with the Ichioka rule of stability $\delta = n_h/2$ has been discussed before[22, 158]. Note in Fig. 7.7 that
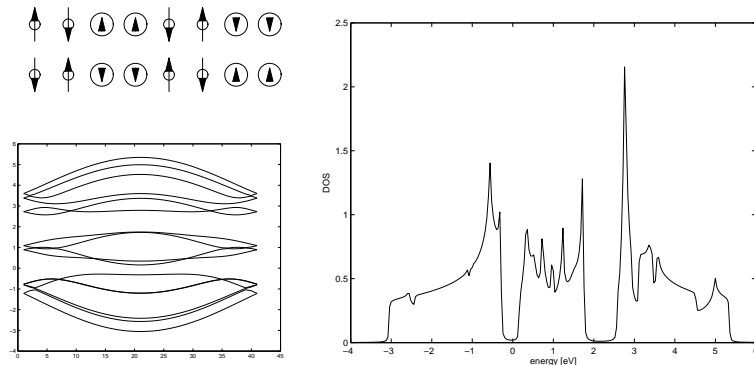

Figure 7.6: For spin periodicity $N = 8$, $n_h = 0.250$, $U = 5.0t$, and $t' = 0$ we obtain the stable bond-centered stripe spin and charge configuration (upper left) and the band-dispersion shown in the lower left image. The spatially averaged DOS is displayed to the right. The Fermi level is at 0.

the mid-gap states generated by the stripes have the largest spectral weight on the stripes. The wavefunction associated with the mid-gap states is localized on the stripes. For stripes of longer extent the mid-gap weight can completely disappear at sites farthest from the stripes as would be expected from Fig. 7.5.

The metallic stripe state can be obtained by including e.g. a next-nearest neighbor hopping term t'. This can be seen from Fig. 7.8 where we plot the 16 bands obtained when $N = 8$, $n_h = 0.250$, $U = 5.0t$ and $t' = 0$ (A), $t' = -0.1t$ (B), and $t' = -0.2t$ (C), respectively. The bands exhibit stronger dispersion when $t' \neq 0$ and the lower of the mid-gap bands cross the Fermi level as seen
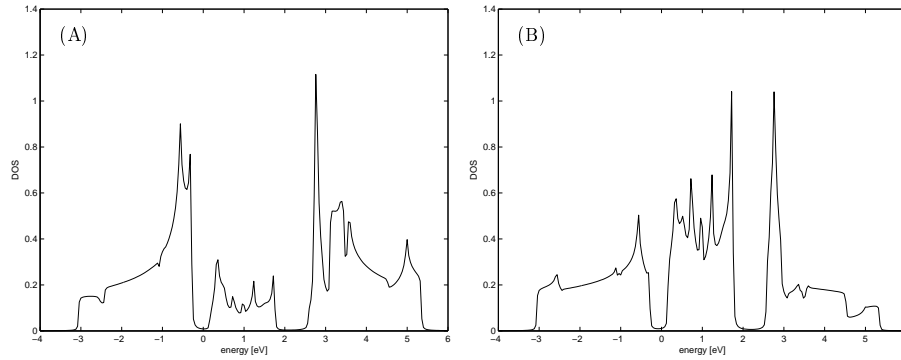
Figure 7.7: Local density of states measured off the bond-centered stripe (A) and on top of a site in the stripe (B) for $n_h = 0.250$, $U = 5.0t$, and $t' = 0.0$. The mid-gap states are clearly seen in these graphs. The Fermi level is at 0. The sum of these two plots generates the DOS shown in Fig. 7.6
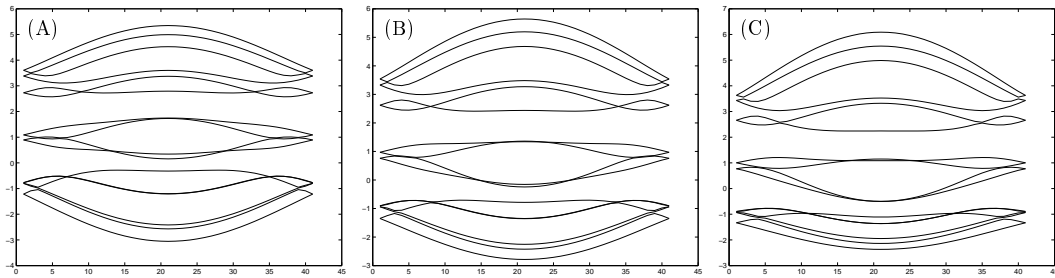

Figure 7.8: Band dispersion as a function of k_y through the center of the reduced Brillouin zone $k_x = 0$ for $t' = 0$ (A), $t' = -0.1t$ (B), and $t' = -0.2t$ (C). The bands show stronger dispersion and cross the Fermi level as we increase $|t'|$. The Fermi level is at 0.

in Fig. 7.8(B) and Fig. 7.8(C). The spatially averaged DOS corresponding to the latter two (i.e. the metallic case) are shown in Fig. 7.9. As opposed to the situation with $t' = 0$ shown to the right in Fig. 7.6, the Fermi level on longer falls in the gap. This is evidence for a metallic stripe phase within the Hartree-Fock approximation of the single-band Hubbard model[158]. Originally it was believed that this state would always be insulating. It is also clear that for situations with spin periodicity N and hole-doping less than $2/N$ the mid-gap bands will be partially filled and we have again the metallic stripe phase. This is because the $N - 2$ bands below the mid-gap bands are completely filled for $n_h \leq 2/N$.

The transition from an insulating to a metallic stripe phase does not have strong effects on the spin and charge density fields. This is evident from the small variations seen in Fig. 7.10.

What happens when we include the non-zero nearest neighbor attraction V in the minimal model? In Fig. 7.11 I show the self-consistent solutions in the
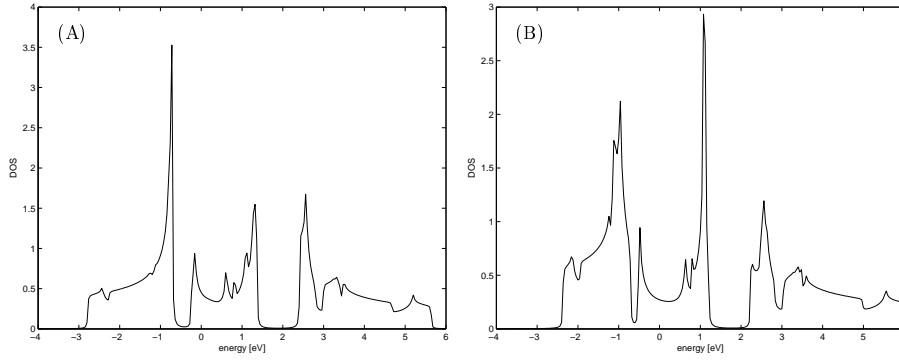
Figure 7.9: Spatially averaged density of states for $t' = -0.1t$ (A), and $t' = -0.2t$ (B). As opposed to the result shown to the right in Fig. 7.6 the Fermi level at zero energy is no longer gapped out.
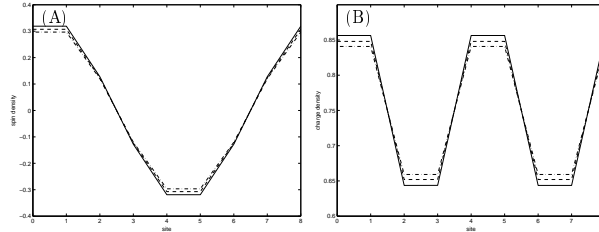

Figure 7.10: The variation of t' causes only minor changes to the self-consistent spin $(-1)^{i_x}\langle S^z \rangle$ and charge n densities. Parameters: $U = 5.0t$, $n_h = 0.25$, $V = 0.0$, $t'' = 0.0$ and $t' = 0.0$ (dash-dotted line), $t' = -0.1t$ (dashed), $t' = -0.2t$ (solid).

case when $U = 5.0t$, $t' = t'' = 0.0t$, $n_h = 0.25$ and $V = 2.0t$ and $V = 1.6t$. As before ($V = 0.0$) the spin periodicity is double the charge period. The nonzero nearest neighbor attraction induces superconductivity as seen in Fig. 7.11C.
 In plotting Fig. 7.11C I used the definition given by Eqn. (7.28). However, in (7.31) and (7.32) I show the raw output of the self-consistent value of the gap parameter in units of t on the x-links and y-links of the 8×2 unit cell for $V = 2.0t$ and $V = 1.6t$, respectively. There we see explicitly that the nearest neighbor attraction V induces the sign difference between x and y links as required for $\mathrm{d}_{x^2-y^2}$-wave pairing symmetry. As expected for a periodic modulation along the x-axis there is no difference between the gap values of the two rows (different y position) for both Δ_x and Δ_y. The gap has the same periodicity as the charge and exhibits a distinct anisotropy between the size of the order on the x-links as opposed to the y-links.

Thus, the static stripe spin and charge ordered phase coexists with the anisotropic d-wave superconducting phase. As seen from Fig. 7.11 the two orders compete. However, the results disprove the common notion that static magnetic stripes cannot coexist with superconducting order.
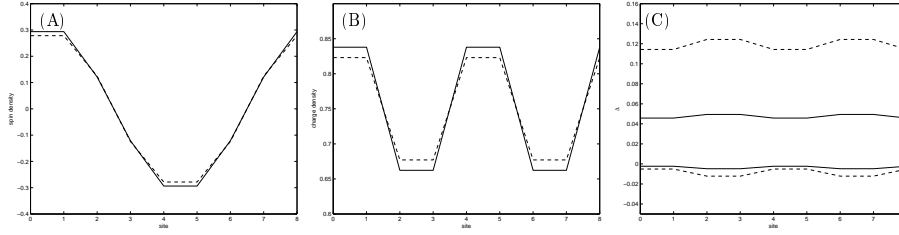
Figure 7.11: Spin density $(-1)^{i_x}\langle S^z\rangle$ (A) and charge density (B) and superconducting pair potential (C) for $U = 5.0t$, $t' = t'' = 0.0$, $n_h = 0.25$ and $V = 2.0t$ (dashed line) and $V = 1.6t$ (solid). In (C) we have also shown the small induced extended s-wave component existing in the stripe superconductor.

Recently, there have been calculations by Podolsky *et al.*[191] and Chen *et al.*[255] that point to the existence of a phase in the underdoped regime with d-wave modulated order. These calculations are attempts to fit the Fourier components of the ordering vector found in the Fourier images of the LDOS maps obtained by STM measurements[190, 78]. Here we see that a competing charge striped phase may be the origin of such a modulated pairing order.

$$
\begin{matrix}
\Delta_x & 0.108 & 0.111 & 0.114 & 0.111 & 0.108 & 0.111 & 0.114 & 0.111 \\
\Delta_x & 0.108 & 0.111 & 0.114 & 0.111 & 0.108 & 0.111 & 0.114 & 0.111 \\
- & - & - & - & - & - & - & - & - \\
\Delta_y & -0.119 & -0.119 & -0.137 & -0.137 & -0.119 & -0.119 & -0.137 & -0.137 \\
\Delta_y & -0.119 & -0.119 & -0.137 & -0.137 & -0.119 & -0.119 & -0.137 & -0.137
\end{matrix}
\tag{7.31}
$$

$$
\begin{matrix}
\Delta_x & 0.043 & 0.044 & 0.045 & 0.044 & 0.043 & 0.044 & 0.045 & 0.044 \\
\Delta_x & 0.043 & 0.044 & 0.045 & 0.044 & 0.043 & 0.044 & 0.045 & 0.044 \\
- & - & - & - & - & - & - & - & - \\
\Delta_y & -0.048 & -0.048 & -0.054 & -0.054 & -0.048 & -0.048 & -0.054 & -0.054 \\
\Delta_y & -0.048 & -0.048 & -0.054 & -0.054 & -0.048 & -0.048 & -0.054 & -0.054
\end{matrix}
\tag{7.32}
$$

The on-site d-wave order parameter was defined in Eqn. (7.28). From the solutions (7.31) and (7.32) it is clear that this order is modulated in accordance with the charge order. However, from the definition of the extended s-wave order

$$
\Delta_i = \left(\Delta_{i+e_x} + \Delta_{i-e_x} + \Delta_{i+e_y} + \Delta_{i-e_y}\right)/4.
\tag{7.33}
$$

it follows that the stripe phase induces a small pairing component of extended s-wave symmetry. This is not surprising since the stripe solutions explicitly breaks the C_4 symmetry of the CuO$_2$ layer. The size of the extended s-wave component is seen in Fig. 7.11C.

In both the case of an insulating and metallic stripe phase, there is a threshold value of V_c above which the superconducting order develops. This value is smaller for the metallic stripes, for instance in the case with $U = 5.0t$ and

$n_h = 0.25$ we have $V_c = 1.55t$ ($t' = 0.0$), $V_c = 1.40t$ ($t' = -0.1$), and $V_c = 1.35t$ ($t' = -0.2$). The values of the critical V_c decrease when lowering the Coulomb repulsion U.

In Fig. 7.12 I show the spatially averaged DOS for the coexisting stripe phase. As expected the superconductivity reintroduces a gap at the Fermi level. The
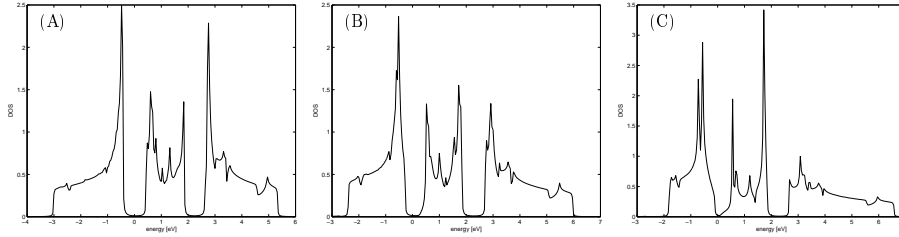

Figure 7.12: Spatially averaged density of states in the coexisting phase of spin and superconducting stripe order ($U = 5.0t$, $V = 2.0t$, $n_h = 0.25$) for $t' = 0.0t$ (A), $t' = -0.1t$ (B), and $t' = -0.2t$ (C). The Fermi level at zero energy falls in the gap.

gap structure, however, does not appear to have the simple d-wave form. This is investigated in more detail in Fig. 7.14 where we show the DOS zoomed in around the Fermi level for various self-consistently determined configurations. First of all, when $U = 0$ we find the usual V-shaped DOS in a d-wave superconductor as seen in Fig. 7.13. When $U \neq 0$ and $V \neq 0$ the final low-energy DOS
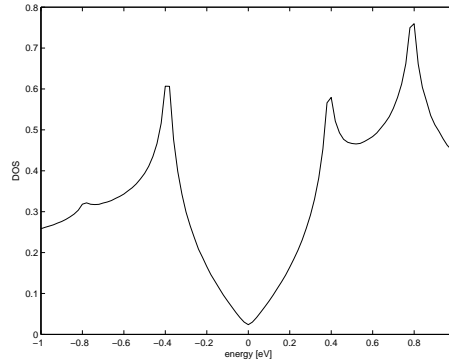
Figure 7.13: DOS in the homogeneous d-wave superconducting phase with $n_h = 0.25$, $U = 0.0t$, $V = 1.5t$ and $t' = 0.0$. To obtain the required doping level the chemical potential is $\mu = -0.640t$.

strongly depends on the ratio U/V and the value of the next-nearest neighbor hopping t'. When U/V is large the nodal quasi-particles in the clean d-wave superconductor are gapped and we obtain a full gap at the Fermi level. For $n_h = 0.25$ this is evidently the case when $U = 5.0t$, $V = 2.0t$ and $t' \leq 0.1t$ as seen in Fig. 7.14(A-B). When t' becomes sufficiently large the bands strongly

disperse and the full gap closes as seen in 7.14(C). The resulting gap is d-wave-like but anisotropic when comparing the weight at positive and negative bias, respectively. A gap anisotropy similar to that presented in Fig. 7.14(C) has already been detected experimentally as seen e.g. in the figures of Ref. [78].

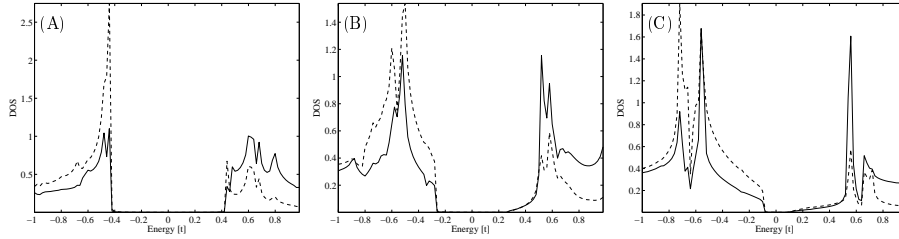What happens at other doping levels? A set of parameters utilized by Ichioka

Figure 7.14: LDOS in the stripe superconducting phase with $n_h = 0.25$, $U = 5.0t$, $V = 2.0t$ and $t' = 0.0$ (A), $t' = -0.1$ (B), and $t' = -0.2$ (C). The solid line is the LDOS at a site on the stripe and the dashed line shows the result on one of the sites off the bond-centered stripe.

and Machida[256] to study the BSCCO STM data is: $n_h = 0.120$, $t' = -0.34t$, and $t'' = 0.23t$. When $V = 0$ this bandstructure stabilizes a vertical stripe phase for $U > 4.0t$. When $V = 1.6t$ the stripe state appears for $U > 4.1t$[13]. By increasing V we can reenter the homogeneous d-wave superconducting state, e.g. for $U = 4.2t$ and $V > 1.9t$. The spin density, charge density and pair
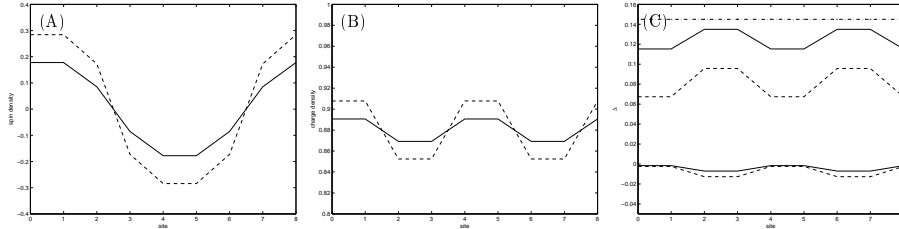
Figure 7.15: Spin density $(-1)^{i_x}\langle S^z\rangle$ (A), charge density (B) and superconducting pair potential (C) as a function of site in the unit cell $(i_x, 0)$. To generate these results we used $V = 1.6t$, $t' = -0.34t$, $t'' = 0.23t$, $n_h = 0.120$ and $U = 4.2t$ (solid line) and $U = 4.3t$ (dashed line). In (C) we also display the induced extended s-wave order (close to zero) and the gap in the homogeneous d-wave superconductor obtained when $U = 0.0$ (dot-dashed).

potential Δ is shown in Fig. 7.15 for $U = 4.2t$ and $U = 4.3t$. These parameters just within the stripe phase generate weak stripe order. Here we clearly see how relatively small changes in U/V can affect the induced superconducting order. The LDOS on one of the bond-centered sites on the stripe (solid line) and off (dashed) the hole-rich stripe is shown in Fig. 7.16 for both $U = 4.2t$

---

[13]In the notation from Ref. [256] we have $V = 2g_s$ for comparison of the results

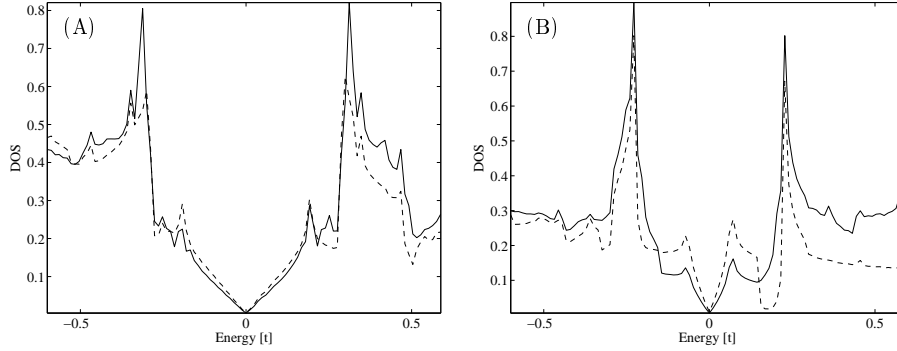**Figure 7.16**: LDOS in the stripe superconducting phase with $n_h = 0.12$, $V = 1.6t$, $t' = -0.34t$, $t'' = 0.23t$ and $U = 4.2t$ (A), and $U = 4.3t$ (B). The LDOS is calculated on the stripe (solid) and off the hole-rich stripe (dashed).

and $U = 4.3t$. As opposed to the conventional d-wave gap displayed in Fig. 7.13, a double peak structure develops inside the gap for these stripe super-conductors. An important difference between the DOS inside and outside the stripe is the distribution of states on either side of the coherence peaks: at the stripe site weight is shifted from inside the superconducting gap to above the gap. This weight redistribution has important consequences for the Fourier components of the DOS. In fact, if we Fourier transform the LDOS

$$N(\mathbf{q}, \omega) = \frac{1}{N} \sum_{\mathbf{r}_i} N(\mathbf{r}_i, \omega) \exp(i\mathbf{q} \cdot \mathbf{r}_i) \tag{7.34}$$

and plot the real part of the Fourier component $N(2\mathbf{q}^*, \omega)$ at double the ordering vector $\mathbf{q}^* = (\pi, 3\pi/4)$ we obtain the graph shown in Fig 7.17. Had the system been a homogeneous d-wave superconductor, this component would be identically zero. Note that $2\mathbf{q}^*$ is the ordering vector of the charge or-
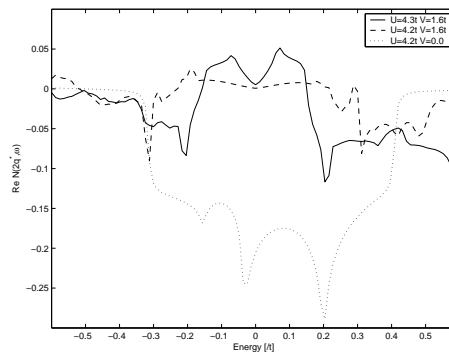

Figure 7.17: Real part of the Fourier component $N(2\mathbf{q}^*, \omega)$ at twice the ordering vector $\mathbf{q}^* = (\pi, 3\pi/4)$ versus energy. Parameters: $n_h = 0.12$, $V = 1.6t$, $t' = -0.34t$, $t'' = 0.23t$ and $U = 4.2t$ (dashed) and $U = 4.3t$ (solid).

der. For larger values of V the pairing potential increases and the crossing of Re$N(2\mathbf{q}^*, \omega)$ and the x-axis moves to larger energies but the overall shape of Re$N(2\mathbf{q}^*, \omega)$ remains very similar to the one shown in Fig. 7.17. When Howald *et al*[75, 190] measured this component by STM studies they obtained a result very similar to the one shown in Fig. 7.17. It is non-trivial to obtain a sign change of this component between low- and high energy. To this end, it is crucial that the d-wave order parameter is modulated as was discussed by Podolsky *et al.*[191] For instance, in Fig. 7.17 I also show the energy dependence of Re$N(2\mathbf{q}^*, \omega)$ (dotted line) for the stripe system without coexisting superconductivity, i.e. with $V = 0.0$. Clearly, this Fourier component does not cross the Re$N(2\mathbf{q}^*, \omega) = 0$ axis.

In a future study it will be interesting to determine whether the gap modulations obtained in the coexisting stripe phase of spin- and charge density waves *and* striped d-wave superconductivity can explain more of the features recently observed in the STM Fourier images[78].

7.3.3 Spectral weight distribution

We may also use expression (7.29) to study the spectral function $A(\mathbf{k}, \omega)$ measured in photoemission. To this end, we need

$$\mathcal{G}_\sigma(\mathbf{k}, ip_n) = \frac{1}{N^2} \sum_{\mathbf{r}_i, \mathbf{r}_j} \mathcal{G}_\sigma(\mathbf{r}_i, \mathbf{r}_j, ip_n) \exp(i\mathbf{k} \cdot (\mathbf{r}_i - \mathbf{r}_j)) \qquad (7.35)$$

where $\mathbf{k}$ extends over the full Brillouin zone. Though the momentum vector in the sums of Eqn. (7.29) only ranges over the reduced zone, we can use that fact that the Bogoliubov-de Gennes equations are invariant under translation of the momentum vector by a reciprocal lattice vector of the reduced zone to obtain

$$A_\sigma(\mathbf{k}, \omega) = -\frac{1}{\pi} \frac{1}{(N_x N_y)^2} \text{Im} \sum_{ni,j} e^{i\mathbf{k} \cdot (i-j)} \left(\frac{u_{n\mathbf{k}\sigma}^*(i) u_{n\mathbf{k}\sigma}(j)}{\omega - E_{n\mathbf{k}\sigma} + i\Gamma} + \frac{v_{n\mathbf{k}\overline{\sigma}}^*(i) v_{n\mathbf{k}\overline{\sigma}}(j)}{\omega + E_{n\mathbf{k}\overline{\sigma}} + i\Gamma} \right),$$
$$(7.36)$$

where we also used that $u_{-\mathbf{k}} = u_{\mathbf{k}}^*$.

The spectral weight is defined as the integral of the spectral function over an energy window $\Delta\omega$ below the Fermi level

$$I_\sigma(\mathbf{k}) = \int_{\mu-\Delta\omega}^{\mu} A_\sigma(\mathbf{k}, \omega) d\omega. \qquad (7.37)$$

Below, the spectral weight $I(\mathbf{k})$ is shown as the sum of both spin parts, i.e. $I(\mathbf{k}) = I_\uparrow(\mathbf{k}) + I_\downarrow(\mathbf{k})$.

The spectral weight has been studied quite extensively within the stripe solutions of the mean-field Hubbard model[22, 157, 157, 256]. Recently, there have been several other studies of $A(\mathbf{k}, \omega)$ in a stripe system[158, 257, 258, 259, 260,

261, 262]. Therefore we refer to the literature for a thorough discussion and calculate, in the following, only some of the most important results.

The parameters $n_h = 0.120$, $t' = -0.34t$, $t'' = 0.23t$, $U = 4.3t$ and $V = 1.6t$ produces a metallic stripe phase. In Fig. 7.18 we show the spectral weight over the whole Brillouin zone when $\Delta w = 0.2t$(A) and $\Delta w = 0.5t$(B). Without the existence of the mid-gap bands these figures would be featureless since there are no states in the original Mott-Hubbard band gap. From Fig. 7.18 it is clear
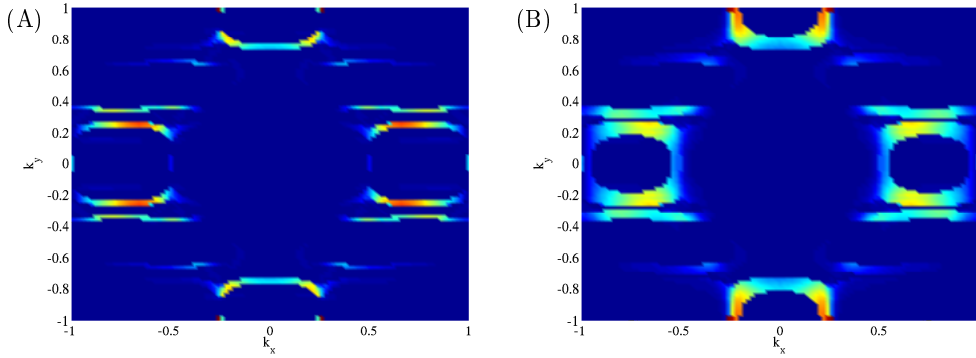

Figure 7.18: Spectral weight as a function of $-\pi < k_x < \pi$ and $-\pi < k_y < \pi$ obtained by integrating the spectral function over a small energy window $\Delta\omega = 0.2t$(A) and $\Delta\omega = 0.5t$(B) below the Fermi level.

that the low-energy weight resides near the anti-nodal regions as expected for partially filled stripes. The nodal region is completely void for spectral weight. These results are generic and do not depend qualitatively on the parameters t', t'' etc.

For $n_h = 0.18$, $t' = -1/6t$ and $U = 4.0t$ we have the spectral weight at the Fermi level ($\Delta\omega = 0.05t$) shown in Fig. 7.19(A). Fig. 7.19(B) shows, for the same set of parameters, the contour plot of the spectral function as a function of energy and wave vector along the symmetry line $(0,0) \rightarrow (\pi,0) \rightarrow (\pi,\pi) \rightarrow (0,0)$ of the original Brillouin zone. The dispersion is similar to the simple tight-binding cosine band except from the following: 1) the very flat band near $(\pi, 0)$, and 2) the opening of gaps resulting in vanishing weight near the nodal region, i.e. near $(\frac{\pi}{2}, \frac{\pi}{2})$ and symmetry related points. The flat band at the anti-nodal point lies just below the Fermi level. The ARPES experiments probe both x- and y-axis aligned stripes. However, superimposing the contour plot probing the other anti-nodal region, e.g. along a line $(0,0) \rightarrow (0,\pi) \rightarrow (-\pi,\pi) \rightarrow (0,0)$ does not affect these conclusions. These results are very well in agreement with the ARPES data on LSCO and Nd-LSCO discussed above.
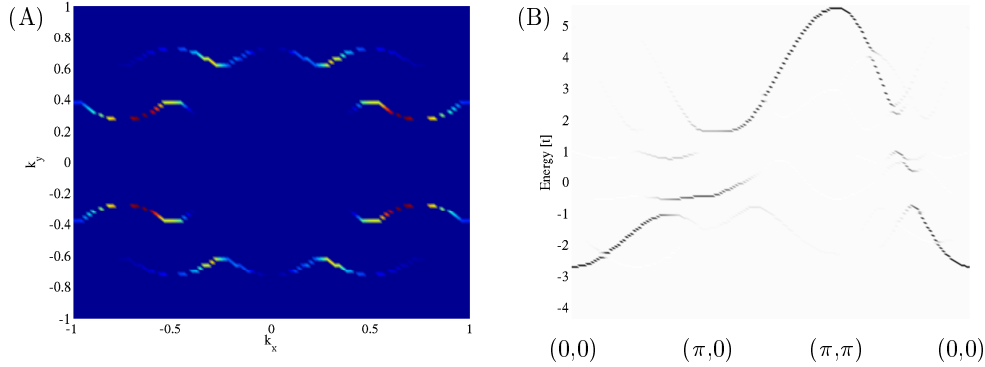
Figure 7.19: (A) Spectral weight at the Fermi level as a function of $-\pi < k_x < \pi$ and $-\pi < k_y < \pi$ obtained by integrating the spectral function over a small energy window $\Delta\omega = 0.05t$. (B) Contour plot of the spectral function along the line $(0,0) \to (\pi,0) \to (\pi,\pi) \to (0,0)$. The fermi level is at zero.

7.3.4 Spectral weight in arrays of disordered stripes

In any real system there is disorder that ruin the perfect stripe array. Therefore, it is important to study the effects of disordered stipes. Unfortunately, it is not possible (due to computer limits) to generalize the above approach to large systems and perform a disorder average. This kind of calculation is, however, straightforward if one compromises the self-consistency. For instance Salkola *et al.*[225] and Granath *et al.*[254] have used a stripe ansatz of the form

$$m(i_x, i_y) = M \prod_{\{i_x^s\}} \Theta(i_x - i_x^s), \qquad (7.38)$$

where $\Theta(x)$ denotes the antisymmetric Heaviside function: $\Theta(x) = -\Theta(-x) = 1$ for $x > 0$ and $\Theta(0) = 0$. The set of integers $\{i_x^s\}$ gives the position of the stripes[14]. Therefore, the product of the ansatz (7.38) and the staggering, $(-1)^{i_x+i_y}m(i_x, i_y)$ produces a site-centered array of anti-phase stripes. The system is translational invariant along the y-axis except from the staggering. For a periodic set, e.g. $\{i_x^s\} = \{... - 8, -4, 0, 4, 8...\}$ we regain the mid-gap bands which display large weight around the Fermi level at the antinodal regions. However, for stripes that are nearest (or next-nearest) neighbors the mid-gap bands shift, and spectral weight is generated around the nodal region. For a large system we show in Fig. 7.20 the calculated distribution of spectral weight in the upper right quadrant of the Brillouin zone $0 < k_x, k_y < \pi$ obtained for at large system by averaging over an ensemble of ten different disordered stripe configurations with an average separation of four lattice constants. Specifically, we choose ten sets of 200 integers randomly between 1...7

---

[14]In this section only, we employ the mean-field decoupling scheme, $\mathbf{S}_i \cdot \mathbf{S}_i \to M_i S_i^z$, of the Hubbard interaction.

to constitute the set of stripe spacings which gives $\{i_x^s\}$.

When the stripe potential is weak $M < 0.25t$ the spectral weight is seen in Fig. 7.20 to lie at the Fermi surface as expected. However, for larger values of M the weight in the nodal region becomes more diffuse whereas the antinodal weight solidifies. The results in Fig. 7.20 are in remarkable agreement with
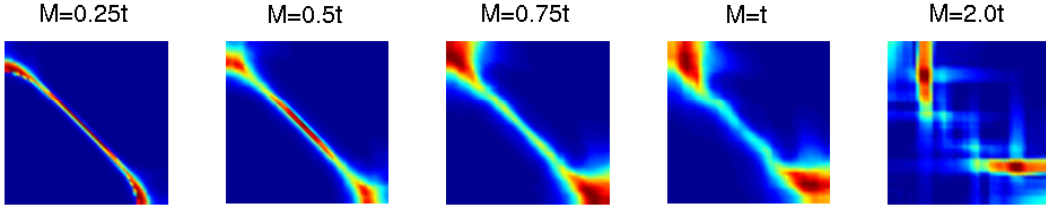

Figure 7.20: Spectral weight as a function of $0 < k_x, k_y < \pi$ obtained by integrating $A(\mathbf{k}, \omega)$ over a small energy window ($\Delta\omega = 0.2t$) below the Fermi level for different values of the spin dependent stripe potential M.

the ARPES measurements on LSCO and Nd-LSCO[224]. For instance, if we compare the images obtained for $M = 1.0t$ to the spectral weight in the upper right quadrant of the Brillouin zone shown in Fig. 7.2(c-d), we see a very good agreement: the antinodal weight in generated by the stripes and the ghosty nodal line by their disordering. It is interesting that the final spectral weight actually resembles the original free Fermi surface even though the electronic structure is completely different.

7.4 Discussion

Another interesting experimental observation is the existence of a "Fermi arc" at very low doping $x < 0.05$ of LSCO as seen by ARPES. At this doping level we know from neutron diffraction that the incommensurate peaks rotate in agreement with an arrangement of diagonal antiphase stripes. As discussed by Granath[263], it is not possible to reproduce the Fermi arc in the spectral weight by the most naive form of site-centered diagonal stripes. However, if the stripes organize *locally* along the Cu-O bonds but *globally* along the nodal direction, i.e. have the stair-case shape, they reproduce quite easily the Fermi arc. For the stair-case stripes there are two important lengths: the stripe distance and the height of the steps. Interestingly, the magnetic structure factor crosses over from putative diagonal to putative vertical/horizontal as the inter-stripe distance is decreased compared to the step height. This agrees with the neutron experiments.

Finally there have been recent calculations of the spectral function from 1D stripe Luttinger liquids[264, 265, 266]. The broad EDC line shapes are guaranteed by the electron fractionalization in these 1D systems. When the Luttinger liquids are coupled to e.g. optical phonons the resulting line shape resembles very well that measured by photoemission[267]

8 Stripes and neutron scattering experiments

Some of the material in this chapter has been submitted by the author and P. Hedegård to Physical Review Letters

8.1 Neutron scattering and a summary of important experimental results

The scattering of slow neutrons off crystals provides a very powerful probe of the quantum states in solids because the energy and wavelength of the neutrons are comparable to the excitations in the crystal. The neutrons interact with solids via 1) the nuclear force leading to neutron-ion scattering with possible emission and absorption of phonons, and 2) the magnetic dipole-dipole interaction between the very weak magnetic moment of the neutron and the magnetic moments in the solid[268]. In the following we focus on the dipole interaction which leads to enhanced neutron scattering signals from magnetically ordered systems.

The magnetic neutron scattering cross section per formula unit is given by

$$\left(\frac{d^2\sigma}{d\Omega dE} \right) = (\gamma r_e)^2 \frac{k_f}{k_i} |F(\mathbf{q})|^2 S(\mathbf{q}, \omega) \tag{8.1}$$

where $k_i(k_f)$ is the initial(final) wave vector of the neutron, $\mathbf{q} = \mathbf{k}_i - \mathbf{k}_f$ the scattering vector, ω the energy loss, γ is the gyromagnetic ratio and $r_e = e^2/m_e c^2$. $F(\mathbf{q})$ denotes the magnetic form factor of the Cu^{2+} ions. The magnetic structure factor, $S(\mathbf{q}, \omega)$, is the Fourier transform of the spin-spin correlation function. $S(\mathbf{q}, \omega)$ is related to the imaginary part of the spin susceptibility $\chi''(\mathbf{q}, \omega)$ through the fluctuation-dissipation theorem

$$S(\mathbf{q}, \omega) = \frac{\chi''(\mathbf{q}, \omega)}{1 - \exp(-\omega\beta)}. \tag{8.2}$$

Since there exists a vast amount of neutron scattering data on the cuprates I restrict the following discussion of the experimental results to features that are relevant for this chapter. A major difficulty in studying the magnetic fluctuations of the cuprate systems is to separate the spin scattering from the phonon scattering and other spurious processes. Papers that review the neutron data on both the YBCO and LSCO systems can be found in the references[269, 270, 271]

In the undoped cuprates, Vaknin *et al.*[272] first used the neutron scattering to identify the Bragg peaks from antiferromagnetic spin order. Magnetic moments of 0.66 μ_B per Cu ion was found, the reduction from $1\mu_B$ is caused by

quantum fluctuations which are rather strong for spin S=1/2 systems. The measured ordering vector, (π, π, π), shows that the successive planes are also antiferromagnetically coupled.

8.1.1   A brief review of neutron scattering results on LSNO

It is firmly established that stripes rule the physics of the insulating nickelate $La_{2-x}Sr_xNiO_4$[273, 274, 275, 276, 277, 278]. Compared to LSCO, the $S = 1/2$ Cu spins are replaced by $S = 1$ Ni spins. From neutron and x-ray diffraction measurements the stripes are known to order diagonally (i.e. along the [110] or [1$\bar{1}$0] directions) in the nickel-oxide layers in the doping range $0.135 < x < 0.5$. Obviously, by studying the stripes in these systems one hopes to determine whether or not the stripes are important for copper-oxide superconductors as well. The charge stripes are found to be well correlated in the planes with a correlation length in excess of 100 Å. At fractional doping, commensurate to the underlying lattice, it is known that the charge stripe ordering is particularly stable due to pinning. The charge-ordering temperature is found to exceed the spin-ordering temperature. The incommensurability δ is approximately linear in the hole concentration n_h, $\delta \approx n_h/2$, up to $n_h = 0.5$.

The spin fluctuations have been measured in e.g. $La_{1.69}Sr_{0.31}NiO_4$ with the result shown in Fig. 8.1[279]. Clearly, spin wave dispersions up to 80 meV
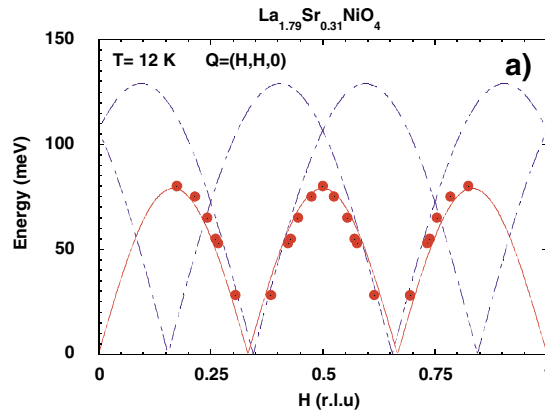
Figure 8.1: Spin wave dispersions as measured by scans of constant energy transfer through the incommensurate points $\mathbf{Q}_\delta = (1/2, 1/2) \pm (\delta, -\delta)$. The blue dot-dashed line shows the spin excitation spectrum obtained in the undoped sample La_2NiO_4 shifted from (π, π) by $\mathbf{Q}_\delta$. Adapted from Ref. [279]

emerging from the incommensurate magnetic Bragg points are observed. A spin-only model defined on an incommensurate spin background captures well this behavior. The branches dispersing toward (π, π) merge around 80 meV to define the commensurate "resonance" in this system. The dot-dashed line shows the spin excitation spectrum obtained in the undoped sample La_2NiO_4 shifted from (π, π) by $\mathbf{Q}_\delta$. Effectively, the doped holes only cause a shift of

the dispersion curves due to their self-organization into stripes. Below, we compare this spin behavior with that measured in the cuprates.

8.1.2 A brief review of neutron scattering results on LSCO and LBCO

The single layer material LSCO can be grown in large crystals and has been extensively studied in neutron scattering measurements. In chapter 6, I discussed the pinning effects of stripes when applying a magnetic field and the effects on neutron and STM measurements. Furthermore, as evidence for the stripe state the presence of elastic Bragg charge and spin peaks in the neodymium doped LSCO samples was pointed out in chapter 5. Below, instead of embarking on a chronological journey of the last decades extensive neutron results on LSCO, I mainly show some recent results obtained by Christensen *et al.*[280] and Tranquada *et al.*[281].

The data of Christensen *et al.*[280] surveyed the magnetic susceptibility $\chi(\mathbf{q}, \omega)$ over the whole Brillouin zone for energy transfers $0 - 40$meV with high resolution in both wave vector $\mathbf{q}$ and energy ω for an underdoped ($x = 0.10$) and optimally doped ($x = 0.163$) LSCO sample. Fig. 8.2 displays the measured spin structure factor as a function of q_x, q_y at constant energies. Except from
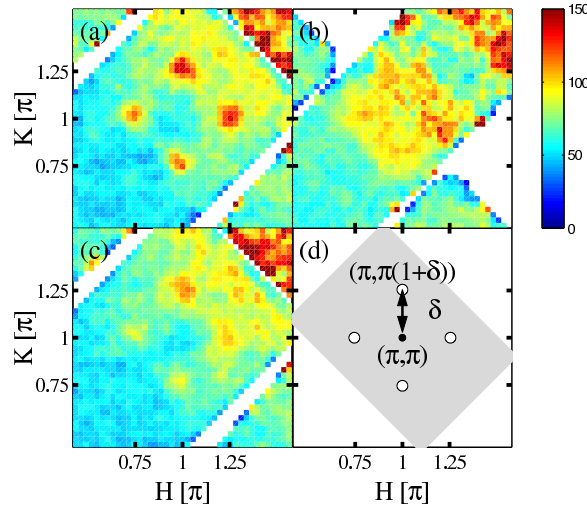
Figure 8.2: Constant energy cuts through the Brillouin zone near (π, π). (a),(b) at T=10K in the superconducting state for (a) $\omega = 10$meV and (b) $\omega = 30$meV. (c) T=40K normal state at $\omega = 10$meV, and (d) shows the incommensurate points and the experimentally probed part of the Brillouin zone. Adapted from Ref. [280].

an intensity loss the response at $\omega = 10$meV looks similar both below (a) and above (c) T_c: four incommensurate peaks positioned at $(\pi, \pi(1 \pm \delta))$ and $(\pi(1 \pm \delta), \pi)$ with $\delta \approx 0.25$. The presence of inelastic incommensurate peaks in

LSCO was initially discovered by Cheong *et al.*[139] in 1991. At higher energy transfer of 30meV the incommensurate peaks appear broad and shifted toward (π, π). Their intensity maximum is centered around $\omega \approx 15$meV.

The dispersion of the incommensurate peaks is seen clearly in the left part of Fig. 8.3 which shows scans through the incommensurate (a,c) and commensurate (b,d) positions at 10meV and 30meV. By mapping out the dispersion

Figure 8.3: Left: constant energy scans along the trajectory shown in the inset. All four graphs are taken in the superconducting phase at T=10K and for $\omega = 10$meV (a-b) and $\omega = 30$meV (c-d). The dashed lines indicate the dispersion. Right: (a) energy dispersion of the incommensurate peaks for the opti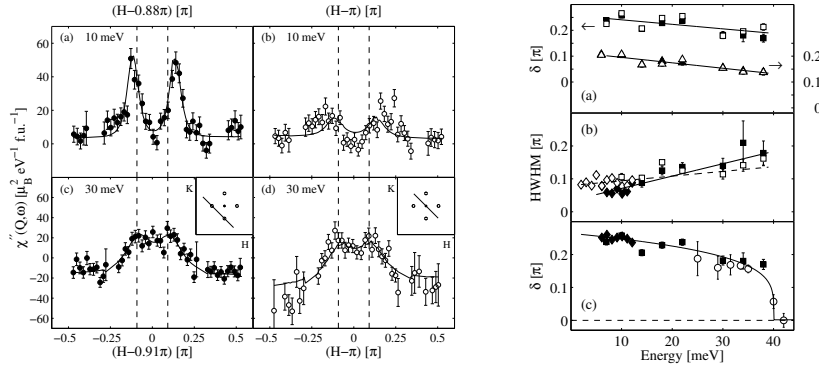mally doped $x = 0.163$ (squares) and the underdoped $x = 0.10$ (triangles) sample. Filled (empty) symbols are for the superconducting (normal) state. (b) shows the energy dependence of the HWHM, and (c) compares the incommensurate dispersion for optimally doped LSCO (filled symbols) to that of YBCO (empty circles). Adapted from Ref. [280].

$\delta(\omega)$ of the incommensurate peaks Christensen *et al.*[280] obtained the results shown on the right in Fig. 8.3. Clearly, the peak positions disperse inward toward (π, π) with increasing energy ω. There is no significant difference between the dispersion in the normal versus the superconducting state. The peak widths (middle graph on the right hand side of Fig. 8.3) are slightly sharper below T_c at low energy $\omega \leq 20$meV. Note that in the superconducting state (filled symbols) there are no points below $\omega \leq 7$meV. This is due to the presence of a spin gap in the magnetic excitation spectrum at optimal doping. In the the lower right image of Fig. 8.3 the dispersion of the incommensurate peaks is compared to the results obtained from a near-optimally doped YBCO sample ($T_c = 89$K). Apart from the crossing at (π, π) and a substantially larger spin gap, the dispersion $\delta(\omega)$ is remarkably similar in the two cuprates. This has led to a recent ubiquitous view of the spin fluctuations in the cuprate materials.

As mentioned in the chapter 5, the spin excitation gap in optimally doped LSCO quickly vanishes when reducing the strontium doping concentration x. Experimentally, it is found that for $x \leq 0.13$ elastic peaks are observed in

LSCO.

How can we understand these results? Assuming that the underdoped LSCO is in the stripe phase, it is characterized by a long-range ordered stripe order parameter which is revealed in the elastic neutron peaks. When increasing the doping x, there is a quantum critical point where the stripe order melts, the order becomes short-range ordered and fluctuating. The Goldstone modes present in the underdoped regime are no longer condensed and we expect a spin excitation gap. In this sense, the main difference between LSCO and YBCO is that the latter cuprate is "longer from the stripe ordered phase", the stripes are highly fluctuating and the spin gap is larger. Recent experiments in the highly underdoped regime (YBCO$_{6.35}$, $T_c = 39$meV) show that a spin gap of $\omega \approx 10$meV prevails[283]. However, in this doping regime there exists static charge order with the expected halved periodicity compared to the incommensurate spin fluctuations. This is another remarkable example of a superconducting Mott insulator with static charge order.

An important question is related to the evolution of the spin excitations at higher energies, i.e. $\omega > 40$meV. Unfortunately, this has not yet been clearly resolved for LSCO. For La$_{1.875}$Ba$_{0.125}$CuO$_4$ however, this was recently measured by Tranquada *et al.*[281, 282] with the results shown in Fig. 8.4. LBCO is known to support a static stripe ordered system which at $x = 1/8$ has strongly suppressed the superconductivity as evidenced by the very low T$_c$=3 K. At T=12 K and at low energy transfer the neutron data is consistent with spin-wave excitations dispersing from the incommensurate Bragg points. These merge at the commensurate (π, π) point at approximately 60 meV. For higher energies the data indicates a $\pi/4$ rotated quartet of maximum intensity peaks which disperse to larger wavevectors q with increased energy transfer. These seem to be connected by lines of substantial weight contrary to the situation at low energy.

Before studying in more detail the spin fluctuations expected in the stripe state, we discuss in the next two sections the neutron scattering data from YBCO (and BSCCO), and then follow what initially seems a different approach to the spin incommensurability, namely that the incommensurate peaks are in fact a natural consequence of nesting effects in a homogeneous d-wave superconducting state.

8.1.3   A brief review of neutron scattering results on YBCO and BSCCO

The most prominent feature of the low-energy magnetic scattering in the YBCO and BSCCO materials is the so-called π-resonance[227, 228, 284, 285, 286, 287, 288, 289]. The resonance was earlier shown to be a possible origin of the so-called peak-dip-hump feature in the ARPES line shape around $(\pi, 0)$ and symmetry related points. In neutron experiments it is revealed in the spin-flip channel with an intensity maximum at (π, π) and an energy around
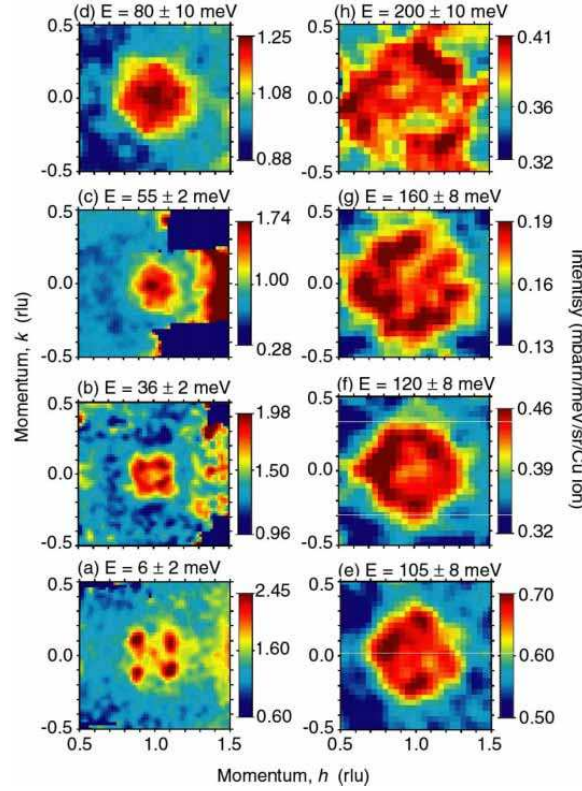
Figure 8.4: Maps similar to Fig. 8.2 for $La_{1.875}Ba_{0.125}CuO_4$ and measured to higher energy transfer. From Tranquada *et al.* Ref. [281].

40meV at optimal doping for both the YBCO and BSCCO materials. Away from optimal doping the resonance energy Ω scales with T_c

$$\Omega \approx 5kT_c. \qquad (8.3)$$

Thus, the gap Δ, which falls monotonically with increased doping, has the opposite doping behavior as Ω.

The resonance has also been found in the single layer material $Tl_2Ba_2CuO_{6+\delta}$[290]. An important question is the dispersion of the resonance mode: the dispersion is downward in the sense that the intensity maximum of the mode moves to incommensurate wave vectors when *decreasing* the energy transfer. This downward dispersion appears to be a generic property of the resonance. The mode does not disperse all the way to zero energy but fades away, and the low-energy part of $Im\chi(\mathbf{q}, \omega)$ is dominated by a large spin gap. The spin gap is an increasing function of the doping with a maximum of 32meV at optimal doping in YBCO. These important features were already presented in Fig. 8.3 for the optimally doped LSCO sample. Now, however, it is evident that an apparent difference between LSCO and YBCO is the *intensity distribution* of

Figure 8.5: Left: (top) constant energy scans in the superconducting phase through the Brillouin zone at the resonance energy 34 meV (left) and at 24.5 meV (right) for YBa$_2$Cu$_3$O$_{6.6}$. (bottom) schematic ove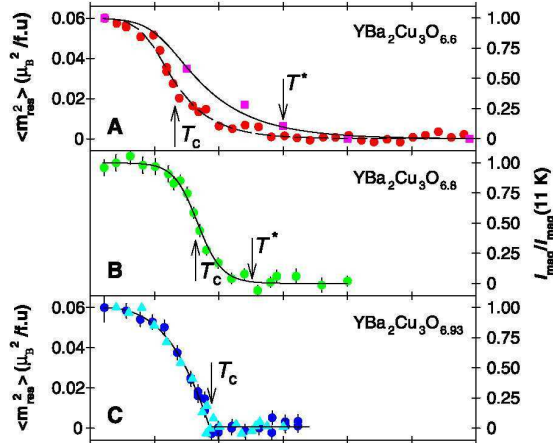rview of the dispersion of the π resonance. Adapted from Ref. [284]. Right: temperature dependence of the resonance intensity for YBCO at three different doping levels. Adapted from Ref. [288].

the incommensurate peaks: as opposed to YBCO, in LSCO the intensity decreases (and the peaks broaden) when approaching (π, π).

The intensity of the resonance strongly increases upon entering the superconducting state as shown in Fig. 8.5. In the overdoped regime there is no sign of a π-resonance above T_c whereas in the underdoped region it clearly prevails into the pseudo-gap phase. In the normal state it was originally believed that the magnetic response was commensurate and weak compared to the resonant intensity below T_c. Recent measurements, however, seem to indicate that the normal state also exhibits incommensurate spin fluctuations.

In the next section I discuss how the salient features of the resonance can be understood from the spin-1 collective mode in a homogeneous d-wave superconductor. Within this approach, we will see that the presence of the superconducting condensate is crucial for the mode to survive.

8.2 Spin susceptibility of a homogeneous d-wave superconductor

There is strong evidence that the superconducting state in YBCO and BSCCO is close to a conventional BCS superconductor with d-wave pairing symmetry. This is true at least in the optimal and overdoped regimes[78]. Therefore, it is important to exhaustively study the spin spectrum of a d$_{x^2-y^2}$-wave superconductor. As is well-known, but also derived in Appendix .1, the bare spin

susceptibility, $\chi^0_{BCS}(\mathbf{q}, i\omega_n)$, of a BCS superconductor is given by

$$
\begin{aligned}
\chi^0_{BCS}(\mathbf{q}, i\omega_n) &= \sum_{\mathbf{k}} \frac{1}{2}\left(1 + \frac{\xi_{\mathbf{k}}\xi_{\mathbf{k+q}} + \Delta_{\mathbf{k}}\Delta_{\mathbf{k+q}}}{E_{\mathbf{k}}E_{\mathbf{k+q}}}\right) \frac{f(E_{\mathbf{k}}) - f(E_{\mathbf{k+q}})}{i\omega_n - (E_{\mathbf{k}} - E_{\mathbf{k+q}})} \\
&+ \frac{1}{4}\left(1 - \frac{\xi_{\mathbf{k}}\xi_{\mathbf{k+q}} + \Delta_{\mathbf{k}}\Delta_{\mathbf{k+q}}}{E_{\mathbf{k}}E_{\mathbf{k+q}}}\right) \frac{f(E_{\mathbf{k}}) + f(E_{\mathbf{k+q}}) - 1}{i\omega_n - (E_{\mathbf{k}} + E_{\mathbf{k+q}})} \\
&+ \frac{1}{4}\left(1 - \frac{\xi_{\mathbf{k}}\xi_{\mathbf{k+q}} + \Delta_{\mathbf{k}}\Delta_{\mathbf{k+q}}}{E_{\mathbf{k}}E_{\mathbf{k+q}}}\right) \frac{1 - f(E_{\mathbf{k}}) - f(E_{\mathbf{k+q}})}{i\omega_n + (E_{\mathbf{k}} + E_{\mathbf{k+q}})}. \quad (8.4)
\end{aligned}
$$

Here, $E_{\mathbf{k}}^2 = \xi_{\mathbf{k}}^2 + \Delta_{\mathbf{k}}^2$ and $\xi_{\mathbf{k}} = \varepsilon_{\mathbf{k}} - \mu$ and $\Delta_{\mathbf{k}} = \frac{\Delta_0}{2}(\cos k_x - \cos k_y)$. The full susceptibility $\chi(\mathbf{q}, i\omega_n)$ is of the RPA form (see below)

$$
\chi(\mathbf{q}, i\omega_n) = \frac{\chi^0_{BCS}(\mathbf{q}, i\omega_n)}{1 - U\chi^0_{BCS}(\mathbf{q}, i\omega_n)}, \quad (8.5)
$$

where U is the Coulomb repulsion. In the $t - J$ model, $\chi(\mathbf{q}, i\omega_n)$ is similar to Eqn. (8.5) but with $U \to J(\cos q_x + \cos q_y)$. Note, that the assumption of a spatially homogeneous phase allows us to write the spin susceptibility solely in momentum space and the remaining problem is to perform the $\mathbf{k}$-sum in Eqn. (8.4). Furthermore, since there is no spin ordering the susceptibility tensor is isotropic and hence carries no cartesian indices. Life will become more complicated in the next section.

In the literature this approach to the spin dynamics was first taken by Wermbter and Tewordt[291], Si *et al.*[292], Bulut *et al.*[293, 294], and Lavagna and Stemmann[295] to understand the NMR and neutron scattering data on LSCO. Later, when higher resolution neutron measurements became available, Dahm *et al.*[296], Brinckmann and Lee[297], Kao *et al.*[298], Norman[299], and Pfeuty and Onufrieva[300] realized the importance of the correct detailed bandstructure $\varepsilon_{\mathbf{k}}$. Rather extensive spin fluctuation studies have also been performed within the spin-fermion[301] model. Finally, as discussed previously, in the SO(5) model there is a natural magnetic Goldstone mode within the superconducting state which exists in the particle-particle channel[243].

In the following we study the salient features of the spin susceptibility in the particle-hole channel resulting from Eqn. (8.4)-(8.5). In particular, this model will be seen to reproduce the experimental detection of a downward dispersion of the resonance mode.

8.2.1   The two-particle continuum of a d-wave superconductor

Since the most important input to Eqn. (8.5) is the bandstructure $\varepsilon_{\mathbf{k}}$ we use a photoemission fit by Norman[299]: $\varepsilon_{\mathbf{k}} = \sum_i c_i \eta_i(\mathbf{k})$ with the coefficients c_i and

basis functions $\eta_i(\mathbf{k})$ given by

c_i	$\eta_i(\mathbf{k})$
0.1197	1
-0.5881	$\frac{1}{2}\left(\cos(k_x) + \cos(k_y)\right)$
0.1461	$\cos(k_x)\cos(k_y)$
0.0095	$\frac{1}{2}\left(\cos(2k_x) + \cos(2k_y)\right)$
-0.1298	$\frac{1}{2}\left(\cos(2k_x)\cos(k_y) + \cos(k_x)\cos(2k_y)\right)$
0.0069	$\cos(2k_x)\cos(2k_y)$

$$(8.6)$$

In Fig. 8.6 we plot the Fermi surface and a set of constant energy contours for this dispersion. The bandstructure fit was performed to optimally doped BSCCO and is believed to be similar to optimally doped YBCO. As opposed
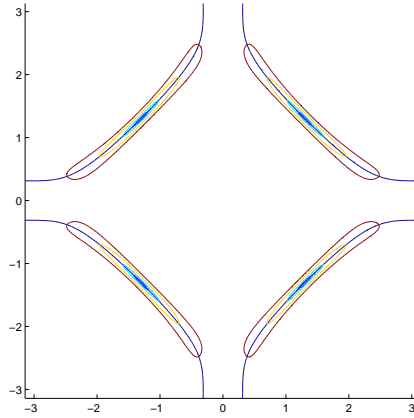
Figure 8.6: Fermi surface and contours of constant energy for the bandstructure in Table 8.6. The opposite sign between nearest and next-nearest neighbor hopping leads to a hole-like Fermi surface. The flat contours of constant energy leads to dynamical nesting that favor peaks in $\chi(\mathbf{q},\omega)$ at connecting wave vectors.

to the banana shaped contours of constant energy encountered earlier, the contours shown in Fig. 8.6 are very flat. We expect strong weight to be present at wave vectors (nesting vectors) connecting the flat parts of the contours.
In the following the $\mathbf{k}$ sums in Eqn. (8.4) is performed numerically by dividing the Brillouin zone in the a 1200×1200 mesh and introducing a small smearing $\Gamma = 0.5$meV. The temperature is set by $kT = \Gamma$ which corresponds to 5.5K. In Fig. 8.7 we plot the bare susceptibilities $\mathrm{Re}\chi^0(\mathbf{q},\omega)$ and $\mathrm{Im}\chi^0(\mathbf{q},\omega)$ for $\mathbf{q} = (\pi, q_y)$ with $q_y = 0.7\pi, 0.8\pi, 0.9\pi, \pi$. The imaginary part clearly reveals a gap by exhibiting a threshold energy to particle-hole excitations. By virtue of the Kramers-Kronig relations the steps in $\mathrm{Im}\chi^0(\mathbf{q},\omega)$ turns into logarithmic singularities in $\mathrm{Re}\chi^0(\mathbf{q},\omega)$. Clearly, the excitation gap $\omega_{\mathbf{q}}$ (the spin-gap) to electron-hole excitations varies with q_y as can be seen from the low-energy part of $\mathrm{Im}\chi^0(\mathbf{q},\omega)$. In Fig. 8.8 we map out the boundary to the continuum,
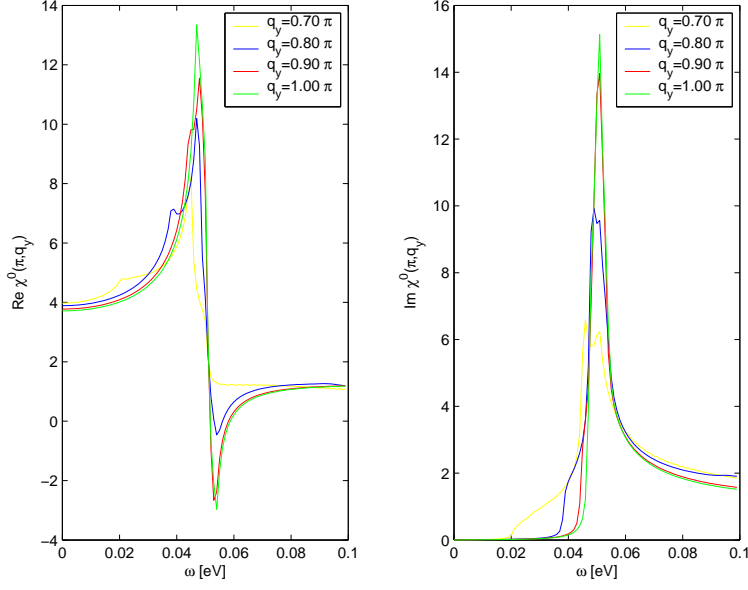
Figure 8.7: The bare spin susceptibility $\mathrm{Re}\chi^0(\mathbf{q},\omega)$ (left) and $\mathrm{Im}\chi^0(\mathbf{q},\omega)$ (right) as a function of energy ω as a selected set of wave vectors $\mathbf{q} = (\pi, q_y)$ with $q_y = 0.7\pi, 0.8\pi, 0.9\pi, \pi$.

$\omega_{\mathbf{q}} = \min_{\mathbf{k}}(E_{\mathbf{k}} + E_{\mathbf{q}+\mathbf{k}})$ where $E_{\mathbf{k}}$ is the quasi-particle energy in the superconducting state. As seen, the continuum edge has a nontrivial downward curvature from the (π, π) point. This is a characteristic feature of d-wave pairing. For a conventional BCS superconductor with s-wave pairing the electron-hole continuum is independent of wave vector, $\omega_{\mathbf{q}} = 2\Delta$ for all $\mathbf{q}$. In the direction (π, q_y) we see that there is a full gap below which there are no magnetic two-particle fluctuations. This conclusion changes along any line where (q_x, q_y) coincides with the node-node scattering vector. From Fig. 8.8 we also see that above the spin gap there is only a very narrow region in $\mathbf{q}$-space near (π, π) where particle-hole excitations are allowed.

It is interesting that recent inelastic neutron scattering experiments by Pailhes *et al.*[302] have found a 'silent band' and new dispersing modes evident in the constant energy scans in the superconducting state of $\mathrm{YBa_2Cu_3O_{6.85}}$. In the picture of Fig. 8.8 the silent band corresponds to the narrow low-energy continuum strip around $q_y = 0.7\pi$ and $q_y = 1.3\pi$ and the new modes to the resonance branches dispersing through these strips into the spin gapped regions at $q_y > 1.3\pi$ and $q_y < 0.7\pi$.
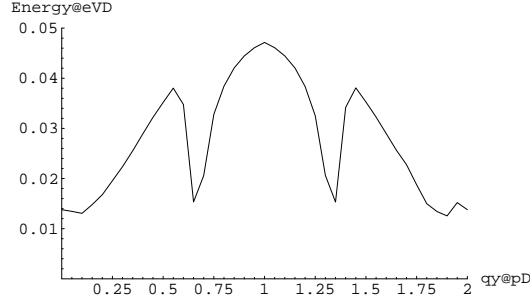
Figure 8.8: Lower edge of the particle-hole continuum along (π, q_y), i.e. $\omega_{\mathbf{q}} = \min_{\mathbf{k}}(E_{\mathbf{k}} + E_{\mathbf{q}+\mathbf{k}})$.

8.2.2   Collective modes in a homogeneous d-wave superconductor

In this subsection I discuss the collective effects that arise in a d-wave superconductor in the presence of interactions, i.e.

$$\chi(\mathbf{q}, i\omega_n) = \frac{\chi^0_{BCS}(\mathbf{q}, i\omega_n)}{1 - J\chi^0_{BCS}(\mathbf{q}, i\omega_n)}. \tag{8.7}$$

We assume a constant superexchange interaction J, and have checked that the omission of the nearest neighbor term, $\cos(q_x) + \cos(q_y)$, leads to only minor changes. As an interlude, one may wonder if the static Stoner criterion $1 - J\mathrm{Re}\chi^0(\mathbf{q}, 0) = 0$ for a spin-density wave (SDW) instability is ever satisfied. It can be shown, however, that for the value of the superexchange interaction J utilized below, the SDW instability is not fulfilled and the superconducting state exhibits only short range spin fluctuations[297].

To study the collective dynamical effects it is evident that energies and wave vectors satisfying the dynamical Stoner criterion

$$1 - J\mathrm{Re}\chi^0(\mathbf{q}, \Omega) = 0 \quad \text{and} \quad \mathrm{Im}\chi^0(\mathbf{q}, \Omega) \text{ small}, \tag{8.8}$$

cause resonances or poles in the final spin susceptibility $\chi(\mathbf{q}, \omega)$. In Fig. 8.9 we plot again the bare susceptibility $\mathrm{Re}\chi^0(\mathbf{Q}, \omega)$ and $\mathrm{Im}\chi^0(\mathbf{Q}, \omega)$ at $\mathbf{q} = \mathbf{Q} = (\pi, \pi)$. From $\mathrm{Re}\chi^0(\mathbf{Q}, \omega)$ we see that if $J = 155\mathrm{meV}$ the resonance condition is fulfilled at some energy $\Omega_{\mathbf{Q}} \approx 40\mathrm{meV}$ that lies below the continuum, i.e. undamped since $\mathrm{Im}\chi^0(\mathbf{Q}, \Omega_{\mathbf{Q}}) = 0$. In this sense the resonance mode is a particle-hole bound state. Note that the value $J = 155\mathrm{meV}$ is very close the the experimental estimates $J \approx t/3 \approx 130\mathrm{meV}$. The full spin susceptibility $\chi(\mathbf{Q}, \omega)$ at $\mathbf{q} = \mathbf{Q} = (\pi, \pi)$ is shown as a function of energy to the right in Fig. 8.9. As can be seen, there is a δ-function like undamped peak around 40meV in agreement with a large number of inelastic neutron scattering experiments on YBCO.
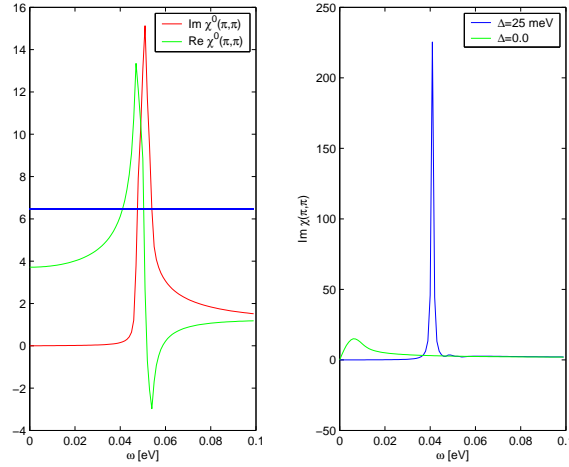
Figure 8.9: Left: $\mathrm{Re}\chi^0(\mathbf{Q},\omega)$ (green) and $\mathrm{Im}\chi^0(\mathbf{Q},\omega)$ (red) with $\mathbf{Q} = (\pi, \pi)$
The vertical line indicates the value $1/J$ with $J = 155\mathrm{meV}$. The intersection
point between $1/J$ and $\mathrm{Re}\chi^0(\mathbf{Q},\omega)$ happens within the gap creating a true
bound state. This is shown to the right where $\mathrm{Im}\chi(\mathbf{Q},\omega)$ exhibits a δ-function
peak at $41\mathrm{meV}$ (blue). The green line shows $\mathrm{Im}\chi(\mathbf{Q},\omega)$ in the normal state.

For other bandstructures approximately similar to the $t-t'$-band the resonance
is also present, even though its intensity and sharpness in energy is different
from the results presented here. The fact that the (π, π) resonance is *not* re-
lated to the bi-layer property of YBCO of BSCCO, as was initially proposed,
is in agreement with the finding of a commensurate resonance in single-layer
$\mathrm{Tl_2Ba_2CuO_{6+\delta}}$[290].
A important question is related to the dispersion of this mode $\Omega_{\mathbf{q}}$ when moving
away from (π, π). In Fig. 8.10 (left) we show the position of the resonance
condition along the line (π, q_y) and Fig. 8.10 (right) displays the full suscepti-
bility $\mathrm{Im}\chi^0(\mathbf{q},\omega)$ as a function of energy at various values of q_y. We see that
indeed the mode disperses downward until it merges with the continuum and
fades away at lower energies. This is exactly what is observed in the neutron
scattering experiments on YBCO.
The downward dispersion of the resonance condition is a feature that is very
sensitive to the bandstructure. For instance, a typical $t-t'$-band does not lead
to a strong incommensurate intensity.
In Fig. 8.11 we show a series of constant energy cuts through the 2D Brillouin
zone. Clearly, there is a incommensurate-commensurate continuous evolution
of the spin exciton with an intensity maximum at (π, π). Again, this seems
consistent with the experimental results discussed in the beginning of this
chapter. The evolution of the resonance energy with doping can also be ex-
plained within this picture. However, since the d-wave superconducting phase
is crucial, there are problems with the existence of the resonance above T_c.
This may be cured by the presence of superconducting fluctuations (preformed
pairs) in the pseudogap phase in underdoped regime. The dramatically differ-
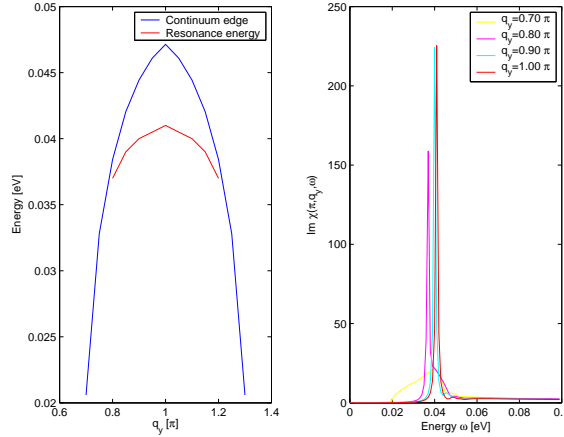
Figure 8.10: Left: Continuum edge (blue) and resonance condition $\mathrm{Re}\chi^0(\mathbf{q}, \Omega) = 1/J$ (green) as a function of q_y with $q_x = \pi$ fixed. The collective mode clearly lives inside the gap and merges with the continuum around $q_x = 0.75\pi$. Right: The full spin susceptibility $\mathrm{Im}\chi(\mathbf{q}, \omega)$ as a function of energy ω. As expected the mode fades away when is crashes into the continuum.

ent behavior in the normal state is illustrated in the right graph of Fig. 8.9 (green line). Clearly, $\mathrm{Im}\chi(\mathbf{q}, \omega)$ is not of resonant behavior.

A striking property of this approach is the lack of structure in $\mathrm{Im}\chi(\mathbf{q}, \omega)$ above the resonance. In fact, the constant energy maps similar to Fig. 8.11 at higher energy (not shown) remain completely featureless. This is contrary to the peak rotation seen in LBCO shown in Fig. 8.4. However, for the LBCO materials around $n_h = 1/8$ the superconductivity is strongly suppressed. This brings about the question of what happens to the incommensurate-commensurate crossover when we reduce the gap Δ. In Fig. 8.12 I plot again the real and imaginary part of $\chi^0(\mathbf{Q}, \omega)$ at the commensurate wave vector $\mathbf{Q} = (\pi, \pi)$ obtained for different values of the maximum gap Δ. From these plots we expect the properties of $\mathrm{Im}\chi(\mathbf{q}, \omega)$ at lower gap values Δ to be similar to the ones at $\Delta = 25\mathrm{meV}$ except from a shift to lower energy of the incommensurate-commensurate crossover. This expectation can be confirmed by constant energy plots (not shown) similar to Fig. 8.11. Again this seems problematic for the recent LBCO data where $T_c = 3\mathrm{K}$ and Δ is (presumably) small while the incommensurate-commensurate crossover happens around 60 meV. Furthermore, even for the YBCO systems, in the underdoped regime the resonance energy is known to scale with T_c (Eqn. 8.3), i.e. it increases as the doping is increased. *This is contrary to the maximum value of the gap Δ which decreases monotonically as the doping is increased.* This latter point is a serious objection to the approach presented in this section.
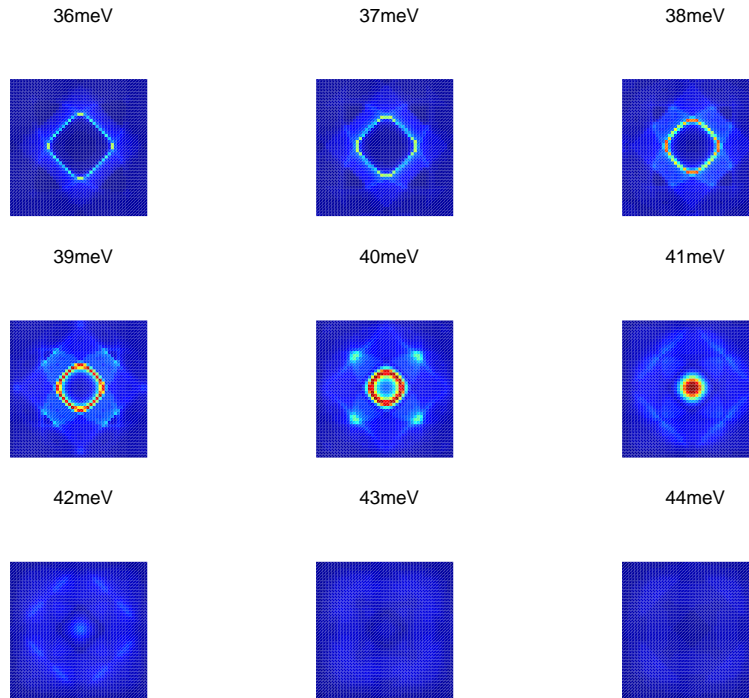
Figure 8.11: Constant energy cuts of $\mathrm{Im}\chi(\mathbf{q},\omega)$ through the 2D Brillouin zone. The images are plotted on the same scale for comparison. The incommensurate peaks are clearly seen to evolve continuously into the resonance at 41meV.

8.3 Spin susceptibility in the stripe phase

In the previous section the spin susceptibility was calculated from the starting point of a homogeneous d-wave BCS superconductor. This approach was fairly successful in reproducing some of the important features of the measured neutron scattering data. What is the motivation for attempting to go beyond the picture of collective modes in a homogeneous d-wave superconductor? Besides the reasons mentioned in the last part of the previous section, we are motivated by the strong experimental evidence for striped phases, particularly in LSCO. Furthermore, the downward dispersion of the collective resonance mode could alternatively be interpreted as the crossing of two magnon branches emerging from incommensurate momentum positions close to (π, π). This latter picture is what we will study in greater detail in the remainder of this chapter.

8.3.1 A spin-only approach to the incommensurate stripe phase

The large U limit of the Hubbard model is given by the t-J-model which, at half filling, reduces to the Heisenberg model due to the constraint of no double

Figure 8.12: Left: $\text{Re}\chi^0(\mathbf{Q},\omega)$ versus energy, $\mathbf{Q} = (\pi,\pi)$, the vertical line indicates the value $1/J$ with $J = 155$meV. The intersection point between $1/J$ and $\text{Re}\chi^0(\mathbf{Q},\omega)$ happens within the gap creating a true bound state. Right: $\text{Im}\chi^0(\mathbf{Q},\omega)$ versus energy

occupancy,

$$H = J \sum_{<ij>} \hat{\mathbf{S}}_i \cdot \hat{\mathbf{S}}_j, \qquad (8.9)$$

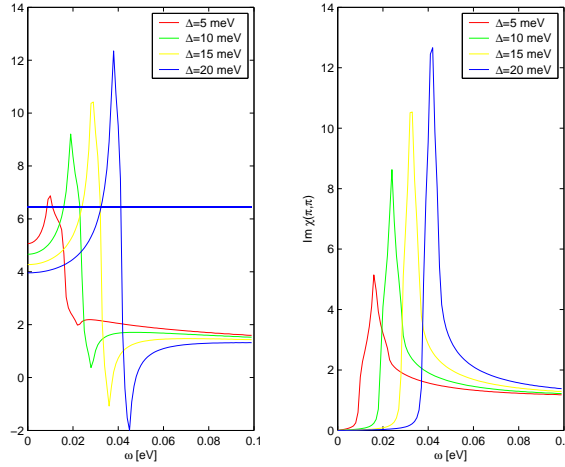with $J = 4t^2/U$. As a first approach to the low energy excitations in an incommensurate stripe phase we might be tempted to forget about the charges for a moment and solve the resulting spin-only problem[303, 304]. By conventional linear spin-wave theory this is indeed what Batista *et al.*[305] and Krüger *et al.*[306] recently did, i.e. use Eqn. (8.9) in a stripe spin state and obtain the corresponding spin waves. The qualitative evolution of the incommensurate peaks have also been discussed within a phenomenological string-stripe model by Hassselmann *et al.*[307]

Fig. 8.13 shows the resulting spin wave dispersion $\omega(q_x, \pi)$ as obtained by Krüger *et al.*[306] in the case of vertical stripes with spacing $p = 3, 4, 5$. The parameter λ determines the exchange coupling J' between the spins across a charge stripe, $J' = \lambda J$, with J being the exchange within a magnetic domain. Clearly, the Goldstone modes disperse to zero energy where they develop into the Bragg peaks expected for the static incommensurate input spin pattern, i.e. at $q_x = \pi \pm 2\pi/2p$ which in units of 2π, as in Fig. 8.13, becomes $q_x = 0.5 \pm 1/2p$. The spin wave branches merge at (π, π) at a finite energy ω_π which depends on both λ and p. Therefore, in the spin-only picture, the resonance is nothing but the energy associated with the lowest spin excitation at (π, π). The linear dependence on $1/p$ ($\omega_\pi = \alpha 1/p$) is in agreement with the neutron scattering measurements on YBCO. This follows from the Yamada relation[141]

$$kT_c \sim \delta = 1/p \qquad (8.10)$$
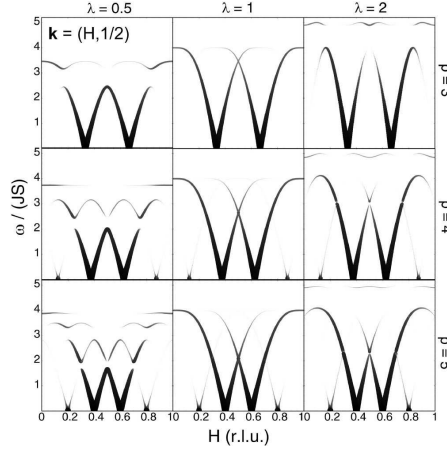
Figure 8.13: Spin wave dispersions for vertical site-centered stripes along (H, π) for different stripe spacings p and couplings (i.e. exchange couplings across the stripes) λ. Adapted from Ref. [306].

and the empirical relation, $\omega_\pi \approx 5kT_c$, for the (π, π) resonance. From the incommensurability δ in LSCO and the measured spin-wave velocity Batista *et al.*[305] predicted a resonance energy of $14 - 16$meV in 10% doped LSCO. This energy is not in agreement with recent inelastic neutron measurements however[280]. Another important discrepancy between the spin-only predictions and the neutron data is the consistent experimental lack of the outward dispersing branches of the spin waves, i.e. the mode dispersing to higher (smaller) values of q_x from the Bragg points $0.5 + 1/2p$ $(0.5 - 1/2p)$. As opposed to the nickel-oxide systems, neutron measurements on the cuprates have never found any evidence for these "wings" seen in all the plots in Fig. 8.13. In this respect the mode dispersion of the spin exciton in a homogeneous superconductor agrees better with the experiments. In the present section however, we insist on the stripe picture but include the charges when obtaining the spin fluctuations.

8.4 Fluctuations around the mean-field state of the minimal model

In this section we study the formalism used to calculate the spin fluctuations around stable spin- and charge configurations found within the minimal model discussed in the previous chapters. We will be mostly interested in fluctuations around the stripe phase.

In chapter 1 we derived the following effective action

$$S_{\text{eff}}(\mathbf{M}, \Delta, \mathbf{H}) = \int d\tau \sum_{ij\sigma} (c_{i\sigma}^*(\partial_\tau - \mu)c_{i\sigma} - [t_{ij}c_{i\sigma}^*c_{j\sigma} + \text{H.c}] - \mu c_{i\sigma}^*c_{i\sigma} - \mathbf{M}_i \cdot \mathbf{S}_i$$

$$+ \quad \left[\Delta_{ij}c_{j\downarrow}c_{i\uparrow} + \Delta_{ij}c^*_{i\uparrow}c^*_{j\downarrow}\right] + \frac{3}{8U}|\mathbf{M}_i|^2 + \frac{1}{V}\Delta^2_{ij} - \mathbf{H}_i \cdot \mathbf{S}_i \Bigg). \quad (8.11)$$

Here, I have here added the source term $-\mathbf{H}_i \cdot \mathbf{S}_i$. By shifting the integration variables $\mathbf{M}_i \to \mathbf{M}_i - \mathbf{H}_i$ of the partition function, the action becomes

$$S_{\text{eff}}(\mathbf{M}, \Delta, \mathbf{H}) = S_{\text{eff}}(\mathbf{M}, \Delta, 0) + \frac{3}{8U}\int d\tau \sum_i \mathbf{H}_i^2 - \frac{3}{4U}\int d\tau \sum_i \mathbf{H}_i \cdot \mathbf{M}_i. \quad (8.12)$$

The fermions can be integrated out of $S_{\text{eff}}(\mathbf{M}, \Delta, 0)$ to obtain, again in terms of the notation of chapter one,

$$S_{\text{eff}}(\mathbf{M}, \Delta, 0) = \int d\tau \left(\sum_i \frac{3}{8U}|\mathbf{M}_i|^2 + \sum_{<ij>} \frac{1}{V}\Delta^2_{ij}\right)$$

$$- \quad \frac{1}{2}\text{Tr} \ln\left[1_{4\times4}\partial_\tau - \mathcal{H}_0(t_{ij}, \mu, \mathbf{M}_i, \Delta_{ij})\right]. \quad (8.13)$$

In the following we write $\mathcal{H}_0(t_{ij}, \mu, \mathbf{M}_i, \Delta_{ij}) = \mathcal{H}_0(\mathbf{M}_i, \Delta_{ij})$ and $1_{4\times4} = 1$. To obtain the spectrum of the bosonic spin excitations we start by expanding the effective action S_{eff} in powers of the deviation $\delta\mathbf{M}_i(\tau)$ from the static mean-field value $\mathbf{M}_i^c$, i.e.

$$\mathbf{M}_i(\tau) = \mathbf{M}_i^c + \delta\mathbf{M}_i(\tau). \quad (8.14)$$

Since the matrix $\mathcal{H}_0$ given by Eqn. (1.38) is linear in $\mathbf{M}_i$ it is evident that we have

$$\mathcal{H}_0(\mathbf{M}_i(\tau)) = \mathcal{H}_0(\mathbf{M}_i^c) + \mathcal{H}_0(\delta\mathbf{M}_i(\tau)), \quad (8.15)$$

with

$$\mathcal{H}_0(\delta\mathbf{M}_i(\tau)) = -(\delta\mathbf{M}_i(\tau) \cdot \frac{\boldsymbol{\sigma}}{2}) \otimes \tau^z, \quad (8.16)$$

where the imaginary time τ should not be confused with the Nambu space Pauli matrices τ^α. Thus, the action becomes

$$S_{\text{eff}}(\mathbf{M}, \Delta, \mathbf{H}) = \int d\tau \left(\sum_i \frac{3}{8U}\left((\mathbf{M}_i^c)^2 + \delta\mathbf{M}_i(\tau)^2 + 2\mathbf{M}_i^c \cdot \delta\mathbf{M}_i(\tau)\right) + \sum_{<ij>} \frac{1}{V}\Delta^2_{ij}\right)$$

$$- \quad \frac{1}{2}\text{Tr} \ln\left[\partial_\tau - \mathcal{H}_0(\mathbf{M}_i^c, \Delta_{ij}) - \mathcal{H}_0(\delta\mathbf{M}_i(\tau), \Delta_{ij})\right]$$

$$+ \quad \frac{3}{8U}\int d\tau \sum_i \mathbf{H}_i^2 - \frac{3}{4U}\int d\tau \sum_i \mathbf{H}_i \cdot (\mathbf{M}_i^c + \delta\mathbf{M}_i(\tau)). \quad (8.17)$$

As usual we may write

$$+ \quad \text{Tr} \ln\left[\partial_\tau - \mathcal{H}_0(\mathbf{M}_i^c, \Delta_{ij}) - \mathcal{H}_0(\delta\mathbf{M}_i(\tau), \Delta_{ij})\right] \quad (8.18)$$

$$= \text{Tr} \ln \left[(\partial_\tau - \mathcal{H}_0(\mathbf{M}_i^c, \Delta_{ij})) \left(1 - (\partial_\tau - \mathcal{H}_0(\mathbf{M}_i^c, \Delta_{ij}))^{-1} \mathcal{H}_0(\delta \mathbf{M}_i(\tau), \Delta_{ij}) \right) \right]$$

$$= \text{Tr} \ln \left[(\partial_\tau - \mathcal{H}_0(\mathbf{M}_i^c, \Delta_{ij})) \left(1 + \mathcal{G}(\mathbf{M}^c) \mathcal{H}_0(\delta \mathbf{M}_i(\tau), \Delta_{ij}) \right) \right]$$

$$= \text{Tr} \ln \left[\partial_\tau - \mathcal{H}_0(\mathbf{M}_i^c, \Delta_{ij}) \right] - \text{Tr} \sum_{n=1}^{\infty} \frac{(-1)^n}{n} \left[\mathcal{G}(\mathbf{M}^c) \mathcal{H}_0(\delta \mathbf{M}_i(\tau), \Delta_{ij}) \right]^n$$

where

$$\mathcal{G}(\mathbf{M}^c) = -\frac{1}{\partial_\tau - \mathcal{H}_0(\mathbf{M}_i^c, \Delta_{ij})}. \tag{8.19}$$

To Gaussian order $(n = 2)$ we then get

$$S_{\text{eff}}(\mathbf{M}, \Delta, \mathbf{H}) = \int d\tau \left(\frac{3}{8U} \sum_i (\mathbf{M}_i^c)^2 + \frac{3}{8U} \sum_i \mathbf{H}_i^2 - \frac{3}{4U} \sum_i \mathbf{H}_i \cdot \mathbf{M}_i^c + \sum_{<ij>} \frac{1}{V} \Delta_{ij}^2 \right) \tag{8.20}$$

$$+ \int d\tau \left(\frac{3}{4U} \sum_i (\mathbf{M}_i^c - \mathbf{H}_i) \cdot \delta \mathbf{M}_i(\tau) - \frac{1}{2} \text{Tr} \, \mathcal{G}(\mathbf{M}^c) \mathcal{H}_0(\delta \mathbf{M}_i(\tau), \Delta_{ij}) \right)$$

$$- \frac{1}{2} \text{Tr} \ln \left[\partial_\tau - \mathcal{H}_0(\mathbf{M}_i^c, \Delta_{ij}) \right]$$

$$+ \int d\tau \left[\sum_i \frac{3}{8U} \delta \mathbf{M}_i(\tau)^2 + \frac{1}{4} \text{Tr} \, \mathcal{G}(\mathbf{M}^c) \mathcal{H}_0(\delta \mathbf{M}_i(\tau), \Delta_{ij}) \mathcal{G}(\mathbf{M}^c) \mathcal{H}_0(\delta \mathbf{M}_i(\tau), \Delta_{ij}) \right],$$

which by virtue of the minimum condition for $\mathbf{M}^c$, becomes

$$S_{\text{eff}}(\mathbf{M}, \Delta, \mathbf{H}) = \int d\tau \left(\frac{3}{8U} \sum_i (\mathbf{M}_i^c)^2 + \frac{3}{8U} \sum_i \mathbf{H}_i^2 - \frac{3}{4U} \sum_i \mathbf{H}_i \cdot \mathbf{M}_i^c + \sum_{<ij>} \frac{1}{V} \Delta_{ij}^2 \right) \tag{8.21}$$

$$- \int d\tau \frac{3}{4U} \sum_i \mathbf{H}_i \cdot \delta \mathbf{M}_i(\tau) - \frac{1}{2} \text{Tr} \ln \left[\partial_\tau - \mathcal{H}_0(\mathbf{M}_i^c, \Delta_{ij}) \right]$$

$$+ \int d\tau \left[\sum_i \frac{3}{8U} \delta \mathbf{M}_i(\tau)^2 + \frac{1}{4} \text{Tr} \, \mathcal{G}(\mathbf{M}^c) \mathcal{H}_0(\delta \mathbf{M}_i(\tau), \Delta_{ij}) \mathcal{G}(\mathbf{M}^c) \mathcal{H}_0(\delta \mathbf{M}_i(\tau), \Delta_{ij}) \right].$$

For the particle-hole bubble in the last term we have

$$+ \frac{1}{4} \text{Tr} \, \mathcal{G}(\mathbf{M}^c) \mathcal{H}_0(\delta \mathbf{M}_i(\tau), \Delta_{ij}) \mathcal{G}(\mathbf{M}^c) \mathcal{H}_0(\delta \mathbf{M}_i(\tau), \Delta_{ij}) \tag{8.22}$$

$$= \frac{1}{16} \int d\tau \sum_{i\alpha} \langle \alpha i \tau | \mathcal{G}(\mathbf{M}^c)(\delta \mathbf{M}^a \sigma^a \otimes \tau^z) \mathcal{G}(\mathbf{M}^c)(\delta \mathbf{M}^b \sigma^b \otimes \tau^z) | \tau i \alpha \rangle$$

$$= \frac{1}{16} \int d\tau d\tau' \sum_{ij} \mathcal{G}_{\alpha\beta}(i\tau; j\tau'\mathbf{M}^c)(\sigma^a \otimes \tau^z)_{\beta\gamma} \mathcal{G}_{\gamma\delta}(j\tau'; i\tau\mathbf{M}^c)(\sigma^b \otimes \tau^z)_{\delta\alpha} \delta\mathbf{M}_i^a(\tau)\delta\mathbf{M}_j^b(\tau'),$$

with summation over all sub- and super indices. We define the kernel K^{ab} by

$$K^{ab} = \frac{1}{2}\mathcal{G}_{\alpha\beta}(i\tau; j\tau'\mathbf{M}^c)(\sigma^a \otimes \tau^z)_{\beta\gamma} \mathcal{G}_{\gamma\delta}(j\tau'; i\tau\mathbf{M}^c)(\sigma^b \otimes \tau^z)_{\delta\alpha} \qquad (8.23)$$

and redefine $\delta\mathbf{M} \to \frac{3}{4U}\delta\mathbf{M}$ ($\delta\mathbf{M}$ dimensionless) to write the action as

$$
\begin{aligned}
S_{\text{eff}}(\mathbf{M}, \Delta, \mathbf{H}) &= \int d\tau \left(\frac{2U}{3}\sum_i (\mathbf{M}_i^c)^2 + \frac{3}{8U}\sum_i \mathbf{H}_i^2 - \sum_i \mathbf{H}_i \cdot \mathbf{M}_i^c + \sum_{<ij>} \frac{1}{V}\Delta_{ij}^2 \right) \\
&\quad - \int d\tau \sum_i \mathbf{H}_i \cdot \delta\mathbf{M}_i(\tau) - \frac{1}{2}\text{Tr} \ln \left[\partial_\tau - \mathcal{H}_0(\mathbf{M}_i^c, \Delta_{ij}) \right] \qquad (8.24) \\
&\quad + \frac{1}{2}\int d\tau d\tau' \sum_{abij} \frac{4U}{3}\left[\delta^{ab}\delta_{ij}\delta(\tau - \tau') + \frac{U}{3}K^{ab} \right] \delta\mathbf{M}_i^a(\tau)\delta\mathbf{M}_j^b(\tau').
\end{aligned}
$$

In the homogeneous case the parts of the action $\tilde{S}_{\text{eff}}(\delta\mathbf{M}, \mathbf{H})$ containing $\delta\mathbf{M}$ (and the $\mathbf{H}^2$ term) is given by

$$
\begin{aligned}
\tilde{S}_{\text{eff}}(\delta\mathbf{M}, \mathbf{H}) &= \frac{3}{8U}\frac{1}{\beta}\sum_{\mathbf{k}\omega_n a} \mathbf{H}^a(\mathbf{k}, \omega_n)\mathbf{H}^{*a}(\mathbf{k}, \omega_n) \qquad (8.25) \\
&\quad - \frac{1}{2}\frac{1}{\beta}\sum_{\mathbf{k}\omega_n a} \left[\delta\mathbf{M}^a(\mathbf{k}, \omega_n)\mathbf{H}^{*a}(\mathbf{k}, \omega_n) + \delta\mathbf{M}^{*a}(\mathbf{k}, \omega_n)\mathbf{H}^a(\mathbf{k}, \omega_n) \right] \\
&\quad + \frac{1}{2}\frac{1}{\beta}\sum_{\mathbf{k},\omega_n a} \frac{4U}{3}\left[\delta^{ab} + \frac{U}{3}K^{ab}(\mathbf{k}, \omega_n) \right] \delta\mathbf{M}^a(\mathbf{k}, \omega_n)\delta\mathbf{M}^{*b}(\mathbf{k}, \omega_n).
\end{aligned}
$$

By integrating out the bosonic mode this reduces to

$$\tilde{S}_{\text{eff}}(\mathbf{H}) = \frac{3}{8U}\frac{1}{\beta}\sum_{\mathbf{k}\omega_n ab} \mathbf{H}^a(\mathbf{k}, \omega_n)\left(\delta^{ab} - \frac{1}{\delta^{ab} + \frac{U}{3}K^{ab}(\mathbf{k}, \omega_n)} \right) \mathbf{H}^{*b}(\mathbf{k}, \omega_n).$$
$$(8.26)$$

For the τ-ordered spin-spin correlation function we have

$$
\begin{aligned}
\chi^{ab}(i\tau; j\tau') &= -\langle T_\tau S_i^a(\tau)S_j^b(\tau')\rangle = -\frac{1}{Z}\int \mathcal{D}[cc^*]S_i^a(\tau)S_j^b(\tau')e^{-S} = \qquad (8.27) \\
&\quad - \frac{1}{Z}\frac{1}{\beta^2}\sum_{\omega_n\omega_n'}\sum_{\mathbf{q}\mathbf{q}'}\int \mathcal{D}[cc^*]S_{\mathbf{q}}^a(\omega_n)S_{\mathbf{q}'}^b(\omega_n')e^{-S}e^{i\mathbf{q}\cdot\mathbf{r}_i - i\omega_n\tau + i\mathbf{q}'\cdot\mathbf{r}_j - i\omega_n'\tau'} =
\end{aligned}
$$

$$- \frac{1}{Z} \frac{1}{\beta^2} \sum_{\omega_n \omega'_n} \sum_{\mathbf{q}\mathbf{q}'} \int \mathcal{D}[cc^*] \frac{\delta^2}{\delta \mathbf{H}^a(-\mathbf{q}, -\omega_n) \delta \mathbf{H}^b(-\mathbf{q}', -\omega'_n)} e^{-S} e^{i\mathbf{q}\cdot\mathbf{r}_i - i\omega_n\tau + i\mathbf{q}'\cdot\mathbf{r}_j - i\omega'_n\tau'}.$$

By use of Eqn. (8.26) we therefore finally get

$$\chi^{ab}(i\tau; j\tau') = -\frac{3}{U} \frac{1}{\beta} \sum_{\mathbf{q}\omega_n} \left(\delta^{ab} - \frac{1}{\delta^{ab} + \frac{U}{3}K^{ab}(\mathbf{q}, \omega_n)} \right) e^{i\mathbf{q}\cdot(\mathbf{r}_i - \mathbf{r}_j) - i\omega_n(\tau - \tau')}, \quad (8.28)$$

or simply

$$\chi^{aa}(\mathbf{q}, \omega_n) = \frac{\chi_0(\mathbf{q}, \omega_n)}{1 - \frac{U}{3}\chi_0(\mathbf{q}, \omega_n)}, \quad (8.29)$$

with $\chi_0 = -K^{aa}$.

In the following we are interested in the ordered phases, i.e. when Δ_{ij} and $\mathbf{M}_i^c$ have acquired a finite expectation value. We denote the axis parallel to the assumed co-linear staggered magnetization as the z-axis. Thus, the order parameter $\mathbf{M}_i$ is of the form

$$\mathbf{M}_i^c = (0, 0, M_i). \quad (8.30)$$

As we know from the staggered antiferromagnet[308], there exists high energy longitudinal amplitude fluctuations above a mode gap that increases rapidly with the Coulomb repulsion U. The low energy spin fluctuations are expected to be transverse to this direction. Therefore, in the following, we restrict the discussion to the case where

$$\delta \mathbf{M}_i(\tau) = (\delta M_i^x(\tau), \delta M_i^y(\tau), 0). \quad (8.31)$$

In this case we can determine the mean-field Greens function $G_{\alpha\beta}(i, \tau; j, \tau'; \mathbf{M}_i^c)$ defined by

$$G_{\alpha\beta}(i, \tau; j, \tau'; \mathbf{M}_i^c) = -\langle i, \tau, \alpha | \frac{1}{\partial_\tau - \mathcal{H}_0(\mathbf{M}_i^c)} | j, \tau', \beta \rangle. \quad (8.32)$$

As opposed to the usual 2×2 Greens function matrices known from the pure magnetic or pure superconducting phases, the Greens function in Eqn. (8.32) is 4×4.

Since the classical mean-field has no dynamics we can also write Eqn. (8.32) as

$$G_{\alpha\beta}(i, j, i\omega_n; \mathbf{M}_i^c) = -\langle i, \alpha | \frac{1}{i\omega_n - \mathcal{H}_0(\mathbf{M}_i^c)} | j, \beta \rangle. \quad (8.33)$$

If the system was in a homogeneous phase of d-wave superconducting order, we can Fourier transform Eqn. (1.38) and obtain

$$\mathcal{H}_0 = \xi_{\mathbf{k}} 1 \otimes \tau^z - \Delta_{\mathbf{k}} \sigma^y \otimes \tau^y, \quad (8.34)$$

where

$$\xi_{\mathbf{k}} = -2t(\cos(k_x) + \cos(k_y)) - 4t'(\cos(k_x)\cos(k_y)) - \mu, \qquad (8.35)$$

$$\Delta_{\mathbf{k}} = \frac{\Delta}{2}(\cos(k_x) - \cos(k_y)), \qquad (8.36)$$

in the case of nearest (t) and next-nearest (t') neighbor hopping integrals and $d_{x^2-y^2}$-wave pairing. In this case we then get for the Greens function

$$G(\mathbf{k}, i\omega_n) = \frac{i\omega_n 1 + \xi_{\mathbf{k}}\sigma^z \otimes 1 + \Delta_{\mathbf{k}}\sigma^y \otimes \tau^y}{(i\omega_n)^2 - \xi_{\mathbf{k}}^2 - \Delta_{\mathbf{k}}^2}, \qquad (8.37)$$

which is nothing but a spin-expanded version of the Nambu Greens function for BCS superconductors. As usual the single-particle excitation energies are given by $E_{\mathbf{k}}^2 = \xi_{\mathbf{k}}^2 + \Delta_{\mathbf{k}}^2$.

On the other hand, when the system is in an pure antiferromagnetic state with $\mathbf{M}_i^c = (0, 0, M_i) = (0, 0, me^{i\mathbf{Q}\cdot\mathbf{r}_i})$ the excitation energies are $E_{\mathbf{k}}^2 = \xi_{\mathbf{k}}^2 + \frac{m}{4}^2$. In fact, to obtain a better feel for the formalism and test the computer routines it is instructive to briefly consider in the following the antiferromagnetic case. Later, we will not be interested in the homogeneous states, i.e. the states which are translational invariant within one or two lattice sites. Instead, we focus on the spin response from stripe phases which are translational invariant within a larger unit cell containing e.g. eight or sixteen lattice sites. In that case the Matsubara algebra is identical to the results above, but the Fourier transform of the real-space indices needs be done with a basis, the number of basis states equal to the number of sites in the unit cell.

8.5 Antiferromagnetic spin waves

Before discussing the general stripe ordered case, it is instructive to consider first the well known antiferromagnet[308]. In this case the Greens function

$$\mathcal{G}(i\tau; j\tau'; M^c) \equiv -\langle i\tau\alpha| \frac{1}{\partial_\tau + \mathcal{H}_0(M^c)} |j\tau'\beta\rangle \qquad (8.38)$$

and $\mathcal{H}_0(M^c)$ are determined from

$$\langle i\tau\alpha|\mathcal{H}_0(M^c)|j\tau'\beta\rangle = \left(-t\delta_{\langle ij\rangle} - t'\delta_{\langle\langle ij\rangle\rangle} - \mu\delta_{i,j}\right)\delta(\tau - \tau')\delta_{\alpha,\beta}$$

$$- \frac{M_i^c}{2}\tau_{\alpha\beta}^3\delta_{i,j}\delta(\tau - \tau') \qquad (8.39)$$

where $\langle\rangle$ $(\langle\langle\rangle\rangle)$ indicate nearest (next-nearest) neighbor sites. In the antiferro-magnetic phase, $M_i^c = M^c \exp(i\mathbf{Q} \cdot \mathbf{r}_i)$. We can multiply Eqn. (8.38) on both sides from the left by $\langle k\tau''\gamma|\partial_\tau + \mathcal{H}_0(M^c)|i\tau\alpha\rangle$ and sum over i, τ, α. In Fourier space the resulting equation becomes

$$-\delta_{\alpha\beta} = (-ip_n + \varepsilon_\mathbf{q} - \mu)\,\mathcal{G}_{\alpha\beta}(\mathbf{q}, p_n) - \frac{M^c}{2}\tau_{\alpha\gamma}^3 \mathcal{G}_{\gamma\beta}(\mathbf{q} - \mathbf{Q}, p_n) \qquad (8.40)$$

where

$$\varepsilon_\mathbf{q} = -2t\left(\cos q_x + \cos q_y\right) - 4t'\cos q_x \cos q_y. \qquad (8.41)$$

In terms of $\xi_\mathbf{q} = \varepsilon_\mathbf{q} - \mu$ and the vector $G(\mathbf{q}, p_n) = (\mathcal{G}(\mathbf{q}, p_n), \mathcal{G}(\mathbf{q} - \mathbf{Q}, p_n))^t$ we have

$$-\begin{pmatrix} \tau^0 \\ \tau^0 \end{pmatrix} = \begin{pmatrix} (-ip_n + \xi_\mathbf{q})\tau^0 & -\frac{M^c}{2}\tau^3 \\ -\frac{M^c}{2}\tau^3 & (-ip_n + \xi_{\mathbf{q}-\mathbf{Q}})\tau^0 \end{pmatrix} G(\mathbf{q}, p_n) \qquad (8.42)$$

Thus

$$G(\mathbf{q}, p_n) = \frac{\begin{pmatrix} (ip_n - \xi_{\mathbf{q}-\mathbf{Q}})\tau^0 - \frac{M^c}{2}\tau^3 \\ (ip_n - \xi_\mathbf{q})\tau^0 - \frac{M^c}{2}\tau^3 \end{pmatrix}}{(-ip_n + \xi_\mathbf{q})(-ip_n + \xi_{\mathbf{q}-\mathbf{Q}}) - (\frac{M^c}{2})^2} \qquad (8.43)$$

and then for $t' = \mu = 0$ (where $\varepsilon_{\mathbf{q}\pm\mathbf{Q}} = -\varepsilon_\mathbf{q}$) the Greens function becomes

$$\mathcal{G}(\mathbf{q}, p_n) = \frac{(ip_n + \varepsilon_\mathbf{q})\tau^0 - \frac{M^c}{2}\tau^3}{(ip_n)^2 - E^2(\mathbf{q})} \qquad (8.44)$$

where $E_\mathbf{q}^2 = \varepsilon_\mathbf{q}^2 + (\frac{M^c}{2})^2$. Armed with this expression, we can attack the bare susceptibility given by Eqn. (8.23). For instance for $\chi_0^{xx}(\mathbf{q}, \omega_n)$ we get

$$
\begin{aligned}
\chi_0^{xx}(\mathbf{q}, \omega_n) &= -\frac{1}{\beta}\sum_{\mathbf{q}'p_n}\mathrm{Tr}_s \frac{1}{(ip_n)^2 - E_{\mathbf{q}'}^2} \begin{pmatrix} 0 & ip_n + \varepsilon_{\mathbf{q}'} - \frac{M^c}{2} \\ ip_n + \varepsilon_{\mathbf{q}'} + \frac{M^c}{2} & 0 \end{pmatrix} \\
&\quad \times \frac{1}{(ip_n + i\omega_n)^2 - E_{\mathbf{q}'+\mathbf{q}}^2}\begin{pmatrix} 0 & ip_n + i\omega_n + \varepsilon_{\mathbf{q}'+\mathbf{q}} - \frac{M^c}{2} \\ ip_n + i\omega_n + \varepsilon_{\mathbf{q}'+\mathbf{q}} + \frac{M^c}{2} & 0 \end{pmatrix} \\
&= -\frac{2}{\beta}\sum_{\mathbf{q}'p_n} \frac{\left[(ip_n + \varepsilon_{\mathbf{q}'})(ip_n + i\omega_n + \varepsilon_{\mathbf{q}'+\mathbf{q}}) - \left(\frac{M^c}{2}\right)^2\right]}{((ip_n)^2 - E_{\mathbf{q}'}^2)((ip_n + i\omega_n)^2 - E_{\mathbf{q}'+\mathbf{q}}^2)}.
\end{aligned} \qquad (8.45)
$$

From the poles and the residues of the function

$$f(z) = \frac{2(z + \varepsilon_{\mathbf{q}'})(z + i\omega_n + \varepsilon_{\mathbf{q}'+\mathbf{q}}) - \left(\frac{M^c}{2}\right)^2}{(z^2 - E_{\mathbf{q}'}^2)((z + i\omega_n)^2 - E_{\mathbf{q}'+\mathbf{q}}^2)} \qquad (8.46)$$

we can immediately perform the fermion Matsubara sum to get

$$
\begin{aligned}
\chi_0^{xx}(\mathbf{q}, \omega_n) &= \sum_{\mathbf{q}'} f(E_{\mathbf{q}'}) \frac{(E_{\mathbf{q}'} + \varepsilon_{\mathbf{q}'})(-E_{\mathbf{q}'} - i\omega_n - \varepsilon_{\mathbf{q}'+\mathbf{q}}) + \left(\frac{M^c}{2}\right)^2}{E_{\mathbf{q}'}((E_{\mathbf{q}'} + i\omega_n)^2 - E_{\mathbf{q}'+\mathbf{q}}^2)} \\
&+ \quad (E_{\mathbf{q}'} \to -E_{\mathbf{q}'}) \\
&+ \quad \sum_{\mathbf{q}'} f(E_{\mathbf{q}'+\mathbf{q}}) \frac{(-i\omega_n + E_{\mathbf{q}'+\mathbf{q}} + \varepsilon_{\mathbf{q}'})(-E_{\mathbf{q}'+\mathbf{q}} - \varepsilon_{\mathbf{q}'+\mathbf{q}}) + \left(\frac{M^c}{2}\right)^2}{E_{\mathbf{q}'+\mathbf{q}}((E_{\mathbf{q}'+\mathbf{q}} - i\omega_n)^2 - E_{\mathbf{q}'}^2)} \\
&+ \quad (E_{\mathbf{q}'+\mathbf{q}} \to -E_{\mathbf{q}'+\mathbf{q}}). \qquad (8.47)
\end{aligned}
$$

The remaining momentum sums are done numerically by dividing the Brillouin zone into many tiny squares and performing the discrete sum. The same expression (8.47) is valid for $\chi_0^{yy}(\mathbf{q}, \omega_n)$ whereas the low-energy spectrum of the longitudinal susceptibility $\chi_0^{zz}(\mathbf{q}, \omega_n)$ is dominated by a mass gap.

For $T = 0$ and $U = 4.0t$, I show in Fig. 8.14(left) the real part of $\chi_0^{xx}(\mathbf{q}, \omega)$ for $q_y = \pi$ as a function of q_x and ω. The full spin susceptibility $\chi^{xx}(\mathbf{q}, \omega)$ is
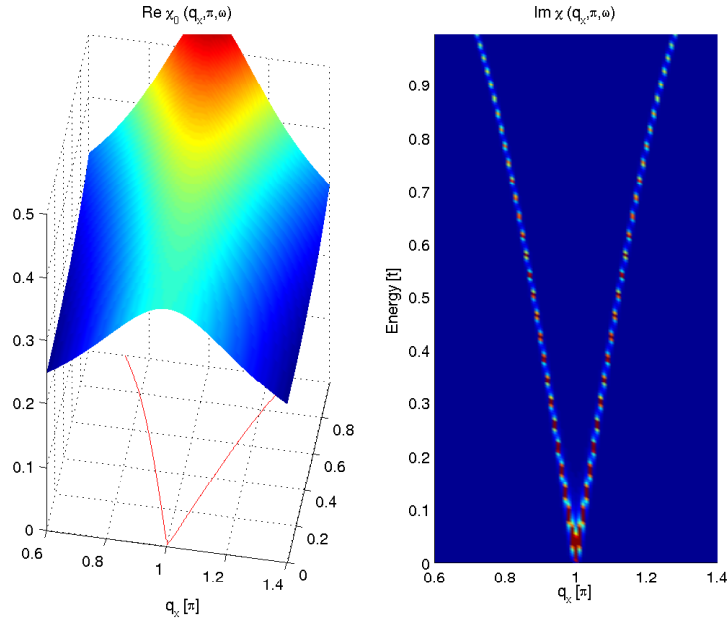
Figure 8.14: (a) The real part of the bare susceptibility $\chi_0^{xx}(q_x, \pi, \omega)$ at $q_y = \pi$ as a function of q_x and the energy ω. The red line shows the contour where the mountain intersects the plane, i.e. where $\text{Re}\chi_0^{xx}(q_x, \pi, \omega) = 3/U$. (b) Similar plot of the full susceptibility $\chi^{xx}(q_x, \pi, \omega)$ which clearly displays the spin waves.

shown in Fig. 8.14(right). Clearly, the transverse susceptibility is dominated

by the antiferromagnetic spin waves dispersing toward (π, π) as the energy decreases. These modes match the resonance condition $1 - \frac{U}{3}\mathrm{Re}\chi_0^{xx}(\mathbf{q}, \omega) = 0$ of the 'bare' susceptibility and agrees with the symmetry considerations of Goldstones theorem. By plotting the imaginary part of the full susceptibility $\chi^{xx}(\mathbf{q}, \omega)$ at constant energies as a function of both q_x and q_y we see in Fig. 8.15 the isotropic dispersion of the spin wave cones.

A crucial ingredient for the Goldstone modes to come out correctly is the
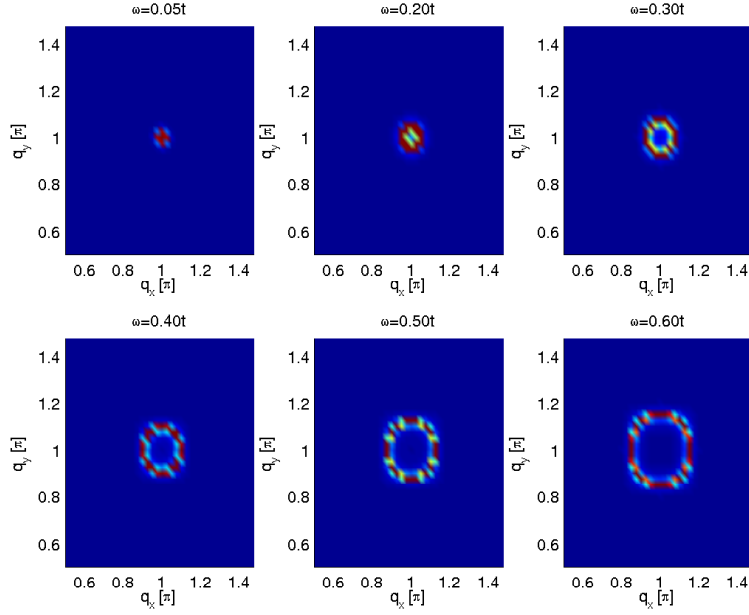
Figure 8.15: Constant energy cuts through the Brillouin zone ($\pi/2 < q_x, q_y < 3\pi/2$ for the half-filled antiferromagnet showing the uniform dispersion of the spin-wave cone centered at (π, π).

self-consistency of the magnetism, i.e. the size of the magnetization M^c must be determined self-consistently from the Hamiltonian. This is because the Coulomb interaction U is the real coupling constant giving rise to a finite M^c and enters the full spin susceptibility in the denominator, $1 - \frac{U}{3}\chi_0^{xx}(\mathbf{q}, \omega)$. In Fig. 8.14 where $U = 4.0t$ the self-consistent antiferromagnetic solution has $\langle S^z \rangle = 0.2556t$ corresponding to $M^c = 4U/3\langle S^z \rangle = 1.3632t$.

We can understand the importance of the self-consistency and the satisfaction of Goldstones theorem (at least the satisfaction of zero-energy modes at the ordering vector $\mathbf{Q}$) by showing that *both lead to the gap equation*. Thus, consider the action S of the ordered antiferromagnet ($t' = \mu = 0$)

$$S = \int d\tau \sum_{\mathbf{q}, p_n \sigma} (-ip_n + \varepsilon_{\mathbf{q}}) c_{\mathbf{q}\sigma}^* c_{\mathbf{q}\sigma} - \frac{M^c}{2} \sigma c_{\mathbf{q}\sigma}^* c_{\mathbf{q}+\mathbf{Q}\sigma} + \frac{3}{8U}(M^c)^2 \qquad (8.48)$$

$$= \int d\tau {\sum_{\mathbf{q}p_n\sigma}}' \begin{pmatrix} c_{\mathbf{q}\sigma}^* \\ c_{\mathbf{q}+\mathbf{Q}\sigma}^* \end{pmatrix} \begin{pmatrix} -ip_n + \varepsilon_{\mathbf{q}} & -\sigma\frac{M^c}{2} \\ -\sigma\frac{M^c}{2} & -ip_n - \varepsilon_{\mathbf{q}} \end{pmatrix} \begin{pmatrix} c_{\mathbf{q}\sigma} \\ c_{\mathbf{q}+\mathbf{Q}\sigma} \end{pmatrix} + \frac{3\beta}{8U}(M^c)^2$$

where $\sum'$ denotes the sum over the folded Brillouin zone, and $\sigma = \pm 1$ for spin up and down respectively. When integrating out the electrons we get for the free energy $F = S/\beta$,

$$
\begin{aligned}
F &= -\frac{1}{\beta} {\sum_{\mathbf{q}p_n\sigma}}' \ln \det \begin{pmatrix} -ip_n + \varepsilon_{\mathbf{q}} & -\sigma\frac{M^c}{2} \\ -\sigma\frac{M^c}{2} & -ip_n - \varepsilon_{\mathbf{q}} \end{pmatrix} + \frac{3}{8U}(M^c)^2 \\
&= -\frac{2}{\beta} {\sum_{\mathbf{q}p_n}}' \ln\left((ip_n)^2 - E_{\mathbf{q}}^2\right) + \frac{3}{8U}(M^c)^2,
\end{aligned}
\tag{8.49}
$$

with $E_{\mathbf{q}}^2 = \varepsilon_{\mathbf{q}}^2 + \left(\frac{M^c}{2}\right)^2$. Requiring M^c to minimize the free energy F, we get

$$0 = \frac{\partial F}{\partial M^c} = \frac{2}{\beta} {\sum_{\mathbf{q}p_n}}' \frac{M^c/2}{\left((ip_n)^2 - E_{\mathbf{q}}^2\right)} + \frac{3}{4U} M^c. \tag{8.50}$$

Performing the frequency sum this condition becomes

$$\sum_{\mathbf{q}} \frac{1}{E_{\mathbf{q}}} \left(1 - 2f(E_{\mathbf{q}})\right) = \frac{3}{U}, \tag{8.51}$$

where the symmetry of $E_{\mathbf{q}}$ was used to extend the sum to the full Brillouin zone. This gap equation yields a relation between U and M^c and the solution is shown graphically in Fig. 8.16.

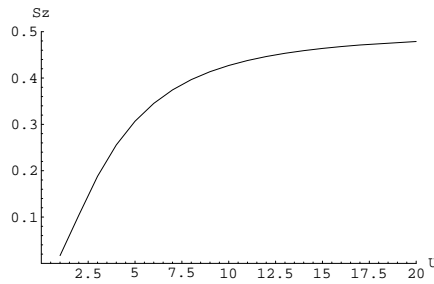On the other hand a necessary condition for a soft transverse mode at the

Figure 8.16: Solution of $\langle S^z \rangle$ as a function of U from the gap equation. This also gives $M^c(U)$ since $M^c = 4U/3\langle S^z \rangle$. Clearly, for $U \to \infty$ the magnetization saturates, i.e. $|\langle S^z \rangle| \to \frac{1}{2}$.

ordering vector $\mathbf{Q} = (\pi, \pi)$ is $1 - \frac{U}{3}\chi_0^{xx}(\mathbf{Q}, 0) = 0$ where

$$
\begin{aligned}
\chi_0^{xx}(\mathbf{Q}, 0) &= -\frac{2}{\beta} \sum_{\mathbf{q}p_n} \frac{(ip_n + \varepsilon_\mathbf{q})(ip_n - \varepsilon_\mathbf{q}) - \left(\frac{M^c}{2}\right)^2}{((ip_n)^2 - E_\mathbf{q}^2)((ip_n)^2 - E_\mathbf{q}^2)} \\
&= -\frac{2}{\beta} \sum_{\mathbf{q}p_n} \frac{1}{(ip_n)^2 - E_\mathbf{q}^2} \\
&= \sum_\mathbf{q} \frac{1}{E_\mathbf{q}} \left(1 - 2f(E_\mathbf{q})\right),
\end{aligned}
\tag{8.52}
$$

which clearly leads to the same gap equation obtained from minimizing the free energy.

In the following we are interested in the states where antiferromagnetism and d-wave superconductivity coexist. For instance in the form of stripe arrays where the system self-organizes into mesoscopic domains of alternating magnetic and superconducting order. In this case we will diagonalize the single-particle Hamiltonian Eqn. (1.37) on a real-space cluster and use the resulting eigensystem to draw conclusions about the spin fluctuations of stripe systems.

8.6 Spin susceptibility in the phase of coexisting stripe and superconducting order

We now return to the question of the spin response from stripe phases. In particular, we are interested in the recent inelastic neutron scattering experiments on LSCO by Christensen *et al.*[280] and LBCO by Tranquada *et al.*[281] There have been recent theoretical progress in understanding these measurements. For instance, Vojta *et al.*[309] and Uhrig *et al.*[310] have found reasonably agreement with the neutron results on the LBCO system from calculations of coupled two-leg spin ladder systems. In these spin-only calculations the starting-point is also a bond-ordered stripe system, but sophisticated treatments of the spin-ladders allows one to go beyond the semi-classical spin-wave approach[305, 306]. The importance of superconductivity is, however, not straightforward to infer from these spin-only models.

In the following we are motivated by the success of the mean-field one-band Hubbard model to describe STM and ARPES data to also apply it to the neutron results. In order to better compare results with other groups[22, 157, 158] we choose the mean-field decoupling scheme of the Hubbard interaction used in the previous chapter, i.e. $U\hat{n}_{i\uparrow}\hat{n}_{i\downarrow} \to U\langle n_{i\uparrow}\rangle\hat{n}_{i\downarrow} + U\langle n_{i\downarrow}\rangle\hat{n}_{i\uparrow} - U\langle n_{i\uparrow}\rangle\langle n_{i\downarrow}\rangle$. Therefore, we use the following expression for the bare transverse susceptibility

derived in the appendix

$$
\begin{aligned}
\chi_0^{xx}(\mathbf{q}, i\omega_n) &= \frac{1}{4(N_x N_y)^2} \sum_{\substack{\mathbf{k}nm \\ ij\sigma}} \left[a_1(u,v) \frac{1 - f(E_{n\mathbf{k}\sigma}) - f(E_{m\mathbf{k}+\mathbf{q}\sigma})}{i\omega_n + E_{m\mathbf{k}+\mathbf{q}\sigma} + E_{n\mathbf{k}\sigma}} \right. \\[2mm]
&+ a_2(u,v) \frac{f(E_{n\mathbf{k}\sigma}) + f(E_{m\mathbf{k}+\mathbf{q}\sigma}) - 1}{i\omega_n - E_{m\mathbf{k}+\mathbf{q}\sigma} - E_{n\mathbf{k}\sigma}} \\[2mm]
&+ b_1(u,v) \frac{f(E_{n\mathbf{k}\sigma}) - f(E_{m\mathbf{k}+\mathbf{q}\bar\sigma})}{i\omega_n + E_{m\mathbf{k}+\mathbf{q}\bar\sigma} - E_{n\mathbf{k}\sigma}} \\[2mm]
&+ \left. b_2(u,v) \frac{f(E_{m\mathbf{k}+\mathbf{q}\sigma}) - f(E_{n\mathbf{k}\bar\sigma})}{i\omega_n + E_{n\mathbf{k}\bar\sigma} - E_{m\mathbf{k}+\mathbf{q}\sigma}} \right] e^{i\mathbf{q}\cdot(j-i)},
\end{aligned} \tag{8.53}
$$

with the coefficients $a_{1(2)}(u,v)$ and $b_{1(2)}(u,v)$ given by the following combinations of the coherence factors u and v

$$
a_1(u,v) = v_{n\mathbf{k}\sigma}^*(i) u_{m\mathbf{k}+\mathbf{q}\sigma}(i) \left(v_{n\mathbf{k}\sigma}(j) u_{m\mathbf{k}+\mathbf{q}\sigma}^*(j) - u_{n\mathbf{k}\sigma}(j) v_{m\mathbf{k}+\mathbf{q}\sigma}^*(j) \right), \tag{8.54}
$$

$$
a_2(u,v) = u_{n\mathbf{k}\sigma}^*(i) v_{m\mathbf{k}+\mathbf{q}\sigma}(i) \left(u_{n\mathbf{k}\sigma}(j) v_{m\mathbf{k}+\mathbf{q}\sigma}^*(j) - v_{n\mathbf{k}\sigma}(j) u_{m\mathbf{k}+\mathbf{q}\sigma}^*(j) \right), \tag{8.55}
$$

$$
b_1(u,v) = u_{n\mathbf{k}\sigma}^*(i) u_{m\mathbf{k}+\mathbf{q}\bar\sigma}(i) \left(u_{n\mathbf{k}\sigma}(j) u_{m\mathbf{k}+\mathbf{q}\bar\sigma}^*(j) + v_{n\mathbf{k}\sigma}(j) v_{m\mathbf{k}+\mathbf{q}\bar\sigma}^*(j) \right) \tag{8.56}
$$

$$
b_2(u,v) = v_{n\mathbf{k}\bar\sigma}^*(i) v_{m\mathbf{k}+\mathbf{q}\sigma}(i) \left(v_{n\mathbf{k}\bar\sigma}(j) v_{m\mathbf{k}+\mathbf{q}\sigma}^*(j) + u_{n\mathbf{k}\bar\sigma}(j) u_{m\mathbf{k}+\mathbf{q}\sigma}^*(j) \right). \tag{8.57}
$$

Here, the site indices i, j belong to the supercell (typically of size 2 by 8) and $\mathbf{k}$ is a Bloch index belonging to the corresponding reduced Brillouin zone. The eigensystem is obtained from a diagonalization of the Bogoliubov-de Gennes equations for each $\mathbf{k}$.

The full susceptibility obtained within linear response is then given by

$$
\chi^{xx}(\mathbf{q}, i\omega_n) = \frac{\chi_0^{xx}(\mathbf{q}, i\omega_n)}{1 - U\chi_0^{xx}(\mathbf{q}, i\omega_n)}, \tag{8.58}
$$

which is similar to the expression (8.29) used previously[15]. The difference in the factor of $2U/3$ (2 from spin summation in (8.29)) versus U in the denominator of Eqn. (8.58) originates from the slightly different mean-field decoupling

---

[15] For a derivation of this result see e.g. the books by S. Doniach and E.H. Sondheimer: *Green's functions for solid state physicists*, or S.W. Lovesey: *Condensed matter physics, Dynamic correlations*. Within linear response, because of the applied magnetic field the z-component of the spin is no longer a constant of the motion. Therefore, terms such as $\langle \hat{c}_{i\uparrow}^\dagger \hat{c}_{i\downarrow} \rangle$ neglected in the decoupling $U\hat{n}_{i\uparrow}\hat{n}_{i\downarrow} \to U\hat{n}_{i\uparrow}\langle \hat{n}_{i\downarrow} \rangle + U\hat{n}_{i\downarrow}\langle \hat{n}_{i\uparrow} \rangle - U\langle \hat{n}_{i\uparrow} \rangle \langle \hat{n}_{i\downarrow} \rangle$ need be taken into account. Inclusion of these terms leads to Eqn. (8.58).

scheme used here.

In the half-filled antiferromagnetic state ($V = n_h = 0.0$) this approach produces the expected spin waves similar to the results shown in Fig. 8.14 and Fig. 8.15. This is plotted in a slightly different way in Fig. 8.17.

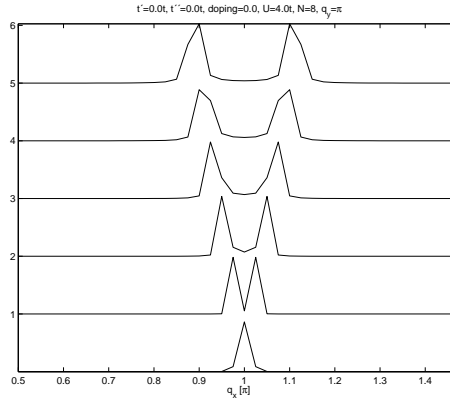There is a subtle problem associated with the numerical studies of models

Figure 8.17: Dispersion of the AF spin waves as seen in plots of $\text{Im}\chi(q_x, q_y = \pi, \omega)$ versus q_x at fixed energy from $\omega = 0.0 - 0.5t$ in steps of $0.1t$. The scans are offset for clarity and the intensity has been normalized for each energy scan. Without this energy normalization it is clear from Fig. 8.14 that the intensity strongly increases when reducing the energy transfer. Parameters: $U = 4.0t$, $n_h = t' = t'' = 0.0$.

that exhibit incommensurate spin or charge density wave order: how does one match the chosen unit cell size with the natural periodicity of the system? For example, imagine that we have a huge system and choose some values of the input parameters such as U, V, t' and the doping n_h. Then we expect the oscillations of, say, the spin density wave to have some wavelength λ whose specific value depends on the value of the parameters. Knowing λ, we could perform fast calculations by splitting the system into unit cells given by the size of this wavelength λ. In this way, instead of diagonalizing an enormous system, we only diagonalize a system with the size of a unit cell but need to perform the sum over Bloch wavevectors belonging to the corresponding reduced Brillouin zone. However, since the formalism has to be set up in the reserve order, we have to find a set of parameters that match our chosen system size. To do this, we use the fact that Goldstones theorem need apply whenever we have a broken continuous symmetry. In particular, when studying systems of size 2×8 and searching for parameters that have this as a stable supercell we search for Goldstone modes positioned at $(2\pi/2, 2\pi/2 \pm 2\pi/8) = (\pi, \pi(1 \pm 1/4))$. This is rather extensive numerical work due to the number of sums in Eqn. (8.53) and the fact that the runs are time-consuming and most results need be discarded since the spin spectrum does not produce the correct Goldstone modes. Of course, this problem is related to the search for, at least, meta-stable states.

The numerical routines can stabilize many stripe states that appear stable, but, in fact, are not even the lowest energy stripe state.

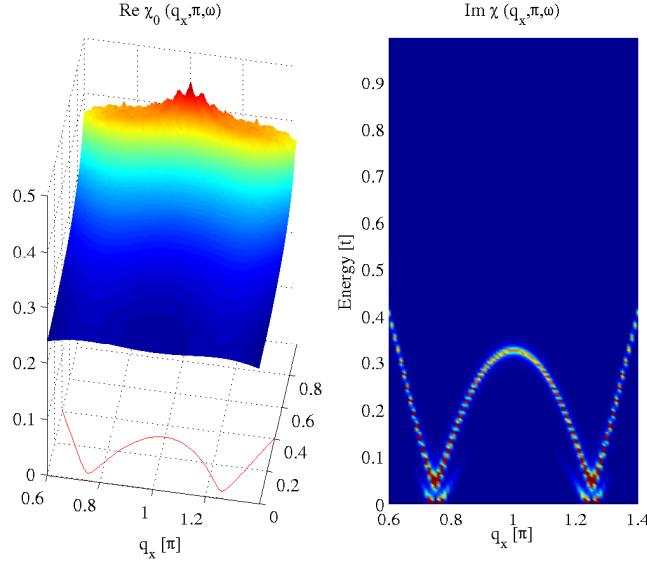In the following we present results first for $V = 0$, i.e. no superconductivity.

Figure 8.18: (a) The real part of the bare susceptibility $\chi_0^{xx}(q_x, \pi, \omega)$ at $q_y = \pi$ as a function of q_x and the energy ω. Parameters: $n_h = 0.125$, $U = 4.0t$, $V = 0.0$, $t' = -0.385t$ and $t'' = 0.10t$. The red line shows the contour where $\text{Re}\chi_0^{xx}(q_x, \pi, \omega) = 1/U$. (b) Similar plot of the full susceptibility $\chi^{xx}(q_x, \pi, \omega)$ which clearly displays the spin waves.

Then, for a chosen Coulomb interaction U and hole doping n_h we tune t' and t'' until the Goldstone modes appear at the correct positions. This tuning of t' and t'' changes the filling of the mid-gap bands until the chosen periodicity matches the chosen overall doping level n_h. The main question we attempt to clarify is dispersion of the spin modes and the associated intensity distribution. In Fig. 8.18a I show the the real part of the bare susceptibility and the contour where it cuts $1/U$ for $n_h = 0.125$, $V = 0$, $U = 4.0t$.

To obtain the Goldstone modes that correctly produce Bragg peaks at $(\pi(1 \pm \frac{1}{4}), \pi)$ the hopping parameters had to be set to $t' = -0.385t$ and $t'' = 0.10t$. Fig. 8.18b shows the imaginary part of the full spin susceptibility for this set of parameters. For a different doping level $n_h = 0.160$ we obtain a similar result for $U = 4.0t$, $V = 0.0$, $t' = -0.13t$, and $t'' = 0.21t$ as seen in Fig. 8.19. In both cases we see clearly the expected spin modes dispersing from $(\pi(1 \pm \frac{1}{4}), \pi)$ similar to the results from the spin-only models seen in Fig. 8.13.

What is the intensity distribution along the spin wave branches? In the antiferromagnet this was isotropic, i.e. equal intensity on the two branches as seen in Fig. 8.17. Along the branches $\text{Re}\chi_0^{xx}(q_x, \pi, \omega) = 1/U$, and therefore $\text{Im}\chi^{xx}(q_x, \pi, \omega) \propto 1/(U^2\text{Im}\chi_0^{xx}(q_x, \pi, \omega))$. Thus, the structure in the imaginary part of the bare susceptibility determines the relative intensity of the two
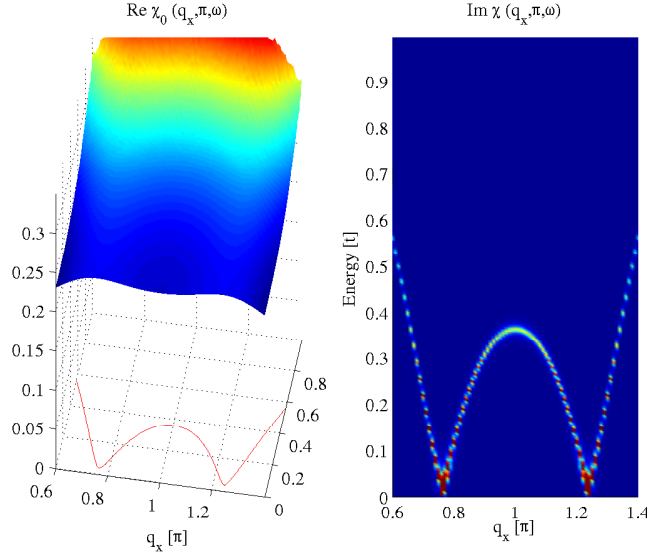
Figure 8.19: Same as Fig. 8.18 but for the following set of parameters: $n_h = 0.160$, $U = 4.0t$, $V = 0.0$, $t' = -0.13t$ and $t'' = 0.21t$.

branches. For the situation without superconductivity $V = 0$, the low-energy form of $\text{Im}\chi_0^{xx}(q_x, \pi, \omega)$ remains featureless resulting in equal intensity ratio between the inner and outer spin mode branch. The intensity monotonically decreases as the energy is increased. Above the resonance energy only the outer branch can be seen.

The spin waves also disperse in q_y. Therefore, it is important to show the dispersion in the full Brillouin zone. In Fig. 8.20 I show the constant energy cuts through the Brillouin zone $\frac{\pi}{2} < q_x, q_y < \frac{3\pi}{2}$ of the imaginary part of the full susceptibility similar to Fig. 8.15. These images have been symmetrized to simulate the equal amounts of vertical/horizontal stripe domains. Clearly, the dispersion is characterized by four cones pivoted at $(\pi(1 \pm \frac{1}{4}), \pi)$. The cones merge in at the (π, π) point around $\omega = 0.32t$ and cause an apparent resonance. Above this energy scale the outer branches cause a diffuse ring that continues to disperse away from the commensurate (π, π) point as the energy increases. The ring shaped response above the (π, π) resonance is the superposition of two rectangles originating from vertical and horizontal stripe domains. The strongest intensity appear where they overlap which happens at points rotated 45 degrees to the original four incommensurate Bragg points. Many of these features are similar to the recent measurements of Tranquada *et al.*[281] The main difference to the LBCO neutron data appears to be the rather strong intensity at isolated points of the outer branches below the resonance energy as seen e.g. at $\omega = 0.20t$ and $\omega = 0.25t$ in Fig. 8.20. Note, however, that even at these energies the strongest intensity is positioned on the inner branches. In the future, we will study further the robustness of this result toward changes in the doping, Coulomb repulsion U and band structure
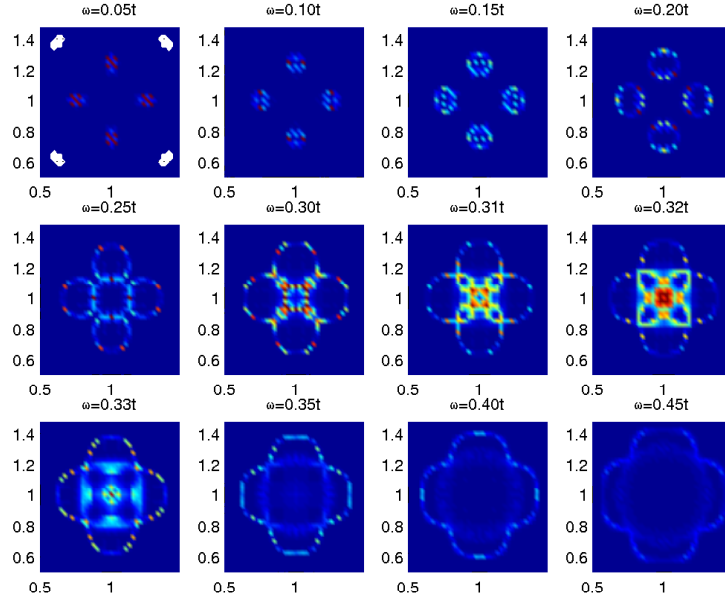
Figure 8.20: Dispersion of the incommensurate spin waves as seen in plots of $\text{Im}\chi(q_x, q_y, \omega)$ versus $\frac{\pi}{2} < q_x, q_y < \frac{3\pi}{2}$ at fixed energy. Parameters: $U = 4.0t$, $V = 0.0$, $n_h = 0.125$, $t' = -0.385t$, $t'' = 0.10t$. The color scale is the same for all images.

parameters. For the parameter set corresponding to the results shown in Fig. 8.19 the 2D constant energy cuts are shown in Fig. 8.21. Qualitatively, we have the same behavior as in Fig. 8.20: incommensurate-commensurate-ring crossover as the energy transfer is increased. Above the resonance the diffuse ring is more square formed, and the band-parameters cause the strongest intensity to be located around the $(0, \pi)$ and $(\pi, 0)$ directions.

What happens when we include the nearest neighbor attraction $V \neq 0$? The existence of the superconducting phase is one of the crucial differences between the nickelates and the cuprates. Since the continuous spin rotation symmetry is still broken, we again expect Goldstone modes condensed around the reciprocal points $(\pi(1 \pm \delta), \pi)$ for vertical stripes with spin periodicity $2/\delta$. However, we also expect the pairing to strongly influence the low-energy form of $\text{Im}\chi_0^{xx}(q_x, q_y, \omega)$. In particular, we know from the homogeneous d-wave BCS superconducting phase that the spin gap, i.e. the lower edge of $\text{Im}\chi_0^{xx}(q_x, q_y, \omega)$ at $q_y = \pi$ has the form shown in Fig. 8.8. For certain parameters one may expect *the wings of the continuum to coincide with the outer branches of the spin waves*. This will strongly over-damp these modes as appears to be the case experimentally[280], at least in LSCO.

For $U = 4.0t$, $V = 1.6t$ and $n_h = 0.125$ we can still find t' and t'' such that the expected Goldstone modes emerge. This is shown in Fig. 8.22. The imagi-
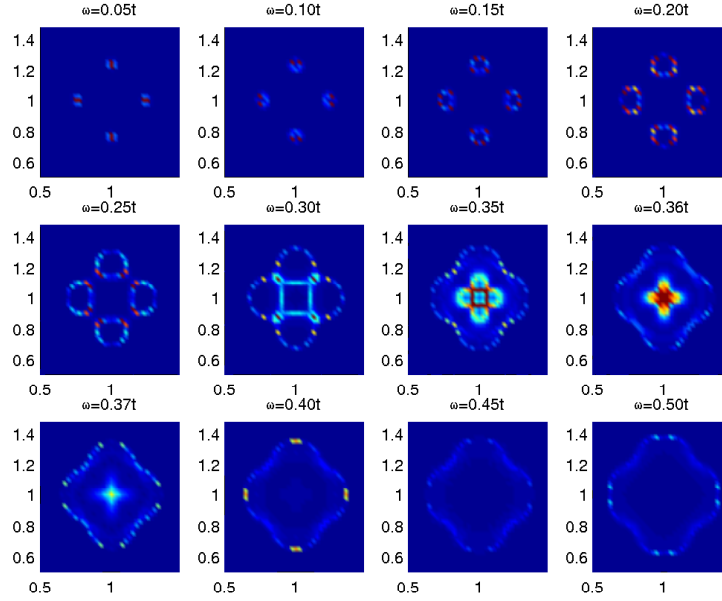
Figure 8.21: Dispersion of the incommensurate spin waves as seen in plots of $\text{Im}\chi(q_x, q_y, \omega)$ versus $\frac{\pi}{2} < q_x, q_y < \frac{3\pi}{2}$ at fixed energy. Parameters: $U = 4.0t$, $V = 0.0$, $n_h = 0.160$, $t' = -0.13t$, $t'' = 0.21t$. The color scale is the same for all images.

nary part of the bare susceptibility $\text{Im}\chi_0^{xx}(q_x, \pi, \omega)$ is shown in Fig. 8.23(left). Clearly, the low-energy region is protected from the damping effects of the particle-hole continuum. In Fig. 8.23(right), we show $\text{Im}\chi_0^{xx}(q_x, \pi, \omega)$ for the self-consistent stripe solution obtained when $U = 4.0t$, $V = 1.6t$, $n_h = 0.160$, $t' = -0.09t$, and $t'' = 0.17t$. For this particular set of parameters, the real part of the bare susceptibility $\text{Re}\chi_0^{xx}(q_x, \pi, \omega)$ and the imaginary part of the full response $\text{Im}\chi^{xx}(q_x, \pi, \omega)$ is shown in Fig. 8.24. From the contour determined by the condition $\text{Re}\chi_0^{xx}(q_x, \pi, \omega) = 1/U$ we find the same spin wave branches as in the graphs above. However, as opposed to the situation when $V = 0$, the continuum of the particle-hole excitations strongly damps the outer branches as these fall inside the particle-hole continuum. This is evident from the full spin susceptibility plotted to the right in Fig. 8.24. Only a diffuse remnant of the outer branches remains. The larger intensity of the inner branch can also be clearly seen from Fig. 8.25 which displays a set of constant energy cuts through the graph in Fig. 8.24. The intensity has been normalized to that at $\omega = 0.05t$.

We find that also at lower doping levels, e.g. at $n_h = 0.100$ and $n_h = 0.125$, it is possible to find band-parameters such that the spin modes appear at $(\pi(1 \pm \frac{1}{4}), \pi)$ *and* the outer branches are damped. For $U = 4.0t$, $V = 1.6t$ and $n_h = 0.125$ this solution exists when $t' = -0.35t$ and $t'' = 0.14t$. Within the minimal model, this is the explanation of the neutron scattering results
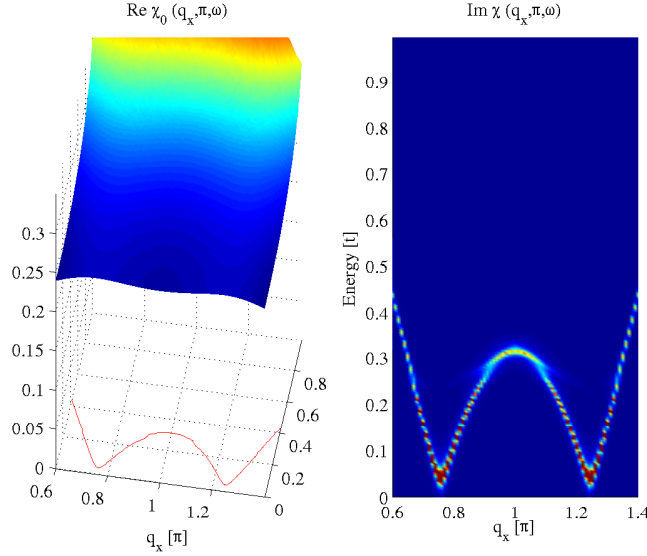
Figure 8.22: (a) The real part of the bare susceptibility $\chi_0^{xx}(q_x, \pi, \omega)$ at $q_y = \pi$ as a function of q_x and the energy ω. Parameters: $n_h = 0.125$, $U = 4.0t$, $V = 1.6t$, $t' = -0.37t$ and $t'' = 0.1t$. The red line shows the contour where $\mathrm{Re}\chi_0^{xx}(q_x, \pi, \omega) = 1/U$. (b) Similar plot of the full susceptibility $\chi^{xx}(q_x, \pi, \omega)$ which clearly displays the spin waves.

by Christensen *et al.*[280] Of course, at doping levels below 1/8 we expect the stripes to be farther apart leading to smaller incommensurability parameter δ and larger required supercells. The results in this limit will be explored in the future.

8.7 Conclusion and discussion of some unanswered questions

So where does all this bring us regarding a consensus on the spin susceptibility of the cuprate materials?

We know that there are stripes in the lanthanum based cuprate materials. Therefore, the stripe state is an appropriate starting point to describe the spin dynamics of these materials. The recently discovered ubiquity in the spin spectrum between the LSCO and YBCO systems shown in Fig. 8.3 hints that the same is true for the other cuprate families. Of course, there exists the possibility that this apparent ubiquity is, in fact, merely a coincidence. In that case, the band-structure and pairing gap of YBCO have conspired with the stripe periodicity and the spin-wave velocity of the LSCO materials to produce a seemingly very similar spin fluctuation spectrum. When this is not the case, the question remains as to what is the best model to describe the stripe state? Here, we used the mean-field decoupling of the one-band Hubbard model which supports incommensurate spin- and charge density wave order.
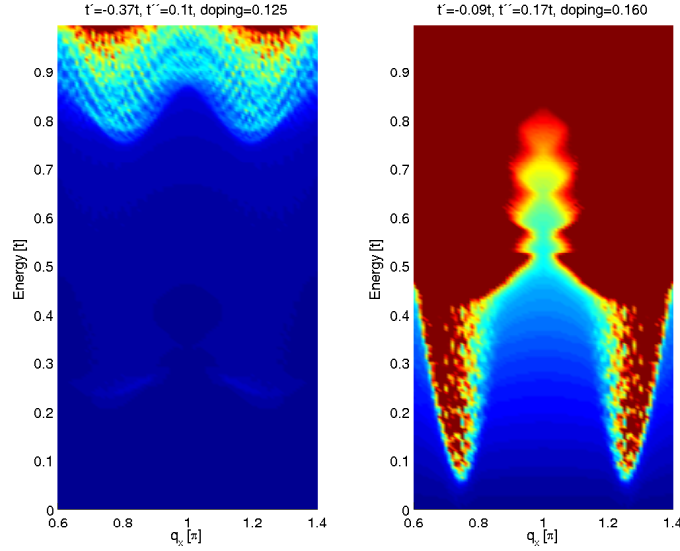
Figure 8.23: The imaginary part of the bare spin susceptibility $\chi_0^{xx}(q_x, \pi, \omega)$ at $q_y = \pi$ as a function of q_x and the energy ω. Parameters: (left) $n_h = 0.125$, $U = 4.0t$, $V = 1.6t$, $t' = -0.37t$ and $t'' = 0.1t$, and (right) $n_h = 0.160$, $U = 4.0t$, $V = 1.6t$, $t' = -0.09t$ and $t'' = 0.17t$

This approach allowed us to include the superconductivity in the transverse spin susceptibility, and the results appear very promising even though more results are required. Particularly, the intensity distribution evident from the constant energy scans of $\text{Im}\chi^{xx}(q_x, \pi, \omega)$) similar to the images in Fig. 8.20 and Fig. 8.21 need be clarified in the coexisting phase of stripes and d-wave superconductivity. From Fig. 8.24 it is clear that the main feature of these plots will be an incommensurate-commensurate crossover at the resonance energy. There will be no sizable outer spin branches. It remains to be seen what is the predictions for the dispersion above the resonance energy.

Experimentally, detailed 2D cuts through the Brillouin zone similar to the data shown in Fig. 8.2, but at higher energy transfer, are very desired.

What about the spin fluctuations in the homogeneous d-wave superconductor discussed in section 8.2 of this chapter? At finite energies the resulting spin susceptibility appears quite close to the experimental results. The spin gap is a direct consequence of the formation of Cooper pairs (and no broken spin rotation symmetry). However, as was pointed out above, in the underdoped regime, the pairing gap and the resonance are directly proportional which is contrary to experiment. The stripe model does not suffer from this problem. Furthermore, for the homogeneous d-wave superconductor we have not found it possible to obtain the rotated square above the commensurate spin resonance as seen by Tranquada *et al.*

Another interesting effect that will be investigated in the future is the effects of modulated hopping parameters. Since the charge modulation causes a dis-
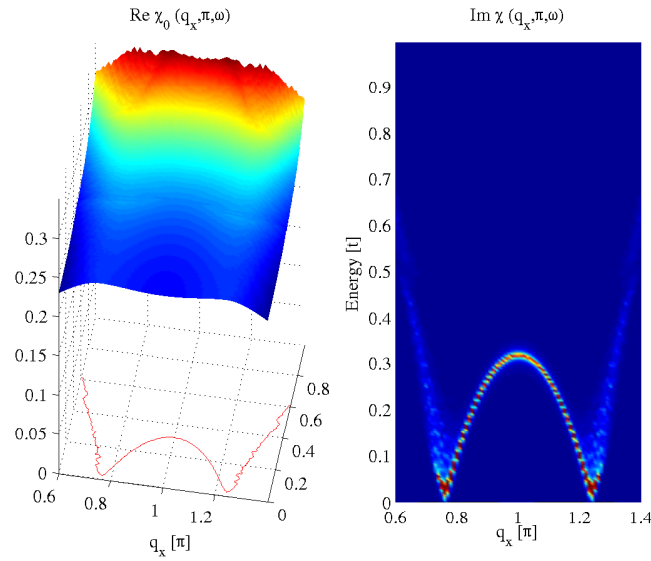
Figure 8.24: (a) The real part of the bare susceptibility $\chi_0^{xx}(q_x, \pi, \omega)$ at $q_y = \pi$ as a function of q_x and the energy ω. Parameters: $n_h = 0.160$, $U = 4.0t$, $V = 1.6t$, $t' = -0.09t$ and $t'' = 0.17t$. The red line shows the contour where $\mathrm{Re}\chi_0^{xx}(q_x, \pi, \omega) = 1/U$. (b) Similar plot of the full susceptibility $\chi^{xx}(q_x, \pi, \omega)$ which clearly displays the spin waves.

placement of the ions one can imagine that the hopping matrix elements, which are known to be very sensitive to the distance between the ions, have a spatial dependence. This introduces another parameter α which determines the value of the overlap integral αt for hopping on to the stripes.

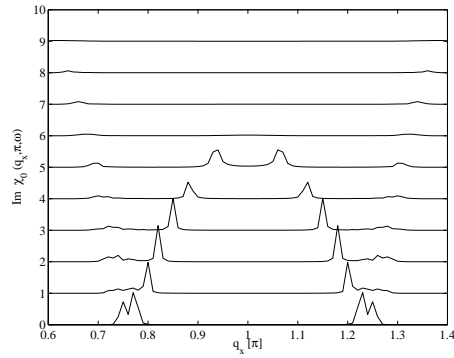**Figure 8.25**: Constant energy scans of the full transverse spin susceptibility $\chi^{xx}(q_x, \pi, \omega)$ at $q_y = \pi$ as a function of q_x. Parameters: $n_h = 0.160$, $U = 4.0t$, $V = 1.6t$, $t' = -0.09t$ and $t'' = 0.17t$. The ten lines correspond to $\chi^{xx}(q_x, \pi, \omega)$ at the energies $\omega = 0.05t - 0.5t$ in steps of $\Delta\omega = 0.05t$. These lines are off-set for clarity.

Appendices

.1 The spin susceptibility

We want to calculate the spin susceptibility in the case of a system that exhibits order that is translational invariant within a certain unit cell. In the case of no Hubbard interaction ($U = 0$) this reduces to the result from a homogeneous BCS superconductor with $d_{x^2-y^2}$-wave pairing symmetry. On the other hand, when the nearest neighbor attractive interaction $V = 0$ we obtain some incommensurate spin order away from half-filling. We start from a real-space formulation even though, of course, in the case of a homogeneous state, it would be easier to work in momentum space. We do not yet specify a Hamiltonian but have in mind the minimal model used previously.

From the definition of the spin susceptibility and the use of Wick's theorem we get

$$
\begin{aligned}
\chi_0^{+-}(\mathbf{r}_i, \mathbf{r}_j, \tau) &= \langle T_\tau \hat{S}_i^+(0) \hat{S}_j^-(\tau) \rangle \\[1em]
&= \langle T_\tau \hat{c}_{i\uparrow}^\dagger(0) \hat{c}_{i\downarrow}(0) \hat{c}_{j\downarrow}^\dagger(\tau) \hat{c}_{j\uparrow}(\tau) \rangle \\[1em]
&= -\langle T_\tau \hat{c}_{j\uparrow}(\tau) \hat{c}_{i\uparrow}^\dagger(0) \rangle \langle T_\tau \hat{c}_{i\downarrow}(0) \hat{c}_{j\downarrow}^\dagger(\tau) \rangle \\[1em]
&\quad - \langle T_\tau \hat{c}_{i\uparrow}^\dagger(0) \hat{c}_{j\downarrow}^\dagger(\tau) \rangle \langle T_\tau \hat{c}_{i\downarrow}(0) \hat{c}_{j\uparrow}(\tau) \rangle.
\end{aligned}
\tag{.1}
$$

Note the sign changes that occur when interchanging two fermion operators. The Bogoliubov-de Gennes transformation is defined by

$$
\hat{c}_{i\sigma}^\dagger = \frac{1}{\sqrt{N}} \sum_{n\mathbf{k}} \left(\hat{\gamma}_{n\mathbf{k}\sigma}^\dagger u_{n\mathbf{k}\sigma}^*(i) e^{-i\mathbf{k}\cdot\mathbf{R}_i} + \sigma \hat{\gamma}_{n\mathbf{k}\overline{\sigma}} v_{n\mathbf{k}\overline{\sigma}}(i) e^{i\mathbf{k}\cdot\mathbf{R}_i} \right),
\tag{.2}
$$

where $\hat{c}_{i\sigma}^\dagger = \hat{c}_\sigma^\dagger(\mathbf{r}_i) = \hat{c}_\sigma^\dagger(i + \mathbf{R}_i)$ and we Fourier transform in the supercell vector $\mathbf{R}_i$ such that the Bloch index $\mathbf{k}$ belongs the the corresponding reduced Brillouin zone. Then we get

$$
\begin{aligned}
\chi_0^{+-}(\mathbf{r}_i, \mathbf{r}_j, \tau) &= -\frac{1}{N^2} \sum_{nm\mathbf{k}\mathbf{k}'} \Big(u_{n\mathbf{k}\uparrow}(j) u_{n\mathbf{k}\uparrow}^*(i) \langle T_\tau \hat{\gamma}_{n\mathbf{k}\uparrow}(\tau) \hat{\gamma}_{n\mathbf{k}\uparrow}^\dagger(0) \rangle \\[1em]
&\quad + v_{n\mathbf{k}\downarrow}(j) v_{n\mathbf{k}\downarrow}^*(i) \langle T_\tau \hat{\gamma}_{n\mathbf{k}\downarrow}^\dagger(\tau) \hat{\gamma}_{n\mathbf{k}\downarrow}(0) \rangle \Big) \\[1em]
&\quad \times \Big(u_{m\mathbf{k}'\downarrow}(i) u_{m\mathbf{k}'\downarrow}^*(j) \langle T_\tau \hat{\gamma}_{m\mathbf{k}'\downarrow}(0) \hat{\gamma}_{m\mathbf{k}'\downarrow}^\dagger(\tau) \rangle
\end{aligned}
\tag{.3}
$$

$$+ \quad v_{m\mathbf{k}'\uparrow}(i)v^*_{m\mathbf{k}'\uparrow}(j)\langle T_\tau\hat{\gamma}^\dagger_{m\mathbf{k}'\uparrow}(0)\hat{\gamma}_{m\mathbf{k}'\uparrow}(\tau)\rangle\Big) e^{-i(\mathbf{k}-\mathbf{k}')\cdot(\mathbf{R}_i-\mathbf{R}_j)}$$

$$- \quad \Big(-u^*_{n\mathbf{k}\uparrow}(i)v_{n\mathbf{k}\uparrow}(j)\langle T_\tau\hat{\gamma}^\dagger_{n\mathbf{k}\uparrow}(0)\hat{\gamma}_{n\mathbf{k}\uparrow}(\tau)\rangle + v_{n\mathbf{k}\downarrow}(i)u^*_{n\mathbf{k}\downarrow}(j)\langle T_\tau\hat{\gamma}_{n\mathbf{k}\downarrow}(0)\hat{\gamma}^\dagger_{n\mathbf{k}\downarrow}(\tau)\rangle\Big)$$

$$\times \quad \Big(u_{m\mathbf{k}'\downarrow}(i)v^*_{m\mathbf{k}'\downarrow}(j)\langle T_\tau\hat{\gamma}_{m\mathbf{k}'\downarrow}(0)\hat{\gamma}^\dagger_{m\mathbf{k}'\downarrow}(\tau)\rangle$$

$$- \quad v^*_{m\mathbf{k}'\uparrow}(i)u_{m\mathbf{k}'\uparrow}(j)\langle T_\tau\hat{\gamma}^\dagger_{m\mathbf{k}'\uparrow}(0)\hat{\gamma}_{m\mathbf{k}'\uparrow}(\tau)\rangle\Big) e^{-i(\mathbf{k}-\mathbf{k}')\cdot(\mathbf{R}_i-\mathbf{R}_j)}$$

where I already used that $\langle\hat{\gamma}_a\hat{\gamma}^\dagger_b\rangle \sim \delta_{a,b}$. By further utilizing the relations

$$\langle T_\tau\hat{\gamma}_n(\tau)\hat{\gamma}^\dagger_n(0)\rangle \quad = \quad (1-f(E_n))e^{-E_n\tau}, \tag{.4}$$

$$\langle T_\tau\hat{\gamma}^\dagger_n(\tau)\hat{\gamma}_n(0)\rangle \quad = \quad f(E_n)e^{E_n\tau}, \tag{.5}$$

$$\langle T_\tau\hat{\gamma}_n(0)\hat{\gamma}^\dagger_n(\tau)\rangle \quad = \quad -f(E_n)e^{E_n\tau}, \tag{.6}$$

$$\langle T_\tau\hat{\gamma}^\dagger_n(0)\hat{\gamma}_n(\tau)\rangle \quad = \quad -(1-f(E_n))e^{-E_n\tau}, \tag{.7}$$

where as usual the Fermi-Dirac distribution function reads, $f(E) = (e^{E\beta}+1)^{-1}$, this becomes

$$\chi^{+-}_0(\mathbf{r}_i,\mathbf{r}_j,\tau) \quad = \quad -\frac{1}{N^2}\sum_{nm\mathbf{k}\mathbf{k}'}\Big(u_{n\mathbf{k}\uparrow}(j)u^*_{n\mathbf{k}\uparrow}(i)(1-f(E_{n\mathbf{k}\uparrow}))e^{-E_{n\mathbf{k}\uparrow}\tau}$$

$$+ \quad v_{n\mathbf{k}\downarrow}(j)v^*_{n\mathbf{k}\downarrow}(i)f(E_{n\mathbf{k}\downarrow})e^{E_{n\mathbf{k}\downarrow}\tau}\Big)$$

$$\times \quad \Big(-u_{m\mathbf{k}'\downarrow}(i)u^*_{m\mathbf{k}'\downarrow}(j)f(E_{m\mathbf{k}'\downarrow})e^{E_{m\mathbf{k}'\downarrow}\tau}$$

$$- \quad v_{m\mathbf{k}'\uparrow}(i)v^*_{m\mathbf{k}'\uparrow}(j)(1-f(E_{m\mathbf{k}'\uparrow}))e^{-E_{m\mathbf{k}'\uparrow}\tau}\Big) e^{-i(\mathbf{k}-\mathbf{k}')\cdot(\mathbf{R}_i-\mathbf{R}_j)}$$

$$+ \quad \Big(u^*_{n\mathbf{k}\uparrow}(i)v_{n\mathbf{k}\uparrow}(j)(1-f(E_{n\mathbf{k}\uparrow}))e^{-E_{n\mathbf{k}\uparrow}\tau} - v^*_{n\mathbf{k}\downarrow}(i)u_{n\mathbf{k}\downarrow}(j)f(E_{n\mathbf{k}\downarrow})e^{E_{n\mathbf{k}\downarrow}\tau}\Big)$$

$$\times \quad \Big(-u_{m\mathbf{k}'\downarrow}(i)v^*_{m\mathbf{k}'\downarrow}(j)f(E_{m\mathbf{k}'\downarrow})e^{E_{m\mathbf{k}'\downarrow}\tau}$$

$$+ \quad v_{m\mathbf{k}'\uparrow}(i)u^*_{m\mathbf{k}'\uparrow}(j)(1-f(E_{m\mathbf{k}'\uparrow}))e^{-E_{m\mathbf{k}'\uparrow}\tau}\Big) e^{-i(\mathbf{k}-\mathbf{k}')\cdot(\mathbf{R}_i-\mathbf{R}_j)}. \tag{.8}$$

Transforming first to Matsubara frequency

$$\chi^{+-}_0(\mathbf{r}_i,\mathbf{r}_j,i\omega_n) = \int_0^\beta d\tau\,\chi^{+-}_0(\mathbf{r}_i,\mathbf{r}_j,\tau)e^{i\omega_n\tau}, \tag{.9}$$

and using the relations

$$f(x)f(y)b(x+y) = 1 - f(x) - f(y), \qquad (.10)$$

$$(1 - f(x))(1 - f(y))b(-x - y) = f(x) + f(y) - 1, \qquad (.11)$$

$$f(x)(1 - f(y))b(x - y) = f(y) - f(x), \qquad (.12)$$

$$(.13)$$

where $b(x) = e^{x\beta} - 1$, we get

$$
\begin{aligned}
\chi_0^{+-}(\mathbf{r}_i, \mathbf{r}_j, i\omega_n) =& \frac{1}{N^2} \sum_{\mathbf{kk'}nm} \Bigg[u_{n\mathbf{k}\uparrow}(j)u_{n\mathbf{k}\uparrow}^*(i)u_{m\mathbf{k'}\downarrow}(i)u_{m\mathbf{k'}\downarrow}^*(j) \frac{f(E_{n\mathbf{k}\uparrow}) - f(E_{m\mathbf{k'}\downarrow})}{i\omega_n + E_{m\mathbf{k'}\downarrow} - E_{n\mathbf{k}\uparrow}} \\
&+ u_{n\mathbf{k}\uparrow}(j)u_{n\mathbf{k}\uparrow}^*(i)v_{m\mathbf{k'}\uparrow}(i)v_{m\mathbf{k'}\uparrow}^*(j) \frac{f(E_{n\mathbf{k}\uparrow}) + f(E_{m\mathbf{k'}\uparrow}) - 1}{i\omega_n - E_{m\mathbf{k'}\uparrow} - E_{n\mathbf{k}\uparrow}} \\
&+ v_{n\mathbf{k}\downarrow}(j)v_{n\mathbf{k}\downarrow}^*(i)u_{m\mathbf{k'}\downarrow}(i)u_{m\mathbf{k'}\downarrow}^*(j) \frac{1 - f(E_{n\mathbf{k}\downarrow}) - f(E_{m\mathbf{k'}\downarrow})}{i\omega_n + E_{m\mathbf{k'}\downarrow} + E_{n\mathbf{k}\downarrow}} \\
&+ v_{n\mathbf{k}\downarrow}(j)v_{n\mathbf{k}\downarrow}^*(i)v_{m\mathbf{k'}\uparrow}(i)v_{m\mathbf{k'}\uparrow}^*(j) \frac{f(E_{m\mathbf{k'}\uparrow}) - f(E_{n\mathbf{k}\downarrow})}{i\omega_n + E_{n\mathbf{k}\downarrow} - E_{m\mathbf{k'}\uparrow}} \\
&+ u_{n\mathbf{k}\uparrow}^*(i)v_{n\mathbf{k}\uparrow}(j)u_{m\mathbf{k'}\downarrow}(i)v_{m\mathbf{k'}\downarrow}^*(j) \frac{f(E_{n\mathbf{k}\uparrow}) - f(E_{m\mathbf{k'}\downarrow})}{i\omega_n - E_{n\mathbf{k}\uparrow} + E_{m\mathbf{k'}\downarrow}} \\
&- u_{n\mathbf{k}\uparrow}^*(i)v_{n\mathbf{k}\uparrow}(j)v_{m\mathbf{k'}\uparrow}(i)u_{m\mathbf{k'}\uparrow}^*(j) \frac{f(E_{n\mathbf{k}\uparrow}) + f(E_{m\mathbf{k'}\uparrow}) - 1}{i\omega_n - E_{n\mathbf{k}\uparrow} - E_{m\mathbf{k'}\uparrow}} \\
&- v_{n\mathbf{k}\downarrow}^*(i)u_{n\mathbf{k}\downarrow}(j)u_{m\mathbf{k'}\downarrow}(i)v_{m\mathbf{k'}\downarrow}^*(j) \frac{1 - f(E_{n\mathbf{k}\downarrow}) - f(E_{m\mathbf{k'}\downarrow})}{i\omega_n + E_{n\mathbf{k}\downarrow} + E_{m\mathbf{k'}\downarrow}} \\
&+ v_{n\mathbf{k}\downarrow}^*(i)u_{n\mathbf{k}\downarrow}(j)v_{m\mathbf{k'}\uparrow}(i)u_{m\mathbf{k'}\uparrow}^*(j) \frac{f(E_{m\mathbf{k'}\uparrow}) - f(E_{n\mathbf{k}\downarrow})}{i\omega_n + E_{n\mathbf{k}\downarrow} - E_{m\mathbf{k'}\uparrow}} \Bigg] e^{-i(\mathbf{k}-\mathbf{k'})\cdot(\mathbf{R}_i - \mathbf{R}_j)}.
\end{aligned}
$$

The measured neutron cross section is proportional to the Fourier transform $\chi_0^{+-}(\mathbf{q}, i\omega_n)$ given by

$$\chi_0^{+-}(\mathbf{q}, i\omega_n) = \sum_{ij, \mathbf{R}_i \mathbf{R}_j} \chi_0^{+-}(\mathbf{r}_i, \mathbf{r}_j, i\omega_n) e^{i\mathbf{q}\cdot[(\mathbf{R}_j + j) - (\mathbf{R}_i + i)]} \qquad (.14)$$

summing over all sites and remembering the notation that $\mathbf{r}_j = \mathbf{R}_j + j$. Regarding the supercell sum

$$\sum_{\mathbf{R}_i \mathbf{R}_j} e^{-i(\mathbf{q}+\mathbf{k}-\mathbf{k}')\cdot(\mathbf{R}_i-\mathbf{R}_j)} \tag{.15}$$

we can uniquely translate $\mathbf{q}$ into the reduced Brillouin zone of the supercells by their reciprocal lattice vectors. However, since the only way the Bloch index enters the Bogoliubov-de Gennes equations is through $\exp(\pm i\mathbf{k}\cdot\mathbf{R}_i)$ it is evident that the resulting eigenvalues $(E_{n\mathbf{k}\sigma})$ and eigenvectors $(u_{n\mathbf{k}\sigma}(i), v_{n\mathbf{k}\sigma}(i))$ are invariant under shifts of $\mathbf{k}$ by a reciprocal supercell lattice vector. Therefore, from a $N_x \times N_y$ unit cell we have simply $\sum_{\mathbf{R}_i \mathbf{R}_j} \exp(-i(\mathbf{q}+\mathbf{k}-\mathbf{k}')\cdot(\mathbf{R}_i-\mathbf{R}_j)) = (N/N_x N_y)^2 \delta(\mathbf{q}+\mathbf{k}-\mathbf{k}')$. Thus, we get

$$
\begin{aligned}
\chi_0^{+-}(\mathbf{q}, i\omega_n) &= \frac{1}{(N_x N_y)^2} \sum_{\substack{\mathbf{k}nm \\ ij}} \left[u_{n\mathbf{k}\uparrow}(j) u_{n\mathbf{k}\uparrow}^*(i) u_{m\mathbf{k}+\mathbf{q}\downarrow}(i) u_{m\mathbf{k}+\mathbf{q}\downarrow}^*(j) \frac{f(E_{n\mathbf{k}\uparrow}) - f(E_{m\mathbf{k}+\mathbf{q}\downarrow})}{i\omega_n + E_{m\mathbf{k}+\mathbf{q}\downarrow} - E_{n\mathbf{k}\uparrow}} \right. \\[2ex]
&+ u_{n\mathbf{k}\uparrow}(j) u_{n\mathbf{k}\uparrow}^*(i) v_{m\mathbf{k}+\mathbf{q}\uparrow}(i) v_{m\mathbf{k}+\mathbf{q}\uparrow}^*(j) \frac{f(E_{n\mathbf{k}\uparrow}) + f(E_{m\mathbf{k}+\mathbf{q}\uparrow}) - 1}{i\omega_n - E_{m\mathbf{k}+\mathbf{q}\uparrow} - E_{n\mathbf{k}\uparrow}} \\[2ex]
&+ v_{n\mathbf{k}\downarrow}(j) v_{n\mathbf{k}\downarrow}^*(i) u_{m\mathbf{k}+\mathbf{q}\downarrow}(i) u_{m\mathbf{k}+\mathbf{q}\downarrow}^*(j) \frac{1 - f(E_{n\mathbf{k}\downarrow}) - f(E_{m\mathbf{k}+\mathbf{q}\downarrow})}{i\omega_n + E_{m\mathbf{k}+\mathbf{q}\downarrow} + E_{n\mathbf{k}\downarrow}} \\[2ex]
&+ v_{n\mathbf{k}\downarrow}(j) v_{n\mathbf{k}\downarrow}^*(i) v_{m\mathbf{k}+\mathbf{q}\uparrow}(i) v_{m\mathbf{k}+\mathbf{q}\uparrow}^*(j) \frac{f(E_{m\mathbf{k}+\mathbf{q}\uparrow}) - f(E_{n\mathbf{k}\downarrow})}{i\omega_n + E_{n\mathbf{k}\downarrow} - E_{m\mathbf{k}+\mathbf{q}\uparrow}} \\[2ex]
&+ u_{n\mathbf{k}\uparrow}^*(i) v_{n\mathbf{k}\uparrow}(j) u_{m\mathbf{k}+\mathbf{q}\downarrow}(i) v_{m\mathbf{k}+\mathbf{q}\downarrow}^*(j) \frac{f(E_{n\mathbf{k}\uparrow}) - f(E_{m\mathbf{k}+\mathbf{q}\downarrow})}{i\omega_n - E_{n\mathbf{k}\uparrow} + E_{m\mathbf{k}+\mathbf{q}\downarrow}} \\[2ex]
&- u_{n\mathbf{k}\uparrow}^*(i) v_{n\mathbf{k}\uparrow}(j) v_{m\mathbf{k}+\mathbf{q}\uparrow}(i) u_{m\mathbf{k}+\mathbf{q}\uparrow}^*(j) \frac{f(E_{n\mathbf{k}\uparrow}) + f(E_{m\mathbf{k}+\mathbf{q}\uparrow}) - 1}{i\omega_n - E_{n\mathbf{k}\uparrow} - E_{m\mathbf{k}+\mathbf{q}\uparrow}} \\[2ex]
&- v_{n\mathbf{k}\downarrow}^*(i) u_{n\mathbf{k}\downarrow}(j) u_{m\mathbf{k}+\mathbf{q}\downarrow}(i) v_{m\mathbf{k}+\mathbf{q}\downarrow}^*(j) \frac{1 - f(E_{n\mathbf{k}\downarrow}) - f(E_{m\mathbf{k}+\mathbf{q}\downarrow})}{i\omega_n + E_{n\mathbf{k}\downarrow} + E_{m\mathbf{k}+\mathbf{q}\downarrow}} \\[2ex]
&\left. + v_{n\mathbf{k}\downarrow}^*(i) u_{n\mathbf{k}\downarrow}(j) v_{m\mathbf{k}+\mathbf{q}\uparrow}(i) u_{m\mathbf{k}+\mathbf{q}\uparrow}^*(j) \frac{f(E_{m\mathbf{k}+\mathbf{q}\uparrow}) - f(E_{n\mathbf{k}\downarrow})}{i\omega_n + E_{n\mathbf{k}\downarrow} - E_{m\mathbf{k}+\mathbf{q}\uparrow}} \right] e^{i\mathbf{q}\cdot(j-i)}.
\end{aligned}
\tag{.16}
$$

The expression for $\chi_0^{-+}(\mathbf{r}_i, \mathbf{r}_j, \tau) = \langle T_\tau \hat{S}_i^-(0) \hat{S}_j^+(\tau) \rangle$ is identical to the result Eqn. (.16) when interchanging the spin indices $\uparrow \leftrightarrow \downarrow$. From the definition of the raising and lowering operators

$$\hat{S}_i^+ = \hat{S}_i^x + i\hat{S}_i^y, \qquad \hat{S}_i^- = \hat{S}_i^x - i\hat{S}_i^y, \tag{.17}$$

it follows that for the transverse spin-spin correlation function $\langle T_\tau \hat{S}_i^x(0)\hat{S}_j^x(\tau)\rangle$ we have

$$\langle T_\tau \hat{S}_i^x(0)\hat{S}_j^x(\tau)\rangle = \frac{1}{4}\left(\langle T_\tau \hat{S}_i^+(0)\hat{S}_j^-(\tau)\rangle + \langle T_\tau \hat{S}_i^-(0)\hat{S}_j^+(\tau)\rangle\right). \quad (.18)$$

Hence, to obtain $\chi_0^{xx}(\mathbf{q}, i\omega_n)$ we simply sum over the spin indices $\sigma, \bar{\sigma}$ in Eqn. .16. Therefore, we can write for the final expression for $\chi_0^{xx}(\mathbf{q}, i\omega_n)$ in the general case of incommensurate spin density wave order

$$\chi_0^{xx}(\mathbf{q}, i\omega_n) = \frac{1}{4(N_x N_y)^2}\sum_{\substack{knm \\ ij\sigma}}\left[a_1(u,v)\frac{1 - f(E_{n\mathbf{k}\sigma}) - f(E_{m\mathbf{k}+\mathbf{q}\sigma})}{i\omega_n + E_{m\mathbf{k}+\mathbf{q}\sigma} + E_{n\mathbf{k}\sigma}}\right.$$

$$+ \quad a_2(u,v)\frac{f(E_{n\mathbf{k}\sigma}) + f(E_{m\mathbf{k}+\mathbf{q}\sigma}) - 1}{i\omega_n - E_{m\mathbf{k}+\mathbf{q}\sigma} - E_{n\mathbf{k}\sigma}}$$

$$+ \quad b_1(u,v)\frac{f(E_{n\mathbf{k}\sigma}) - f(E_{m\mathbf{k}+\mathbf{q}\bar{\sigma}})}{i\omega_n + E_{m\mathbf{k}+\mathbf{q}\bar{\sigma}} - E_{n\mathbf{k}\sigma}}$$

$$+ \quad \left.b_2(u,v)\frac{f(E_{m\mathbf{k}+\mathbf{q}\sigma}) - f(E_{n\mathbf{k}\bar{\sigma}})}{i\omega_n + E_{n\mathbf{k}\bar{\sigma}} - E_{m\mathbf{k}+\mathbf{q}\sigma}}\right]e^{i\mathbf{q}\cdot(j-i)}$$

where

$$a_1(u,v) = v_{n\mathbf{k}\sigma}^*(i)u_{m\mathbf{k}+\mathbf{q}\sigma}(i)\left(v_{n\mathbf{k}\sigma}(j)u_{m\mathbf{k}+\mathbf{q}\sigma}^*(j) - u_{n\mathbf{k}\sigma}(j)v_{m\mathbf{k}+\mathbf{q}\sigma}^*(j)\right), (.19)$$

$$a_2(u,v) = u_{n\mathbf{k}\sigma}^*(i)v_{m\mathbf{k}+\mathbf{q}\sigma}(i)\left(u_{n\mathbf{k}\sigma}(j)v_{m\mathbf{k}+\mathbf{q}\sigma}^*(j) - v_{n\mathbf{k}\sigma}(j)u_{m\mathbf{k}+\mathbf{q}\sigma}^*(j)\right), (.20)$$

$$b_1(u,v) = u_{n\mathbf{k}\sigma}^*(i)u_{m\mathbf{k}+\mathbf{q}\bar{\sigma}}(i)\left(u_{n\mathbf{k}\sigma}(j)u_{m\mathbf{k}+\mathbf{q}\bar{\sigma}}^*(j) + v_{n\mathbf{k}\sigma}(j)v_{m\mathbf{k}+\mathbf{q}\bar{\sigma}}^*(j)\right), (.21)$$

$$b_2(u,v) = v_{n\mathbf{k}\bar{\sigma}}^*(i)v_{m\mathbf{k}+\mathbf{q}\sigma}(i)\left(v_{n\mathbf{k}\bar{\sigma}}(j)v_{m\mathbf{k}+\mathbf{q}\sigma}^*(j) + u_{n\mathbf{k}\bar{\sigma}}(j)u_{m\mathbf{k}+\mathbf{q}\sigma}^*(j)\right). (.22)$$

In the normal state, the expression for $\chi_0^{xx}(\mathbf{q}, i\omega_n)$ reads

$$\chi_0^{xx}(\mathbf{q}, i\omega_n) = \frac{1}{4(N_x N_y)^2}\sum_{\substack{knm \\ ij\sigma}}\left[u_{n\mathbf{k}\sigma}^*(i)u_{m\mathbf{k}+\mathbf{q}\bar{\sigma}}(i)u_{n\mathbf{k}\sigma}(j)u_{m\mathbf{k}+\mathbf{q}\bar{\sigma}}^*(j)\right.$$

$$\times \left.\frac{f(E_{n\mathbf{k}\sigma}) - f(E_{m\mathbf{k}+\mathbf{q}\bar{\sigma}})}{i\omega_n + E_{m\mathbf{k}+\mathbf{q}\bar{\sigma}} - E_{n\mathbf{k}\sigma}}\right]e^{i\mathbf{q}\cdot(j-i)}. \quad (.23)$$

In the case when all the spatial structure of the eigenfunctions u, v is contained in the exponential factors and there is spin degeneracy, this expression reduces

to

$$\chi_{BCS}^0(\mathbf{q}, i\omega_n) = \sum_{nm\mathbf{k}} g_1(u, v) \frac{f(E_\mathbf{k}) - f(E_{\mathbf{k+q}})}{i\omega_n - (E_\mathbf{k} - E_{\mathbf{k+q}})} \tag{.24}$$

$$+ \quad g_2(u, v) \frac{f(E_\mathbf{k}) + f(E_{\mathbf{k+q}}) - 1}{i\omega_n - (E_\mathbf{k} + E_{\mathbf{k+q}})} \tag{.25}$$

$$+ \quad g_3(u, v) \frac{1 - f(E_\mathbf{k}) - f(E_{\mathbf{k+q}})}{i\omega_n + (E_\mathbf{k} + E_{\mathbf{k+q}})}, \tag{.26}$$

where

$$g_1(u, v) = (|u_{n\mathbf{k}}|^2 |u_{m\mathbf{k+q}}|^2 + |v_{n\mathbf{k}}|^2 |v_{m\mathbf{k+q}}|^2 + u_{n\mathbf{k}}^* v_{n\mathbf{k}} u_{m\mathbf{k+q}} v_{m\mathbf{k+q}}^*$$

$$+ \quad u_{n\mathbf{k}} v_{n\mathbf{k}}^* u_{m\mathbf{k+q}}^* v_{m\mathbf{k+q}}) \tag{.27}$$

$$g_2(u, v) = (|u_{n\mathbf{k}}|^2 |v_{m\mathbf{k+q}}|^2 - u_{n\mathbf{k}}^* v_{n\mathbf{k}} u_{m\mathbf{k+q}} v_{m\mathbf{k+q}}^*) \tag{.28}$$

$$g_3(u, v) = (|v_{n\mathbf{k}}|^2 |u_{m\mathbf{k+q}}|^2 - u_{n\mathbf{k}}^* v_{n\mathbf{k}} u_{m\mathbf{k+q}} v_{m\mathbf{k+q}}^*). \tag{.29}$$

In the particular case of a homogeneous superconducting state we have the well-known expressions for the coherence factors $u_\mathbf{k}$ and $v_\mathbf{k}$ fully described by the momentum quantum number $\mathbf{k}$

$$u_\mathbf{k}^2 = \frac{1}{2}\left(1 + \frac{\xi_\mathbf{k}}{E_\mathbf{k}}\right) \tag{.30}$$

$$v_\mathbf{k}^2 = \frac{1}{2}\left(1 - \frac{\xi_\mathbf{k}}{E_\mathbf{k}}\right) \tag{.31}$$

with eigenvalues $E_\mathbf{k}^2 = \xi_\mathbf{k}^2 + \Delta_\mathbf{k}^2$ and the single-particle dispersion $\xi_\mathbf{k} = \varepsilon_\mathbf{k} - \mu$. Inserting these expressions into Eqn. (.24) we find after some algebra

$$\chi_{BCS}^0(\mathbf{q}, i\omega_n) = \sum_\mathbf{k} \frac{1}{2}\left(1 + \frac{\xi_\mathbf{k}\xi_{\mathbf{k+q}} + \Delta_\mathbf{k}\Delta_{\mathbf{k+q}}}{E_\mathbf{k}E_{\mathbf{k+q}}}\right) \frac{f(E_\mathbf{k}) - f(E_{\mathbf{k+q}})}{i\omega_n - (E_\mathbf{k} - E_{\mathbf{k+q}})} \tag{.32}$$

$$+ \quad \frac{1}{4}\left(1 - \frac{\xi_\mathbf{k}\xi_{\mathbf{k+q}} + \Delta_\mathbf{k}\Delta_{\mathbf{k+q}}}{E_\mathbf{k}E_{\mathbf{k+q}}}\right) \frac{f(E_\mathbf{k}) + f(E_{\mathbf{k+q}}) - 1}{i\omega_n - (E_\mathbf{k} + E_{\mathbf{k+q}})}$$

$$+ \quad \frac{1}{4}\left(1 - \frac{\xi_\mathbf{k}\xi_{\mathbf{k+q}} + \Delta_\mathbf{k}\Delta_{\mathbf{k+q}}}{E_\mathbf{k}E_{\mathbf{k+q}}}\right) \frac{1 - f(E_\mathbf{k}) - f(E_{\mathbf{k+q}})}{i\omega_n + (E_\mathbf{k} + E_{\mathbf{k+q}})}.$$

This expression is indeed the well-known BCS expression for the spin suscepti-
bility. However, for $d_{x^2-y^2}$-wave pairing symmetry the gap function is momen-
tum dependent. In particular, the relation, $\Delta_{\mathbf{k}+\mathbf{Q}} = -\Delta_{\mathbf{k}}$ with $\mathbf{Q} = (\pi, \pi)$,
has important consequences for the observables in the d-wave superconducting
state.

.2   Introduction to the SO(5) theory

In this appendix the SO(5) non-linear σ-model (NLσM) introduced by Zhang in 1996, is presented [182]. In particular, I discuss a SO(5) symmetric Hamiltonian in the Fermi sector, the motivation for Eqn. (7.7)-(7.10), and the origin of the π mode in the superconducting state. For a recent review article on the SO(5) theory see Ref. [311].

Assume that antiferromagnetism and d-wave superconductivity constitute the important order parameters at zero temperature. Instead of the construction of a Hamiltonian from specific microscopic considerations, the SO(5) model unifies the SO(3) and SO(2) symmetries known to exist in the antiferromagnetic and superconducting regime of the phase diagram, respectively. This unification is performed by means of a new 5D order parameter dubbed the *superspin*. Thus, the approach is phenomenological and resembles a Ginzburg-Landau theory for the high-T$_c$ superconductors.

In the antiferromagnetic phase Haldane[312] has shown that the low-energy dynamics of the isotropic Heisenberg antiferromagnet is described by a continuum field theory shown to be the SO(3) NLσM with the effective Lagrangian density

$$\mathcal{L}(\mathbf{r}) = \frac{1}{2}\chi\,(\partial_\tau \mathbf{n})^2 - \frac{1}{2}\rho|\nabla_{\mathbf{r}}\mathbf{n}|^2 \quad \text{with} \quad |\mathbf{n}|^2 = 1. \qquad (.33)$$

Here, $\mathbf{n}$ denotes the continuous unit-vector field describing the slow variation of the spins, while χ and ρ are the spin susceptibility and spin stiffness, respectively. The first term of the Lagrangian density is the kinetic energy resulting from the rotational degrees of freedom, while the second contribution is the potential energy arising from the "tension" between neighboring spins. The verification of the SO(3) NLσM as an appropriate description of the low-energy sector of antiferromagnets was given in 1988 by Chakravarty *et al.* [313].

The SO(5) approach generalizes the NLσM to the case of high-T$_c$ superconductors. The superspin is a generalized spin, which *unifies* antiferromagnetism and d-wave superconductivity into a single five dimensional vector $\mathbf{n} = (n_1, n_2, n_3, n_4, n_5)$. Here n_1 and n_5 are identified with the real and the imaginary part of the usual d-wave superconducting order parameter while the remaining three components $\mathbf{m} = (n_2, n_3, n_4)$ are identified with the antiferromagnetic order parameter

$$\mathbf{m} = \frac{1}{2}\sum_{\mathbf{p}} c^\dagger_{\mathbf{p}+\mathbf{Q}}\boldsymbol{\tau} c_{\mathbf{p}}, \qquad (.34)$$

where $c_{\mathbf{p}} = \begin{pmatrix} c_{\mathbf{p}\uparrow} \\ c_{\mathbf{p}\downarrow} \end{pmatrix}$ and $\boldsymbol{\tau}$ denotes the Pauli matrices and $\mathbf{Q}$ is the antiferromagnetic ordering vector.

The generators of infinitesimal rotations in the antiferromagnetic subspace (n_2, n_3, n_4) and the superconducting subspace (n_1, n_5) is the total spin $\mathbf{S}$ and charge Q, respectively. Orthogonal rotations *between* these two sectors is generated by the six π-operators defined by

$$\boldsymbol{\pi}^\dagger = \frac{1}{2} \sum_{\mathbf{p}} \varphi_{\mathbf{p}} c_{\mathbf{p}+\mathbf{Q}}^\dagger \left(\boldsymbol{\tau} \tau_y \right) c_{-\mathbf{p}}^\dagger, \qquad \boldsymbol{\pi} = \left(\boldsymbol{\pi}^\dagger \right)^\dagger, \qquad (.35)$$

where $\boldsymbol{\pi} = (\pi_x, \pi_y, \pi_z)$ and $c_{\mathbf{p}}^\dagger = \begin{pmatrix} c_{\mathbf{p}\uparrow}^\dagger \\ c_{\mathbf{p}\downarrow}^\dagger \end{pmatrix}$, and $\varphi_{\mathbf{p}} = \frac{1}{2}\mathrm{sign}\left(\cos p_x - \cos p_y \right)$.

In general there are $\frac{1}{2}N(N-1)$ symmetry generators in SO(N). If, however, we want the above ten operators $(Q, \mathbf{S}, \boldsymbol{\pi}, \boldsymbol{\pi}^\dagger)$ to be a complete representation of the generators L_{ab} $(= -L_{ba})$ of the SO(5) Lie group, they must satisfy the SO(5) Lie algebra. Using the definition

$$L_{ab} = \begin{pmatrix} 0 & & & & \\ \pi_x^\dagger + \pi_x & 0 & & & \\ \pi_y^\dagger + \pi_y & -S_z & 0 & & \\ \pi_z^\dagger + \pi_z & S_y & -S_x & 0 & \\ -Q & i\left(\pi_x^\dagger - \pi_x\right) & i\left(\pi_y^\dagger - \pi_y\right) & i\left(\pi_z^\dagger - \pi_z\right) & 0 \end{pmatrix}, \qquad (.36)$$

it is straightforward, but tedious, to verify that indeed these generators L_{ab} satisfy the Lie algebra commutation relations

$$[L_{ab}, L_{cd}] = i\left(\delta_{ac} L_{bd} - \delta_{ad} L_{bc} - \delta_{bc} L_{ad} + \delta_{bd} L_{ac} \right). \qquad (.37)$$

The introduction of the SO(5) generalized angular momenta L_{ab} given by equation (.36) allows the superspin $\mathbf{n}$ to be defined as a vector representation of the SO(5) Lie algebra. This follows from the commutation relation

$$[L_{ab}, n_c] = i\delta_{ac} n_b - i\delta_{bc} n_a, \qquad (.38)$$

which can be verified by directly inserting the expressions for L_{ab} and $\mathbf{n}$. Equation (.38) shows that the generators L_{ab} rotate the components of the superspin into each other. Because the orthogonal transformations preserve the length of the superspin vector, $\mathbf{n}^2 = |\psi|^2 + \mathbf{m}^2 = 1$. This introduces the convenient geometric picture of the superspin lying on a 5D sphere with the antiferromagnetic and superconducting phases appearing as 3D and 2D projections, respectively. In this unified description, the two subspaces are no longer independent, but coupled by a simple rotation of the superspin.

The low-energy dynamics of the cuprates are described by the SO(5) NLσM

$$\mathcal{L}(\mathbf{r}) = \frac{1}{2}\chi \sum_a \left(\partial_\tau n_a \right)^2 - \frac{1}{2}\rho \sum_a |\nabla_{\mathbf{r}} n_a|^2, \qquad |\mathbf{n}|^2 = 1, \qquad (.39)$$

in terms of the generalized susceptibilities χ_c, χ_s, χ_π and the stiffness ρ_c, ρ_s, ρ_π in the charge, spin, and π sector, respectively.

The following model will modify the SO(5) symmetric NLσM (.39) by introducing two additionally symmetry breaking terms. First of all, the chemical potential μ breaks the symmetry because it couples only to the electric charge L_{15}, which is just *one* of the ten SO(5) generators. Secondly, an *ad hoc* potential V given by

$$V(\mathbf{n}) = -\frac{g}{2}\left(n_2^2 + n_3^2 + n_4^2\right) = -\frac{g}{2}\mathbf{m}^2, \quad g > 0, \tag{.40}$$

will explicitly break the symmetry by favoring an antiferromagnetic ground state at half-filling ($\mu = 0$) and low temperatures $T < T_N$.

Below, it will be shown how the symmetry breaking terms V and μ *partially compensate* each other (and vanish completely at the transition point) such that the SO(5) symmetry is still approximately valid.

Taking these three symmetry breaking terms into account, the Lagrangian density (.39) can be written

$$\mathcal{L}(\mathbf{r}) = \sum_{a<b} \frac{\chi_{ab}}{2}\omega_{ab}^2(\mathbf{n}) - \sum_{a<b} \frac{\rho_{ab}}{2}v_{ab}^2(\mathbf{n}) - V(\mathbf{n}), \tag{.41}$$

where

$$w_{ab}(\mathbf{n}) = n_a\left(\partial_\tau n_b - 2\mu\left[\delta_{b1}n_5 - \delta_{b5}n_1\right]\right) - (a \leftrightarrow b), \tag{.42}$$

and

$$v_{ab}(\mathbf{n}) = n_a\nabla_{\mathbf{r}}n_b - (a \leftrightarrow b), \tag{.43}$$

and $\nabla_{\mathbf{r}} = (\partial_x, \partial_y)$. In the isotropic case where $\chi_\pi = \chi_s = \chi_c \equiv \chi$, expression (.41) simplifies to

$$\begin{aligned}\mathcal{L}(\mathbf{r}) &= \frac{1}{2}\chi\sum_a\left(\partial_\tau n_a\right)^2 - \frac{1}{2}\rho\sum_a|\nabla_{\mathbf{r}}n_a|^2 + (2\mu)\chi\left(n_1\partial_\tau n_5 - n_5\partial_\tau n_1\right) \\[2mm] &+ \frac{(2\mu)^2}{2}\chi\left(n_1^2 + n_5^2\right) + \frac{1}{2}g\left(n_2^2 + n_3^2 + n_4^2\right).\end{aligned} \tag{.44}$$

Thus the effective potential V_{eff} for the static solutions become

$$V_{\text{eff}} = -\frac{g}{2}\left(n_2^2 + n_3^2 + n_4^2\right) - \frac{(2\mu)}{2}\chi\left(n_1^2 + n_5^2\right). \tag{.45}$$

Clearly, this reveals a competition between the antiferromagnetic and superconducting order parameters with g favoring the antiferromagnetic sphere (n_2, n_3, n_4) and μ favoring the superconducting plane (n_1, n_5). Minimizing

V_{eff} with the constraint $f^2 + \mathbf{m}^2 = 1$ (by using *e.g.* the method of Lagrange multipliers) leads to a phase transition between the antiferromagnetic and superconducting phases at

$$\mu = \mu_c \equiv \frac{1}{2}\sqrt{\frac{g}{\chi}}. \tag{.46}$$

Below this critical chemical potential μ_c, the system is in the antiferromagnetic phase ($\mathbf{m}^2 = 1, f^2 = 0$) while $\mu > \mu_c$ leads to a superconducting state ($\mathbf{m}^2 = 0, f^2 = 1$). From (.46) it follows that when $g = 0$, any finite value of the chemical potential will flop the superspin into the superconducting plane. In the anisotropic situation where $\chi_c \neq \chi_\pi$ more complex phase diagrams with coexisting order is possible as shown by Zhang[182].

Turning, briefly to the discussion of the collective modes, we expect from Goldstone's theorem that new bosons arise from the higher symmetry of the action. For instance, when the superspin vector is fixed in the (n_1, n_5) plane the SO(2) gauge invariance is spontaneously broken, and a new triplet mode from the spin sector is expected. The collective modes are identified with the Gaussian fluctuations of the superspin around the minima, and are determined from the Lagrange equations of motion with a second order expansion of the Lagrangian density (.41).

For simplicity, it is convenient again to consider the isotropic situation where $\chi_\pi = \chi_s = \chi_c \equiv \chi$. Without loss of generality, we may choose the two ground state superspin configurations to be

$$\mathbf{n}_0 = \mathbf{n}_{\text{af}} = (0, 1, 0, 0, 0) \quad \text{for} \quad \mu < \mu_c, \tag{.47}$$

$$\mathbf{n}_0 = \mathbf{n}_{\text{sc}} = (1, 0, 0, 0, 0) \quad \text{for} \quad \mu > \mu_c, \tag{.48}$$

corresponding to antiferromagnetism and superconductivity, respectively. Allowing infinitesimal deviations $\delta\mathbf{n}$ the vectors become

$$\mathbf{n} = \mathbf{n}_{\text{af}} + \delta\mathbf{n} = (\delta n_1, 1, \delta n_3, \delta n_4, \delta n_5), \tag{.49}$$

$$\mathbf{n} = \mathbf{n}_{\text{sc}} + \delta\mathbf{n} = (1, \delta n_2, \delta n_3, \delta n_4, \delta n_5). \tag{.50}$$

The deviations $\delta\mathbf{n}$ are the dynamical variables of the following discussion. The vectors (.49) and (.50) do not contain deviations in the ground state coordinate because that turns out to lead to third order contributions.

By a simple expansion to second order of the Lagrangian density

$$\mathcal{L}(\mathbf{n}) = \mathcal{L}(\mathbf{n}_0 + \delta\mathbf{n}) = \mathcal{L}(\mathbf{n}_0) + \mathcal{L}^{(2)}(\delta\mathbf{n}) = \mathcal{L}(\mathbf{n}_0) + \frac{1}{2}\delta\mathbf{n} \cdot \frac{\partial^2 \mathcal{L}}{\partial \delta\mathbf{n}^2}(\mathbf{n}_0) \cdot \delta\mathbf{n}, \tag{.51}$$

where the first derivative disappears at the extremum, the second order terms

become

$$\mathcal{L}_{\text{af}}^{(2)}(\delta\mathbf{n}) \;=\; \frac{1}{2}\chi\sum_{a\neq 2}(\partial_\tau\delta n_a)^2 - \frac{1}{2}\rho\sum_{a\neq 2}(\nabla_\mathbf{r}\delta\mathbf{n_a})^2 \tag{.52}$$

$$- \;(2\mu)\chi\left(\delta n_1\partial_\tau\delta n_5 - \delta n_5\partial_\tau\delta n_1\right) + \left(\frac{(2\mu)^2}{2}\chi - \frac{g}{2}\right)\left(\delta n_1^2 + \delta n_5^2\right),$$

$$\mathcal{L}_{\text{sc}}^{(2)}(\delta\mathbf{n}) \;=\; \frac{1}{2}\chi\sum_{a\neq 1}(\partial_\tau\delta n_a)^2 - \frac{1}{2}\rho\sum_{a\neq 1}(\nabla_\mathbf{r}\delta\mathbf{n_a})^2 \tag{.53}$$

$$+ \;\left(\frac{g}{2} - \frac{(2\mu)^2}{2}\chi\right)\left(\delta n_2^2 + \delta n_3^2 + \delta n_4^2\right).$$

By using Lagrange's equations of motion

$$\partial_\tau\frac{\partial\mathcal{L}^{(2)}}{\partial(\partial_\tau\delta n_a)} + \nabla_\mathbf{r}\cdot\frac{\partial\mathcal{L}^{(2)}}{\partial(\nabla_\mathbf{r}\delta n_a)} = \frac{\partial\mathcal{L}^{(2)}}{\partial\delta n_a}, \tag{.54}$$

the collective modes can be readily obtained.
For instance, in the superconducting ground state ($\mu > \mu_c$) this results in the following equations

$$\chi\partial_\tau^2\delta n_5 \;=\; \rho\nabla^2\delta n_5, \tag{.55}$$

$$\chi\partial_\tau^2\delta n_{2,3,4} \;=\; \rho\nabla^2\delta n_{2,3,4} + \left(g - (2\mu)^2\chi\right)\delta n_{2,3,4}, \tag{.56}$$

where Eqn. (.55) is the standard sound mode in the superconductor. By means of the Anderson-Higgs mechanism this is rendered massive and turned into a plasmon mode. The second equation reveals the antiferromagnetic fluctuations in the superconducting phase. This new Goldstone mode has the following dispersion relation

$$\omega_{2,3,4}(q) = \sqrt{\frac{\rho q^2 - g + (2\mu)^2\chi}{\chi}}. \tag{.57}$$

Hence, the energy gap at $q = 0$ of this collective mode also disappears at μ_c. I light of the above picture this corresponds to a solidification of the quantum superfluid of Cooper pairs to an antiferromagnetic crystal. In the SO(5) model we *identify* this new mode with the π resonance mode known from inelastic neutron scattering experiments.

The problem of constructing exact SO(5) symmetric Fermionic models was first solved in 1997 by Burgess *et al.*[314], Henley [245] and Rabello *et al.* [244]. They showed how the construction of bilinears from a SO(5) spinor leads to a natural definition of exact SO(5) symmetric microscopic Hamiltonians. In

the case of SO(N) one of the most important representations is the *spinor representation* with the introduction of N matrices Γ^a satisfying the following anticommutator

$$\left\{ \Gamma^a, \Gamma^b \right\} = 2\delta^{ab}. \tag{.58}$$

This set of matrices is called a Clifford algebra. The spinor representation of the SO(N) *generators* Γ^{ab} can now be written as

$$\Gamma^{ab} = -\frac{i}{2} \left[\Gamma^a, \Gamma^b \right]. \tag{.59}$$

This can be verified explicitly by inserting Γ^{ab} into (.37). The Pauli and Dirac[16] matrices are well-known sets satisfying the Clifford condition from equation (.58). In the first case a spinor representation is formed by the usual Pauli spinors $\Psi_{\mathbf{p}}^t = (c_{\mathbf{p}\uparrow}, c_{\mathbf{p}\downarrow})$. From these, one can construct exact SO(3) symmetric models by taking the scalar product of two SO(3) vectors $\mathbf{n_p} = \Psi_{\mathbf{p}}^\dagger \boldsymbol{\tau} \Psi_{\mathbf{p}}$ as we saw in the discussion of the Hubbard model. Indeed the scalar product is rotation invariant.

In the case of SO(5) symmetry these ideas can be readily extended by using five 4×4 generalized Pauli matrices Γ^α given by

$$\Gamma^1 = \begin{pmatrix} 0 & -i\tau_y \\ i\tau_y & 0 \end{pmatrix}, \tag{.60}$$

$$\Gamma^\alpha = \begin{pmatrix} \tau_\alpha & 0 \\ 0 & \tau_\alpha^t \end{pmatrix} \qquad \alpha = x, y, z, \tag{.61}$$

$$\Gamma^5 = \begin{pmatrix} 0 & \tau_y \\ \tau_y & 0 \end{pmatrix}, \tag{.62}$$

where the superscript t indicates transposition. Since the Pauli matrices form a Clifford algebra, so will the Γ-matrices.

Expecting the following constructed Hamiltonian to *unify* antiferromagnetism and superconductivity we define the spinor

$$\Psi_{\mathbf{P}}^t = \left(c_{\mathbf{p}\uparrow}, c_{\mathbf{p}\downarrow}, \varphi_{\mathbf{p}}\, c^\dagger_{-\mathbf{p}+\mathbf{Q}\uparrow}, \varphi_{\mathbf{p}}\, c^\dagger_{-\mathbf{p}+\mathbf{Q}\downarrow} \right), \tag{.63}$$

where $\varphi_{\mathbf{p}} \equiv \text{sign}\,(\cos p_x - \cos p_y)$, and $\mathbf{Q} = (\pi, \pi)$ is the antiferromagnetic ordering vector. As was mentioned earlier the sign factor $\varphi_{\mathbf{p}}$ closes the SO(5) algebra exactly.

If restricting the momenta $\mathbf{p}, \mathbf{p}'$ to be given within the first magnetic Bril-

---

[16]With the usual notation γ_n with $n = 0, 1, 2, 3$, it is the set $\{\gamma_0, i\gamma_1, i\gamma_2, i\gamma_3\}$ that satisfy the Clifford relation.

louin zone, it is seen that the spinor $\Psi_{\mathbf{p}}$ satisfies the anticommutation relations

$$\left\{\Psi_{\mathbf{p}\alpha}^{\dagger}, \Psi_{\mathbf{p}'\beta}\right\} = \delta_{\alpha\beta}\delta(\mathbf{p} - \mathbf{p}'), \tag{.64}$$

$$\left\{\Psi_{\mathbf{p}\alpha}^{\dagger}, \Psi_{\mathbf{p}'\beta}^{\dagger}\right\} = \{\Psi_{\mathbf{p}\alpha}, \Psi_{\mathbf{p}'\beta}\} = 0, \tag{.65}$$

which simply follows from the fact that each component satisfies the anticommutation relations.

The SO(5) spinor Eqn. (.63) can be used to construct the SO(5) vector (the superspin)

$$\mathbf{n} = \frac{1}{4}\sum_{\mathbf{p}} \Psi_{\mathbf{p}}^{\dagger}\mathbf{\Gamma}\Psi_{\mathbf{p}+\mathbf{Q}}. \tag{.66}$$

Similarly the generators in this representation can be written as

$$L_{ab} = \frac{1}{4}\sum_{\mathbf{p}} \Psi_{\mathbf{p}}^{\dagger}\Gamma^{ab}\Psi_{\mathbf{p}}. \tag{.67}$$

For instance, by a simple expansion the operator L_{12} is seen to be

$$L_{12} = \frac{i}{4}\sum_{\mathbf{p}} \varphi_{\mathbf{p}} \left(c_{\mathbf{p}\uparrow}^{\dagger}c_{-\mathbf{p}+\mathbf{Q}\uparrow}^{\dagger} - c_{\mathbf{p}\downarrow}^{\dagger}c_{-\mathbf{p}+\mathbf{Q}\downarrow}^{\dagger} + c_{\mathbf{p}\uparrow}c_{-\mathbf{p}+\mathbf{Q}\uparrow} - c_{\mathbf{p}\downarrow}c_{-\mathbf{p}+\mathbf{Q}\downarrow}\right) = -\left(\pi_x^{\dagger} + \pi_x\right), \tag{.68}$$

in agreement with the definition given by equation (.36).

An important property of the spinor representation is that it allows a simple of constructing exact SO(5) invariant interactions,

$$H_{\text{int}} = -\sum_{\mathbf{pp'q}} V(\mathbf{q}) \left(\Psi_{\mathbf{p}}^{\dagger}\mathbf{\Gamma}\Psi_{\mathbf{p}+\mathbf{q}}\right) \cdot \left(\Psi_{\mathbf{p'}}^{\dagger}\mathbf{\Gamma}\Psi_{\mathbf{p'}-\mathbf{q}}\right), \tag{.69}$$

where $V(\mathbf{q})$ is a coupling strength dependent on the momentum transfer $\mathbf{q} = \mathbf{p} - \mathbf{p}'$. Being the scalar product of two SO(5) vectors, H_{int} is manifestly SO(5) symmetric[17].

Of course a fully rotational symmetric model cannot possibly be correct since it implies that the superconducting and antiferromagnetic phases have the same single-particle excitation spectra. However, the d-wave superconductor has gap nodes, while an antiferromagnet has a large energy gap in the charge excitation spectrum. For instance, a mean-field calculation with $\mathbf{\Delta}(\mathbf{q}) = -\sum_{\mathbf{p'}} V(\mathbf{q})\langle\Psi_{\mathbf{p'}}^{\dagger}\mathbf{\Gamma}\Psi_{\mathbf{p'}-\mathbf{Q}}\rangle$ and in the limit where $\mathbf{q} = \mathbf{Q}$ the total

---

[17]In general a SO(5) spinor bilinear will have 4×4 = 16 components. These can be decomposed (Schur's Lemma) into a direct sum of a scalar, a vector and an antisymmetric tensor (1+5+10 = 16). In the above expression for H_{int} only the vector interaction term has been included since this seems to capture all the essential physics.

Hamiltonian can be written as

$$H = \sum_{\mathbf{p}} \Psi_{\mathbf{p}}^{\dagger} \left(\varepsilon_{\mathbf{p}}\delta_{\mathbf{pp'}} + \mathbf{\Delta} \cdot \mathbf{\Gamma}\delta_{\mathbf{p'p+Q}}\right)\Psi_{\mathbf{p'}} = \sum_{\mathbf{p}} \Psi_{\mathbf{p}}^{\dagger}\underline{\underline{H}}\Psi_{\mathbf{p'}}. \tag{.70}$$

Inverting the matrix $(\omega\underline{I} - \underline{H})$ to find the Green function gives

$$G_{\alpha\beta}(\mathbf{p}, \mathbf{p'}, \omega) = \frac{(\omega + \varepsilon_{\mathbf{p}})\delta_{\alpha\beta}\delta_{\mathbf{pp'}} + \mathbf{\Delta} \cdot \mathbf{\Gamma}_{\alpha\beta}\delta_{\mathbf{pp'+Q}}}{\omega^2 - \varepsilon_{\mathbf{p}}^2 - |\mathbf{\Delta}|^2 + i\delta}. \tag{.71}$$

These last three equations (.69-.71) and the SO(5) concomitant π mode explain the starting point of the studies of the peak-dip-hump structure (see Eqns. (7.7-7.10)) in the single particle spectral function as a result of coupling between the electrons and the π mode.

In the antiferromagnetic regime where $\varphi_{\mathbf{p}}$ completely vanishes from $\mathbf{\Delta}$, the quasi-particle excitation spectrum $E_{\mathbf{p}} = \sqrt{\varepsilon_{\mathbf{p}}^2 + |\mathbf{\Delta}|^2}$ (given as usual by the poles of the Green function) contains a full s-wave gap. In the superconducting state the topological form of the spectrum is the same, but a sign change appears across the nodes because the $\varphi_{\mathbf{p}}$ factor survives in this state. An important question is therefore how to slightly break the SO(5) symmetry such that the physically correct excitation spectra emerge. Additionally, one has to figure out what are the further consequences of the symmetry breaking terms. This is usually done by constructing the corresponding effective low-energy Lagrangian.

In complete agreement with the discussion of the SO(5) NLσM, Rabello *et al.* [244] proposed the following symmetry-breaking terms

$$H_\mu \quad = \quad -2\mu L_{15} = -2\mu Q, \tag{.72}$$

$$H_g \quad = \quad -g\sum_{\mathbf{pp'}}\sum_{a=2,3,4}\left(\Psi_{\mathbf{p}}^{\dagger}\Gamma^a\Psi_{\mathbf{p+Q}}\right)\left(\Psi_{\mathbf{p'}}^{\dagger}\Gamma^a\Psi_{\mathbf{p'+Q}}\right), \tag{.73}$$

between the antiferromagnetic and superconducting states. Thus, the total Hamiltonian H reads

$$H = H_{\text{kin}} + H_{\text{int}} + H_g + H_\mu \tag{.74}$$

The expressions for H_μ and H_g are identical to $H_\mu = -2\mu L_{15}$ and $V(n) = -\frac{g}{2}\left(n_2^2 + n_3^2 + n_4^2\right)$ introduced in the discussion of the SO(5) NLσM. By repeating the mean-field calculation presented in (.70) and (.71) with H_μ and H_g included, Rabello *et al.* showed that indeed the effect of H_g is to remove the gap nodes of the antiferromagnetic spectrum, while leaving the d-wave superconducting gap unaffected [244]. Thus, the microscopic representation of the SO(5) model also predicts antiferromagnetic order at half-filling and

d-wave superconductivity away from half-filling. Furthermore, it was shown that the Goldstone mode spectra including the mass gap produced by the symmetry-breaking terms are identical to the spectra obtained by the SO(5) NLσM. Therefore, H_μ and H_g are observed again to partially compensate each other such that the concept of SO(5) symmetry is still approximately valid.

References

[1] J.G. Bednorz and K.A. Müller, Z. Phys. B **64**, 189 (1986).

[2] S. Chakravarty, H-Y. Kee, and K. Völker, Nature **428**, 53 (2004).

[3] Y.J. Uemura *et al.*, Phys. Rev. Lett **66**, 2665 (1991).

[4] J.L. Tallon, and J.W. Loram, Physica C **349 1-2**, 53 (2001).

[5] N. Miyakawa *et al.*, Phys. Rev. Lett. **80**, 157 (1998).

[6] V.J. Emery, and S.A. Kivelson, Nature **374**, 434 (1995); E. Carlson *et al.*, Phys. Rev. Lett. **83**, 612 (1999).

[7] H. Ding *et al.*, Nature **382**, 51 (1996).

[8] A.G. Loeser *et al.*, Science **273**, 325 (1996).

[9] Z.A. Xu *et al.* Nature **406**, 486 (2000).

[10] C.M. Varma *at al.*, Phys. Rev. Lett. **63**, 1996 (1989).

[11] C.M. Varma *at al.*, Phys. Rev. Lett. **64**, 497 (1990).

[12] A. Kaminski *et al.*, Phys. Rev. Lett. **84**, 1788 (2000).

[13] T. Valla *et al.*, Science, **285**, 2110 (2000).

[14] E. Dagotto, Rev. Mod. Phys. **66**, 763 (1994); T. Timusk and B. Statt, Rep. Prog. Phys. **62**, 61 (1999); M.R. Norman and C. Pepin, cond-mat/0302347.

[15] J. Orenstein, and A.J. -millis, Science **288**, 468 (2000).

[16] J. Zaanen, G.A. Sawatzky, and J.W. Allen, Phys. Rev. Lett. **55**, 418 (1985).

[17] V.J. Emery, Phys. Rev. Lett. **58**, 2794 (1987).

[18] C.M. Varma, S. Schmit-Rink and E. Abrahams, Solid State. Comm. **62**, 681 (1987).

[19] F.C. Zhang and T.M. Rice, Phys. Rev. B **37**, 3759 (1988).

[20] M.E. Simon and A.A. Aligia, Phys. Rev. B **52**, 7701 (1995).

[21] S. Daul, D.J. Scalapino and S.R. White, Phys. Rev. Lett. **84**, 4188 (2000).

[22] I. Martin *et al.* Europhys. Lett. **56**, 849 (2001); Int. J. Mod. Phys. **14**, 3567 (2000).

[23] Y. Wang, and A.H. McDonald, Phys. Rev. B **52**, R3876 (1995).

[24] J.-X. Zhu, and C.S. Ting, Phys. Rev. Lett. **87**, 147002 (2001).

[25] P.W. Anderson, Phys. Rev. **110**, 827 (1958).

[26] B.M. Andersen, and P. Hedegård, Phys. Rev. B **66**, 104515 (2002).

[27] A.F. Andreev, Sov. Phys. JETP **19**, 1228 (1964).

[28] M. Sigrist, D.B. Bailey, and R.B. Laughlin, Phys. Rev. Lett. **74**, 3249 (1995).

[29] P.G. de Gennes and D. Saint-James, Phys. Lett. **4**, 151 (1963).

[30] L.J. Buchholtz and G. Zwicknagl, Phys. Rev. B **23**, 5788 (1981).

[31] C-R.Hu, Phys. Rev. Lett. **72**, 1526 (1994).

[32] For a review see, T. Löfwander, V.S. Shumeiko, and G. Wendin, Supercond. Sci. Thecnol. **14**, R53 (2001).

[33] C. Bruder, Phys. Rev. B **41**, 4017 (1990).

[34] M. Sigrist, Prog. Theo. Phys. **99**, 899 (1998).

[35] J. Geerk, X.-X. Xi, and G. Linker, Z. Phys. B **73**, 329 (1988).

[36] S. Kashiwaya *et al.*, Physica B **194-6**, 2199 (1994). Phys. Rev. Lett. **72**, 1526 (1994).

[37] For a review see, TS. Kashiwaya and Y. Tanaka, Rep. Prog. Phys. **63**, 1641 (2000).

[38] Z-X. Shen *et al.*, Phys. Rev. Lett. **70**, 1553 (1993).

[39] D.J. van Harlingen, Rev. Mod. Phys. **67**, 515 (1995).

[40] S. Kashiwaya, Y. Takana, M. Koyanagi, and M. Kajimura, Phys. Rev. B **53**, 2667 (1996).

[41] M. Covington *et al.*, Phys. Rev. Lett. **79**, 277 (1997).

[42] M. Fogelström, D. Rainer and J.A. Sauls, Phys. Rev. Lett. **79**, 281 (1997); M. Fogelström and S-K. Yip, Phys. Rev. B. **57**, R14060 (1998).

[43] C. Honerkamp, K. Wakabayashi, and M. Sigrist, Europhys. Lett. **50** (3), 368 (2000).

[44] B. Lake *et al.*, Nature **415**, 299 (2002).

[45] B. Khaykovich *et al.*, Phys. Rev. B **67**, 054501 (2003).

[46] E. Merzbacher, "Quantum Mechanics", Wiley Int. Edition, (1970).

[47] K. Kuboki, J. Phys. Soc. Jap. **68**, 3150 (1999).

[48] M. Matsumoto and H. Shiba, J. Phys. Soc. Jap. **64**, 3385 (1995), **64**, 4867 (1995), **65**, 2194 (1996).

[49] S.H. Pan *et al.*, Phys. Rev. Lett. **85**, 1536 (2000).

[50] I. Maggio-Aprile *et al.*, Phys. Rev. Lett. **75**, 2754 (1995).

[51] B.M. Andersen, H. Bruus, and P. Hedegård, Phys. Rev. B **61**, 6298 (2000).

[52] J-X. Zhu and C.S. Ting, Phys. Rev. Lett. **87**, 147002 (2001).

[53] R.I. Miller *et al.*, Phys. Rev. Lett. **88**, 137002 (2002).

[54] V.F. Mitrovic *et al.*, Nature **413**, 501 (2001).

[55] B.M. Andersen, and P. Hedegård, Phys. Rev. B, **67**, 8127 (2003).

[56] H.C. Manoharan, C.P. Lutz, and D.M. Eigler, Nature **403**, 512 (2000).

[57] J. Tersoff and D.R. Hamann, Phys. Rev. B **31**, 805 (1985).

[58] I. Giaever, Phys. Rev. Lett. **5**, 464 (1960).

[59] A. Yazdani *et al.*, Phys. Rev. Lett. **83**, 176 (1999).

[60] E.W. Hudson *et al.*, Science **285**, 88 (1999).

[61] A. Yazdani *et al.*, Science **275**, 1767 (1997).

[62] S.H. Pan *et al.*, Nature **403**, 746 (2000).

[63] J.X. Zhu, C.S. Ting and C.R. Hu, Phys. Rev. B **62**, 6027 (2000).

[64] I. Martin, A.V. Balatsky, and J. Zaanen, Phys. Rev. Lett. **88**, 097003 (2002).

[65] S. Chakravarty, A. Sudbo, P.W. Anderson, and S. Strong, Science **261**, 337 (1993).

[66] D. Pines, Physica C **282-287**, 273 (1997).

[67] E.W. Hudson *et al.*, Nature **411**, 920 (2001).

[68] J. Zaanen, Nature **422**, 569 (2003).

[69] L. Bürgi *et al.*, J. Elec. Spec. Relat. Phenom. **109**, 33 (2000).

[70] L. Petersen *et al.*, J. Elec. Spec. Relat. Phenom. **109**, 97 (2000).

[71] J.E. Hoffman *et al.*, Science **297**, 1148 (2002).

[72] K. McElroy *et al.*, Nature **422**, 592 (2003).

[73] Q.-H. Wang and D.-H. Lee, Phys. Rev. B **67**, 020511, (2003).

[74] T. Pereg-Barnea, and M. Franz, Phys. Rev. B **68**, 180506 (2003).

[75] C. Howald *et al.*, Phys. Rev. B **67**, 014533 (2003).

[76] S.A. Kivelson *et al.* Rev. Mod. Phys. **75**, 1201 (2003).

[77] M. Vershinin *et al.*, Science **303**, 1995 (2004).

[78] K. McElroy *et al.*, cond-mat/0404005.

[79] L. Yu, Acta Phys. Sin. **21**, 75 (1965).

[80] H. Shiba, Prog. Theo. Phys. **40**, 435 (1968).

[81] A.A. Abrikosov, and L.P. Gorkov, Zh. Eksp. Teor. Fiz. **39**, 1781 (1962) [Sov. Phys. JETP **12**, 1243 (1961).]

[82] A. Sakurai, Prog. Theo. Phys. **44**, 1472 (1970).

[83] M.I. Salkola, A.V. Balatsky, and J.R. Schrieffer, Phys. Rev. B **55**, 12648 (1997).

[84] J.M. Byers, and M.E. Flatte, *Solid State Physics*, edited by H. Ehrenreich and F. Spaepen (Academic Press, New York, 1999) Vol. 52, pp 137-228.

[85] A.V. Balatsky, M.I. Salkola and A. Rosengren, Phys. Rev. B **51** 15547 (1995); M.I. Salkola, A.V. Balatsky and D.J. Scalapino, Phys. Rev. Lett. **77**, 1841 (1996).

[86] R. Joynt, J. Low. Temp. Phys. **109**, 811 (1997).

[87] A.M. Finkelstein *et al.* Physica (Amsterdam) **168C**, 370 (1990).

[88] H. Alloul *et al.* Phys. Rev. Lett. **67**, 3140 (1991); A.V. Mahajan *et al.*, *ibid* **72**, 3100 (1994).

[89] J. Bobroff *et al.* Phys. Rev. Lett. **83**, 4381 (1999).

[90] P. Mendels *et al.* Europhys. Lett. **46**, 678 (1999).

[91] M.H. Julien *et al.* Phys. Rev. Lett. **84**, 3422 (2000).

[92] Y. Chen, and C.S. Ting, Phys. Rev. Lett. **92**, 077203 (2004).

[93] Z. Wang and P.A. Lee, Phys. Rev. Lett. **89**, 217002 (2002).

[94] A. Polkovnikov, S. Sachdev and M. Vojta, Phys. Rev. Lett. **86**, 296 (2001).

[95] G.B. Martins *et al.*, Phys. Rev. Lett. **78**, 3563 (1997).

[96] A. Polkovnikov, Phys. Rev. B, 65, 064503 (2002).

[97] K. Ingersent, and Q. Si, cond-mat/9810226.

[98] S. Sachdev, Rev. Mod. Phys. **75**, 913 (2003).

[99] D. Morr and N.A. Stavropoulos, Phys. Rev. B **66**, 140508 (2002).

[100] L. Zhu, W.A. Atkinson and P.J. Hirschfeld, cond-mat/0208008.

[101] D.J. Derro, E.W. Hudson, K.M. Lang, S.H. Pan, J.C. Davis, J.T. Markert, and A.L. de Lozanne, Phys. Rev. Lett. **88**, 097002 (2002).

[102] M.E. Flatte and D.E. Reynolds, Phys. Rev. B **61**, 14810 (2000).

[103] D. Morr and N.A. Stavropoulos, cond-mat/0205328.

[104] Y. Onishi, Y. Ohashi, Y. Shingaki, and K. Miyake, J. Phys. Soc. Jpn. **65**, 675 (1996); U. Michelucci, F. Venturini and A.P. Kampf, cond-mat/0107621.

[105] J.M. Byers, M.E. Flatte and D.J. Scalapino, Phys. Rev. Lett. **71**, 3363 (1993).

[106] B.M. Andersen, P. Hedegård and H. Bruus, Phys. Rev. B, **67**, 134528 (2003).

[107] M. Vojta, Y. Zhang and S. Sachdev, Phys. Rev. Lett. **85**, 4940 (2000); Phys. Rev. **62**, 6721 (2000).

[108] A.V. Balatsky, Phys. Rev. Lett. **80**, 1972 (1998).

[109] R.B. Laughlin, Phys. Rev. Lett. **80**, 5188 (1998).

[110] M.E. Flatte, Phys. Rev. B **61**, 14920 (2000); J.-M. Tang and M.E. Flatte, Phys. Rev. B **66**, 060504 (2002).

[111] B.M. Andersen, Phys. Rev. B **68**, 094518 (2003).

[112] B.M. Andersen, Brazilian Journal of Physics **33**, 775 (2003).

[113] S. Chakravarty, R.B. Laughlin, D.K. Morr, and C. Nayak, Phys. Rev. B **63**, 094503 (2001).

[114] B.I. Halperin, and T.M. Rice, Solid State Phys. **21**, 116 (1968).

[115] I. Affleck, and J.B. Marston, Phys. Rev. B **37**, 3774 (1988); J.B. Marston, and I. Affleck, Phys. Rev. B **39**, 11538 (1989).

[116] X.-G. Wen, and P.A. Lee, Phys. Rev. Lett. **76**, 503 (1996).

[117] X.-G. Wen, and P.A. Lee, Phys. Rev. Lett. **78**, 4111 (1997).

[118] S. Chakravarty, C. Nayak, and S. Tewari, cod-mat/0306084.

[119] H.K. Nguyen, and S. Chakravarty, Phys. Rev. B **65**, 180519 (2002); S. Chakravarty, H.-Y. Kee, and C. Nayak, Int. J. Mod. Phys. B **15**, 2901 (2001).

[120] X. Yang, and C. Nayak, Phys. Rev. B **65**, 064523 (2002).

[121] C. Stock *et al.*, Phys. Rev. B **66**, 024505 (2002).

[122] J-X. Zhu, W. Kim, C.S. Ting, and J.P. Carbotte, Phys. Rev. Lett. **87**, 197001 (2001).

[123] Q-H. Wang, Phys. Rev. Lett. **88**, 057002 (2002).

[124] D. Morr, Phys. Rev. Lett. **89**, 106401 (2002).

[125] D. Zhang, and C.S. Ting, Phys. Rev. B **67**, 100506 (2003).

[126] L. Zhu, W.A. Atkinson, and P.J. Hirschfeld, Phys. Rev. B **69**, 060503 (2004)

[127] L. Capriotti, D.J. Scalapino, and R.D. Sedgewick, cond-mat/0302563.

[128] D.K. Morr, and A.V. Balatsky, Phys. Rev. Lett. **90**, 067005 (2003).

[129] T. Pereg-Barnea, and M. Franz, cond-mat/0401594.

[130] M. Norman, Phys. Rev. B **63**, 092509 (2001).

[131] X.J. Zhou *et al.*, Phys. Rev. Lett. **86**, 5578 (2001).

[132] B.M. Andersen, unpublished.

[133] C. Bena *et al.*, cond-mat/0311299.

[134] C. Bena *et al.*, cond-mat/0405468.

[135] E.W. Carlson, V.J. Emery, S.A. Kivelson, and D. Orgad, cond-mat/0206217; S.A. Kivelson *et al.* Rev. Mod. Phys **75**, 1201 (2003).

[136] A.H. Castro Neto and C Morais Smith, cond-mat/0304094.

[137] J.M. Tranquada *et al.*, Nature **375**, 561 (1995).

[138] N. Ichikawa *et al.* Phys. Rev. Lett **85**, 1738 (2000).

[139] S-W. Cheong *et al.* Phys. Rev. Lett. **67**, 1791 (1991).

[140] Q. Si *et al.* Phys. Rev. B **47**, 9055 (1993) (and references therein).

[141] K. Yamada *et al.* Phys. Rev. B. **57**, 6165 (1998).

[142] H.A. Mook *et al.* Nature **404**, 729 (2000).

[143] H.A. Mook, P. Dai, and F. Dogan, Phys. Rev. Lett. **88**, 097004 (2002).

[144] J.M. Tranquada, D.J. Buttrey, and V. Sachan, Phys. Rev. B **54**, 12318 (1996).

[145] S. Wakimoto *et al.* Phys. Rev. B **60**, R769 (1999); S. Wakimoto *et al.* Phys. Rev. B **63**, 172501 (2001).

[146] M. Matsuda, Phys. Rev. B **62**, 9148 (2000).

[147] Y. Ando *et al.* Phys. Rev. Lett. **87**, 017001 (2001).

[148] Y. Ando, cond-mat/0206332.

[149] Y. Ando *et al.*, J. Low Temp. Phys. **131**, 793 (2003).

[150] Y. Ando *et al.* Phys. Rev. Lett. **92**, 197001 (2004).

[151] M.P. Lilly *et al.*, Phys. Rev. Lett. **82**, 394 (1999).

[152] M.P. Lilly *et al.*, Phys. Rev. Lett. **83**, 824 (1999).

[153] Y. Ando *et al.* Phys. Rev. Lett. **88**, 137005 (2002).

[154] J. Zaanen and O. Gunnarsson, Phys. Rev. B **40**, 7391 (1989).

[155] D. Poilblanc and T.M. Rice, Phys. Rev. B **39**, 9749 (1989); K. Machida, Physica C **158**, 192 (1989); M. Inui and P.B. Littlewood, Phys. Rev. B **44**, 4415 (1991).

[156] H. Schultz, Phys. Rev. Lett. **64**, 1445 (1990).

[157] K. Machida and M. Ichioka, Jour. Phys. Soc. Jpn. **68**, 2168 (1999).

[158] M. Ichioka and K. Machida, Jour. Phys. Soc. Jpn. **68**, 4020 (1999).

[159] V.J. Emery and S.A. Kivelson, Physica C **209**, 594 (1993).

[160] V.J. Emery, S.A. Kivelson, and H.Q. Lin, Phys. Rev. Lett. **64**, 475 (1990).

[161] S. Rommer, S.R. White, and D.J. Scalapino, Phys. Rev. B **61**, 13424 (2000).

[162] C.S. Shin, Y.C. Chen, and T.K. Lee, cond-mat/0104067.

[163] S. Hellberg and E. Manousakis, Phys. Rev. Lett. **78**, 4609 (1997); Phys. Rev. B **61**, 11787 (2000).

[164] W.O. Putikka, M.U. Luchini, and T.M. Rice, Phys. Rev. Lett. **68**, 538 (1992).

[165] S.R. White and D.J. Scalapino, Phys. Rev. Lett. **80**, 1272 (1998); Phys. Rev. Lett. **81**, 3227 (1998).

[166] O. Zacher Phys. Rev. B **65**, 174411 (2002).

[167] W.V. Liu and E. Fradkin, Phys. Rev. Lett. **86**, 1865 (2001).

[168] H. Eskes *et al.*, Phys. Rev. B **54**, R724 (1996); Phys. Rev. B **58**, 6963 (1998).

[169] N. Hasselmann, A.H. Castro Neto, and C. Morais Smith, Phys. Rev. B **65**, R220511 (2002).

[170] C. Morais Smith *et al.*, Phys. Rev. B **58**, 453 (1998).

[171] Yu.A. Dimashko *et al.*, Phys. Rev. B **60**, 88 (1999).

[172] S.A. Kivelson, E. Fradkin, and V.J. Emery, Nature **393**, 550 (1998).

[173] S. Sorella *et al.* Phys. Rev. Lett. **88**, 117002 (2002).

[174] A.R. Moodenbaugh *et al.* Phys. Rev. B **38**, 4596 (1988).

[175] R.M Fye, M.J. Martins, and R.T. Scalettar, Phys. Rev. B **42**, 6809 (1990).

[176] S. Chakravarty and S.A. Kivelson, Phys. Rev. B **64**, 064511 (2001).

[177] S.R. White and D.J. Scalapino, Phys. Rev. B **55**, 6504 (1997).

[178] S.R. White and D.J. Scalapino, Phys. Rev. B **60**, R753 (1999).

[179] V.J. Emery *et al.* Phys. Rev. Lett. **85**, 2160 (2000).

[180] E. Arrigoni, E. Fradkin, and S.A. Kivelson, cond-mat/0309572.

[181] B.M. Andersen and P. Hedegård, Journal of Low Temperature Physics **131(3)**, 281-285 (2003).

[182] S.C. Zhang, Science **275**, 1089 (1997).

[183] D.P. Arovas, A.J. Berlinsky, C. Kallin and S.-C. Zhang, Phys. Rev. Lett. **79**, 2871 (1997).

[184] D. Vaknin *et al*, Physica C **329**, 109 (2000).

[185] S. Katano *et al.*, Phys. Rev. B **62**, R14677 (2000).

[186] V.F. Mitrovic *et al.*, Nature **413**, 501 (2001).

[187] V.F. Mitrovic *et al.*, Phys. Rev B **67**, 220503 (2003).

[188] K. Kakuyanagi *et al.*, Phys. Rev. Lett. 90, 197003 (2003).

[189] J.E. Hoffman *et al.*, Science **295**, 466 (2002).

[190] C. Howald *et al.*, cond-mat/0208442.

[191] D. Podolsky *et al.*, Phys. Rev. B **67**, 094514 (2003).

[192] D. Zhang, and C.S. Ting, Phys. Rev. B **69**, 012501 (2004); *ibid* **67** 100506 (2003).

[193] H.D. Chen, J.-P. Hu, S. Capponi, E. Arrigoni and S.-C. Zhang, Phys. Rev. Lett **89**, 137004 (2002).

[194] A. Polkovnikov, S. Sachdev, and M. Vojta, Phys. Rev. B **65**, 220509 (2002).

[195] B. Lake *et at.*, Nature **400**, 43 (1999).

[196] B. Lake *et at.*, Science **291**, 1759 (2001).

[197] E. Demler, S. Sachdev, Y. Zhang, Phys. Rev. Lett. **87**, 067202 (2001).

[198] Y. Zhang, E. Demler, and S. Sachdev, Phys. Rev. B **66**, 094501 (2002).

[199] S.A. Kivelson *et al.*, Phys. Rev. B **66**, 144516 (2002).

[200] J-X. Zhu, C.S. Ting, Phys. Rev. Lett **87**, 147002 (2001).

[201] A. Ghosal, C. Kallin, A.J. Berlinsky, Phys. Rev. B **66**, 214502 (2002).

[202] Y. Chen and C.S. Ting, Phys. Rev. B **65** 180513 (2002), Y. Chen, H.Y. Chen and C.S. Ting, cond-mat/0203283.

[203] M. Franz, D.E. Sheeny and Z. Tesanovic, Phys. Rev. Lett. **88**, 257005 (2002).

[204] J-X. Zhu, I. Martin and A.R. Bishop, Phys. Rev. Lett. **89** 067003 (2002).

[205] M. Veilette, Y.B. Bazaliy, A.J. Berlinsky and C. Kallin, Phys. Rev. Lett. **83**, 2413 (1999).

[206] C. Howald, H. Eisaki, N. Kaneko and A. Kapitulnik, cond-mat/0201546; C. Howald, H. Eisaki, N. Kaneko, M. Greven and A. Kapitulnik, cond-mat/0208442.

[207] O. Zachar, S.A. Kivelson, V.J.Emery, Phys. Rev. B **57**, 1422 (1998).

[208] D.W. Lynch, and C.G. Olson,*Photoemission Studies of High-temperature Superconductors (Cambridge Studies in Low Temperature Physics)*, Cambridge University Press (1999).

[209] K. Tanaka *et al.*, cond-mat/0312575.

[210] D.S. Marshall *et al.*, Phys. Rev. Lett. **76**, 4841 (1996).

[211] M. R. Norman and H. Ding, Phys. Rev. B **57**, R11089 (1998).

[212] P. Schwaller *et al.*, Eur. Phys. J. B **18**, 215 (2000).

[213] P.V. Bogdanov *et al.*, Phys. Rev. Lett. **85**, 2581 (2000).

[214] D.L. Feng *et al.*, Phys. Rev. Lett. **86**, 5550 (2001).

[215] A. Ino *et al.*, J. Phys. Soc. Jpn. **68**, 1496 (1999).

[216] A. Ino *et al.*, Phys. Rev. B. **62**, 4137 (2000).

[217] A. Ino *et al.*, Phys. Rev. B **65**, 094504 (2002).

[218] T. Yoshida *et al.*, Phys. Rev. Lett **91**, 027001 (2003).

[219] A. Damascelli, Z.X. Shen, and Z. Hussain, Rev. Mod. Phys. **75**, 473 (2003).

[220] J.C. Campuzano, M.R. Norman, and M. Randeria, cond-mat/0209476.

[221] M.R. Norman, and C. Pepin, cond-mat/0302347.

[222] Q. Huang *et al.*, Phys. Rev. B **40**, 9366 (1989).

[223] X.J. Zhou *et al.*, Science **286**, 268 (1999).

[224] X.J. Zhou *et al.*, Phys. Rev. Lett. **86**, 5578 (2001)

[225] I.M. Salkola, V.J. Emery, and S.A. Kivelson, Phys. Rev. Lett. **77**, 155 (1996).

[226] T. Yoshida *et al.*, Phys. Rev. B **63**, 220501 (2001).

[227] J. Rossat-Mignod *et al.*, Physica C **185-189**, 86 (1991); H. A. Mook *et al.*, Phys. Rev. Lett. **70**, 3490 (1993); H. F. Fong *et al.*, Phys. Rev. Lett. **75**, 316 (1995).

[228] H. F. Fong *et al.*, Nature **398**, 588 (1999).

[229] C. G. Olson *et al.*, Phys. Rev. B, **42**, 381 (1991); Z. X. Shen *et al.*, Phys. Rev. Lett. **70**, 1553 (1993); H. Ding *et al.*, Phys. Rev. Lett. **74**, 2784 (1995).

[230] D. L. Feng *et al.*, Science, **289**, 277 (2000).

[231] D. S. Dessau *et al.*, Phys. Rev. Lett. **66**, 2160 (1991); Phys. Rev. B **45**, 5095 (1992).

[232] H. Ding *et al.*, Phys. Rev. Lett. **76**, 1533 (1996).

[233] A. Kaminski *et al.*, condmat/0004482.

[234] D. H. Lu *et al.*, Phys. Rev. Lett. **86**, 4370 (2001).

[235] Z. X. Shen and J. R. Schrieffer, Phys. Rev. Lett. **78**, 1771 (1997).

[236] T. Dahm, Phys. Rev. B **52**, 14051 (1996); T. Dahm, D. Manske, and L. Tewordt, Phys. Rev. B **54**, 602 (1996).

[237] A. Abanov and A. V. Chubukov, Phys. Rev. Lett. **83**, 1652 (1999); A. Abanov and A. V. Chubukov, Phys. Rev. B **61**, R9241 (2000)

[238] M. R. Norman *et al.*, Phys. Rev. Lett. **79**, 3506 (1997).

[239] J. C. Campuzano *et al.*, Phys. Rev. Lett. **83**, 3709 (1999).

[240] M. Eschrig and M. R. Norman, Phys. Rev. Lett. **85**, 3261 (2000).

[241] J.-P. Hu and S.-C. Zhang, condmat/0108273

[242] S.H. Pan *et. al.*, App. Phys. Lett. **73**, 58 (1998).

[243] E. Demler and S.-C. Zhang, Phys. Rev. Lett. **75**, 4126 (1995); E. Demler, H. Kohno, and S.-C. Zhang, Phys. Rev. B, **58**, 5719 (1998).

[244] S. Rabello, H. Kohno, E. Demler, and S.-C. Zhang, Phys. Rev. Lett. **80**, 3586 (1998).

[245] C.L. Henley, Phys. Rev. Lett. **80**, 3590 (1998).

[246] R. Eder, W. Hanke, and S.-C. Zhang, Phys. Rev B, **57**, 13781 (1997).

[247] J. R. Schrieffer, *Theory of Superconductivity*, Frontiers in physics, The Benjamin/Cummings Publishing Com. Inc. (1964).

[248] M. R. Norman, M. Randeria, H. Ding, and J. C. Campuzano, Phys. Rev. B **52**, 615 (1995).

[249] M. Randeria *et al.*, Phys. Rev. Lett. **74**, 4951 (1995).

[250] A. Bansil and M. Lindross, Phys. Rev. Lett. **83**, 5154 (1999).

[251] S. Hüfner, *Photoelectron Spectroscopy*, Berlin Springer-Verlag (1996).

[252] J. R. Schrieffer, D. J. Scalapino and J. W. Wilkins, Phys. Rev. Lett. **10**, 336 (1963); D. J. Scalapino, in *Superconductivity*, edited by R. D. Parks, New York, Volume 1, 561 (1969).

[253] J. M. Rowell, P. W. Anderson and D. E. Thomas, Phys. Rev. Lett. **10**, 334 (1963).

[254] M. Granath *et al.*, Phys. Rev. B **65**, 184501 (2002).

[255] H.D. Chen *et al.* cond-mat/0402323.

[256] M. Ichioka, and K. Machida, J. Phys. Soc. Jpn. **71**, 1836 (2002).

[257] G. Seibold *et al.*, cond-mat/9906108.

[258] T. Tohyama *et al.*, Phys. Rev. Lett. **82**, 4910 (1999).

[259] M. Fleck *et al.*, Phys. Rev. Lett. **84**, 4962 (2000).

[260] M.G. Zacher *et al.*, Phys. Rev. Lett. **85**, 2585 (2000).

[261] R.S. Markiewicz, Phys. Rev. B **62**, 1252 (2000).

[262] R. Eder, and Y. Ohta, cond-mat/0308184.

[263] M. Granath, cond-mat/0401063.

[264] E.W. Carlson *et al.*, Phys. Rev. B **62**, 3422 (2000)

[265] D. Orgad *et al*, Phys. Rev. Lett. **86**, 4362 (2001).

[266] M. Vojta, Y. Zhang, and S. Sachdev, Int. J. Mod. Phys. B **14**, 3719 (2000).

[267] I.P. Bindloss, and S.A. Kivelson, cond-mat/0402457.

[268] S.W. Lovesey, *Theory of neutron scattering from condensed matter*, Volume 2, Clarendon Press, Oxford (1984).

[269] P. Dai *et al.*, Phys. Rev. B **63**, 054525 (2001).

[270] P. Bourges, in *Neutron Scattering in Novel Materials*, (8th PSI Summer School on Neutron scattering, Zuoz, Switzerland), Ed. A. Furrer (World Scientific, 2000). cond-mat/0009373.

[271] K. Lefmann *et al.*, *unpublished*.

[272] D. Vaknin *et al.*, Phys. Rev. Lett. **58**, 2802 (1987).

[273] J.M. Tranquada *et al.*, Phys. Rev. Lett. **73**, 1003 (1994); Phys. Rev. B **52**, 3581 (1995).

[274] C.H. Chen *et al.*, Phys. Rev. Lett. **71**, 2461 (1993)

[275] J.M. Tranquada *et al.*, Phys. Rev. Lett. **79**, 2133 (1997)

[276] H. Yoshizawa *et al.*, Phys. Rev. B **61**, R854 (2000).

[277] S.H. Lee *et al.*, Phys. Rev. Lett. **88**, 126401 (2002).

[278] A.T. Boothroyd *et al.*, Phys. Rev. B **67**, 100407 (2003).

[279] P. Bourges *et al.*, Phys. Rev. Lett. **90**, 147202 (2003).

[280] N.B. Christensen *et al.*, cond-mat/0403439.

[281] J.M. Tranquada *et al.*, cond-mat/0401621.

[282] M. Fujita *et al.*, cond-mat/0403396.

[283] H.A. Mook, P. Dai, and F. Dogan, Phys. Rev. Lett.**88**, 097004 (2002).

[284] H.A. Mook *et al.*, Nature **395**, 580 (1998).

[285] M. Arai *at al.*, Phys. Rev. Lett. **83**, 608 (1999).

[286] P. Bourges *et al.*, Science **288**, 1234 (2000).

[287] P. Dai *et al.*, Nature **406**, 965 (2000).

[288] P. Dai *et al.*, Science **284**, 1344 (1999).

[289] D. Reznik *et al.*, cond-mat/0307591.

[290] H. He *et al.*, Science **295**, 1045 (2002).

[291] S. Wermbter, and L. Tewordt, Phys. REv. B **43**, 10530 (1991).

[292] Q. Si *et al.*, Phys. Rev. B **45**, 4930 (1992); Phys. Rev. B **47**, 9055 (1993).

[293] N. Bulut *et al.*, Phys. Rev. Lett. **64**, 2723 (1990).

[294] N. Bulut, and D.J. Scalapino, Phys. Rev. B **47**, 3419 (1993); Phys. Rev. B **50**, 16078 (1994).

[295] M. Lavagna, and G. Stemmann, Phys. Rev. B **49**, 4235 (1994).

[296] T. Dahm, D. Manske, and L. Tewordt, Phys. Rev. B **58**, 12454 (1998).

[297] J. Brinckmann, and P.A. Lee, Phys. Rev. Lett. **82**, 2915 (1999); Phys. Rev. B **65**, 014502 (2001).

[298] Y.-J. Kao, Q. Si, and K. Levin, Phys. Rev. B **61**, R11898 (2000).

[299] M. Norman, Phys. Rev. B **63**, 092509 (2001).

[300] F. Onufrieva, and P. Pfeuty, Phys. Rev. B **65**, 054515 (2002).

[301] A.V. Chubukov, B. Janko, and O. Tchernyshyov, Phys. Rev. B **63**, 180507 (2001).

[302] S. Pailhes *et al.*, cond-mat/0403609.

[303] A.H. Castro Neto, and D. Hone, Phys. Rev. Lett. **76**, 2165 (1996).

[304] C.N.A. Duin, and J. Zaanen, Phys. Rev. Lett. **78**, 3019 (1997).

[305] C.D. Batista, G. Ortiz, and A.V. Balatsky, Phys. Rev. B **64**, 172508 (2001).

[306] F. Krüger, and S. Scheidl, Phys. Rev. B **67**, 134512 (2003); cond-mat/0401354.

[307] N. Hasselmann *et al.*, Phys. Rev. Lett. **82**, 2135 (1999).

[308] E. Fradkin, *Field theories of condensed matter systems*, Frontiers in Physics (Addison-Wesley, 1991).

[309] M. Vojta, and T. Ulbricht, cond-mat/0402377.

[310] G.S. Uhrig, K.P. Schmidt, and M. Grüninger, cond-mat/0402659.

[311] E. Demler, W. Hanke, and S.C. Zhang, cond-mat/0405038.

[312] F.D.M. Haldane, Phys. Rev. Lett. **50**, 1153 (1983).

[313] S. Chakravarty, Nelson, and B.I. Halperin, Phys. Rev. Lett. **60**, 1057 (1988); Phys. Rev. B **39**, 2344 (1989).

[314] C.P. Burgess *et al.*, Phys. Rev. B **57**, 8549 (1998).